Department of Physics
Indian Institute of Technology Guwahati
Ph.D. Thesis

Some studies of the semileptonic B-meson decays via the neutral and charged current exchanges.

Ipsita Ray

Supervisor: Dr. Soumitra Nandi
May, 2023.

TH-3118_176121005

TH-3118_176121005

Some studies of the semileptonic B-meson decays via the neutral and charged current exchanges.

A thesis submitted by

Ipsita Ray

to

Indian Institute of Technology Guwahati
for the award of the degree of
Doctor of Philosophy in Physics

Department of Physics
Indian Institute of Technology Guwahati
Guwahati - 781039, Assam, India

TH-3118_176121005

TH-3118_176121005

Declaration

The work contained in the thesis entitled **"Some studies of the semileptonic B-meson decays via the neutral and charged current exchanges."** has been carried out at the Department of Physics, Indian Institute of Technology Guwahati, India by me under the supervision of Dr. Soumitra Nandi. The material of this thesis has not been submitted elsewhere for any other degree. Works presented in the thesis are all my own unless referenced to the contrary in the text.

Ipsita Ray
Department of Physics
Indian Institute of Technology Guwahati
Guwahati - 781039, India.

Date: 23.05.23

TH-3118_176121005

TH-3118_176121005

Certificate

It is certified that the work contained in the thesis entitled **"Some studies of the semileptonic B-meson decays via the neutral and charged current exchanges."** by Ms. Ipsita Ray, a Ph.D. student of the Department of Physics, Indian Institute of Technology Guwahati is carried out under my supervision and has not been submitted elsewhere for the award of any other degree.

Dr. Soumitra Nandi
Associate Professor
Department of Physics
Indian Institute of Technology Guwahati
Guwahati - 781039, India

Date: 23.05.23

TH-3118_176121005

TH-3118_176121005

To

My Parents (Utpal Kumar Ray and Pratiti Ray)

and

in memory of my grandparents

TH-3118_176121005

TH-3118_176121005

Acknowledgement

I feel grateful towards several people who have helped and supported me throughout my life in so many ways.

First of all, I express my sincerest gratitude to my supervisor Dr. Soumitra Nandi for his constant support and encouragement during my Ph.D tenure which helped me to pursue my Ph.D work so smoothly. It has been a wonderful opportunity for me to work with him and the experiences I have gained during this period will help me in my future endeavors. I have always been motivated by his knowledge and dedication for work. I have benefited a lot from the discussions on the research projects and also various aspects of high energy physics. I feel really privileged to work with him and thank him for giving me an opportunity to be involved in some interesting projects which I have enjoyed to be a part of.

I would like to thank my doctoral committee members - Dr. Debasish Borah, Dr. Arunansu Sil and Dr. Sovan Chakraborty for their valuable suggestions during the yearly assessments of my research work. I am highly thankful to my collaborators Dr. Sunando Patra and Dr. Aritra Biswas for their support and useful suggestions from which I have learnt a lot. I also thank all the high energy faculty members Dr. Subhaditya Bhattacharya, Dr. Poulose Poulose, Dr. Santabrata Das, Dr. Sayan Chakrabarti, Dr. Meduri C Kumar, Dr. Debaprasad Maity, Dr. Bibhas Ranjan Majhi, Dr. Udit Raha and Dr. Bipul Bhuyan of IIT Guwahati for useful discussions on various relevant topics in the journal club meetings.

I would also like to acknowledge the instructors who taught us during the PhD course work - Dr. Meduri C Kumar, Dr. Udit Raha, Dr. P.K Giri and Dr. P.K Padmanabhan.

I thank all HODs (Prof. Subhradip Ghosh, Prof. Perumal Alagarsamy) during my Ph.D study. I would like to thank all the technical assistants, academic and non-academic staff of the department who helped me in various ways during my research period.

It is my pleasure to thank my seniors Dr. Srimoy Bhattacharya, Sneha Jaiswal, Dr. Lopamudra Mukherjee and juniors Shantanu Sahoo, Lipika Kolay and Utsab Dey, who have helped me in several ocassions. I have discussed several things with them which helped me clarify my understanding. I also thank Dr. Ria Sain, Dr. Rishav Roshan, Dr. Dibyendu Nanda and Dr. Kajal Samanta for useful discussions on various topics.

I would like to thank all my batchmates without whom my Ph.D life wouldn't have

TH-3118_176121005

been so memorable. Thank you Madhurima for always being so supportive and helpful in various academic (specially latex-related problems) and non-academic issues. I also thank Arghyajit, Devabrat, Devender, Manisha, Santa, Neetu, Shilpi, Prajna, Pragya, Dhriti, Pronoy, Sanket, Samit and Subrata for the beautiful memories we created together. I am highly thankful to all the friends I have met in my life for their support and encouragement.

Most importantly, I am extremely grateful to my parents Mr. Utpal Kumar Ray and Mrs. Pratiti Ray for their love and encouragement throughout my life. I owe everything to them. I thank Prasangsha and his family members for their constant encouragement. I also thank all my relatives and cousins for their immense love and support.

I miss my paternal and maternal grandparents, who have passed away but have left a vivid memory of their affection and blessings for me. This thesis is dedicated to their memories.

TH-3118_176121005

Abstract

This thesis focuses on the study of the semileptonic $B(B_s)$ meson decays via the neutral and charged current exchanges. The charged current transitions occur at tree level in the Standard Model (SM) and the branching fractions of the semileptonic decays of B mesons to lighter leptons (electron and muon) in the final state as considered in this thesis have been determined to be mostly SM-like. In such cases, the charged current transitions provide an important avenue for the clean extraction of the Cabibbo-Kobayashi-Maskawa (CKM) matrix elements which is very crucial for understanding the CKM structure of the Standard Model and for precise theoretical predictions of several observables. In this thesis, we have studied the extraction of the CKM elements $|V_{ub}|$, $|V_{cb}|$, and the ratio $|V_{ub}|/|V_{cb}|$ which are relatively less precisely known. It has been observed that the extracted values of $|V_{cb}|$ and $|V_{ub}|$ from the inclusive decays are larger as compared to those extracted from the corresponding exclusive decays ($B \to D^{(*)}\ell\nu$ and $B \to \pi\ell\nu$). The discrepancy between the exclusive and inclusive determinations is more for $|V_{ub}|$. Explaining this discrepancy with new physics is difficult as pointed out in some of the earlier analyses in the literature. These are the long standing puzzles, so far no convincing arguments addressing these puzzles are available in the literature. This could be due to our lack of understanding of the non-perturbative unknowns. Also the methodology adopted by the Heavy Flavor Averaging Group (HFLAV) for the exclusive determination from $B \to \pi\ell\nu$ decays is not very clean. In this thesis, we have studied the $B \to \pi\ell\nu$ decay modes reconsidering other possible ways of analyzing the available data and pin-point the source of the discrepancy as mentioned above. We have utilized the newly available inputs on the form-factors from Light Cone Sum Rules (LCSR) approach along with the Lattice QCD computations. It has been found that the BaBar 2011 dataset is in tension with the other datapoints and it is also influential in the extraction of $|V_{ub}|^{exc}$ and could be the probable source of discrepancy between the exclusive and inclusive determinations. We have also considered other exclusive $b \to u\ell\nu$ channels for eg. $B \to \rho(\omega)\ell\nu$ for a combined extraction of $|V_{ub}|$ and the exclusive $b \to c\ell\nu$ channels for eg. $B(B_s) \to D^{(*)}(D_s^{(*)})\ell\nu$ for combined extraction of $|V_{cb}|$. We have obtained the ratio $|V_{ub}|/|V_{cb}|$ from the experimental measurements and form factor inputs in the mesonic $b \to c(u)l\nu$ decays independently and also after incorporating the ratio $\mathrm{BR}(B_s \to K\mu\nu)/\mathrm{BR}(B_s \to D_s\mu\nu) \propto |V_{ub}|^2/|V_{cb}|^2$ in the two bins of $B_s \to K$ momentum transfer measured by LHCb. Our value for $|V_{ub}|/|V_{cb}|$

TH-3118_176121005

is consistent with the determination from the ratio of partial rates of baryonic decays $\mathrm{BR}(\Lambda_b \to p\mu\nu)/\mathrm{BR}(\Lambda_b \to \Lambda_c\mu\nu)$ from LHCb.

Apart from the charged current transitions, we have also studied the Flavor Changing Neutral Current (FCNC) transitions which being loop-suppressed in the SM are highly sensitive to new physics (NP) effects at higher energy scales and any deviation of the experimental measurements from the SM predictions signify the possibility of beyond SM (BSM) particles. Over the last few years, the low-energy experiments in B physics have shown some anomalous results indicating an indirect hint of new physics. In the neutral current sector in the $B(B_s) \to K^{(*)}(\Phi)$ modes, the various experimental collaborations have measured several observables, such as the Lepton Flavor Universality Violating observables $R_{K^{(*)}} = \mathcal{B}(\bar{B} \to K^{(*)}\mu^+\mu^-)/\mathcal{B}(\bar{B} \to K^{(*)}e^+e^-)$ and a plenty of angular observables, out of which some have shown deviation from their respective SM expectations. This thesis addresses this issue by extending the SM framework with dimension six operators in a model-independent effective field theory approach to find out the operator or sets of operators which can provide plausible explanation to the present data. In general in a NP model, besides the one-operator scenarios, some multi operator scenarios may also contribute to the processes under study and may provide possible explanation to the observed anomalous results which necessitates the role of model selection. In this regard, we have employed Akaike Information Criterion and Cross-Validation to select the best possible combinations of operators most compatible with the available data in this channel. In addition to the $b \to s\ell\ell$ channels, we have also analysed the exclusive $b \to d\ell\ell$ ($B \to \pi\ell\ell$ and $B \to \rho\ell\ell$) transitions in this thesis which may offer another window to look for beyond SM phenomenon. The non-vanishing direct CP asymmetry and low branching ratios of these decay modes in the SM further motivates a systematic analysis of these modes within the framework of the SM and also in some NP scenarios. We have predicted several observables in these channels for eg. the branching fractions, direct CP asymmetries, isospin asymmetry and various angular observables in the SM and also compared the sensitivities of these observables towards the different NP scenarios. If the future measurements report a deviation with respect to the SM predictions in these channels, it will be possible to identify the type of new physics interaction from the pattern of the results.

TH-3118_176121005

TH-3118_176121005

List of publications included in this Thesis:

- **"New physics in $b \to sll$ decays with complex Wilson coefficients"**,
  Aritra Biswas, Soumitra Nandi, Sunando Kumar Patra, Ipsita Ray,
  arXiv: 2004.14687 (hep-ph)
  Published in Nucl.Phys.B 969 (2021) 115479

- **"A closer look at the extraction of $|V_{ub}|$ from $B \to \pi l \nu$"**,
  Aritra Biswas, Soumitra Nandi, Sunando Kumar Patra, Ipsita Ray,
  arXiv: 2103.01809 (hep-ph)
  Published in JHEP 07 (2021) 082

- **"Study of the $b \to d\ell\ell$ transitions in the Standard Model and test of New Physics sensitivities"**,
  Aritra Biswas, Soumitra Nandi, Sunando Kumar Patra, Ipsita Ray,
  arXiv: 2208.14463

- **"Constraining the ratio $|V_{ub}|/|V_{cb}|$ from exclusive decays."**, in preparation with Aritra Biswas and Soumitra Nandi.

TH-3118_176121005

Contents

TH-3118_176121005

TH-3118_176121005

भारतीय प्रौद्योगिकी संस्थान गुवाहाटी • Indian Institute of Technology Guwahati •

TH-3118_176121005

List of Figures

TH-3118_176121005

TH-3118_176121005

TH-3118_176121005

List of Tables

TH-3118_176121005

TH-3118_176121005

TH-3118_176121005

TH-3118_176121005

TH-3118_176121005

TH-3118_176121005

Chapter 1

Introduction

Over the years, there have been significant scientific breakthroughs aiming to understand the fundamental laws of nature that are essential in making up the world we live in. Human civilization has strived to perceive the microscopic as well as the macroscopic aspects, from the small-scale structures like atoms and molecules to the universe at a large scale. The advancement in science proceeds through the parallel progress in experimental discoveries and theoretical ideas. Any existing theory needs to be substantiated by active experimentation, or else it is discarded, thus opening the possibilities for newer theories. A successful theory is the one that can provide possible explanations for the observations as well as pave the way for future discoveries or give predictions that can be verified in the experiments.

The Standard Model (SM) of elementary particles has succeeded in explaining many observations in the high energy experiments [9–11]. The SM theory beautifully accommodates the three fundamental forces of nature: strong, electromagnetic and weak forces. Also, the SM is successful in explaining the classification of all elementary particles. The experimental confirmation of the existence of quarks led to widespread acceptance of the Standard Model. It also gave predictions for the Z and W bosons, the charm and the top quark which were later discovered [12–19]. In the SM, elementary particle's masses are obtained via the Higgs mechanism in which the essential ingredient is the Higgs boson. The experimental validation of the SM was complete with the revelation of the Higgs boson at the Large Hadron Collider (LHC) in 2012 [20, 21].

Though being a successful theory so far, there are some observed phenomenon which signify that the SM isn't the complete theory of nature, for example, the presence of dark matter [22], the origin of nonzero neutrino masses [23–26], matter-antimatter asymmetry [27, 28] and accelerating expansion of the universe [29] can't be explained within the realm of the SM. Also, there are concerns like the Higgs mass hierarchy problem [30] and the strong CP problem [31, 32] for which the SM does not have suitable answers. The radiative correction to the square of the Higgs mass at the first order receives a quadratically divergent term arising from the contribution of Standard Model fermions in

TH-3118_176121005

the loops, thus resulting in a correction which may be somewhat larger than the mass of the Higgs Boson in the Standard Model. As it is pretty evident that the SM isn't the ultimate theory, it is possible that there might be some more fundamental theory at the high energy scales with new heavy particles. In such cases, the correction to the mass of the Higgs can be very large and thus, extreme finetuning cancellation is required between the large bare mass and large quantum corrections, leaving a result in the same ballpark as the observed Higgs mass. The strong-CP problem is related to the small value of the θ parameter associated with an additional term in the QCD Lagrangian, which arises from one of the redefinitions of the quark fields.

$$\mathcal{L} = \theta \frac{g^2}{16\pi^2} F^a_{\mu\nu} \tilde{F}^{\mu\nu a} \tag{1.1}$$

where g is the strong coupling constant, $F^a_{\mu\nu}$ represents gluon field strength tensors, $\tilde{F}^{\mu\nu a} = \frac{1}{2}\epsilon^{\mu\nu\rho\sigma} F^a_{\rho\sigma}$ and $\epsilon^{\mu\nu\rho\sigma}$ is the anti-symmetric tensor. The above term is CP violating and can contribute to the neutron electric dipole moment (EDM), but CP violation hasn't yet been observed in the experiments involving only strong interactions. The parameter $\theta << 10^{-10}$ radians from current experimental limits on neutron EDM [33].

Another interesting feature which the SM can't explain is the hierarchy observed in the couplings and the quarks' and leptons' masses of different generations. These open problems signify the need to extend the SM further with the inclusion of new particles, which can either be directly searched at the high-energy colliders or can be indirectly probed through their virtual effects in low-energy experiments. Though there hasn't been any evidence of direct production of beyond Standard Model particles at the colliders so far, there may be a significant advancement in the direct search for new particles in the near future with an increase in the luminosity reached and the mass scales probed at the existing and future colliders. Thus, for the present scenario, one plausible way to study the New Physics (NP) effects is through the deviations of various precision observables from their respective predictions in the SM in the ongoing experiments.

In this regard, the decays of the K, D, B and B_s mesons, called flavoured mesons, offer excellent ground to test the various aspects of the SM and to search for possible signatures of new physics beyond the SM (BSM). The discovery of the Kaons in 1947 in the cosmic rays led to the establishment of the theory of quark mixing. Moreover, CP violation was observed in $K^0 - \bar{K^0}$ mixing for the first time in 1964 [34], and direct CP violation was discovered in the decays of Kaon by Fermilab's KTeV experiment and CERN's NA48 experiment in the early 2000s [35]. The charmed mesons (D meson) discovered at the Stanford Linear Accelerator Center by the Mark I detector in 1976 are the lightest particles containing charm quarks. The theoretical aspect in these decays is the non-perturbative QCD affecting predictions in charm physics. In charm decays, CP violation was first observed by LHCb in 2019 by measuring the nonzero difference in the CP asymmetries

TH-3118_176121005

(time-integrated) of $D^0 \to \pi^+\pi^-$ and $D^0 \to K^+K^-$ decays [36]. Recently, a nonzero mass difference has been observed in the neutral charm eigenstates by LHCb [37]. The B meson decays were first fully reconstructed in 1983 by the CLEO collaboration [38]. Measurements of CP violation have been performed in $B^0 - \bar{B}^0$ oscillations through studies on the time-dependence of the neutral B-meson decays to charmonium final states [39, 40]. Also, the BaBar and LHCb have measured the direct CP violation in $B^0 \to K^+\pi^-$ [41] and $B_s^0 \to K^-\pi^+$ [42] decays, respectively. Oscillations are also observed in the B_s systems [43].

This thesis mostly focuses on the studies of the semileptonic $B(B_s)$-meson decays. There is a huge advantage with the b quark: its mass is just right ($\Lambda_{QCD}/m_b \sim 0.2$) to ensure a systematic expansion in $1/m_b$. Since the B meson has a low transition rate (lifetime $\sim 10^{-12}$ s), its detection is relatively easy in experiments. Thus, the study of the decays and mixings in the B-hadron systems remains an extensive area of research both from the experimental and theoretical viewpoints providing further insights into our understanding of the SM and BSM.

In the subsequent sections of Chapter 1, a brief overview of flavor physics in the SM is provided (more detailed reviews can be found in refs. [44–46]). The present experimental status of various observables in the flavor sector is also presented.

1.1 The Standard Model flavor sector

The Standard model consists of these basic ingredients :

- The gauge symmetry of the model: $SU(3)_C \times SU(2)_L \times U(1)_Y$ with eight gluons, three weak bosons and a photon. Here, $SU(3)_C$ constitutes the strong interactions of the gluons and quarks, which carry color charges. The $SU(2)_L$ and $U(1)_Y$ speak for the weak isospin and hypercharge interactions, respectively.

- Matter representations: The left-handed lepton and quark doublets are represented by L_L^i and Q_L^i, respectively. The down-type and up-type quark singlets are d_R^i, u_R^i, and e_R^i are the lepton singlets which are right-handed. There is also a complex scalar Higgs field Φ. In table 1.1, gauge quantum nos. of the SM fields are provided.

- The non-zero value of the vacuum expectation of Φ results in the breaking of $SU(2)_L \times U(1)_Y$ spontaneously to $U(1)_{EM}$.

The renormalizable Lagrangian in its most general form in the SM is given below:

$$\mathcal{L}_{SM} = \mathcal{L}_{kin} + \mathcal{L}_{Higgs} + \mathcal{L}_{Yuk} \tag{1.2}$$

TH-3118_176121005

	$SU(3)_C$	$SU(2)_L$	$U(1)_Y$
Q_L^i	3	2	1/6
u_R^i	3	1	2/3
d_R^i	3	1	-1/3
L_L^i	1	2	-1/2
e_R^i	1	1	-1
Φ	1	2	1/2

Table 1.1: The gauge quantum numbers of the SM particle content.

where the different contributions are given as

$$\mathcal{L}_{kin} = \frac{-1}{4} \sum_{groups} (F_{\mu\nu}^a)^2 + \sum_{rep's} \bar{\psi} i \not{D} \psi \tag{1.3}$$

$$\mathcal{L}_{Higgs} = |D_\mu \Phi|^2 + \mu^2 \Phi^\dagger \Phi - \lambda (\Phi^\dagger \Phi)^2 \tag{1.4}$$

$$\mathcal{L}_{Yuk} = y_{ij}^e \bar{L}^i \Phi e_R^j + y_{ij}^d \bar{Q}^i \Phi d_R^j + y_{ij}^u \bar{Q}^i \tilde{\Phi} u_R^j, \tag{1.5}$$

where the covariant derivative is

$$D^\mu = \partial^\mu + i g_s G_a^\mu T^a + i g W_b^\mu L^b + i g' B^\mu Y. \tag{1.6}$$

Here, G_a^μ, W_b^μ, and B^μ are the gluon fields, weak bosons, and the hypercharge boson, respectively. T^as and L^bs are the generators of $SU(3)_C$ and $SU(2)_L$, respectively, while the Ys are $U(1)_Y$ charges. The couplings g', g and g_s, correspond to the strengths of each force mentioned above.

The $\mathcal{L}_{kin}$ in eq. 1.3 represents the kinetic term associated with the gauge fields and the fermions while the $\mathcal{L}_{Higgs}$ in eq. 1.4 describes the Higgs kinetic term and the potential which plays a vital role in the spontaneous symmetry breaking. Here, μ^2 is taken to be negative in order to induce electroweak symmetry breaking and $\lambda > 0$ is chosen to ensure vacuum stability.

The term $\mathcal{L}_{Yuk}$ defined in eq. 1.5 refers to the Yukawa part of the Lagrangian, where $\tilde{\Phi} = i\sigma_2 \, \Phi^\dagger$, σ_2 being one of the Pauli matrices. Here, y_{ij}^e and $y_{ij}^{d,u}$ represent the lepton and quark Yukawa couplings, respectively. The first term in eq. 1.5 represents the Lepton Yukawa term, and the last two terms refer to the quark Yukawa sector. Due to the spontaneous symmetry breaking, the scalar field Φ gets a vacuum expectation value (vev), $\langle \Phi \rangle = (0, \frac{v}{\sqrt{2}})$, which after substituting in eq. 1.5, the masses for the leptons and quarks are obtained as

$$m_{ij}^{L,q} = \frac{v}{\sqrt{2}} y_{ij}^{L,q}. \tag{1.7}$$

The Yukawa couplings consist of a large number of free parameters. The quark Yukawa's are described by ten physical parameters, six of them represent the masses of the quarks,

TH-3118_176121005

and the rest of the four are essential to parameterize the Cabibbo-Kobayashi-Maskawa (CKM) Matrix. The structure of the CKM matrix and the relevant phenomenology is discussed in detail in the following subsection 1.1.1.

1.1.1 The Cabibbo-Kobayashi-Maskawa Matrix

As we discussed in the last section, after the spontaneous symmetry breaking, the Higgs vev yields the following mass terms for quarks

$$\mathcal{L}_{mass} = m^d_{ij}\bar{d^i_L}d^j_R + m^u_{ij}\bar{u^i_L}u^j_R \tag{1.8}$$

where the mass matrices are given in eq. 1.7. The Yukawa matrices and hence the mass matrices m^qs aren't diagonal in general and contain several unphysical parameters. Thus, we move to a basis where these mass matrices are diagonal which we call the mass basis. One can diagonalize the matrices in the flavour basis through a bi-unitary transformation to remove the unphysical parameters. The two unitary matrices V^q_R and V^q_L can be chosen so that

$$\hat{m}^q_{ij} = (V^q_L)_{ik} m^q_{kl} (V^{q\dagger}_R)_{lj}, \tag{1.9}$$

This diagonalization rotates the left chiral and right chiral fields as

$$q^i_L = (V^q_L)_{ij} q'^j_L, \qquad q^i_R = (V^q_R)_{ij} q'^j_R. \tag{1.10}$$

In the above equations, the left hand side represents the field in the interaction basis, while the right hand side corresponds to the linear combination of the fields in the mass basis. Here, we work in the mass basis and drop the prime.

The proportionality between the mass matrices and the Yukawa matrices renders diagonal Yukawa interactions in the mass basis whereas the W coupling is off-diagonal. On transforming to the mass basis from the interaction basis, we have

$$\mathcal{L}_{Wqq} = -\frac{g}{2}\bar{Q}_L\gamma^\mu W^a_\mu T_a Q_L + h.c. \rightarrow -\frac{g}{\sqrt{2}}\bar{U}_L\gamma^\mu (V_{uL}V^\dagger_{dL}) D_L W^+_\mu + h.c, \tag{1.11}$$

where $W^\pm_\mu = (W^1_\mu \pm W^2_\mu)/\sqrt{2}$. In the denominator of eq. 1.11, the factor of $\sqrt{2}$ results from the normalization of the $W^\pm$ states with respect to the $W^{1,2}$ states.

The CKM matrix is identified as

$$V_{CKM} = V_{uL}V^\dagger_{dL} \tag{1.12}$$

Thus, the CKM matrix arises from a basis rotation and is the only source of flavor-changing interactions of quarks within the SM. Also, the CKM matrix is unitary i.e $V_{CKM}V^\dagger_{CKM}$ = **1**.

The unitarity condition of the CKM matrix and redefinition of the quark fields help

TH-3118_176121005

to reduce the initial nine complex elements of the CKM matrix to three real numbers (the three mixing angles) and one phase (the only source of CP-violation within the SM). The CKM elements are transformed as $V_{ij} \to e^{i(a_j^d - a_i^u)} V_{ij}$ under the field redefintions $u_L^i \to e^{ia_i^u} u_L^i$ and $d_L^i \to e^{ia_i^d} d_L^i$. Thus, the moduli of the elements $|V_{ij}|$ and the combinations $V_{ai}V_{aj}^*/V_{bi}V_{bj}^*$ are phase-convention independent quantities.

The CKM matrix can be parameterized in several ways. The Standard Parametrization is given as [47]:

$$\begin{pmatrix} c_{13}c_{12} & c_{13}s_{12} & s_{13}e^{-i\delta} \\ -c_{23}s_{12} - c_{12}s_{23}s_{13}e^{i\delta} & c_{23}c_{12} - s_{12}s_{23}s_{13}e^{i\delta} & c_{13}s_{23} \\ s_{23}s_{12} - c_{12}c_{23}s_{13}e^{i\delta} & -s_{23}c_{12} - s_{12}c_{23}s_{13}e^{i\delta} & c_{13}c_{23} \end{pmatrix} \tag{1.13}$$

where $s_{ij} = \sin\theta_{ij}$ and $c_{ij} = \cos\theta_{ij}$ $(i, j = 1,2,3)$. θ_{ij}s are the three mixing parameters and δ is the CKM phase. From experiments, we know that all mixing angles are small and they follow the hierarchy $s_{13} \ll s_{23} \ll s_{12} \ll 1$ [48]. The most useful parameterization is the Wolfenstein parameterization [49], according to which each CKM element is expressed as an expansion in the parameter, $\lambda = |V_{us}| \sim 0.22$. We need four independent parameters to describe all the elements of a 3×3 unitary matrix. According to Wolfenstein, these parameters are (λ, A, ρ, η), where η is the CP-violating phase. Hence, following this parametrization, the CKM matrix can be expressed as

$$\begin{pmatrix} 1 - \frac{\lambda^2}{2} & \lambda & A\lambda^3(\rho - i\eta) \\ -\lambda & 1 - \frac{\lambda^2}{2} & A\lambda^2 \\ A\lambda^3(1 - \rho - i\eta) & -A\lambda^2 & 1 \end{pmatrix} + O(\lambda^4) \tag{1.14}$$

From the unitarity of the CKM matrix, we obtain the following constraints:

$$\sum_m V_{mn}V_{mk}^* = \delta_{nk}, \qquad \sum_n V_{mn}V_{kn}^* = \delta_{mk}. \tag{1.15}$$

From these constraints, we will get six vanishing combinations for the off-diagonal elements. These combinations are represented as triangles in the complex $\rho - \eta$ plane. Among these relations, the particularly interesting one is given below

$$V_{ud}V_{ub}^* + V_{cd}V_{cb}^* + V_{td}V_{tb}^* = 0. \tag{1.16}$$

This equation contains the sum of three terms of the same order in the Wolfenstein parameter λ. It is called "The Unitarity Triangle" as it looks more like a triangle than a line as represented in fig. 1.1.

In terms of the elements of the CKM matrix, the angles of the unitarity triangle are

TH-3118_176121005

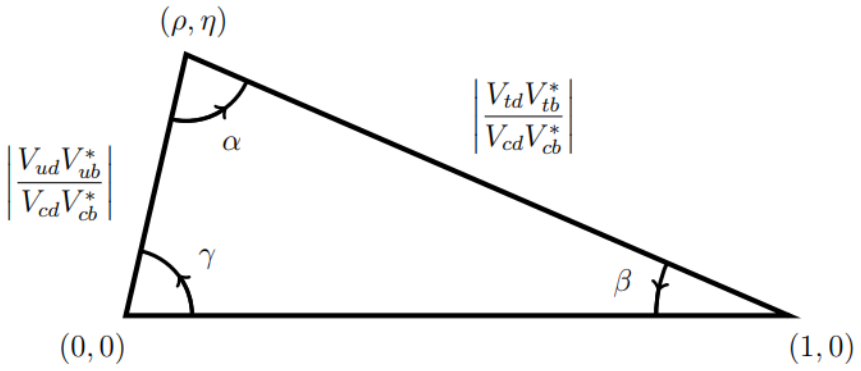

Figure 1.1: Unitarity Triangle in the complex $\rho - \eta$ plane.

expressed as

$$\alpha = \arg\Big(-\frac{V_{tb}^* V_{td}}{V_{ub}^* V_{ud}}\Big), \quad \beta = \arg\Big(-\frac{V_{cb}^* V_{cd}}{V_{tb}^* V_{td}}\Big), \quad \gamma = \arg\Big(-\frac{V_{ub}^* V_{ud}}{V_{cb}^* V_{cd}}\Big) \tag{1.17}$$

and the length of the sides are given as

$$R_u = \frac{|V_{ub}^* V_{ud}|}{|V_{cb}^* V_{cd}|} = \sqrt{\rho^2 + \eta^2}, \qquad R_t = \frac{|V_{tb}^* V_{td}|}{|V_{cb}^* V_{cd}|} = \sqrt{(1-\rho)^2 + \eta^2} \tag{1.18}$$

From the normalization, the length of the remaining side will become unity. Constraining the sides and angles of the unitarity triangle is central to understanding the SM's fundamental aspects and the CP-violating effects. The angles and sides are determined from different processes, as will be discussed in section 1.3.

1.2 Charged versus neutral currents in the Standard Model

By choosing the mass basis for the quarks, only the W-boson couplings are flavor off-diagonal i.e. they can couple to different generations of the quark mass eigenstates, whereas the interactions of neutral bosons are flavor conserving. Thus, in the SM, the flavor-changing charged current (FCCC) interactions occur at tree level, while flavor-changing neutral current (FCNC) interactions are prohibited at tree level by having universal or diagonal couplings in the mass basis. The relevant Standard Model bosons mediating neutral current interactions are the photon, gluons, the Higgs and the Z boson.

The gluons and photon are protected from tree-level FCNCs as long as QCD and QED remain unbroken. This is because the gauge symmetry forces the kinetic terms to be universal. Hence the couplings of the gluons and photon to fermions will be diagonal. The Higgs couplings are diagonal in the mass basis due to the proportionality between the Higgs couplings to the fermions and the fermion mass matrices.

For the Z boson, the Lagrangian describing the coupling to up-type quarks,

TH-3118_176121005

$$\mathcal{L} = \frac{g}{\cos\theta_W}\left[\bar{u}_L^i\gamma_\mu\left(\frac{1}{2} - \frac{2}{3}\sin^2\theta_W\right)u_L^i + \bar{u}_R^j\gamma_\mu\left(-\frac{2}{3}\sin^2\theta_W\right)u_R^j\right]Z^\mu \tag{1.19}$$

where θ_W is the Weinberg angle.

From a unitary rotation of the quark fields on moving to the mass basis (only the first term in the above equation is considered),

$$\mathcal{L} = \frac{g}{\cos\theta_W}\left[\bar{u}_L^i V_{uL}\gamma_\mu\left(\frac{1}{2} - \frac{2}{3}\sin^2\theta_W\right)V_{uL}^\dagger u_L^i\right]Z^\mu \tag{1.20}$$

Thus, the triviality of the flavor structure

$$V_{uL}V_{uL}^\dagger = 1 \tag{1.21}$$

prevents any tree-level FCNCs.

We have studied the semileptonic decays of B mesons via the charged and neutral current exchanges which provide two avenues for very interesting phenomenological implications. The charged current transitions, occurring at tree level in the SM offer important insights into the structure of the CKM matrix. The extraction of the CKM elements from the semileptonic and leptonic modes, where the hadronic and leptonic currents factorise is clean as compared to the hadronic modes which involve the complex and unknown QCD interactions. The various processes considered in the determinations of the CKM elements will be discussed in section 1.3. On the other hand, the only way to generate FCNCs in the SM is through loop-level transitions (involving penguin and box contributions) with the W bosons and up-type quarks in the loops. The FCNC transitions are thus potential probes of physics at higher energy scales, and the inconsistency of the measured observables with respect to the SM predictions signal the presence of new physics. Though the charged current transitions may also be mediated by new particles in some extensions of the SM and can probe new dynamics, we haven't explored this possibility in this thesis. A detailed discussion on the FCNC processes considered in this thesis will be presented in section 1.4.

1.3 Determination of the CKM elements

The determination of the CKM elements precisely is necessary for understanding the mechanism of quark-mixing in the Standard Model and its implications for CP violation. The extraction of the CKM elements corresponding to the lighter quarks is attained through direct measurements involving tree level processes in the SM, whereas those involving top quark are mostly determined indirectly through loop-level FCNC transitions. Below we discuss the various processes involved in the measurements of the CKM elements [50, 51]:

- $|V_{ud}|$ - The study of superallowed $0^+ \to 0^+$ nuclear beta decays provides the most

TH-3118_176121005

precise determination [52]. Other probable channels are neutron and pion β decays ($n \to pe\bar{\nu}$ and $\pi^+ \to \pi^0 e\bar{\nu}$), though the pion β decay is phase space suppressed [53].

- $|V_{us}|$ - Apart from the tree-level semileptonic $K \to \pi l\nu$ and leptonic $K \to \mu\nu$ decays [54], hyperon decays [55, 56] and hadronic τ decays to strange particles also provide measurement of this element [57, 58].

- $|V_{cd}|$ - This element is extracted from leptonic $D \to l\nu$ [59, 60] and semileptonic $D \to \pi l\nu$ decays [61]. Another method is from neutrino scattering data off a fixed target composed mostly of u and d quarks. The cross-section for double muon production by neutrino beams from a charm final state is proportional to $|V_{cd}|^2$ [62, 63].

- $|V_{cs}|$ - The direct determination comes from semileptonic $D \to Kl\nu$ [64, 65], leptonic $D_s \to l\nu$ decays [66–68] and also flavor-tagged $W^+ \to c\bar{s}$ decay (measured by Delphi experiment) [69].

- $|V_{cb}|$ - This element is extracted from exclusive semileptonic decays like $B \to D^{(*)}l\nu$ [70, 71] and inclusive decays like $B \to X_c l\nu$ [72]. For the inclusive case, the total semileptonic decay rate is described through the Operator Product Expansion (OPE) and the non perturbative unknowns are obtained from final state lepton and hadron energy distributions, whereas the determination from exclusive decays relies on the calculation of the hadronic form factors.

- $|V_{ub}|$ - The most relevant exclusive decays are $B \to \pi l\nu$ and $B \to \rho(\omega, \eta)l\nu$ [73–77] and inclusive decays are $B \to X_u l\nu$ [1, 72]. The determination of $|V_{ub}|$ from the respective inclusive decay is not clean as compared to the extractions of $|V_{cb}|$ from $B \to X_c l\nu$ decays. The $b \to cl\nu$ decays provide large background which necessitates experimental cuts to separate the $b \to u$ transitions from the background, thus restricting the phase-space region where the measurement of the decay-rate could be done. In the allowed phase-space region, usual OPE can't be applied and one has to rely on the non-perturbative shape functions, which complicates the theoretical understanding of this decay. These shape-functions are modeled by various QCD-approaches, thus rendering the values of $|V_{ub}|$ extracted from these modes model dependent.

- $|V_{tb}|$ - This element is extracted from single top production processes or on-shell decays of top quark to Wb [78, 79]. The top quark is identified by measuring the invariant mass of the W and b jet [80, 81].

- $|V_{ts}|$ and $|V_{td}|$ - These elements are determined by the indirect measurements through $B - \bar{B}$ oscillations dominated by top quark box contributions or loop-suppressed rare B and K decays [50, 82].

TH-3118_176121005

The Unitarity Triangle (UT) angles can be constrained by measuring the CP-violating observables. The most precisely measured angle of the CKM unitarity triangle is β. $\sin 2\beta$ is obtained from $b \to c\bar{c}s$ transitions (Charmonium modes) for which the present world average from measurements by LHCb [83] and B-factories [84, 85] is: $\sin 2\beta = 0.699 \pm 0.017$ [50]. The least precisely known angle of the CKM unitarity triangle is α which suffers from larger theory uncertainties as compared to other angles. $\sin 2\alpha$ is directly measured from time-dependent CP asymmetries in $b \to u\bar{u}d$ transitions. Combining all the measurements in $B \to \pi\pi$, $B \to \rho\pi$ and $B \to \rho\rho$ decay modes which are related by isospin symmetries, $\alpha = (85.2^{+4.8}_{-4.3})^\circ$ [50, 51]. As seen from eq. 1.17, γ is the only angle independent of the CKM elements including the top quark and thus can be determined exclusively from tree-level B decays, $B_{(s)} \to D_{(s)}K^{(*)}$ and $B^{\mp} \to D^{(*)}K^{(*)\mp}$ [86–88]. Combining the measurements, $\gamma = (65.9^{+3.3}_{-3.5})^\circ$ [50]. The UTfit [48] and CKMfitter [89] collaborations perform global fits of the measurements in various channels for determining the CKM matrix elements with Wolfenstein parametrization either within the SM framework or in some specific NP scenarios.

In this thesis, we have focused on the extraction of the CKM elements $|V_{ub}|$ and $|V_{cb}|$ from exclusive semileptonic decays of $B(B_s)$ mesons to lighter leptons ($\ell = e, \mu$) in the final state. $B \to \pi(\rho, \omega)\ell\nu$ and $B_s \to K\ell\nu$ channels are used to determine $|V_{ub}|$ and $B \to D^{(*)}\ell\nu$ and $B_s \to D_s^{(*)}\ell\nu$ modes for $|V_{cb}|$. In the SM, the differential decay rate w.r.t. the dilepton invariant mass squared q^2 for B meson decaying to pseudoscalar mesons $\bar{B} \to P\ell\nu_\ell$ is a function of the form factors $f_{+,0}(q^2)$ and the CKM element $|V_{qb}|$ ($q = u, c$) and is given as [90]

$$\begin{aligned}\frac{d\Gamma}{dq^2} =& \frac{G_F^2|V_{qb}|^2}{24\pi^3 m_B^2 q^4}\left(q^2 - m_l^2\right)^2 \left|p(q^2, m_B, m_P)\right| \times \\ & \left[\left(1 + \frac{m_l^2}{2q^2}\right) m_B^2 \left|p(q^2, m_B, m_P)\right|^2 \left|f_+\left(q^2\right)\right|^2 + \frac{3m_l^2}{8q^2}\left(m_B^2 - m_P^2\right)^2 \left|f_0\left(q^2\right)\right|^2\right].\end{aligned} \tag{1.22}$$

where $\left|p(q^2, m_B, m_P)\right| = \sqrt{\lambda(q^2, m_B, m_P)}/2m_B$ with $\lambda(q^2, m_B, m_P) = ((m_B - m_P)^2 - q^2)((m_B + m_P)^2 - q^2)$. Here, P stands for the final state pseudoscalar meson.

The differential decay width for B meson decaying to vector mesons $\bar{B} \to V\ell\nu_\ell$ is given as [90].

$$\begin{aligned}\frac{d\Gamma}{dq^2} =& \frac{G_F^2|V_{qb}|^2}{192\pi^3 m_B^3} q^2 \sqrt{\lambda(q^2, m_B, m_V)}\left(1 - \frac{m_l^2}{q^2}\right)^2 \times \\ & \left\{\left[\left(1 + \frac{m_l^2}{2q^2}\right)\left(H_{V,+}^2 + H_{V,-}^2 + H_{V,0}^2\right) + \frac{3}{2}\frac{m_l^2}{q^2} H_{V,t}^2\right]\right\},\end{aligned} \tag{1.23}$$

where the hadronic amplitudes are given as:

TH-3118_176121005

$$H_{V,\pm}(q^2) = (m_B + m_V)A_1(q^2) \mp \frac{\sqrt{\lambda(q^2)}}{m_B + m_V} V(q^2)\,, \tag{1.24a}$$

$$H_{V,0}(q^2) = \frac{m_B + m_V}{2m_V\sqrt{q^2}}\left[-(m_B^2 - {m_V}^2 - q^2)A_1(q^2) + \frac{\lambda(q^2)}{(m_B + m_V)^2} A_2(q^2)\right], \tag{1.24b}$$

$$H_{V,t}(q^2) = -\sqrt{\frac{\lambda(q^2)}{q^2}} A_0(q^2) \tag{1.24c}$$

.

Thus, from the above equations, we observe that the CKM elements can be extracted from the available data on the partial branching fractions in the respective channels and the determinations of the form factors from various approaches. Knowing the dependence of the form factors on the kinematically allowed q^2 (or the recoil angle w of the final state meson) region helps to determine the shape of the decay rate distribution. For the determination of the form factors, Lattice-QCD (LQCD) calculations provide the most precise estimates, which are most effective in the high q^2 regime. Light-cone sum rules (LCSR) and QCD factorization/soft-collinear effective theory results are used for the low q^2 region where Lattice QCD results aren't reliable. Section 2.1.2 contains a detailed discussion on the form factors.

1.4 Flavor-Changing Neutral Current transitions

As discussed in section 1.2, the flavor changing neutral current transitions occur at loop-level in the SM and are heavily suppressed in comparison to the charged current processes. Thus, if in any BSM scenario, such transitions are mediated at tree level, that would dominate the SM contribution and the virtual effects of new interactions can be observed in the low energy precision experiments through the deviations of the observables from their predictions in the SM. The well known formalism to study such processes is the effective Hamiltonian approach which will be discussed in detail in section 2.1.1.2.

In this thesis, we have studied the exclusive $b \to s\ell\ell$ and $b \to d\ell\ell$ transitions. With the plethora of data available in the $b \to s\ell\ell$ channels over the last decade and with an objective to explain the anomalous results observed in the low energy experiments, as will be discussed in section 1.5, it is very necessary to perform an analysis of the new physics effects with the currently available data, letting the data to decide the BSM scenario most compatible with the present data. An analysis with the available experimental data in these modes has been performed in chapter 3. In similar spirit to $b \to s\ell\ell$ modes, $b \to d\ell\ell$ decay modes are also FCNC processes but have some interesting features. These

TH-3118_176121005

modes have non-vanishing direct CP asymmetry in the SM as the parts of the amplitude proportional to $\lambda_u = V_{ub}V_{ud}^*$ and $\lambda_t = V_{tb}V_{td}^*$ have same order of Cabibbo suppression, whereas for $b \to s\ell\ell$ decay modes, the part of the amplitude proportional to $\lambda_u = V_{ub}V_{us}^*$ is doubly Cabibbo suppressed and often neglected. Therefore, a relatively large CP violation may be present in the $b \to d\ell\ell$ decays within the SM, which further motivates towards a robust, systematic and precise analysis of these modes within the framework of the SM. In addition, in the SM, due to the CKM suppression in $b \to d\ell\ell$ transitions, the decay rates are suppressed as compared to the $b \to s\ell\ell$ channels. Therefore, the NP effects in $b \to d\ell\ell$ transitions can be easily discriminated as compared to that in $b \to s\ell\ell$ decays. An involved analysis with the exclusive $b \to d\ell\ell$ modes in the SM and some NP scenarios has been performed in chapter 5. Below we present the expressions for the differential decay rates w.r.t q^2 and the angular observables corresponding to a final state pseudoscalar or vector meson.

For B meson decay to a pseudoscalar meson $\bar{B} \to P\ell\ell$, the double differential rate with respect to q^2 and $\cos\theta$ (θ is the angle between $\bar{B}$ and ℓ^- in the dilepton center of mass frame) [91] :

$$\frac{d^2\Gamma_l}{dq^2 d\cos\theta} = a_l(q^2) + b_l(q^2)\cos\theta + c_l(q^2)\cos^2\theta, \tag{1.25}$$

where a_l, b_l and c_l are functions of the QCD form factors as given in eq. B.4. Section 2.1.2 contains the details about the form factors.

The angular distribution

$$\frac{d\Gamma_l}{d\cos\theta} = A_l + B_l\cos\theta + C_l\cos^2\theta \tag{1.26}$$

is written in terms of the q^2- integrated coefficients.

$$A_l = \int_{q^2_{min}}^{q^2_{max}} dq^2 a_l(q^2), \qquad B_l = \int_{q^2_{min}}^{q^2_{max}} dq^2 b_l(q^2), \qquad C_l = \int_{q^2_{min}}^{q^2_{max}} dq^2 c_l(q^2) \tag{1.27}$$

The q^2- integrated decay rate Γ_l, F_H and the forward-backward asymmetry A_{FB} of the dilepton system are written in terms of these q^2- integrated coefficients [91]:

$$\Gamma_l = 2(A_l + \frac{1}{3}C_l), \qquad A_{FB} = \frac{B_l}{\Gamma_l}, \qquad F_H = \frac{2}{\Gamma_l}(A_l + C_l) \tag{1.28}$$

The decay distribution for B meson decay to a vector meson $\bar{B} \to \bar{V}(\to \bar{M}_1\bar{M}_2)l^+l^-$ can be described in terms of four kinematic variables: q^2 and the three angles θ_V, θ_l and ϕ [92]. According to the theory convention [92, 93], θ_l is measured between $\bar{V}$ and l^-, θ_V is the angle between $\bar{V}$ and $\bar{M}_1$ and ϕ is the angle between the two planes containing the lepton and hadron pairs.

TH-3118_176121005

$$\frac{d^4\Gamma}{dq^2 d\cos\theta_l d\cos\theta_V d\phi} = \frac{9}{32\pi} J(q^2, \theta_l, \theta_V, \phi) \tag{1.29}$$

where,

$$\begin{aligned} J(q^2, \theta_l, \theta_V, \phi) = {} & J_1^s sin^2\theta_V + J_1^c cos^2\theta_V + (J_2^s sin^2\theta_V + J_2^c cos^2\theta_V) cos2\theta_l \\ & + J_3 sin^2\theta_V sin^2\theta_l cos2\phi + J_4 sin2\theta_V sin2\theta_l cos\phi \\ & + J_5 sin2\theta_V sin\theta_l cos\phi \\ & + (J_6^s sin^2\theta_V + J_6^c cos^2\theta_V) cos\theta_l + J_7 sin2\theta_V sin\theta_l sin\phi \\ & + J_8 sin2\theta_V sin2\theta_l sin\phi + J_9 sin^2\theta_V sin^2\theta_l sin2\phi. \end{aligned} \tag{1.30}$$

The explicit expressions for the angular coefficients (J's) given in eqn 1.30 in terms of the transversity amplitudes corresponding to the decays are given in eq. A.4 and the transversity amplitudes are expressed as functions of the QCD form factors according to A.1.

For the CP-conjugated process $B \to V(\to M_1 M_2) l^+ l^-$, the angular decay rate distribution is obtained from eq. 1.30 with the replacement $J_i \to \tilde{J}_i \equiv \xi_i \bar{J}_i$ where, $\xi_i = 1$ for i $\in$ 1,2,3,4,7 and -1 for i $\in$ 5,6,8,9 [92]. Here, the angular coefficients $\tilde{J}_i$ is formed from the helicity amplitude $\tilde{A}_H \equiv A_H(\bar{B} \to f)$, on the other hand the $\bar{J}_i$ is formed from $\bar{A}_H \equiv A_H(\bar{B} \to \bar{f})$. The definitions for the associated CP-averaged (S_i) and CP-asymmetric (A_i) observables obtained from the decay distributions are given by

$$S_i = \frac{J_i + \bar{J}_i}{(d\Gamma + d\bar{\Gamma})/dq^2}, \qquad A_i = \frac{J_i - \bar{J}_i}{(d\Gamma + d\bar{\Gamma})/dq^2}, \tag{1.31}$$

where

$$\frac{d\Gamma + d\bar{\Gamma}}{dq^2} = \frac{1}{4}(6J_1^s + 3J_1^c - J_2^c - 2J_2^s) + \frac{1}{4}(6\bar{J}_1^s + 3\bar{J}_1^c - \bar{J}_2^c - 2\bar{J}_2^s) \tag{1.32}$$

The main source of theoretical uncertainties in these decay modes arise from the hadronic form factors and other ill known non-perturbative dynamics. Thus, it is very important to construct observables free from the hadronic uncertainties for precision tests of the SM. To reduce the theoretical uncertainties, certain ratios of the CP-averaged observables are defined known as optimized observables [94] for which there is cancellation of hadronic form factors to first order. The definitions are taken from [95]

$$\begin{aligned} P_1 &= \frac{2S_3}{1 - F_L}, \qquad P_2 = \frac{2}{3}\frac{A_{FB}}{(1 - F_L)}, \\ P_3 &= \frac{-S_9}{1 - F_L}, \qquad P'_{i=4,5,6,8} = \frac{S_{j=4,5,7,8}}{\sqrt{F_L(1 - F_L)}} \end{aligned} \tag{1.33}$$

For the decays such as $B^0 \to K^{*0}(\to K^+\pi^-)\ell\ell$ and $B^\pm \to \rho^\pm(\to \pi^\pm\pi^0)\ell\ell$, the initial

TH-3118_176121005

state B meson flavor can be determined from the decay products at both the LHCb and Belle and the observables corresponding to tagged events can be directly obtained from 1.29.

- The tagged decay rate distribution and the corresponding branching fraction

$$\left\langle \frac{d\Gamma}{dq^2} \right\rangle^{\text{Tag}} = \frac{1}{4}(3J_1^c + 6J_1^s - J_2^c - 2J_2^s), \qquad \langle BR \rangle^{\text{Tag}} = \tau_{B^+} \left\langle \frac{d\Gamma}{dq^2} \right\rangle^{\text{Tag}} \tag{1.34}$$

- Optimized observables:

$$\begin{aligned}
\langle P_1 \rangle^{\text{Tag}} &= \frac{J_3}{2J_{2s}}, & \langle P_2 \rangle^{\text{Tag}} &= -\frac{J_{6s}}{8J_{2s}}, & \langle P_3 \rangle^{\text{Tag}} &= \frac{J_9}{4J_{2s}}, \\
\left\langle P_4' \right\rangle^{\text{Tag}} &= -\frac{J_4}{2\sqrt{-J_2^c J_2^s}}, & \left\langle P_5' \right\rangle^{\text{Tag}} &= \frac{J_5}{2\sqrt{-J_2^c J_2^s}}, & \left\langle P_6' \right\rangle^{\text{Tag}} &= -\frac{J_7}{2\sqrt{-J_2^c J_2^s}}, \\
\left\langle P_8' \right\rangle^{\text{Tag}} &= \frac{J_8}{2\sqrt{-J_2^c J_2^s}}, & \langle A_{FB} \rangle^{\text{Tag}} &= -\frac{3}{4}\frac{J_6^s}{\left\langle \frac{d\Gamma}{dq^2} \right\rangle^{\text{Tag}}}, & \langle F_L \rangle^{\text{Tag}} &= -\frac{J_2^c}{\left\langle \frac{d\Gamma}{dq^2} \right\rangle^{\text{Tag}}}
\end{aligned} \tag{1.35}$$

The observables for the CP conjugate mode are obtained by replacing $J_i \to \bar{J}_i$ in the above equations.

On the contrary, when the final state is a CP-eigenstate, for eg. $B_s \to \phi(\to K^+K^-)\ell\ell$ and $B^0 \to \rho^0(\to \pi^+\pi^-)\ell\ell$, the same final state is produced from B or $\bar{B}$ decays resulting in interference between decay and mixing. In such cases, tagging of the initial state B meson flavor isn't possible at the LHCb. In that case, only the observables obtained from the CP-averaged distribution can be measured at LHCb:

$$\frac{d\Gamma(B \to f) + d\Gamma(\bar{B} \to f)}{dq^2 d\cos\theta_l d\cos\theta_f d\phi} = \sum_i [J_i + \tilde{J}_i] f_i(\theta_l, \theta_f, \phi) = \sum_i [J_i + \xi_i \bar{J}_i] f_i(\theta_l, \theta_f, \phi), \tag{1.36}$$

whereas at Belle, also the observables corresponding to tagged $\bar{B}(B)$ decays as well as the observables obtained from the CP-asymmetric distribution can be measured.

$$\frac{d\Gamma(B \to f) - d\Gamma(\bar{B} \to f)}{dq^2 d\cos\theta_l d\cos\theta_f d\phi} = \sum_i [J_i - \tilde{J}_i] f_i(\theta_l, \theta_f, \phi) = \sum_i [J_i - \xi_i \bar{J}_i] f_i(\theta_l, \theta_f, \phi). \tag{1.37}$$

Chapter 5 contains a detailed analysis on these modes and the observables that can be measured at the Belle and LHCb.

TH-3118_176121005

1.5 Experimental status

In this section, we will present the current experimental status of several observables relevant to the decay modes considered in this thesis. The B-hadron decays have gained a lot of attention in the recent years with various groundbreaking experiments being carried out by the experimental collaborations like Belle, BaBar, LHCb, CMS and ATLAS with the aim of either directly observing the signals of new particles or measuring the observables precisely predicted in the SM. Over the last few years, some puzzling results have been observed in the low-energy precision experiments in B physics. In the neutral current sector, the observables $R_{K^{(*)}} = \mathcal{B}(\bar{B} \to K^{(*)}\mu^+\mu^-)/\mathcal{B}(\bar{B} \to K^{(*)}e^+e^-)$ [96, 97] are defined which conserved the Lepton Flavor Universality (LFU) of weak interactions in the SM. The respective measurements have shown deviation from their respective SM expectations $\sim 3\,\sigma$. A few angular observables in the $B \to K^*\ell\ell$ channel have also shown deviations from their predictions in the SM, the most interesting one among them being the optimized observable P_5' defined in eq. 1.33. Very recently, the LHCb have measured these observables, where P_5' shows a deviation of $\sim 3\,\sigma$ [98]. The reason for these discrepancies can be either the presence of poorly understood non-local effects or the presence of one or more beyond the SM interactions.

Other golden channels for the $b \to s$ FCNC transitions are the purely leptonic decay channel $B_s^0 \to \mu^+\mu^-$ [99, 100] which have small branching fractions in the SM and the radiative decays $B_{(s)} \to K^*(\phi)\gamma$ [101]. The inclusive $B \to X_s\gamma$ rate (X_s refers to any final state hadron containing strange quarks) has precise SM prediction, making it an excellent probe of beyond-SM phenomenon [102]. In the $b \to s\ell\ell$ sector, plenty of observables have been measured by various experimental collaborations [96–98, 103–107], thus providing a thorough understanding on the ways to handle the hadronic uncertainties and as a result define observables that are more sensitive to NP. The construction of observables that either vanish or are strongly suppressed in the SM provide additional avenues to look for possible new physics effects through their precise non-zero measurements. As discussed in section 1.4, the $b \to d\ell\ell$ transitions offer another window to look for BSM phenomenon due to their low branching fractions in the SM. Till date, there is less amount of information available on the relevant exclusive decay modes. The LHCb collaboration has observed the $B^+ \to \pi^+\mu^+\mu^-$ decay for the first time at $5.2\,\sigma$ [108] and in [109], it has provided measurements of the partial branching fractions in bins of q^2, whereas there is no data available on $B \to \rho\ell\ell$ decays. Thus, the precise theoretical predictions of various observables pertaining to these modes is extremely essential which can be further verified in the future experiments and any deviation from SM predictions will provide possible hints of new dynamics.

The CKM elements $|V_{cb}|$ and $|V_{ub}|$ are relatively less precisely known till date as seen from the entries [50].

TH-3118_176121005

$$V_{CKM} = \begin{pmatrix} 0.97435 \pm 0.00016 & 0.22500 \pm 0.00067 & 0.00369 \pm 0.00011 \\ 0.22486 \pm 0.00067 & 0.97349 \pm 0.00016 & 0.04182^{+0.00085}_{-0.00074} \\ 0.00857^{+0.00020}_{-0.00018} & 0.04110^{+0.00083}_{-0.00072} & 0.999118^{+0.000031}_{-0.000036} \end{pmatrix} \tag{1.38}$$

As mentioned in section 1.3, the tree-level semileptonic transitions such as $B \to \pi\ell\nu_l$ and $B \to D^{(*)}\ell\nu_l$ offer cleaner probes for the extraction of the elements $|V_{ub}|$ and $|V_{cb}|$, respectively, and such decays have been extensively studied by the Belle and BaBar collaborations [70, 71, 73–76], where the measurements on the binned partial branching fractions are provided which are proportional to $|V_{ub}|^2$ or $|V_{cb}|^2$. For the semileptonic decays of $B^{\pm}$ or B_q $(q = d, s)$ mesons to a pseudoscalar or vector meson, respectively, the detailed mathematical expressions for the respective rates $d\Gamma/dq^2$ are provided in eqs. 1.22 and 1.23. Also, a discrepancy exists for a long time between the inclusive and exclusive determinations for both $|V_{cb}|$ and $|V_{ub}|$ from semileptonic B-meson decays (known as the exclusive-inclusive puzzle), which calls for a combined effort from the theoretical and experimental fronts. The most up-to-date results on the extracted values of $|V_{ub}|$ and $|V_{cb}|$ can be seen from the particle data group (PDG) [72]:

$$|V_{ub}|^{exclusive} = (3.70 \pm 0.16) \times 10^{-3}, \quad |V_{ub}|^{inclusive} = (4.25 \pm 0.12^{+0.15}_{-0.14}) \times 10^{-3} \tag{1.39}$$

$$|V_{cb}|^{exclusive} = (39.5 \pm 0.9) \times 10^{-3}, \quad |V_{cb}|^{inclusive} = (42.2 \pm 0.8) \times 10^{-3}, \tag{1.40}$$

where the errors represent the experimental and theoretical uncertainties. The exclusive and inclusive values are in mutual disagreement (by $\geq 2.2\sigma$). In chapter 4, we have analysed the $B \to \pi l\nu$ channel for extracting $|V_{ub}|^{exc.}$ with the aim to understand the possible source of discrepancy between the exclusive and inclusive measurements.

Recently, the Belle collaboration has measured the values of $|V_{ub}|$ from inclusive spectra with hadronic-tagging by four different methods, like Bosch-Lange-Neubert-Paz (BLNP) [110–112], Dressed Gluon Exponentiation (DGE) [113], Gambino-Giordano-Ossola-Uraltsev (GGOU) [114], and Aglietti-Di-Ferrera-Ricciardi (ADFR) [115]. From an arithmetic average of these values, they obtain [1]

$$|V_{ub}|^{inclusive} = (4.10 \pm 0.28) \times 10^{-3}\,. \tag{1.41}$$

This happens to be the most precise determination till date.

As seen from fig 1.1, the side opposite the well determined angle β in the unitarity triangle is proportional to the ratio $|V_{ub}|/|V_{cb}|$. This ratio has been measured from the partial rates of $\Lambda_b \to p\mu\nu$ normalized to $\Lambda_b \to \Lambda_c\mu\nu$ by LHCb [116].

$$\frac{|V_{ub}|}{|V_{cb}|} = (0.83 \pm 0.04_{\rm exp} \pm 0.04_{\rm th}) \times 10^{-1} \tag{1.42}$$

TH-3118_176121005

The first uncertainty is experimental and the second results from the uncertainty in LQCD prediction.

Recently, there has also been a measurement of the ratio BR($B_s \to K\mu\nu$)/BR($B_s \to D_s\mu\nu$) from LHCb [8] in two bins of the $B_s \to K$ momentum transfer, namely $q^2 < 7$ GeV^2 and $q^2 > 7$ GeV^2 with $B_s \to D_s\mu\nu$ acting as the normalization channel:

$$\begin{aligned} R_{\rm BF}^{\rm low} &= (0.166 \pm 0.008({\rm stat}) \pm 0.007({\rm syst}) \pm 0.005(D_s)) \times 10^{-2}, \\ R_{\rm BF}^{\rm high} &= (0.325 \pm 0.021({\rm stat})^{+0.016}_{-0.017}({\rm syst}) \pm 0.009(D_s)) \times 10^{-2}. \end{aligned} \tag{1.43}$$

Here, the uncertainties are due to the statistical and systematic errors, and due to the errors associated with the measured value of the branching fraction of $D_s^- \to K^+K^-\pi^-$. From these branching ratios, the ratio has been obtained in the respective bins.

$$\begin{aligned} \frac{|V_{ub}|}{|V_{cb}|}({\rm low}) &= (0.61 \pm 0.02_{\rm exp} \pm 0.03_{\rm th}) \times 10^{-1}, \\ \frac{|V_{ub}|}{|V_{cb}|}({\rm high}) &= (0.95 \pm 0.04_{\rm exp} \pm 0.07_{\rm th}) \times 10^{-1}, \end{aligned} \tag{1.44}$$

where the theoretical uncertainties correspond to the form factor integrals and D_s^- branching fraction and experimental uncertainties are statistical and systematic. In chapter 6, we have analysed the mesonic $b \to c(u)l\nu$ modes simultaneously for a combined extraction of $|V_{cb}|^{exc}$ and $|V_{ub}|^{exc}$, also incorporating the measurements on the ratio of the branching fractions in the two bins given in eq. 1.43 to study the impact of these inputs on the extracted value of $|V_{ub}|/|V_{cb}|$.

In the subsequent chapters, we present a brief outline of the basic theoretical tools necessary for flavor phenomenology, mainly the concept of effective field theories and the statistical techniques used in our analysis related to interpreting the experimental data and discuss about the various contributions to this thesis.

TH-3118_176121005

Chapter 2

Methodology

2.1 Theoretical Framework

2.1.1 Effective Hamiltonian Approach

The Effective field theory (EFT) is an important framework to deal with phenomena that are spread over a multitude of energy or length scales, such as the electroweak scale determining flavor-changing transitions of quarks and the scale of strong interactions related to the formation of hadrons. Every EFT has a scale of validity upto which it is valid. The scale hierarchy is the fundamental concept behind the idea of EFTs. This theoretical framework allows the separation of short-distance effects from long-distance QCD in an effective Hamiltonian approach.

This formalism is based on the Operator Product Expansion in which the effective Hamiltonian is expressed as a sum over all possible operators multiplied by the corresponding Wilson Coefficients. The amplitude $\mathcal{A}$ for any process is given as [117]

$$\mathcal{A} = \langle \mathcal{H}_{\text{eff}} \rangle = \sum_i C_i(\mu) \mathcal{O}_i(\mu) \tag{2.1}$$

where μ is the renormalization group (RG) scale. $\mathcal{O}_i$ are a set of local operators with dimension d_i and C_i are the respective Wilson coefficients (WCs). $C_i s$ encode the short distance effects from the Standard Model ($W^{\pm}$, Z bosons and the top quark) or the new physics dynamics.

In an EFT framework, the most important steps involved are the matching between the full and the effective theory at the relevant scale and renormalization group running from one scale to another. Considering the Standard Model as the underlying theory, through the procedure of matching the amplitudes in the full theory with those in the EFT, the SM contributions to the Wilson coefficients are evaluated at the electroweak scale $\mu = m_W$. The Wilson coefficients are then evolved down to the b-quark mass scale $\mu = m_b$ according to their RG equations since it is the relevant scale for all observables related to the B-hadron decays considered in this thesis.

TH-3118_176121005

$$\frac{dc_i(\mu)}{d\log\mu} = \sum_j \frac{1}{16\pi^2}\gamma_{ij}c_j \tag{2.2}$$

Here γ_{ij} is the anomalous dimension matrix.

For the contributions from new physics to the process under study, through the matching between the amplitudes in the NP model and the EFT, the WCs are evaluated at a high-energy scale $\mu = \Lambda$ which are then run down to the electroweak scale and finally to the m_b scale. However, in this thesis, we directly constrain the new physics Wilson coefficients from experimental data.

Both the Flavor-Changing Charged and Neutral Current transitions can be studied in this formalism as discussed below.

2.1.1.1 Charged current transitions

The effective Hamiltonian for semileptonic charged current transitions of B mesons with all possible dimension-six four fermion operators in the absence of right handed neutrinos is given as [90]:

$$\mathcal{H}_{\text{eff}} = \frac{4G_F}{\sqrt{2}}V_{qb}[(\delta_{l\tau} + C^l_{V_1})\mathcal{O}^l_{V_1} + C^l_{V_2}\mathcal{O}^l_{V_2} + C^l_{S_1}\mathcal{O}^l_{S_1} + C^l_{S_2}\mathcal{O}^l_{S_2} + C^l_T\mathcal{O}^l_T] \tag{2.3}$$

where G_F is the Fermi constant. The four-Fermi operators are defined by

$$\begin{aligned}
\mathcal{O}^l_{V_1} &= (\bar{q}_L\gamma^\mu b_L)(\bar{l}_L\gamma_\mu\nu_{lL}),\\
\mathcal{O}^l_{V_2} &= (\bar{q}_R\gamma^\mu b_R)(\bar{l}_L\gamma_\mu\nu_{lL}),\\
\mathcal{O}^l_{S_1} &= (\bar{q}_L b_R)(\bar{l}_R\nu_{lL}),\\
\mathcal{O}^l_{S_2} &= (\bar{q}_R b_L)(\bar{l}_R\nu_{lL}),\\
\mathcal{O}^l_T &= (\bar{q}_R\sigma^{\mu\nu} b_L)(\bar{l}_R\sigma_{\mu\nu}\nu_{lL})
\end{aligned} \tag{2.4}$$

where $q = u, c$ corresponding to $b \to u\ell\nu$ or $b \to c\ell\nu$ transitions considered in this thesis. In the SM, only the operator $\mathcal{O}^l_{V_1}$ contributes to the decay width.

2.1.1.2 Neutral current transitions

The effective Hamiltonian for semileptonic FCNC transitions of B mesons for eg. $b \to s\ell\ell$ at the scale $\mu \sim m_b$ after integrating out the heavy degrees of freedom is given by [92] :

$$\mathcal{H}_{eff} = -\frac{4\,G_F}{\sqrt{2}}\left(\lambda_t\mathcal{H}^{(t)}_{eff} + \lambda_u\mathcal{H}^{(u)}_{eff}\right), \tag{2.5}$$

where $\lambda_m = V_{mb}V^*_{ms}$ $(m = u, c, t)$ are the CKM factors. The combination $\lambda_c = V_{cb}V^*_{cs}$ is eliminated by using the unitarity relation $\lambda_u + \lambda_c + \lambda_t = 0$.

TH-3118_176121005

$$\begin{aligned}\mathcal{H}_{eff}^{(t)} &= C_1\mathcal{O}_1^c + C_2\mathcal{O}_2^c + \sum_{i=3,..,6,S,P}(C_i\mathcal{O}_i + C_i'\mathcal{O}_i') + \sum_{i=7,8,9,10}(\tilde{C}_i\tilde{\mathcal{O}}_i + \tilde{C}_i'\tilde{\mathcal{O}}_i') \\ \mathcal{H}_{eff}^{(u)} &= C_1(\mathcal{O}_1^c - \mathcal{O}_1^u) + C_2(\mathcal{O}_2^c - \mathcal{O}_2^u)\,. \end{aligned} \tag{2.6}$$

The operator basis is given as [92, 118]:

$$\begin{aligned}\mathcal{O}_1^p &= (\bar{s}_L\gamma_\mu T^a p_L)(\bar{p}_L\gamma^\mu T^a b_L), \\ \mathcal{O}_2^p &= (\bar{s}_L\gamma_\mu p_L)(\bar{p}_L\gamma^\mu b_L), \\ \mathcal{O}_3 &= (\bar{s}_L\gamma_\mu b_L)\sum_q(\bar{q}\gamma^\mu q), \\ \mathcal{O}_4 &= (\bar{s}_L\gamma_\mu T^a b_L)\sum_q(\bar{q}\gamma^\mu T^a q), \\ \mathcal{O}_5 &= (\bar{s}_L\gamma_{\mu_1}\gamma_{\mu_2}\gamma_{\mu_3} b_L)\sum_q(\bar{q}\gamma^{\mu_1}\gamma^{\mu_2}\gamma^{\mu_3} q), \\ \mathcal{O}_6 &= (\bar{s}_L\gamma_{\mu_1}\gamma_{\mu_2}\gamma_{\mu_3} T^a b_L)\sum_q(\bar{q}\gamma^{\mu_1}\gamma^{\mu_2}\gamma^{\mu_3} T^a q)\end{aligned}$$

$$\begin{aligned}\tilde{\mathcal{O}}_7 &= \frac{e}{g^2}m_b(\bar{s}\sigma_{\mu\nu}P_R b)F^{\mu\nu}, & \tilde{\mathcal{O}}_7' &= \frac{e}{g^2}m_b(\bar{s}\sigma_{\mu\nu}P_L b)F^{\mu\nu}, \\ \tilde{\mathcal{O}}_8 &= \frac{1}{g}m_b(\bar{s}\sigma_{\mu\nu}T^a P_R b)G^{\mu\nu}, & \tilde{\mathcal{O}}_8' &= \frac{1}{g}m_b(\bar{s}\sigma_{\mu\nu}T^a P_L b)G^{\mu\nu}, \\ \tilde{\mathcal{O}}_9 &= \frac{e^2}{g^2}(\bar{s}\gamma_\mu P_L b)(\bar{l}\gamma^\mu l), & \tilde{\mathcal{O}}_9' &= \frac{e^2}{g^2}(\bar{s}\gamma_\mu P_R b)(\bar{l}\gamma^\mu l), \\ \tilde{\mathcal{O}}_{10} &= \frac{e^2}{g^2}(\bar{s}\gamma_\mu P_L b)(\bar{l}\gamma^\mu\gamma_5 l), & \tilde{\mathcal{O}}_{10}' &= \frac{e^2}{g^2}(\bar{s}\gamma_\mu P_R b)(\bar{l}\gamma^\mu\gamma_5 l), \\ \mathcal{O}_S &= \frac{e^2}{16\pi^2}m_b(\bar{s}P_R b)(\bar{l}l), & \mathcal{O}_S' &= \frac{e^2}{16\pi^2}m_b(\bar{s}P_L b)(\bar{l}l), \\ \mathcal{O}_P &= \frac{e^2}{16\pi^2}m_b(\bar{s}P_R b)(\bar{l}\gamma_5 l), & \mathcal{O}_P' &= \frac{e^2}{16\pi^2}m_b(\bar{s}P_L b)(\bar{l}\gamma_5 l)\end{aligned} \tag{2.7}$$

Here $p = u, c$ and T^as are the $SU(3)_C$ generators. The effective Hamiltonian and the operator basis corresponding to $b \to d\ell\ell$ transitions can be obtained by replacing $s \to d$ in the above equations.

$\mathcal{O}_1^p$, $\mathcal{O}_2^p$ are the four-quark current-current operators, $\mathcal{O}_{3..6}$ are the quark penguin operators, $\tilde{\mathcal{O}}_7$ and $\tilde{\mathcal{O}}_8$ are the photon dipole and chromomagnetic operators and $\tilde{\mathcal{O}}_{9,10}$ are the semileptonic operators. The primed operators with opposite chirality to the unprimed ones vanish or are highly suppressed in the SM, as are $\mathcal{O}_{S^{(\prime)},P^{(\prime)}}$. We don't consider the contributions to operators $\mathcal{O}_i'$ for $1 \leq$ i ≤ 6. These operators are present in some BSM scenarios but their impact turns out to be highly constrained.

As discussed in section 2.1.1, the Wilson coefficients encode short-distance physics and

TH-3118_176121005

possible NP effects. The WCs corresponding to new interactions are directly constrained from data considering them as free parameters and it is one of the main objectives for the $b \to s\ell\ell$ transitions considered in this thesis. The SM contributions to the WCs are calculated at the scale $\mu = m_W$ up to next-to-next-to leading order (NNLO) and expressed as a perturbative expansion in the strong coupling constant $\alpha_s(\mu_W)$ [118, 119]. They are then evolved down to scale $\mu = m_b$ using renormalization group equations, given in eq. 2.2 which require a calculation of anomalous dimension matrices $\gamma(\alpha_s)$ up to three-loop accuracy. After incorporating the QCD corrections, the coefficients C_9 and C_7 modify and appear as combinations of the other $C_i's$. Therefore, it is convenient to define the effective Wilson coefficients: C_9^{eff} and C_7^{eff} [92].

$$\begin{aligned} C_7^{eff} &= \frac{4\pi}{\alpha_s} C_7 - \frac{1}{3} C_3 - \frac{4}{9} C_4 - \frac{20}{3} C_5 - \frac{80}{9} C_6, \\ C_9^{eff} &= \frac{4\pi}{\alpha_s} C_9 + Y(q^2) \end{aligned} \tag{2.8}$$

where $Y(q^2)$ is given in [92]. The four-quark current-current operators $\mathcal{O}_1^p$, $\mathcal{O}_2^p$ and quark-penguin operators $\mathcal{O}_{3..6}$ contribute to C_9^{eff} which also includes the leading order (LO) charm-loop effects.

Besides the terms proportional to the form factors, the amplitudes also contain certain "non-factorizable" effects that are related to the matrix elements of the purely hadronic operators $\mathcal{O}_{1..6}$ and the chromomagnetic dipole operator $\mathcal{O}_8$ with virtual photon emission. In particular, these effects include the contributions from the "hard" corrections to the weak vertex, hard-spectator corrections and the contributions from the weak annihilation (WA) diagrams. There are no such corrections for the semileptonic operators. In the QCD-factorization (QCDF) approach, one can systematically calculate such effects where the most general factorization formula for a heavy to light transition amplitude at leading order in $1/m_b$ reads schematically [120]:

$$\mathcal{T}_a^i = C_a^i \xi_P + \phi_B \otimes T_a^i \otimes \phi_F, \tag{2.9}$$

where "a" stands for the polarization of the final state vector meson ($a \to \parallel$ or $\perp$), $i = u, t$, ξ_P is the "soft" form factor and T_a^i is the hard-scattering kernel convoluted with heavy and light meson light-cone wave functions ϕ_B and ϕ_F, respectively. The vertex corrections to the four-quark operators contribute to C_a^i, which can have factorizable and non-factorizable parts at order α_s:

$$C_a^i = C_a^{i(0)} + \frac{\alpha_s C_F}{4\pi} \left(C_a^{i(f)} + C_a^{i(nf)} \right) \tag{2.10}$$

$C_a^{i(0)}$ is the leading order contribution in α_s. Similarly, the contribution from the WA

TH-3118_176121005

diagram will appear in T_a^i at the leading order in the expansion of the strong coupling constant. At order α_s there will be factorizable as well as non-factorizable contributions in T_a^i given by $T_a^{i(1)}$. T_a^i is expanded as

$$T_a^i = T_a^{i(0)} + \frac{\alpha_s C_F}{4\pi} T_a^{i(1)} \tag{2.11}$$

As can be seen from [120], in the QCDF framework, the factorizable corrections arise when the full QCD form factors are expressed in terms of the soft form factors $\xi_P s$. Since we will be using the form factors defined in full QCD in this thesis, we need to add only the non-factorizable corrections. These contributions are added to the naive factorisation amplitudes as given in eq. B.2 for decays to pseudoscalar mesons and in eq. A.1 for decays to vector mesons [92].

$$\begin{aligned}
\Delta A_{\perp,L,R}^{QCDF} &= \sqrt{2} N \frac{2m_b}{q^2}(m_B^2 - q^2)\big(\mathcal{T}_\perp^{(t),WA+nf} + \hat{\lambda}_u \mathcal{T}_\perp^{(u),WA+nf}\big), \\
\Delta A_{||,L,R}^{QCDF} &= -\Delta A_{\perp,L,R}^{QCDF}, \\
\Delta A_{0,L,R}^{QCDF} &= \frac{N(m_B^2 - q^2)^2}{m_V m_B^2 \sqrt{q^2}} m_b \big(\mathcal{T}_{||}^{(t),WA+nf} + \hat{\lambda}_u \mathcal{T}_{||}^{(u),WA+nf}\big).
\end{aligned} \tag{2.12}$$

Here, $\hat{\lambda}_u = \lambda_u/\lambda_t$. N is expressed as in eq. A.2.

Information from long-distance physics is encoded in the light-cone distribution amplitudes (LCDA), $\Phi_{B,\pm}$ for the B meson and ϕ_F for the final state mesons. For B meson, the light-cone distribution amplitudes are written as [121, 122],

$$\Phi_{B,+}(\omega) = \frac{\omega}{\omega_0^2} e^{-\omega/\omega_0}, \quad \Phi_{B,-}(\omega) = \frac{1}{\omega_0} e^{-\omega/\omega_0}. \tag{2.13}$$

These enter the decay amplitude through the moments $\lambda_{B,+}^{-1}(q^2)$ and $\lambda_{B,-}^{-1}(q^2)$ [121, 122]

$$\lambda_{B,+}^{-1} = \int_0^\infty d\omega \frac{\Phi_{B,+}(\omega)}{\omega} = \omega_0^{-1} \tag{2.14}$$

and

$$\lambda_{B,-}^{-1}(q^2) = \int_0^\infty d\omega \frac{\Phi_{B,-}(\omega)}{\omega - q^2/M_B - i\epsilon} = \frac{e^{-q^2/(M_B\omega_0)}}{\omega_0}[-\mathrm{Ei}\left(q^2/M_B\omega_0\right) + i\pi]. \tag{2.15}$$

Here $\mathrm{Ei}(z)$ is the exponential integral function. $\lambda_{B,-}^{-1}$ appears via the weak annihilation term in the decay amplitudes, and the imaginary part in eq. (2.15) acts as an important source of strong phase which is necessary for CP violation. As can be seen from ref. [123], at the leading order, the contribution in $\mathcal{T}_a^{(t)}(q^2)$ and $\mathcal{T}_a^{(u)}(q^2)$ from the weak annihilation diagrams is proportional to $\lambda_{B,-}^{-1}(q^2)\hat{T}_{a,-}^{(0,t)}$ and $\lambda_{B,-}^{-1}(q^2)\hat{T}_{a,-}^{(0,u)}$, respectively. The imaginary

TH-3118_176121005

part of $\lambda_{B,-}^{-1}(q^2)$ (eq. 2.15) is highly q^2 dependent and has large values at low q^2 compared to that at high q^2 regions. The contribution in neutral B decays from $\hat{T}_{a,-}^{(0,u)}$ is negligible. However, for charged B decays, numerically $\hat{T}_{a,-}^{(0,u)} > \hat{T}_{a,-}^{(0,t)}$ since $\hat{T}_{a,-}^{(0,u)}$ is proportional to the WC $C_2 \sim 1$ whereas $\hat{T}_{a,-}^{(0,t)}$ is proportional to a linear combination of $C_3 \sim -0.005$ and $C_4 \sim -0.08$. Due to this reasoning, $\mathcal{T}_a^{(u)}(q^2)$ is more sensitive to the variation of q^2 as compared to $\mathcal{T}_a^{(t)}(q^2)$ leading to large CP asymmetry for the charged B decays as compared to the neutral B decays. The CP asymmetry for B^0 decays is small, as weak annihilation is mostly mediated by loop-suppressed QCD penguins.

The light-cone distribution amplitude in the leading twist for light mesons in the final state is given by [124, 125],

$$\phi_{F,a}(u) = 6u(1-u)\Big[1 + a_{1,a}\, C_1^{(3/2)}(2u-1) + a_{2,a}\, C_2^{(3/2)}(2u-1)\Big], \tag{2.16}$$

where $C_n^{(3/2)}(x)$ are the Gegenbauer polynomials and $a_{n,a}$ are the Gegenbauer moments.

2.1.2 Decay constants and Form Factors

The hadronic matrix elements of the form $\langle 0|\bar{q}'\Gamma q|h\rangle$ or $\langle h'|\bar{q}'\Gamma q|h\rangle$ (h and h' refer to the initial and final state hadrons) for the leptonic or semileptonic transitions are expressed in terms of appropriate decay constants or form factors which are non-perturbative quantities and serve as dominant sources of uncertainties for the theoretical predictions of several observables in the flavor sector. These are functions of only Lorentz scalars, q^2 which is the squared four-momentum transferred to the dilepton system in a semileptonic transition.

The hadronic matrix elements for B- decay to a pseudoscalar meson are given as [90],

$$\langle P(k)|\bar{f}\gamma_\mu b|B(p)\rangle = \left[(p+k)_\mu - \frac{m_B^2 - m_P^2}{q^2} q_\mu\right] f_+(q^2) + q_\mu \frac{m_B^2 - m_P^2}{q^2} f_0(q^2)\,, \tag{2.17}$$

where $f_+(0) = f_0(0)$ to cancel the divergence at $q^2 = 0$.

$$\langle P(k)|\bar{f}\sigma_{\mu\nu} b|B(p)\rangle = -i(p_\mu k_\nu - k_\mu p_\nu)\frac{2f_T(q^2)}{m_B + m_P} \tag{2.18}$$

The hadronic matrix elements for B decay to a vector meson [90, 126],

$$\begin{aligned}\langle V(k)|\bar{f}\gamma_\mu(1-\gamma_5)b|B(p)\rangle = -i\epsilon_\mu^*(m_B+m_V)A_1(q^2) + i(2p-q)_\mu(\epsilon^*\cdot q)\,\frac{A_2(q^2)}{m_B+m_V} \\ + iq_\mu(\epsilon^*\cdot q)\,\frac{2m_V}{q^2}\,\big[A_3(q^2) - A_0(q^2)\big] + \epsilon_{\mu\nu\rho\sigma}\epsilon^{*\nu}p^\rho k^\sigma\,\frac{2V(q^2)}{m_B+m_V},\end{aligned} \tag{2.19}$$

$$\text{with } A_3(q^2) \;=\; \frac{m_B+m_V}{2m_V}\,A_1(q^2) - \frac{m_B-m_V}{2m_V}\,A_2(q^2) \;\text{ and }\; A_0(0) = A_3(0) \tag{2.20}$$

TH-3118_176121005

$$\langle V(k)|\bar{f}\sigma_{\mu\nu}q^{\nu}(1+\gamma_5)b|B(p)\rangle = i\epsilon_{\mu\nu\rho\sigma}\epsilon^{*\nu}p^{\rho}k^{\sigma}\,2T_1(q^2) + T_2(q^2)\left[\epsilon^*_{\mu}(m_B^2-m_V^2)-(\epsilon^*\cdot q)\,(2p-q)_{\mu}\right] + T_3(q^2)(\epsilon^*\cdot q)\left[q_{\mu}-\frac{q^2}{m_B^2-m_V^2}\,(2p-q)_{\mu}\right], \tag{2.21}$$

with $T_1(0) = T_2(0)$. ϵ_μ is the polarization vector of the final state meson. f represents the quark in the final state meson in the above equations.

Thus, knowing the variation of the form-factors over the whole q^2 region helps to determine the shape of the decay rate distribution. As discussed in section 1.3, different approaches are more reliable in different kinematic regions for the estimation of the form factors. Therefore, in order to extrapolate the information contained in a restricted q^2 region to the whole range, it is crucial to have a parametrization of the form-factors satisfying the general properties of unitarity, analyticity and crossing symmetry. The basic idea involves a change of variables from q^2 to z resulting in a mapping of the semileptonic region $0 < q^2 < t_-$ onto a unit circle in the complex z plane.

$$z(q^2) = \frac{\sqrt{t_+ - q^2} - \sqrt{t_+ - t_0}}{\sqrt{t_+ - q^2} + \sqrt{t_+ - t_0}}, \tag{2.22}$$

where $t_\pm \equiv (m_B \pm m_F)^2$ and $t_0 \equiv t_+(1-\sqrt{1-t_-/t_+})$, where F denotes the final state meson. t_0 is a free parameter that governs the size of z in the semileptonic phase space. The form factors are analytic functions of q^2 except at physical poles and branch cuts above the production threshold. They can be expanded as a simple power series in z:

$$P_i(q^2)\phi_i(q^2,t_0)f_i(q^2) = \sum_{k=0}^{\infty} a_i^{(k)}(t_0)z(q^2,t_0)^k \tag{2.23}$$

Since the absolute value $|z|$ is small in the semileptonic region and the z-expansion coefficients are constrained to be small by unitarity, only the first few terms suffice to describe the form factor shape accurately, which leads to a faster convergence of the series. The Blaschke factors $P_i(q^2)$ are chosen to vanish at any subthreshold poles to ensure analyticity of $f_i(q^2)$ and the outer functions $\phi_i(q^2,t_0)$ can be any analytic function of q^2. There are several parametrizations in the literature to parametrize the form factors, Bourrely-Caprini-Lellouch (BCL) [127], Bharucha-Straub-Zwicky (BSZ) [4] and Boyd-Grinstein-Lebed (BGL) [128], the details are given in the following subsections.

2.1.2.1 BSZ parametrization

According to BSZ, the parametrization of any form-factor reads [4]:

$$f_i(q^2) = \frac{1}{1-q^2/m_{R,i}^2}\sum_{k=0}^{N} a_k^i\left[z(q^2)-z(0)\right]^k, \tag{2.24}$$

TH-3118_176121005

where $m_{R,i}$ denotes the masses of sub-threshold resonances compatible with the quantum numbers of the respective form factors, as given in table 2.1 and a_k^is are the coefficients of expansion. The advantage with this parametrization is that the value of the form factor at $q^2 = 0$ is among the fit parameters. Also, in BSZ parametrization, the kinematical constraint $f_+(q^2 = 0) = f_0(q^2 = 0)$ directly leads to the relation $a_0^+ = a_0^0$ among the coefficients.

F_i	J^P	$m_{R,i}^{b\to d(u)}$ (GeV)	$m_{R,i}^{b\to s}$ (GeV)
f_0	0^+	5.540	5.630
A_0	0^-	5.279	5.366
f_+, f_T, T_1, V	1^-	5.325	5.415
T_2, T_3, A_1, A_2	1^+	5.724	5.829

Table 2.1: Masses of resonances of quantum numbers J^P for the parameterization of the form factors f_i for $b \to d(u)$ and $b \to s$ transitions.

2.1.2.2 BCL parametrization

According to BCL, f_+ and f_0 are as follows [127]:

$$f_+(z) = \frac{1}{1 - q^2/m_{B^*}^2} \sum_{n=0}^{N_z-1} b_n^+ \left[z^n - (-1)^{n-N_z} \frac{n}{N_z} z^{N_z}\right], \tag{2.25}$$

$$f_0(z) = \sum_{n=0}^{N_z-1} b_n^0 z^n, \tag{2.26}$$

where m_{B^*} is the mass of the B^* resonance. Here, $b_n^{0/+}$ are the coefficients of the expansion which are free parameters and they obey the unitarity constraint

$$\Sigma(b^{0/+}, N_z) \equiv \sum_{m,n=0}^{N_z} B_{mn}\, b_m^{0/+} b_n^{0/+} \leq 1, \tag{2.27}$$

where the element B_{mn} satisfies $B_{mn} = B_{nm} = B_{0|m-n|}$, the details for which can be seen from [127, 129]. This expansion obeys the known asymptotic behaviour near the $B\pi$ threshold: $Im(f_+(q^2)) \sim (q^2 - t_+)^{3/2}$. Therefore, at $q^2 = t_+$ ($z = -1$), the derivative of the form factor must satisfy

$$\frac{df_+}{dz}\Big|_{z=-1} = 0. \tag{2.28}$$

This constraint is used to remove an independent degree of freedom from the series expansion in z. For the scalar form factor f_0 or it's derivative there are no such constraints available at any value of z, so a further degree of freedom can't be removed in the series expansion of $f_0(z)$. In refs. [130, 131], the functional form of f_0 does not include the pole factor $\frac{1}{1-q^2/m_{B^*}^2}$ as used in the BSZ parametrization, according to the argument that

TH-3118_176121005

the scalar B^* meson whose mass is expected to be above the $B\pi$ threshold has not been observed experimentally yet.

2.1.2.3 BGL parametrization

In the BGL method of parametrization, the form factors $(f_+, f_0, g, f, F_1, F_2)$ can be expressed as an expansion in z as [128]

$$\mathcal{F}_i(z) = \frac{1}{P_i(z)\phi_i(z)} \sum_{j=0}^{N} a_j^i z^j, \tag{2.29}$$

where z is related to the recoil variable w ($w = v_B.v_F$ with v_B and v_F being the four-velocities of B meson and the final state meson) as

$$z = \frac{\sqrt{w+1} - \sqrt{2}}{\sqrt{w+1} + \sqrt{2}}. \tag{2.30}$$

w is related to the momentum transferred (q^2) as $q^2 = m_B^2 + m_F^2 - 2m_B m_F w$. The functions $P_i(z)$, called the Blaschke factors, are given by

$$P_i(z) = \prod_p \frac{z - z_p}{1 - z z_p}, \tag{2.31}$$

which are used to eliminate the poles at $z = z_p$ where,

$$z_p = \frac{\sqrt{(m_B + m_F)^2 - m_P^2} - \sqrt{4 m_B m_F}}{\sqrt{(m_B + m_F)^2 - m_P^2} + \sqrt{4 m_B m_F}}. \tag{2.32}$$

Here m_P denotes the pole masses, details are given in [6]. We provide the pole masses used in $B \to D^{(*)}$ and $B_s \to D_s^{(*)}$ channels in this thesis in tables 2.2 and 2.3 respectively.

Form factor involved	$B_c^{(*)}$ pole masses (GeV)
f_+ and g	6.32847, 6.91947, 7.030
f and F_1	6.73847, 6.750, 7.145, 7.150
F_2	6.27447, 6.8712, 7.250
f_0	6.70347, 7.122

Table 2.2: Pole masses used in the $B \to D^{(*)}$ modes.

The outer functions $\phi_i(z)$ are chosen to be [132]

TH-3118_176121005

Form factor involved	$B_c^{(*)}$ pole masses (GeV)
f_+	6.32847, 6.91947, 7.030, 7.280
g	6.32847, 6.91947, 7.030, 7.280, 7.365
f and F_1	6.73847, 6.750, 7.145, 7.150
F_2	6.27447, 6.8712, 7.250
f_0	6.70347, 7.122

Table 2.3: Pole masses used in the $B_s \to D_s^{(*)}$ modes.

$$\begin{aligned}
\phi_{f_+} &= \frac{8r^2}{m_B}\sqrt{\frac{8n_I}{3\pi\tilde{\chi}_{1^-}^T(0)}}\frac{(1+z)^2(1-z)^{1/2}}{[(1+r)(1-z)+2\sqrt{r}(1+z)]^5}, \\
\phi_{f_0} &= r(1-r^2)\sqrt{\frac{8n_I}{\pi\tilde{\chi}_{0^+}^L(0)}}\frac{(1-z^2)(1-z)^{1/2}}{[(1+r)(1-z)+2\sqrt{r}(1+z)]^4}
\end{aligned} \tag{2.33}$$

for pseudoscalar mesons in the final state and

$$\begin{aligned}
\phi_f &= \frac{4r}{m_B^2}\sqrt{\frac{n_I}{6\pi\chi_{1^+}^T(0)}}\frac{(1+z)(1-z)^{3/2}}{[(1+r)(1-z)+2\sqrt{r}(1+z)]^4}, \\
\phi_g &= 16r^2\sqrt{\frac{n_I}{3\pi\tilde{\chi}_{1^-}^T(0)}}\frac{(1+z)^2(1-z)^{-1/2}}{[(1+r)(1-z)+2\sqrt{r}(1+z)]^4}, \\
\phi_{\mathcal{F}_1} &= \frac{4r}{m_B^3}\sqrt{\frac{n_I}{6\pi\chi_{1^+}^T(0)}}\frac{(1+z)(1-z)^{5/2}}{[(1+r)(1-z)+2\sqrt{r}(1+z)]^5}, \\
\phi_{\mathcal{F}_2} &= 8\sqrt{2}r^2\sqrt{\frac{n_I}{\pi\tilde{\chi}_{1^+}^L(0)}}\frac{(1+z)^2(1-z)^{-1/2}}{[(1+r)(1-z)+2\sqrt{r}(1+z)]^4}
\end{aligned} \tag{2.34}$$

for vector mesons in the final state.

Constants	Values
G_F	1.166×10^{-5} GeV^{-2}
$\chi_{1^-}^T$ (0) (for g and f_+)	5.131×10^{-4} GeV^{-2}
$\chi_{1^+}^T$ (0) (for f and F_1)	3.894×10^{-4} GeV^{-2}
$\chi_{0^-}^L$ (0) (for F_2)	1.9421×10^{-2} GeV^{-2}
$\chi_{0^+}^L$ (0) (for f_0)	6.204×10^{-3} GeV^{-2}

Table 2.4: Various inputs relevant to this thesis [6].

Here, $r = m_F/m_B$ and the other inputs can be found in [6]. The values of the constants are provided in table 2.4. These coefficients satisfy the following weak unitarity constraints

TH-3118_176121005

:

$$\sum_{j=0}^{N}(a_j^{f_+})^2 < 1, \quad \sum_{j=0}^{N}(a_j^{f_0})^2 < 1, \quad \sum_{j=0}^{N}(a_j^{g})^2 < 1, \quad \sum_{j=0}^{N}(a_j^{f})^2 + (a_j^{\mathcal{F}_1})^2 < 1, \quad \sum_{j=0}^{N}(a_j^{\mathcal{F}_2})^2 < 1. \tag{2.35}$$

Furthermore, the kinematical constraints on the form factors, at zero and maximum recoil are given as

$$\mathcal{F}_1(1) = m_B(1-r)f(1), \tag{2.36}$$

$$\mathcal{F}_2(w_{max}) = \frac{1+r}{m_B^2(1+w_{max})(1-r)r}\mathcal{F}_1(w_{max}). \tag{2.37}$$

2.2 Statistical tools

The developments in theoretical physics must go parallel with active experimentation which is very crucial for validation of the existing hypotheses or building up of new hypotheses in compliance with the observed data. Over the last few years, there has been a significant progress in high energy physics from both the theoretical and experimental fronts in terms of the precision achieved in the theoretical predictions and the experimental measurements. As discussed in sections 1.3 and 1.4, there are several low energy observables which can be measured with very good accuracy in different experiments. The interesting observables are those for which the SM predictions deviate significantly from their respective measured values, providing hints for some BSM physics. Thus, with the plenty of data in various decay channels available in the past few years and in the coming years, the need for statistical methods remains for extracting meaningful information from the experimental data and verifying the agreement with the model predictions. Statistics offers a way to interprate the observations, typical tasks include:

- Simulating a physical process - modelling
- Measuring the value and uncertainty of a parameter — point and interval estimation.
- Comparing one hypothesis against another — hypothesis testing.
- Comparing one hypothesis against all others — Goodness of fit.

There has been advancement in High Energy Physics through the interplay of top-down (theory-guided) and bottom-up (data-driven) approaches. Since the 80's, the SM has been a roadmap that led to the discovery of the W and Z bosons, the top quark, and the Higgs boson (top-down approach), but the experimental observations which the SM fails to explain necessitates the formulation of competent theories beyond the SM through the data-driven approach. In the following sub-sections, we discuss the important ideas of the statistical methods incorporated in this thesis related to parameter estimation and selection of competent hypotheses compatible with the observed data.

TH-3118_176121005

2.2.1 χ^2 Analysis and goodness-of-fit test

In high energy physics, Reduced χ^2 analysis is one of the most popular methods for point and error estimation. Parameters of the theory are obtained by performing a test of significance (goodness of fit) by defining a χ^2 statistic which is a function of the parameters.

For a set of N independent measurements y_i at known points x_i, we assume that the measurement y_i is Gaussian with mean $\mu(x_i;\theta)$ and variance σ_i^2. The log-likelihood function contains the sum of the squares

$$\chi^2(\theta) = -2lnL(\theta) + constant = \sum_i^N \frac{(y_i - \mu(x_i;\theta))^2}{\sigma_i^2} \tag{2.38}$$

The values of the parameters maximizing the likelihood are the same as those which minimize χ^2.

If the y_is are not independent but have a covariance matrix $V_{ij} = cov[y_i, y_j]$, then χ^2 is defined as

$$\chi^2(\theta) = (y - \mu(\theta))^T V^{-1} (y - \mu(\theta)) \tag{2.39}$$

where $y = (y_1, ..., y_N)$ is the (column) vector of measurements, $\mu(\theta)$ is the corresponding vector of predicted values.

The objective of χ^2 analysis is to minimize the χ^2 statistic or maximize the chances of agreement between the data and the fitted function. Thus, the minimum value of χ^2 can be used for assessing the goodness-of-fit. p-value is a quantity which quantifies how much the data agrees with a given hypothesis, defined as:

$$p = \int_{\chi^2_{min}}^{\infty} f(z; n_d) dz \tag{2.40}$$

assuming that the test-statistic follows a χ^2 probability distribution function (p.d.f.) $f(z; n_d)$ and n_d is the number of degrees of freedom. The mean of the χ^2 distribution equals n_d in general, and thus, the quantity χ^2/n_d defined as reduced χ^2 seems to offer a simple insight in the following ways:

- If $\chi^2_{red} > 1$ for any case, it is treated as a "poor" fit.
- The comparison between competing hypotheses considering a particular set of data is carried out by analyzing the χ^2_{red} values corresponding to each hypothesis. The one with the χ^2_{red} value closest to 1 is the best hypothesis.

Keeping aside the simplicity of this technique, there are some serious pitfalls, the major one being the fact that the value of χ^2 obtained is uncertain and subject to the noise present in the data. This uncertainty should also be reflected in the value of χ^2_{red}, but is generally neglected. Thus, the method of χ^2_{red} isn't reliable to assess the convergence or

TH-3118_176121005

compare various hypotheses and this calls for alternative methods. In order to assess the goodness-of-fit of some model to a given dataset, one should first inspect the distribution of residuals. The true model with parameter values and a-priori known measurement errors σ_i has the normalized residuals [133]

$$R_i = \frac{(y_i - \mu(x_i;\theta))}{\sigma_i} \tag{2.41}$$

distributed according to a Gaussian with mean $\mu = 0$ and variance $\sigma^2 = 1$. For any model, if the normalized residuals are plotted in a histogram and the histogram shows statistically significant deviation from the Gaussian, the model is ruled out. If on the other hand, the difference between the histogram and Gaussian isn't significant, that would signify that either the model is the true model or the number of datapoints aren't sufficient to discover the deviation. One of the methods to quantify comparison of the residuals to the Gaussian is Kolmogorov-Smirnov (KS) test where the empirical cumulative distribution function (CDF) of a sample is compared to a theoretical CDF by quantifying the distance between the distributions. Under the assumption that the sample is drawn from the given distribution, this distance (KS-statistic) has a known probability distribution. The KS-statistic for the particular sample is then compared to its known probability distribution. Another method to compare the residual distribution to the Gaussian is Shapiro-Wilks (SW) test [134] which is the first test which detected departures from normality using skewness and/or kurtosis. Other popular methods are 'Anderson-Darling', 'Cramer-von Mises', 'Jarque-Bera' etc. In all such tests, the validity of a hypothesis depends on whether the probability of the goodness of fit test is above or below the significance of 5 %. Among all the fitted models, the ones with the p-value of the residual distribution above 5 % are considered as the plausible explanation of the data; the rest are ruled out.

2.2.2 Model selection

As discussed in the previous section, one of the major goals of statistical analysis is to select the best model out of all the competing hypotheses for a given dataset and this calls for the role of 'model selection'. Model selection needs to take both goodness of the fit and the complexity of the competing models into account. According to the concept of parsimony [135], a model representing the truth is obtained with the minimum possible number of parameters for efficiently representing the data. If we try to fit the dataset with a model with fewer parameters, the model doesn't fit to the given dataset well and there is the problem of underfitting and high bias. On the other hand, a model with a large number of parameters can fit the observed data very well, but it suffers from the possibility of just fitting the noise leading to overfitting and has poor predictive power for a newer datapoint. Thus, such models have large variance as the model performance greatly varies between the training and test datasets. The important problem, therefore,

TH-3118_176121005

is to optimize the number of parameters required to explain a certain observation. The best model is the one with the number of parameters just right to have minimum bias and minimum variance known as the bias-variance trade-off. Several methods are available in the literature capable of achieving this, we discuss a few of them in the following subsections.

2.2.2.1 $\Delta\chi^2$

When the competing models are nested i.e. one is a subset or extension of the other, $\Delta\chi^2$ test is useful for comparing the models. According to Wilk's theorem [136], when the model with fewer free parameters is true and certain conditions are satisfied, the quantity $\Delta\chi^2$ corresponding to the difference of χ^2 between the two models should follow a χ^2 distribution with the number of degrees of freedom equal to the difference in the number of free parameters in the two models. Thus, one can compute the p-value and decide whether a model be accepted or rejected in favor of the other.

2.2.2.2 Akaike's Information Criteria

This method is based on the empirical log-likelihood function at its maximum point. 'Akaike's information criterion' (AIC) is defined as [137]:

$$\mathrm{AIC} = \chi^2_{\mathrm{min}} + 2\mathrm{K} \tag{2.42}$$

where K is the number of estimable parameters and χ^2_{min} is the χ^2 value for the fitted model. The model with the minimum AIC value is considered to be "closest" to the unknown reality. AIC may perform poorly if the number of parameters is comparable to the size of the sample. To account for the small sample-size, Sugiura derived a second-order variant of AIC.

The small sample-corrected Akaike's Information Criterion (AICc) is defined as [138, 139]

$$\mathrm{AIC}c = \chi^2_{min} + 2K + \frac{2K(K+1)}{n-K-1}\,, \tag{2.43}$$

where n is the sample-size. In the literature, AICc is preferably used when n/K < 40.

AICc is the likelihood penalized by the degrees of freedom. Thus, AICc accounts for uncertainty in the data (-2Log(L)) and makes the assumption that more parameters lead to higher risk of over-fitting (2K). The candidate models are ranked in increasing orders of $\Delta\mathrm{AIC}c^i = \mathrm{AIC}c^i$ - $\mathrm{AIC}c^{min}$. The best model depicting the truth has minimum $\mathrm{AIC}c^i$ and thus $\Delta\mathrm{AIC}c^i = 0$, stating that as the model complexity increases, the chances for it getting selected in the model selection procedure decreases. In table 2.5, we provide the level of support for a model corresponding to the value of $\Delta\mathrm{AIC}c$.

TH-3118_176121005

ΔAICc^i	Level of Empirical Support for Model i
0 - 2	Substantial
4 - 7	Considerably Less
> 10	Essentially None

Table 2.5: The values of ΔAICc^i for analysis of various models.

2.2.2.3 Cross-validation

For model selection, 'cross-validation' (CV) is the most generally applicable, powerful and computationally expensive method [133]. The most straightforward and expensive version of cross-validation is "leave-one-out cross-validation" (LOOCV). It simultaneously tests the predictive power of the model as well as minimizes the bias and variance together. In LOOCV, one of the data points isn't considered and the remaining sample, called the training set is optimized for a particular model. Then that result is used to find the predicted squared error (SE) for the left out data point, which is defined for the i^{th} observable as given below

$$SE = \frac{(\mathcal{O}_i^{exp} - \mathcal{O}_i^{theory})^2}{\sqrt{(\sigma_{exp}^2 + \sigma_{theory}^2)}}, \tag{2.44}$$

where σ_{exp} and σ_{theory} are the experimental and theory errors of the i^{th} observable. This process is repeated for all data points and a mean-squared-error (MSE) is obtained using all those residuals. This process is repeated for all models. The models with the least MSE are the best ones.

2.2.3 Bayesian data analysis

The Bayesian approach has the important characteristic of explicitely using the probability for quantifying uncertainty. Considering n measurements of a random variable x, distributed according to some p.d.f $f(x;\theta)$, the likelihood function for the data $x = (x_1, ...x_n)$ for a given value of the parameter θ can be written as

$$L(\theta|x) = P(x|\theta) = f_{\text{joint}}(x|\theta) = \prod_{i=1}^{n} f(x_i;\theta) \tag{2.45}$$

The interesting quantity to know is the conditional p.d.f. for θ given the data $P(\theta|x, H)$ which is obtained from the Bayes' theorem:

$$P(\theta|x, H) = \frac{P(x|\theta, H)P(\theta|H)}{\int P(x|\theta', H)P(\theta'|H)d\theta'} \tag{2.46}$$

Here H represents the overall hypothesis space, $P(\theta|H)$ is the prior probability density for the parameter θ, signifying the information sbout θ before considering data. $P(\theta|x, H)$ is known as the posterior probability density for the parameter θ in the presence of data.

TH-3118_176121005

In Bayesian statistics, both the observables and the parameters are treated as random variables. Thus, from the knowledge of the probability distribution function of the data $P(x|\theta, H)$ and prior probabilities for the parameters, we can determine the probability for the parameter to attain a specific value and can directly determine the parameter spaces in the presence of observations. Generally, priors are considered to be uniform(flat) : the posterior density function is proportional to the likelihood function and the parameter value that maximizes the posterior density is the same as that which maximizes the likelihood (in one dimension). Given the observations x_0 and assuming $L(\theta) = P(x_0|\theta)$, the value $\hat{\theta}$ that maximizes Likelihood offers an estimate of the true value of the parameter, whereas the uncertainty is obtained from the square root of the estimator's variance.

TH-3118_176121005

Chapter 3

New physics in $b \to s\ell\ell$ decays with complex Wilson coefficients

3.1 Introduction

In this chapter[1], we have analysed the new physics effects in the exclusive Flavor Changing Neutral Current $b \to s\ell\ell$ transitions in a model-independent effective theory approach with dimension-six operators with the objective of providing a plausible explanation to the perceived anomalous results in flavor physics, as discussed in section 1.5. The effective Hamiltonian and the operator basis for the $b \to s\mu^+\mu^-$ transitions are discussed in section 2.1.1.2. The analysis has been performed with the most recent data obtained from various experimental collaborations while comparing the outcome with that from the relatively old dataset. As a first step, we check whether each of the single-operator scenarios can independently explain the present data and find that the operator $\mathcal{O}_9 = \frac{e^2}{g^2}(\bar{s}\gamma_\mu P_L b)(\bar{\mu}\gamma^\mu \mu)$ is the only one-operator scenario for not only real but also complex Wilson coefficient that can accommodate the present data. It is thus tempting to look for other possible combinations of these operators with the potential to explain the present data, which is achieved through the procedure of model selection, as discussed in section 2.2.2.

In section 3.2, we first discuss the theory related to the FCNC transition considered in this chapter, in section 3.3, we mention about the experimental inputs used in this analysis. In section 3.4, we provide details of the analysis method considering initially the one-operator scenarios and subsequently employ state-of-the-art model selection tools to pick out the best possible combinations of the operators capable of explaining the data. Finally, in section 3.5, we summarize the main results obtained in this chapter.

[1]The main results and other contents of this chapter have been published in [140].

TH-3118_176121005

3.2 Theory

As seen in section 2.1.1.2, for a proper organization of the perturbative expansion of the WCs, a normalization factor $16\pi^2/g^2$ has been introduced in front of the operators $\tilde{\mathcal{O}}_i^{(\prime)}$ $(i = 7, .., 10)$ [118]. The new WCs are treated as free parameters and fitted directly from data. Therefore, the discussion on this choices of a proper normalization is more relevant in the context of the SM operators and the corresponding WCs, in particular, in their renormalization group evolution equation. For these operators and the corresponding WCs, it is possible to change the normalization to another commonly used basis [7, 141]:

$$\mathcal{O}_i^{(\prime)} = \frac{g^2}{16\pi^2}\tilde{\mathcal{O}}_i^{(\prime)} \quad \text{and} \quad C_i^{(\prime)} = \frac{16\pi^2}{g^2}\tilde{C}_i^{(\prime)}. \tag{3.1}$$

In this chapter, we have considered the NP effects in the following set of operators:

$$\begin{aligned}
&\mathcal{O}_7' = \frac{e}{16\pi^2} m_b(\bar{s}\sigma_{\mu\nu}P_L b)F^{\mu\nu}, \quad \mathcal{O}_9 = \frac{e^2}{16\pi^2}(\bar{s}\gamma_\mu P_L b)(\bar{\mu}\gamma^\mu\mu), \quad \mathcal{O}_9' = \frac{e^2}{16\pi^2}(\bar{s}\gamma_\mu P_R b)(\bar{\mu}\gamma^\mu\mu),\\
&\mathcal{O}_{10} = \frac{e^2}{16\pi^2}(\bar{s}\gamma_\mu P_L b)(\bar{\mu}\gamma^\mu\gamma_5\mu), \quad \mathcal{O}_{10}' = \frac{e^2}{16\pi^2}(\bar{s}\gamma_\mu P_R b)(\bar{\mu}\gamma^\mu\gamma_5\mu), \quad \mathcal{O}_S = \frac{e^2}{16\pi^2} m_b(\bar{s}P_R b)(\bar{\mu}\mu),\\
&\mathcal{O}_S' = \frac{e^2}{16\pi^2} m_b(\bar{s}P_L b)(\bar{\mu}\mu), \qquad \mathcal{O}_P = \frac{e^2}{16\pi^2} m_b(\bar{s}P_R b)(\bar{\mu}\gamma_5\mu), \quad \mathcal{O}_P' = \frac{e^2}{16\pi^2} m_b(\bar{s}P_L b)(\bar{\mu}\gamma_5\mu)\,.
\end{aligned} \tag{3.2}$$

The relevant WCs are the following: C_7', ΔC_9, C_9', ΔC_{10}, C_{10}', $C_S^{(\prime)}$, and $C_P^{(\prime)}$.

The NP contributions to operators $\mathcal{O}_{9,10}$ are given by $\Delta C_{9,10}$. We have not explored the possibility of new physics effects in $\mathcal{O}_7$ which is tightly constrained from the available data on inclusive and exclusive radiative decays. However, we have considered new physics effects in the chirality flipped operator $\mathcal{O}_7'$, the real part of the corresponding WC C_7' is also tightly constrained from the data. Section 2.1.1.2 contains an elaborate discussion on the theoretical framework relevant to the FCNC transitions and section 1.4 describes the various observables that can be extracted from the decay distributions corresponding to pseudoscalar or vector meson in the final state.

3.3 Experimental Inputs

In this section, we categorically present the experimental inputs in our analysis. Our main analysis is based on the following data sets:

- **Likelihood dataset 2020:**

  (1) Measured values of the angular observables in $B^0 \to K^{*0}\mu^+\mu^-$ decays in different bins, gathered from ref. [98] (LHCb).

TH-3118_176121005

(2) For $B^{(0,+)} \to K^{(0,+)}\mu^+\mu^-$ decays, we consider: (i) The LHCb and Belle measurements on the (differential) branching fractions in different bins which are taken from [142] and [143], respectively. (ii) Isospin asymmetries measured by Belle [143] and LHCb [142]. (iii) Binned data on the angular observables for $B^+ \to K^+\mu^+\mu^-$ (A_{FB} and F_H) obtained from CMS (ref. [104]). (iv) The inputs on R_K have been taken from refs. [96] (LHCb) and [143] (Belle) where the Belle results for different bins are also included.

(3) For $B \to K^*\mu^+\mu^-$ decays, we include: (i) Binned data on the differential branching fraction from LHCb for $B^0 \to K^{*0}\mu^+\mu^-$ and $B^+ \to K^{*+}\mu^+\mu^-$ decays, taken from ref. [103] and [142], respectively. (ii) The measured values of the angular observables in $B^0 \to K^{*0}\mu^+\mu^-$ decays in different bins gathered from [144] (ATLAS). (iii) The measured values of P_4' and P_5' for $B^0 \to K^{*0}\mu^+\mu^-$ by Belle in ref. [145]. (iv) Isospin-asymmetry measurements corresponding to $B \to K^*\mu^+\mu^-$ from LHCb (ref. [142]). Furthermore, the measured values of $R_{K^{*(+,0)}}$ in different bins are taken from refs. [97] and [106], respectively.

(4) Binned data on the differential branching fractions and angular observables (CP-averaged and asymmetric) for $B_s \to \phi\mu^+\mu^-$ (LHCb) from ref. [105]. Other inputs are: (i) $\mathrm{BR}(B \to X_s\gamma)_{E_\gamma > 1.6\,\mathrm{GeV}}$ [146], (ii) $\mathrm{BR}(B^{+/0} \to K^*\gamma)$ [147],(iii) $\overline{\mathrm{BR}}(B_s \to \phi\gamma)$ [148], (iv) $Br(B_s \to \mu\mu)$ [149].

For the purpose of comparison we perform our analysis over two other datasets apart from the set mentioned above, which we call the (i) Moment 2016 dataset, (ii) Likelihood 2016 dataset, which are as given below

- **Moments dataset 2016:** Values for the angular observables measured by the "Method of moments" in $B^0 \to K^{*0}\mu^+\mu^-$ decays in different bins, gathered from refs. [95] (LHCb).
- **Likelihood dataset 2016:** Values for the angular observables following "Unbinned Maximum likelihood" method in $B^0 \to K^{*0}\mu^+\mu^-$ decays in different bins, gathered from refs. [95] (LHCb).

The only difference between the datasets mentioned above is subject to the angular observables in the $B^0 \to K^{*0}\mu^+\mu^-$ sector due to LHCb. The inputs discussed in items (2), (3) and (4) of our primary dataset (**Likelihood dataset 2020**) are included in the **Moments dataset 2016** and **Likelihood dataset 2016** as well. Apart from the datasets discussed above, we have also carried out an analysis without considering the inputs on CP-asymmetric observables in $B_s \to \phi\mu\mu$ channel.

In addition to other inputs (e.g. CKM matrix elements) [150], we have included the lattice input $f_{B_s} = 0.2284 \pm 0.0037$ GeV [151] in all the fits. In [98], LHCb did not update the measurement on CP-asymmetric observables in $B^0 \to K^{*0}\mu^+\mu^-$ decays. Therefore,

TH-3118_176121005

Observables	LHCb 2016 [95]	LHCb 2020 [98]	pull wrt LHCb 2016	pull wrt LHCb 2020
$A_{FB}^{[0.1,0.98]}$	-0.003 ± 0.058	-0.004 ± 0.04	1.43	2.03
$S_3^{[1.1,2.5]}$	-0.077 ± 0.096	-0.107 ± 0.052	-0.82	-2.08
$S_7^{[1.1,2.5]}$	-0.219 ± 0.099	-0.107 ± 0.063	-2.31	-1.86
$S_8^{[1.1,2.5]}$	-0.098 ± 0.116	-0.174 ± 0.075	-0.9	-2.4
$S_9^{[1.1,2.5]}$	-0.119 ± 0.096	-0.112 ± 0.054	-1.25	-2.07
$P_1^{[1.1,2.5]}$	-0.451 ± 0.579	-0.617 ± 0.297	-0.8	-2.12
$P_3^{[1.1,2.5]}$	0.350 ± 0.292	0.324 ± 0.148	1.2	2.2
$P_6^{'[1.1,2.5]}$	-0.463 ± 0.212	-0.226 ± 0.128	-2.29	-1.94
$P_8^{'[1.1,2.5]}$	-0.208 ± 0.248	-0.366 ± 0.158	-0.89	-2.4
$S_5^{[4,6]}$	-0.146 ± 0.078	-0.204 ± 0.053	2.41	2.43
$S_7^{[4,6]}$	-0.016 ± 0.081	-0.136 ± 0.053	-0.26	-2.66
$P_2^{[4,6]}$	0.042 ± 0.088	0.105 ± 0.069	-2.65	-2.48
$P_5^{'[4,6]}$	-0.300 ± 0.160	-0.439 ± 0.117	2.96	2.85
$P_6^{'[4,6]}$	-0.032 ± 0.167	-0.293 ± 0.117	-0.26	-2.6
$S_7^{[1.1,6]}$	-0.077 ± 0.050	-0.09 ± 0.034	-1.69	-2.86
$P_6^{'[1.1,6]}$	-0.166 ± 0.11	-0.197 ± 0.076	-1.66	-2.83

Table 3.1: List of a few observables with pulls > 2 from the 'Likelihood dataset 2020' and 'Likelihood dataset 2016'. The superscripts on the observables indicate the q^2 range in GeV^2. The corresponding SM predictions can be seen from [7].

List of few more observables with pull > 2 which are common to all the datasets		
Observables	Measured values	Respective pulls
$BR(B^0 \to K^0\mu^+\mu^-)^{[1,6]}$ Belle [143]	$(3.1 \pm 1.9) \times 10^{-8}$	-3.9
$A_I(B \to K\mu^+\mu^-)^{[1,6]}$ Belle [143]	-0.52 ± 0.19	-2.8
$P_4'(B^0 \to K^{*0}\mu^+\mu^-)^{[4,6]}$ ATLAS [144]	0.64 ± 0.38	2.97
$S_4(B^0 \to K^{*0}\mu^+\mu^-)^{[4,6]}$ ATLAS [144]	0.32 ± 0.18	2.87
$F_H(B^+ \to K^+\mu^+\mu^-)^{[2,4.3]}$ CMS [104]	0.85 ± 0.35	2.34

Table 3.2: The data with pulls > 2 which are common to all the datasets. The superscripts on the observables indicate the q^2 range in GeV^2.

to check whether they provide tighter constraints on the complex WCs, we incorporate those measurements [95] in a different fit along with the dataset defined as **Likelihood dataset 2020**. We consider the bins for $q^2 \leq 6$ GeV^2 to avoid any contamination from the charm resonances.

3.4 Analysis and Results

3.4.1 One-operator scenarios

With a total of 224 observables in the 'Likelihood dataset 2020', we perform a frequentist statistical analysis optimizing a χ^2 statistic which is a function of the relevant WCs (real

TH-3118_176121005

as well as complex) in the one-operator scenarios. Separate covariance matrices are constructed for statistical (systematic) uncertainties wherever necessary. In the post-process for each fit, we obtain the corresponding fit-quality using p-value. For the analysis with all data, we obtain a very poor quality fit for all the one operator scenarios with the respective p-values $<< 1\%$ which implies that there must be some data points that are in tension with the others. We find that $\mathcal{O}_9$ is the only one operator scenario in both the analyses with complex as well as real WCs having a relatively better p-value, though it is $< 1\%$, whereas in all other one operator scenarios, the fit quality is very poor, with the respective p-values ≈ 0.

To look for a possibility of improvement in the statistical significance of the fits, we have computed the pulls of the SM estimates w.r.t the corresponding measured values for all the observables. The pull corresponding to the i^{th} observable $\mathcal{O}_i$ is defined as:

$$\text{pull}_i = \frac{\mathcal{O}_i^{exp} - \mathcal{O}_i^{SM}}{\Delta\mathcal{O}_i} \tag{3.3}$$

where $\Delta\mathcal{O}_i$ corresponds to the uncertainty of the measurements, including theoretical uncertainties. From our analysis, we find a few angular observables (listed in table 3.1) for the likelihood dataset 2020 whose measured values have pulls greater than 2 w.r.t the corresponding SM estimates. The table also shows the pulls corresponding to the likelihood dataset 2016 for the same observables comparing which we find that the current measured values of a few observables have larger pulls than the corresponding measured values from the 2016 dataset. The observables measured by other experimental collaborations like ATLAS, CMS ad Belle having pull > 2 have been listed in table 3.2.

Besides this, using results of the fit to all data, we compare the fitted values (in an NP scenario) of each observable to their measured values by defining the pull, which for the i^{th} observable is given by

$$\text{pull}_i^{NP} = \frac{\mathcal{O}_i^{exp} - \mathcal{O}_i(C_k^{NP})}{\Delta\mathcal{O}_i}. \tag{3.4}$$

Here, $\mathcal{O}_i(C_k^{NP})$ is the predicted value of the i^{th} observable in a new physics scenario with the best fit value of C_k^{NP}. A few observations from the pull analyses of eq. 3.4 is as follows:

(1) Apart from $\mathcal{O}_9$, in all the other one-operator NP scenarios, the data points listed in tables 3.1 and 3.2 with a pull > 2 are also selected with a $\text{pull}^{NP} > 2$.

(2) Only for the one-operator scenario $\mathcal{O}_9$, the three data points: $P_5^{\prime\,[4,6]}(LHCb)$, $S_5^{[4,6]}(LHCb)$, and $P_2^{[4,6]}(LHCb)$ have $\text{pull}^{NP} < 2$.

(3) Apart from the data points given in table 3.1 and 3.2, the LFUV data points $R_{K^{*0}}^{[0.045,1.1]}(LHCb)$, $R_{K^{*0}}^{[1.1,6]}(LHCb)$, and $R_K^{[1.1,6]}(LHCb)$ also have pull > 2 compared to their SM estimates. However, in different NP scenarios, the estimates

TH-3118_176121005

Observables in **List-1** with the respective pulls in the one-operator scenario $\mathcal{O}_9$	
$BR(B^0 \to K^0\mu^+\mu^-)^{[1,6]}$ (Belle) $\to$ -2.92	$S_7^{[4,6]}$ (LHCb) $\to$ - 2.56
$P_4^{'}(B^0 \to K^{*0}\mu^+\mu^-)^{[4,6]}$ (ATLAS) $\to$ 2.90	$P_6^{'\,[4,6]}$ (LHCb) $\to$ - 2.50
$S_4(B^0 \to K^{*0}\mu^+\mu^-)^{[4,6]}$ (ATLAS) $\to$ 2.86	$BR(B^+ \to K^+\mu^+\mu^-)^{[1,6]}$ (Belle)$\to$ 2.39
$A_I(B \to K\mu^+\mu^-)^{[1,6]}$ (Belle) $\to$ -2.81	$\frac{dB}{dq^2}(B^+ \to K^+\mu^+\mu^-)^{[0.1,0.98]}$ (LHCb)$\to$ 2.18
$S_7^{[1.1,6]}$ (LHCb) $\to$ - 2.64	$S_5(B^0 \to K^{*0}\mu^+\mu^-)^{[4,6]}$ (ATLAS)$\to$ 2.10
$P_6^{'\,[1.1,6]}$ (LHCb) $\to$ - 2.61	$P_5^{'}(B^0 \to K^{*0}\mu^+\mu^-)^{[4,6]}$ (ATLAS) $\to$ 2.02

Table 3.3: The respective values of pull^{NP} obtained using eq. 3.4 for the observables in **List-1** for the one-operator scenario $\mathcal{O}_9$ with complex WC. For the scenario with real WC also, these observables have pull$^{NP} > 2$. The superscripts on the observables indicate the q^2 range in GeV^2.

of pull^{NP} for $R_{K^{*0}}^{[1.1,6]}(LHCb)$ and $R_K^{[1.1,6]}(LHCb)$ are < 2, though, pull$^{NP} > 2$ for $R_{K^{*0}}^{[0.045,1.1]}(LHCb)$ in various NP scenarios including $\mathcal{O}_9$. We have included all these important LFUV observables in our fits. We will use the notation $R_{K^*}^{Low}$ and $R_{K^*}^{Central}$ from now on to represent R_{K^*} corresponding to $q^2 \in [0.045, 1.1]\text{GeV}^2$ and $[1.1, 6]\text{GeV}^2$, respectively.

(4) In all the NP scenarios, a few additional data points are selected with a pull$^{NP} \gtrsim 2$. The data points which are common among all of them are the following: $P_5^{'}(B^0 \to K^{*0}\mu^+\mu^-)^{[4,6]}$ (ATLAS), $S_5(B^0 \to K^{*0}\mu^+\mu^-)^{[4,6]}$ (ATLAS), $\frac{dB}{dq^2}(B^+ \to K^+\mu^+\mu^-)^{[0.1,0.98]}$ (LHCb) and $BR(B^+ \to K^+\mu^+\mu^-)^{[1,6]}$ (Belle).

(5) The data points mentioned in item 4 above (which are common to all other datasets) are picked up with a pull$^{NP} > 2$ in the analyses with the Moments 2016 and Likelihood 2016 datasets as well.

Following the above discussion and with the primary intention to get a fit with allowed p-values, we prepare a list of data as given below which we will drop while fitting,

- **List-1**: This list is prepared from the **Likelihood dataset 2020**. It contains the observables listed in tables 3.1 and 3.2 for the same dataset with a pull > 2.5. As discussed above, the optimised observable $P_5^{'\,[4,6]}$ has not been included in this list. It also includes $P_5^{'}(B^0 \to K^{*0}\mu^+\mu^-)^{[4,6]}$ (ATLAS), $S_5(B^0 \to K^{*0}\mu^+\mu^-)^{[4,6]}$ (ATLAS), $\frac{dB}{dq^2}(B^+ \to K^+\mu^+\mu^-)^{[0.1,0.98]}$ (LHCb) and $BR(B^+ \to K^+\mu^+\mu^-)^{[1,6]}$ (Belle). Including all these, the list contains 12 data points for which the respective values of pull^{NP} are given for the one-operator scenario $\mathcal{O}_9$ with complex WCs in table 3.3.

We repeat the fits with one operator after dropping these 12-data points from our complete list. We have noticed a considerable improvement in the overall fit quality for all the one-operator scenarios, though still very poor in comparison to $\mathcal{O}_9$. For $\mathcal{O}_9$ considering both real and complex W.Cs, we have presented the corresponding results in table 3.4. We have repeated the fit with the new 'Likelihood 2020 datasets' in two more subsets:

TH-3118_176121005

(i) without considering the inputs from the CP-asymmetric observables in $B_s \to \phi\mu\mu$, (ii) including the inputs from the CP-asymmetric observables in $B \to K^*\mu\mu$ from 'Likelihood 2016 datasets'. For comparison, the results for these different datasets corresponding to the one-operator scenario $\mathcal{O}_9$ are presented in the same table 3.4. The allowed confidence intervals for $Re(\Delta C_9)$ are consistent with each other for all the three different fits, and large imaginary contributions are allowed by the present data even after dropping the CP-asymmetric observables in $B_s \to \phi\mu\mu$ and $B \to K^*\mu\mu$ from the fit. We have given the values of the respective χ^2_{SM} and mentioned the corresponding p-values (in SM) for all the three different scenarios. For all these cases, following ref. [152] we have calculated Pull_{SM} which is defined as

$$\text{Pull}_{\text{SM}} = \sqrt{2}\text{Erf}^{-1}[F(\Delta\chi^2_{\text{SM}}; n_{\text{dof}})], \quad \text{with } \Delta\chi^2_{\text{SM}} = \chi^2_{SM} - (\chi^2_{min})_{NP}. \tag{3.5}$$

Here, F is the χ^2 cumulative distribution function and n_{dof} is the associated number of degrees of freedom. We compare the respective NP scenarios against the SM by defining Pull_{SM}. A large value of this quantity indicates a large deviation from the SM.

Fit scenario: Likelihood dataset 2020 ($\chi^2_{SM} = 288.9$, p-value (%) in SM = 0.035)			
χ^2_{Min}/DOF	p-value (%)	Pull_{SM}	confidence intervals
206.5/211	57.4	9.1	$Re(\Delta C_9) \to -1.05 \pm 0.11$
202.9/210	62.5	9.0	$Re(\Delta C_9) \to -1.10 \pm 0.11$
			$Im(\Delta C_9) \to 1.27^{+0.33}_{-0.43}$
Fit scenario: Likelihood dataset 2020 without CP-asymmetric observables in $B_s \to \phi\mu\mu$ ($\chi^2_{SM} = 297.6$, p-value (%) in SM = 9×10^{-4})			
χ^2_{Min}/DOF	p-value (%)	Pull_{SM}	confidence intervals
198.2/199	50.2	10	$Re(\Delta C_9) \to -1.05 \pm 0.11$
194.9/198	54.8	9.9	$Re(\Delta C_9) \to -1.11^{+0.13}_{-0.12}$
			$Im(\Delta C_9) \to -1.36^{+0.44}_{-0.34} \cup [0.84,\ 1.59]$
Fit scenario: Likelihood dataset 2020 + CP-asymmetric observables in $B \to K^*\mu\mu$ from LHCb Likelihood dataset 2016 ($\chi^2_{SM} = 322.1$, p-value (%) in SM = 0.09)			
χ^2_{Min}/DOF	p-value (%)	Pull_{SM}	confidence intervals
239.8/246	60	9.1	$Re(\Delta C_9) \to -1.06 \pm 0.11$
238.1/245	61.2	8.9	$Re(\Delta C_9) \to -1.09 \pm 0.11$
			$Im(\Delta C_9) \to -1.11^{+0.62}_{-0.40}$

Table 3.4: Fit results for the frequentist analysis in one-operator($\mathcal{O}_9$) scenarios with real and complex WCs after dropping the observables given in **List-1**. The cases without the CP-asymmetric observables in $B_s \to \phi\mu\mu$, and including the CP-asymmetric observables in $B \to K^*\mu\mu$ are presented separately. The parameter uncertainties are estimated from profile likelihoods.

The 1-D and 2-D profile likelihoods for the real and imaginary WCs have been depicted as 1-CL plots in fig. 3.1. The allowed confidence intervals for $Re(\Delta C_9)$ are consistent in

TH-3118_176121005

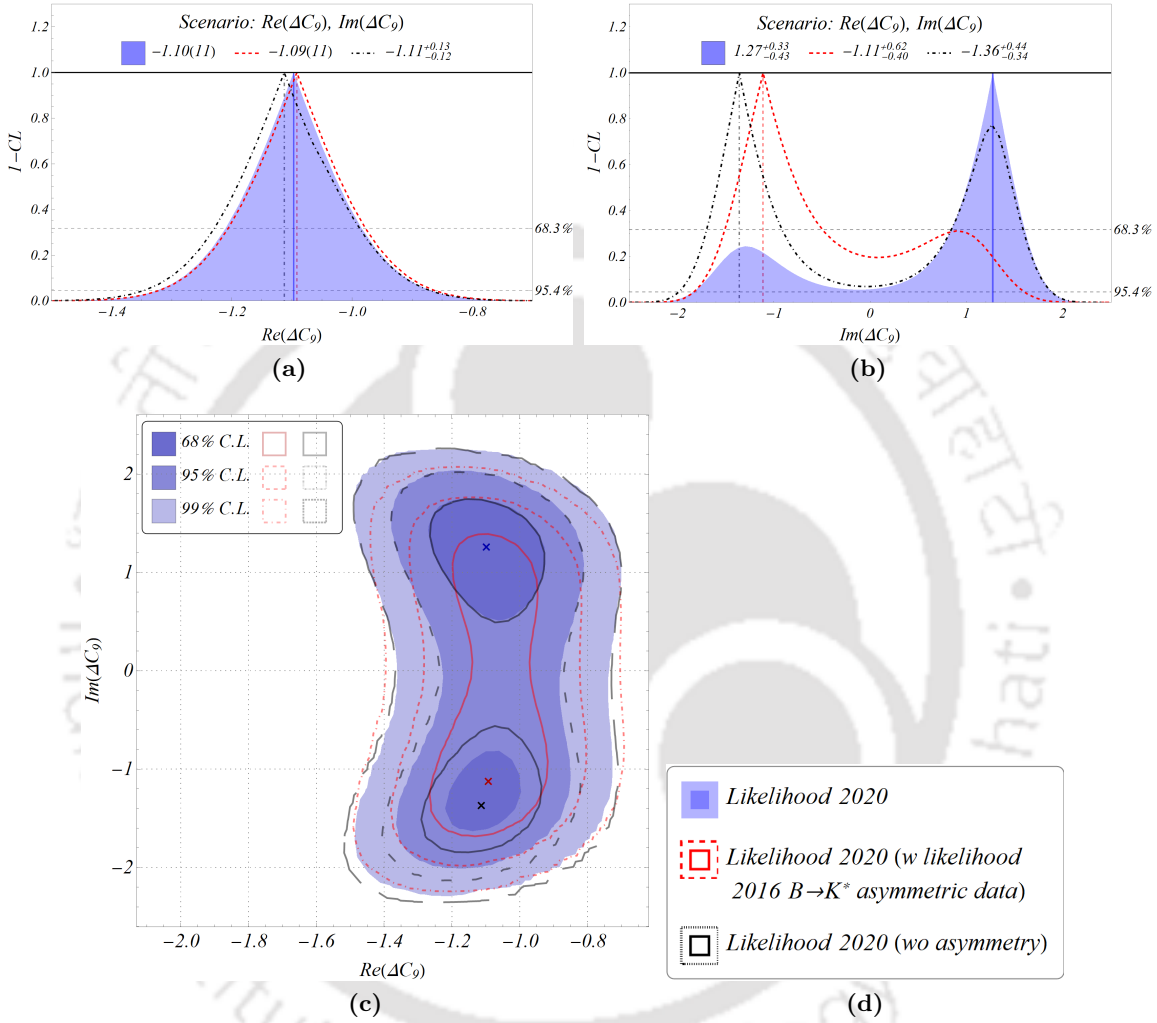

Figure 3.1: One and two-parameter profile-likelihoods corresponding to the single operator scenario $\mathcal{O}_9$ with complex WC in different fit scenarios as discussed in table 3.4. (a) and (b) display the one parameter profile likelihoods for the real and imaginary parts of ΔC_9 while fig. (c) displays the two parameter profile likelihood. The filled, blue contour corresponds to the new "Likelihood 2020 dataset" and the red dashed contour to the same dataset including the CP-asymmetric observables in $B \to K^*$ from "Likelihood 2016 dataset", respectively. The black, dot-dashed contour represents the "Likelihood 2020" data with all the asymmetric observables (due to $B_s \to \phi\mu\mu$ modes) removed. The corresponding legends are shown in figure (d).

TH-3118_176121005

all the three fit scenarios. At $68.3\%CL$, we note a significant shift in the allowed regions of $Im(\Delta C_9)$ in the fits with and without the CP-asymmetric observables in $B \to K^*$ modes, and they are almost mirror images of each other. The fit to the datasets without the CP-asymmetric observables in $B \to K^*$ modes has a slight preference for positive solutions for $Im(\Delta C_9)$, whereas the fit to the datasets with all the CP-asymmetric observables in $B \to K^*$ and $B_s \to \phi$ modes prefers negative solutions for $Im(\Delta C_9)$, though positive solutions are also allowed. In the fit with all the CP-asymmetric observables dropped, both positive and negative solutions for $Im(\Delta C_9)$ are allowed and both of them can be considered favorable. As can be seen from fig. 3.1c, at $68.3\%CL$ we have two disconnected regions that are almost symmetric w.r.t zero; while at $95\%CL$ we get a zero consistent solution. In particular, we have checked that the χ^2_{min} for the negative and positive solutions are 194.93 and 195.03, respectively, signifying the preference for the negative solution.

These observations can be understood from a study of the dependencies of the CP-asymmetric and other associated angular observables in $B \to K^*$ and $B_s \to \phi$ decay modes on $Im(\Delta C_9)$. We have figured out a few CP-asymmetric observables in $B_s \to \phi\mu\mu$ decays, for example, $A_8^{[0.1,2]}$ and $A_8^{[2,5]}$ for which, at the present level of accuracy, the current measured values prefer positive values of $Im(\Delta C_9)$. On the other hand, the CP-asymmetric observables $A_8^{[0.1,0.98]}$, $A_8^{[1.1,2.5]}$, $A_8^{[1.1,6]}$ and $A_8^{[2.5,4]}$ in $B \to K^*$ modes favor negative values of $Im(\Delta C_9)$, though positive values are also allowed. The dependence of these observables on $Im(\Delta C_9)$ for the best fit value of $Re(\Delta C_9)$ are shown in figure 3.2. The data for the $B \to K^*$ modes being relatively more precise play the dominant role in choosing the favorable solutions for $Im(\Delta C_9)$ when combined with the CP-asymmetric observables in $B_s \to \phi$ channel.

In all the three fit scenarios, with and without the CP-asymmetric observables, a considerable value of $Im(\Delta C_9)$ is allowed and large values of $Im(\Delta C_9)$ are allowed even when the CP-asymmetric observables in $B \to K^*$ and $B_s \to \phi$ decays are not included in the fit, though at $95\%CL$ the solutions are consistent with zero. The requirement of a large $Im(\Delta C_9)$, even in the absence of any CP-asymmetric observables can be understood by looking at the dependence of some CP-averaged observables on $Im(\Delta C_9)$. In figs. 3.3a, 3.3b, 3.3c and 3.3d, we have shown the variation of F_L, A_{FB}, P_5' and R_{K^+} in some specific bins respectively with $Im(\Delta C_9)$ for the allowed values of $Re(\Delta C_9)$ (at $68\%CL$), as given in Table 3.4. As is evident from the figures, we require a large non-zero $Im(\Delta C_9)$ to explain the experimental observations within their 1-σ confidence interval in a few specified q^2-bins. Moreover, the allowed values are symmetric about $Im(\Delta C_9) = 0$. Though it is too early to conclude, at the moment it might be hinting towards the possibility of a large imaginary contribution to ΔC_9. However, further assertions and hence solid conclusions must be subject to more precise data, hopefully in the near future.

As mentioned earlier, we present our results based on the most recent 'likelihood'

TH-3118_176121005

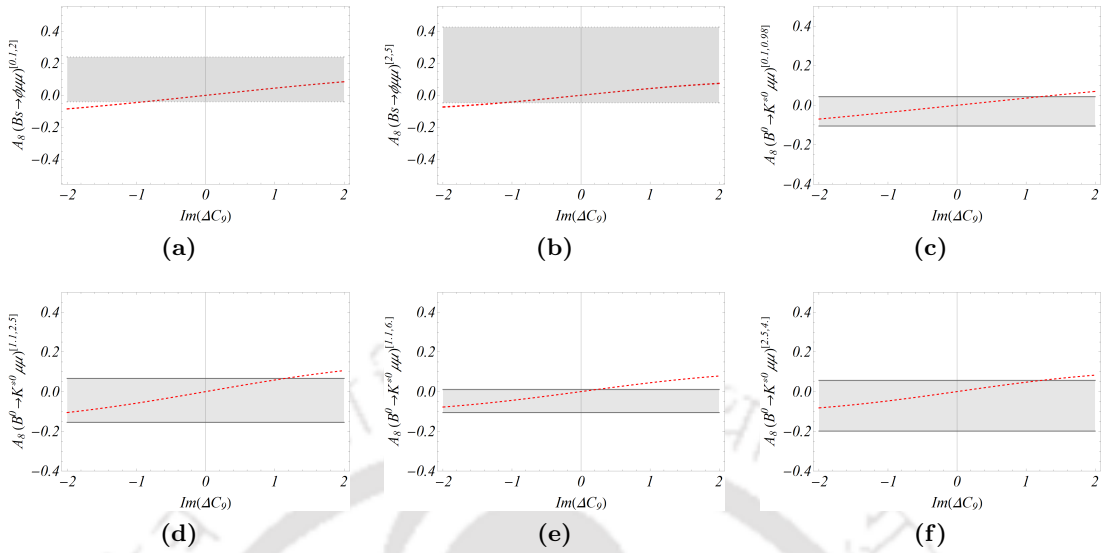

Figure 3.2: Sensitivity of a few CP asymmetric observables in $B_s \to \phi\mu\mu$ and $B \to K^*\mu\mu$ decays to the Imaginary part of ΔC_9. The grey bands represent the current LHCb bounds.

data (by LHCb). To understand the trend of the data, we carry out a fit using the old-data (Run-1: Likelihood and moments) on angular observables from LHCb [95] with complex WCs. The 'Likelihood datasets 2016' and 'Moment datasets 2016' contain a total of 259 and 281 data points respectively. For the 'moment datasets', including all these observables, one can fit the one-operator scenario $\mathcal{O}_9$ with an allowed p-value. However, it is difficult to fit the other one-operator scenarios. On the other hand, for 'Likelihood datasets 2016', fit to any NP scenario, including all the observables has a fit-probability $p << 3$ %. As discussed earlier, the data points: $P_5'(B^0 \to K^{*0}\mu^+\mu^-)^{[4,6]}$ (ATLAS), $S_5(B^0 \to K^{*0}\mu^+\mu^-)^{[4,6]}$ (ATLAS), $\frac{dB}{dq^2}(B^+ \to K^+\mu^+\mu^-)^{[0.1,0.98]}$ (LHCb) and $BR(B^+ \to K^+\mu^+\mu^-)^{[1,6]}$ (Belle), and the ones given in table 3.2 are common to all the datasets. To be consistent with the earlier analyses, we prepare another list consisting of these observables only:

- **List-2**: It includes $P_5'(B^0 \to K^{*0}\mu^+\mu^-)^{[4,6]}$ (ATLAS), $S_5(B^0 \to K^{*0}\mu^+\mu^-)^{[4,6]}$ (ATLAS), $\frac{dB}{dq^2}(B^+ \to K^+\mu^+\mu^-)^{[0.1,0.98]}$ (LHCb) and $BR(B^+ \to K^+\mu^+\mu^-)^{[1,6]}$ (Belle) in addition to the observables listed in table 3.2 with a pull > 2.5.

For the one-operator scenarios, the comparative results are shown in Table 3.5. We have dropped the observables given in **List-1** for the "Likelihood 2020 datasets" and in **List-2** for the "Likelihood 2016 datasets" and "Moments 2016 datasets". We find that $\mathcal{O}_9$ is the only one operator scenario that can comfortably explain all these data-sets, and a large value of $Im(\Delta C_9)$ is allowed by the current data. The fit with the "Moment-dataset" results in appreciable fit probabilities for all the one operator scenarios, as seen from table 3.5. As can be seen from table 3.5, the magnitude of the best fit value of $Re(\Delta C_9)$,

TH-3118_176121005

Dataset	χ^2/DOF	p-val(%)	Value	χ^2/DOF	p-val(%)	Value
	$C_7^{'}$			ΔC_9		
Likelihood 2020	279.5/210	9.4×10^{-2}	$Re(C_7^{'}) \to$ -0.039±0.013 $Im(C_7^{'}) \to$ -0.026±0.101	202.89/210	62.5	$Re(\Delta C_9) \to$ -1.10±0.11 $Im(\Delta C_9) \to$ 1.27±0.37
Likelihood 2016	306.45/249	0.7	$Re(C_7^{'}) \to$ -0.03±0.01 $Im(C_7^{'}) \to$ -0.002±0.025	235.79/249	71.6	$Re(\Delta C_9) \to$ -1.21±0.14 $Im(\Delta C_9) \to$ -1.25±0.44
Moments 2016	291.85/271	18.4	$Re(C_7^{'}) \to$ -0.031±0.016 $Im(C_7^{'}) \to$ -0.0057±0.0300	241.7/271	89.9	$Re(\Delta C_9) \to$ -1.24±0.18 $Im(\Delta C_9) \to$ 1.19±0.48
	$C_9^{'}$			ΔC_{10}		
Likelihood 2020	287.9/210	2.9×10^{-2}	$Re(C_9^{'}) \to$ -0.077±0.149 $Im(C_9^{'}) \to$ -0.70±0.54	276.17/210	0.15	$Re(\Delta C_{10}) \to$ 0.64±0.18 $Im(\Delta C_{10}) \to$ 1.79±0.29
Likelihood 2016	310.72/249	0.47	$Re(C_9^{'}) \to$ -0.13±0.15 $Im(C_9^{'}) \to$ -0.15±0.71	303.22/249	1.1	$Re(\Delta C_{10}) \to$ 0.39±0.15 $Im(\Delta C_{10}) \to$ 0.45±0.50
Moments 2016	295.4/271	14.8	$Re(C_9^{'}) \to$ -0.060±0.148 $Im(C_9^{'}) \to$ -0.084±0.423	281.7/271	31.5	$Re(\Delta C_{10}) \to$ 0.51±0.14 $Im(\Delta C_{10}) \to$ -0.11±0.68
	$C_{10}^{'}$			C_S		
Likelihood 2020	278.1/210	0.1	$Re(C_{10}^{'}) \to$ 0.33±0.11 $Im(C_{10}^{'}) \to$ -0.21±0.81	288.55/210	2.6×10^{-2}	$Re(C_S) \to$ -0.029±0.483 $Im(C_S) \to$ -0.032±0.440
Likelihood 2016	303.0/249	1.1	$Re(C_{10}^{'}) \to$ 0.33±0.11 $Im(C_{10}^{'}) \to$ 0.02±0.28	311.19/249	0.4	$Re(C_S) \to$ -0.04±0.04 $Im(C_S) \to$ 0.0017±0.3043
Moments 2016	290.2/271	20.2	$Re(C_{10}^{'}) \to$ 0.28±0.12 $Im(C_{10}^{'}) \to$ -0.0030±0.3175	295.4/271	14.8	$Re(C_S) \to$ -0.027±0.279 $Im(C_S) \to$ 0.030±0.251
	C_P			$C_S^{'}$		
Likelihood 2020	288.52/210	2.6×10^{-2}	$Re(C_P) \to$ -0.0075±0.0135 $Im(C_P) \to$ 0.003±0.241	288.51/210	2.6×10^{-2}	$Re(C_S^{'}) \to$ -0.044±0.053 $Im(C_S^{'}) \to$ 0.0055±0.3001
Likelihood 2016	311.22/249	0.4	$Re(C_P) \to$ -0.0047±0.1564 $Im(C_P) \to$ 0.02±0.85	311.22/249	0.4	$Re(C_S^{'}) \to$ -0.04±0.17 $Im(C_S^{'}) \to$ -0.01±0.62
Moments 2016	295.2/271	15	$Re(C_P) \to$ 0.26±0.12 $Im(C_P) \to$ -0.019±0.847	295.4/271	14.8	$Re(C_S^{'}) \to$ -0.035±0.157 $Im(C_S^{'}) \to$ -0.020±0.263
	$C_P^{'}$					
Likelihood 2020	288.49/210	2.6×10^{-2}	$Re(C_P^{'}) \to$ 0.0078±0.0125 $Im(C_P^{'}) \to$ -0.002±0.182			
Likelihood 2016	311.2/249	0.4	$Re(C_P^{'}) \to$ 0.007±0.013 $Im(C_P^{'}) \to$ -0.0027±0.2648			
Moments 2016	295.4/271	14.8	$Re(C_P^{'}) \to$ 0.0061±0.0135 $Im(C_P^{'}) \to$ 0.0021±0.3384			

Table 3.5: Comparitive study of the results obtained from the analysis of different datasets. The results are presented only for the complex Wilson coefficients (WC). For the 'Likelihood 2020 datasets', we have dropped the data points given in **List-1**, while in the analyses involving the 'Likelihood 2016 datasets' and 'Moments 2016 datasets', we have dropped the inputs given in **List-2**.

TH-3118_176121005

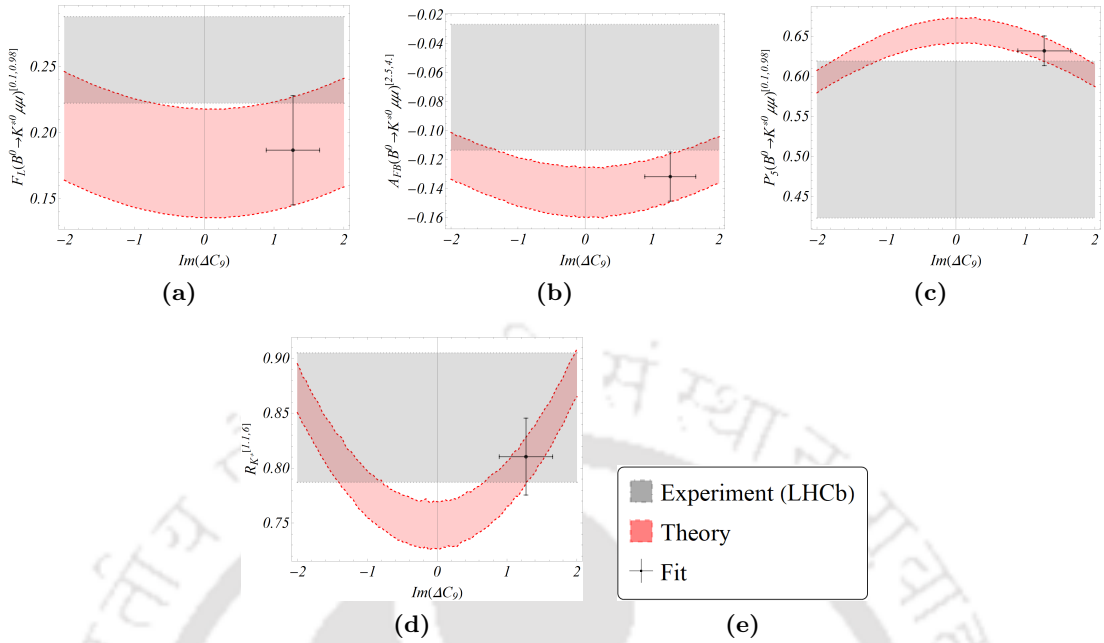

Figure 3.3: Sensitivity of a few of CP symmetric observables to the Imaginary part of ΔC_9.

corresponding to the new Likelihood (LHCb) dataset reduces by $\approx 10\%$ as compared to the one obtained from the old Likelihood-dataset.

3.4.2 $\Delta C_9 = -\Delta C_{10}$ scenario

We also carry out the fit for the interesting scenario $\Delta C_9 = -\Delta C_{10}$ which arises in certain model dependent analyses such as the Leptoquark models. As seen from table 3.6, the analysis with the 'Moment datasets' shows this scenario to be a favorable solution for the data, which is in agreement with earlier observations ([7, 153]). For the NP scenario as mentioned above, we have done a comparative study with the different datasets. At first, we have carried out the fit to this scenario for the "Likelihood 2020 datasets" after dropping the inputs given in 'List-1', the p-value for which is $\sim 6\%$, which is considered as a marginally significant result. Therefore, to look for a possibility of improvement in the quality of fit, we have prepared a list with the following observables,

- **List-3**: It contains all the observable in table 3.2 and the observables from LHCb likelihood 2020 dataset in table 3.1 with a pull > 2 excluding the following: $A_{FB}^{[0.1,0.98]}$, $P_5^{\prime\,[4,6]}$, $S_5^{[4,6]}$, and $P_2^{[4,6]}$ [2]. On top of this, we have dropped few more observables like $P_5^{\prime}(B^0 \to K^{*0}\mu^+\mu^-)^{[4,6]}$ (ATLAS), $S_5(B^0 \to K^{*0}\mu^+\mu^-)^{[4,6]}$ (ATLAS), $\frac{dB}{dq^2}(B^+ \to K^+\mu^+\mu^-)^{[0.1,0.98]}$ (LHCb) and $BR(B^+ \to K^+\mu^+\mu^-)^{[1,6]}$ (Belle). Overall, this list

[2]Note that the only available data on $A_{FB}^{[0.1,0.98]}$ is from LHCb; therefore, we keep it in our analysis, though these measurements have large errors and a pull > 2. Following the earlier discussion, we don't drop $P_5^{\prime\,[4,6]}$, $S_5^{[4,6]}$, and $P_2^{[4,6]}$ from the analysis.

TH-3118_176121005

contains 19 data points.

The new physics scenario $\Delta C_9 = -\Delta C_{10}$					
Fit scenario	Data dropped	χ^2_{Min}/DOF	p-value (%)	Pull_{SM}	Confidence intervals
Likelihood datasets 2020	**List-1**	243.02/211	6.4	6.8	$Re(\Delta C_9) = -Re(\Delta C_{10}) \to -0.55 \pm 0.08$
	$\chi^2_{SM} = 288.9$	242.58/210	6.1	6.5	$Re(\Delta C_9) = -Re(\Delta C_{10}) \to -0.59 \pm 0.12$
	$p_{SM} = 0.035$ %				$Im(\Delta C_9) = -Im(\Delta C_{10}) \to 0.45 \pm 0.49$
	List-3	209.8/204	37.6	6.8	$Re(\Delta C_9) = -Re(\Delta C_{10}) \to -0.54 \pm 0.08$
	$\chi^2_{SM} = 255.4$	209.6/203	36	6.4	$Re(\Delta C_9) = -Re(\Delta C_{10}) \to -0.56 \pm 0.10$
	$p_{SM} = 0.96$ %				$Im(\Delta C_9) = -Im(\Delta C_{10}) \to 0.27 \pm 0.56$
Likelihood datasets 2016	**List-2**	269.15/250	19.3	6.5	$Re(\Delta C_9) = -Re(\Delta C_{10}) \to -0.54 \pm 0.09$
	$\chi^2_{SM} = 311.5$	268.84/249	18.5	6.2	$Re(\Delta C_9) = -Re(\Delta C_{10}) \to -0.54 \pm 0.09$
	$p_{SM} = 0.56$ %				$Im(\Delta C_9) = -Im(\Delta C_{10}) \to -0.16 \pm 0.28$
Moment datasets 2016	**List-2**	260.82/272	67.6	5.9	$Re(\Delta C_9) = -Re(\Delta C_{10}) \to -0.49 \pm 0.09$
	$\chi^2_{SM} = 295.6$	260.72/271	66.2	5.6	$Re(\Delta C_9) = -Re(\Delta C_{10}) \to -0.49 \pm 0.09$
	$p_{SM} = 16.6$ %				$Im(\Delta C_9) = -Im(\Delta C_{10}) \to 0.14 \pm 0.43$

Table 3.6: The case study of new physics scenario $\Delta C_9 = -\Delta C_{10}$ in different fit procedure.

Additional observables in **List-3** with the respective pulls in the one-operator scenario $\mathcal{O}_9$
$S_3(B^0 \to K^{*0}\mu^+\mu^-)^{[1.1,2.5]}$ (LHCb) $\to$ - 2.06
$S_8(B^0 \to K^{*0}\mu^+\mu^-)^{[1.1,2.5]}$ (LHCb) $\to$ - 2.37
$S_9(B^0 \to K^{*0}\mu^+\mu^-)^{[1.1,2.5]}$ (LHCb) $\to$ - 2.07
$P_1(B^0 \to K^{*0}\mu^+\mu^-)^{[1.1,2.5]}$ (LHCb) $\to$ - 2.08
$P_3(B^0 \to K^{*0}\mu^+\mu^-)^{[1.1,2.5]}$ (LHCb) $\to$ 2.20
$P_8^{'}(B^0 \to K^{*0}\mu^+\mu^-)^{[1.1,2.5]}$ (LHCb) $\to$ - 2.36
$F_H(B^+ \to K^+\mu^+\mu^-)^{[2,4.3]}$ (CMS) $\to$ 2.34

Table 3.7: The respective values of pull^{NP} for the additional observables in **List-3** for the one-operator scenario $\mathcal{O}_9$ with complex WC. The superscripts on the observables indicate the q^2 range in GeV^2.

In table 3.7, the respective pulls for the additional observables in **List-3** for the one-operator scenario $\mathcal{O}_9$ is shown. For the scenario $\Delta C_9 = -\Delta C_{10}$ also, these observables have similar pulls. We repeat the fit for the new physics scenario as mentioned above after dropping the 19 data points as listed in **List-3**. The corresponding results are given in the second row of the table 3.6, which shows improvement in the fit quality in terms of the respective p-values.

In table 3.8, we have compared the predicted values of the observables from **List-3** (or in **List-1**) in the one operator scenario $\mathcal{O}_9$ with the respective measured values from LHCb and other experiments. The observables $P_6^{'}$, $P_8^{'}$, P_1 and P_3 are related to S_7, S_8, S_3 and S_9, respectively. Therefore, any observed deviations in $P_6^{'}$, $P_8^{'}$, P_1 and P_3 are related to those in S_7, S_8, S_3 and S_9, respectively. Based on all these and the discussions above, a few useful remarks about the data points in **List-3** or **List-1** are as follows:

- We have dropped the two data points $BR(B^0 \to K^0\mu^+\mu^-)^{[1,6]}$ and $BR(B^+ \to K^+\mu^+\mu^-)^{[1,6]}$ measured by Belle, which have large errors as compared to LHCb. As can be seen from table 3.8, the measured values of these branching fractions

TH-3118_176121005

Observables from **List-1 or List-3**	Other Experiment	LHCb	NP prediction ($\mathcal{O}_9$)
$BR(B^0 \to K^0\mu^+\mu^-)^{[1,6]}$ (Belle)	$(0.31 \pm 0.19) \times 10^{-7}$ (Belle)	$(0.92 \pm 0.17) \times 10^{-7}$	$(1.12 \pm 0.21) \times 10^{-7}$
$BR(B^+ \to K^+\mu^+\mu^-)^{[1,6]}$ (Belle)	$(2.3 \pm 0.4) \times 10^{-7}$ (Belle)	$(1.21 \pm 0.07) \times 10^{-7}$	$(1.19 \pm 0.22) \times 10^{-7}$
$A_I(B \to K\mu^+\mu^-)^{[1,6]}$ (Belle)	-0.52 ± 0.19 (Belle)	N.A.	0.0020 ± 0.0006
$S_4^{[4,6]}$ (ATLAS)	0.32 ± 0.18 (ATLAS)	-0.145 ± 0.057	-0.21 ± 0.01
$P_4^{'[4,6]}$ (ATLAS)	0.64 ± 0.38 (ATLAS)	-0.312 ± 0.116	-0.45 ± 0.01
$P_5^{'[4,6]}$ (ATLAS)	0.26 ± 0.39 (ATLAS)	-0.439 ± 0.117	-0.48 ± 0.05
$S_5^{[4,6]}$ (ATLAS)	0.13 ± 0.20 (ATLAS)	-0.204 ± 0.053	-0.22 ± 0.03
$\frac{dB}{dq^2}(B^+ \to K^+\mu^+\mu^-)^{[0.1,0.98]}$	N.A.	$(0.33 \pm 0.02) \times 10^{-7}$	$(0.22 \pm 0.05) \times 10^{-7}$
$F_H(B^+ \to K^+\mu^+\mu^-)^{[2,4.3]}$	0.85 ± 0.35 (CMS)	N.A.	0.0225 ± 0.0005

Table 3.8: The predicted values of the observables listed in **List-3** (or in **List-1**) for the one operator scenario $\mathcal{O}_9$ which are compared with the correspoding measured values by LHCb and a few other experiments.

by Belle and LHCb are not consistent with each other, at least within their 1-σ error bars. In the new physics scenario ($\mathcal{O}_9$), with the respective parameter spaces favored by all the analysed data points, the predicted values are in good agreement with that measured by LHCb while these are in tension with Belle. Also, we have dropped $\frac{dB}{dq^2}(B^+ \to K^+\mu^+\mu^-)^{[0.1,0.98]}$ from LHCb, as can be seen from the table 3.8, its predicted value is in tension with the measured one, though this data point has minimal impact on the fit probability (p-value).

- The measured value of $A_I(B \to K\mu^+\mu^-)^{[1,6]}$ by Belle has large errors and the allowed NP solution has negligible impact on this observable.

- We have presented our main analyses after dropping the data points $P_4'^{[4,6]}$, $P_5'^{[4,6]}$, $S_4^{[4,6]}$ and $S_5^{[4,6]}$ measured by ATLAS since these data points have large pulls and are inconsistent with the relatively precise data from LHCb. The allowed NP solution can easily accommodate these LHCb data points alongside all the other data considered in the analyses, while the respective ATLAS data largely deviate from the ones predicted in the allowed NP scenario.

- We have dropped the data points $P_6^{'[1.1,6]}$, $P_6^{'[4,6]}$, $S_7^{[1.1,6]}$ and $S_7^{[4,6]}$ from LHCb. For the same observables, we include the data points in three other small q^2 bins in the region $0.1 \leq q^2 \leq 4\ GeV^2$. These observables have very low sensitivity to the variation of ΔC_9 [94, 154]. We have observed that it is hard to explain the current measured values in the above-mentioned bins for the allowed NP solutions.

- CMS has measured $F_H(B^+ \to K^+\mu^+\mu^-)^{[2,4.3]}$ with an error $\approx 40\%$. The corresponding prediction in the NP scenario $\mathcal{O}_9$, given in table 3.8 is consistent with the respective SM prediction: (0.0224 ± 0.0004). It is hard to explain the current observation by CMS in the allowed NP scenario. Similar arguments hold for the observables $P_1^{[1.1,2.5]}$, $P_3^{[1.1,2.5]}$, $P_8^{'[1.1,2.5]}$, $S_3^{[1.1,2.5]}$, $S_8^{[1.1,2.5]}$, and $S_9^{[1.1,2.5]}$ as these observables are

TH-3118_176121005

insensitive to ΔC_9 [92, 94, 154].

3.4.3 Model selection

As seen above, $\mathcal{O}_9$ is the only one-operator scenario that can comfortably explain the present 'Likelihood 2020' dataset. In the future, more precise data might prefer more complex multi-operator scenarios or models. In this analysis, in order to measure model performance and select the best model from a set of potential models we use the small-sample-corrected Akaike's Information Criterion (AICc), given in eq. 2.43 and the "leave-one-out cross-validation" (LOOCV) methods discussed in section 2.2.2.3. Although leave-one-out-cross-validation (LOO-CV) is asymptotically equivalent to AICc, there are differences between the two. While AICc penalizes the model more with increasing complexity, Cross-validation (CV) just looks at the test set performance of the model, without any further assumptions. Thus models with low MSE but not selected by AICc may have more parameters.

Model	ΔAICc	$\text{MSE}_{X-\text{Val}}$	χ^2_{Min}/DOF	p-val (%)	Pull_{SM}	Result
585	0.	0.989	189.05/206	79.6	9.0	$\text{Re}(\Delta C_9) \to$ -1.36±0.24, $\text{Im}(\Delta C_9) \to$ 2.05±0.36 $\text{Re}(C_9') \to$ 0.57±0.23, $\text{Im}(C_9') \to$ 0.14±0.25 $\text{Re}(\Delta C_{10}) \to$ 0.51±0.22, $\text{Im}(\Delta C_{10}) \to$ -0.53±0.46
18	2.015	0.942	199.41/210	68.9	9.2	$\text{Re}(\Delta C_9) \to$ -1.08±0.099, $\text{Re}(C_9') \to$ 0.50±0.18
697	3.506	0.971	188.25/204	77.9	8.7	$\text{Re}(\Delta C_9) \to$ -1.4±0.24, $\text{Im}(\Delta C_9) \to$ 1.93±0.49 $\text{Re}(C_9') \to$ 0.56±0.23, $\text{Im}(C_9') \to$ 0.31±0.5 $\text{Re}(\Delta C_{10}) \to$ 0.52±0.22, $\text{Im}(\Delta C_{10}) \to$ -0.51±0.41 $\text{Re}(C_{10}') \to$ -0.032±0.177, $\text{Im}(C_{10}') \to$ 0.75±0.82
529	3.791	0.977	197.05/208	69.6	8.9	$\text{Re}(\Delta C_9) \to$ -1.11±0.11, $\text{Im}(\Delta C_9) \to$ -0.12±0.46 $\text{Re}(C_9') \to$ 0.42±0.23, $\text{Im}(C_9') \to$ -1.21±0.41
641	4.946	1.011	189.69/204	75.6	8.6	$\text{Re}(C_7') \to$ -0.0075±0.0136, $\text{Im}(C_7') \to$ -0.015±0.037 $\text{Re}(\Delta C_9) \to$ -1.07±0.13, $\text{Im}(\Delta C_9) \to$ -0.061±0.296 $\text{Re}(C_9') \to$ 0.61±0.25, $\text{Im}(C_9') \to$ -1.98±0.4 $\text{Re}(\Delta C_{10}) \to$ 0.59±0.21, $\text{Im}(\Delta C_{10}) \to$ 0.051±1.254
530	5.479	0.993	198.74/208	66.6	8.8	$\text{Re}(\Delta C_9) \to$ -1.34±0.26, $\text{Im}(\Delta C_9) \to$ 1.95±0.44 $\text{Re}(\Delta C_{10}) \to$ 0.32±0.23, $\text{Im}(\Delta C_{10}) \to$ -0.56±0.57
513	5.492	0.98	202.89/210	62.5	9.0	$\text{Re}(\Delta C_9) \to$ -1.1±0.11, $\text{Im}(\Delta C_9) \to$ 1.27±0.37

Table 3.9: The selected models pass the criterion of $\Delta\text{AIC}_c \leq 6$ and $\text{MSE}_{\text{X-val}} < 1.5$ for the Likelihood 2020 dataset after dropping the observables mentioned in List-1. For all the selected models, we have calculated Pull_{SM}, with $\chi^2_{SM} = 288.9$ and p-value of SM = 0.035 %. The parameter uncertainties are obtained from hessian matrix.

As seen from eq. 3.2, there are 9 operators. Considering all the Wilson Coefficients to be real, there are $\sum_{k=1,9}(9!/k!(9-k)!) = 511$ possible combinations. If we consider the WCs to be complex in general, disregarding the combinations with a mixture of real and complex WCs, there are exactly those many cases where the WCs are complex. In total, there are 1022 possible combinations where the WCs are either all real or all complex. Among several competing models, we select the best ones that explain the data by using the conservative limit of $\Delta\text{AIC}c \leq 6$ and with a low value of $\text{MSE}_{\text{X-val}} < 1.5$. The idea is to check that the selected scenarios in AIC_c should not have a very high MSE score. Out of

TH-3118_176121005

these 1022 possible combinations, only a few are selected by these criteria and are listed in table 3.9. We rank the selected models according to the value of $\Delta\text{AIC}c$. We find that $\mathcal{O}_9$ with complex WC, though not the best model, is the only one-operator scenario passing all the selection criteria. Some two, three and four-operator scenarios are selected, and all of these contain $\mathcal{O}_9$ (with real or complex WC) as one of the operators. The best model is a three-operator scenario: $[\mathcal{O}_9, \mathcal{O}_9^{'}, \mathcal{O}_{10}]$ with complex WCs. As expected, the real parts of the WCs are large and also a large non-zero contribution to $Im(\Delta C_9)$ is required in all the selected cases. Note that we have obtained the above results in the absence of the CP-asymmetric observables from $B \to K^*$ decays.

Model	ΔAIC_c	$\text{MSE}_{X-\text{val}}$	$\chi^2_{\text{Min}}/\text{DOF}$	p-val (%)	Pull_{SM}	Values
18	0.	0.948	232.7/245	70.4	9.2	$\text{Re}(\Delta C_9) \to$ -1.079±0.099, $\text{Re}(C_9^{'}) \to$ 0.50±0.18
585	1.466	0.981	225.87/241	75.0	8.8	$\text{Re}(\Delta C_9) \to$ -1.13±0.11, $\text{Im}(\Delta C_9) \to$ -0.0073±0.2829 $\text{Re}(C_9^{'}) \to$ 0.61±0.23, $\text{Im}(C_9^{'}) \to$ 1.77±0.39 $\text{Re}(\Delta C_{10}) \to$ 0.46±0.21, $\text{Im}(\Delta C_{10}) \to$ 0.23±0.32
529	2.310	0.977	230.9/243	70.1	8.9	$\text{Re}(\Delta C_9) \to$ -1.12±0.11, $\text{Im}(\Delta C_9) \to$ 0.0094±0.4714 $\text{Re}(C_9^{'}) \to$ 0.46±0.22, $\text{Im}(C_9^{'}) \to$ 1.03±0.45
697	4.598	0.974	224.74/239	73.7	8.5	$\text{Re}(\Delta C_9) \to$ -1.25±0.16, $\text{Im}(\Delta C_9) \to$ -0.098±0.381 $\text{Re}(C_9^{'}) \to$ 0.59±0.24, $\text{Im}(C_9^{'}) \to$ 1.78±0.42 $\text{Re}(\Delta C_{10}) \to$ 0.44±0.22, $\text{Im}(\Delta C_{10}) \to$ 0.52±0.43 $\text{Re}(C_{10}^{'}) \to$ -0.063±0.173, $\text{Im}(C_{10}^{'}) \to$ 0.26±0.28
2	5.032	0.964	239.77/246	60.0	9.1	$\text{Re}(\Delta C_9) \to$ -1.06±0.11
513	5.402	0.982	238.1/245	61.2	8.9	$\text{Re}(\Delta C_9) \to$ -1.09±0.11, $\text{Im}(\Delta C_9) \to$ -1.11±0.46
641	5.430	0.993	225.58/239	72.4	8.5	$\text{Re}(C_7^{'}) \to$ -0.0059±0.0134, $\text{Im}(C_7^{'}) \to$ -0.0094±0.0282 $\text{Re}(\Delta C_9) \to$ -1.12±0.12, $\text{Im}(\Delta C_9) \to$ -0.054±0.309 $\text{Re}(C_9^{'}) \to$ 0.66±0.26, $\text{Im}(C_9^{'}) \to$ 1.8±0.41 $\text{Re}(\Delta C_{10}) \to$ 0.48±0.21, $\text{Im}(\Delta C_{10}) \to$ 0.33±0.43
20	5.569	0.967	238.27/245	60.9	8.9	$\text{Re}(\Delta C_9) \to$ -1.11±0.11, $\text{Re}(C_{10}^{'}) \to$ -0.13±0.11

Table 3.10: Same as table 3.9, however, now the inputs from $B \to K^*$ asymmetric observables from the 2016 Likelihood dataset are included. Here also, $\text{Pull}_{\text{SM}} > 8\,\sigma$ for all the selected models with $\chi^2_{SM} = 322.1$ and p-value of SM = 0.46 %.

To study the impact of the asymmetric observables from $B \to K^*$ modes on the ranking of the candidate models, we have carried out a model selection analysis incorporating these datapoints, the corresponding details are provided in table 3.10. There are a few changes in the ranking of the respective models as compared to table 3.9. Now in the AIC_c ranking, the two operator scenario $[\mathcal{O}_9, \mathcal{O}_9^{'}]$ with real WCs is slightly ahead of the three operator scenario $[\mathcal{O}_9, \mathcal{O}_{10}, \mathcal{O}_9^{'}]$ (model-585) with complex WCs. This is due to a slight increase in the value of χ^2_{min}/DOF for the model-585. Also, the two operator scenario $[\mathcal{O}_9, \mathcal{O}_{10}^{'}]$ with real WCs is now selected by the data with $\Delta\text{AIC}_c = 5.569$ and $\text{MSE}_{X-\text{val}} = 0.967$. We note from table 3.10 that in all the two or more operator scenarios, the two operators $\mathcal{O}_9$ and $\mathcal{O}_9^{'}$ are common and $Im(C_9^{'})$ has a sizable positive contribution that is not consistent with zero at 68% confidence interval (CI). However, $Im(\Delta C_9)$ is consistent with zero even at 68% CI, though it could be large within the allowed interval since the estimated error is large. The differences in the allowed CIs of $Im(\Delta C_9)$ between the results presented in

TH-3118_176121005

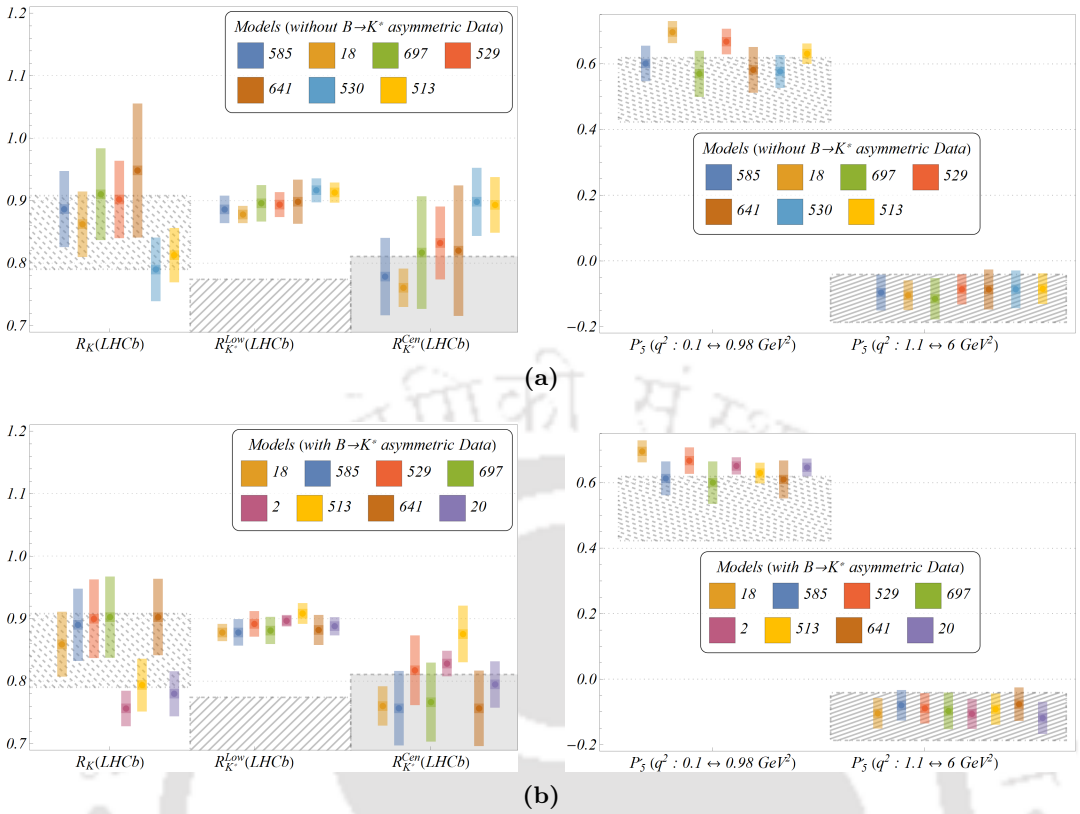

(a)

(b)

Figure 3.4: (a) Predictions of $R_K^{(*)}$ and P_5' in the different q^2 regions in our selected models given in table 3.9. Shaded regions are corresponding experimental 1σ CLs. (b) Same as fig. 3.4a for the selected models given in table 3.10.

tables 3.9 and 3.10 could be because a large positive value of $Im(\Delta C_9)$ is not allowed by the CP-asymmetric data in $B \to K^*$ modes (see Figs. 3.2c, 3.2d, 3.2e and 3.2f).

Fig. 3.4a shows the predictions of $R_K^{(*)}$ and P_5' in different q^2 bins for our selected models from table 3.9, while comparing them with the corresponding measurements. Here the correlations between the SM and the NP parameters have been neglected. In all the models, the predictions are consistent with the measurements of $R_K^{(*)}$ by Belle. Our best model can accommodate all the observed data on $R_K^{(*)}$ and P_5' at 1-σ CL, except the $R_{K^*}^{low}(LHCb)$. In fact, none of the selected models can explain the $R_{K^*}^{low}(LHCb)$ at 1-σ. At low-q^2 the $B \to K^*\ell\ell$ decay rates are dominated by $1/q^2$ enhanced photon contributions and as pointed out earlier in several model independent analyses [153, 155, 156], a NP contact interaction that explains R_K and $R_{K^*}^{Cen}$ affects $R_{K^*}^{Low}$ typically by at most 10%. Also, the possibility of explaining $R_{K^*}^{Low}$ with tensor operators has been addressed in ref. [157], which we are not considering in this analysis (see also [158]). Note that in all the selected models, the predicted results are consistent with their respective measured values at 2-σ. Similar predictions/comparisons are provided in Fig. 3.4b for the selected models in table 3.10.

TH-3118_176121005

3.5 Summary

We have analyzed the new physics effects in $b \to s\ell\ell$ decays, based on the data available till date following a model-independent effective field theory approach with dimension-six operators. We have found that $\mathcal{O}_9$ is the only one-operator scenario with both real and complex WC (with a large non-zero imaginary part), which can provide a plausible explanation of the given data. This is the case even if all the CP-asymmetric observables are dropped from the fit. We have pointed out the corresponding CP-averaged and CP-asymmetric observables which could be the probable source of such large imaginary contributions. Given the data, we have used the method of model selection incorporating both AIC_c and cross-validation to pinpoint the best possible combination of operators with real and complex WC, which can best explain the data. The scenario with $\mathcal{O}_9$ is the only one-operator scenario which passes the test. However, there are a few two, three and four-operator scenarios which have passed all the criteria set by the selection methods. Allowed confidence intervals of the new WCs are shown. For the selected models, we have provided predictions for various observables and compared them.

TH-3118_176121005

Chapter 4

A closer look at the extraction of $|V_{ub}|$ from $B \to \pi l \nu$.

4.1 Introduction

In this chapter[1], we relook into the precision extraction of the CKM element $|V_{ub}|$ from tree level semileptonic $b \to u\ell\nu_\ell$ ($\ell = e, \mu$) decays incorporating the available experimental data and the new Lattice and LCSR inputs on the form-factors. In this regard, both exclusive decays ($B \to \pi l\nu$), and inclusive decays ($B \to X_u \ell\nu_\ell$) play important roles as discussed in section 1.5. At present the extracted values are given in eq. 1.39. Apart from the issue with the inclusive determination of $|V_{ub}|$ as discussed in section 1.3, the extraction from $B \to \pi l\nu$ decay modes is also not clean. The methodology adopted by the Heavy Flavor Averaging Group (HFLAV) involves a two-stage procedure for the extraction of $|V_{ub}|^{exc.}$. In the first stage, using the available data on the differential $B \to \pi l\nu$ decay rates from BaBar(11) [73], Belle(11) [74], BaBar(12) [75], and Belle(13) [76], they obtain an average squared four-momentum transfer (q^2) spectrum from a binned maximum-likelihood fit to determine the average partial branching fraction in each q^2 interval. As presented in their review [160], the quality of this fit is not good, and the p-value is around 6%. In the second fit, this average q^2 spectrum along with the lattice and LCSR (at $q^2 = 0$) inputs had been used to extract $|V_{ub}|$ which is a reasonably good fit with p-value $\sim 47\%$ [160]. On repeating a similar fit mentioned above to obtain the average q^2 spectrum, we have arrived at an even worse quality of fit with a p value < 1 %. A frequentist fit of probability < 5 % is usually considered to be of negligible significance and any further fit (in the second stage), using the outcome of this fit may result in biased predictions for $|V_{ub}|$. It thus becomes essential to consider other possible ways of analysing the available data and identify the source of tension in the fits. We discuss the details in the next sections.

In section 4.2, after discussing the motivation behind this work, we provide a com-

[1]The main results and other contents of this chapter have been published in [159].

TH-3118_176121005

parison with the existing literature and mention about the various inputs (experimental measurements and form-factor inputs from lattice and LCSR) used in this analysis. In section 4.3, we discuss about the analysis technique and present the $|V_{ub}|^{exc.}$ values obtained in various fit scenarios considered in this work compared to some of the $|V_{ub}|^{inc.}$ determinations. Finally, in section 4.4, we conclude summarizing the main results obtained in this chapter.

4.2 Motivation

4.2.1 Comparison with existing literature

HFLAV combines all these measurements in the following way:

- At first, a binned maximum-likelihood fit to determine the average partial branching fraction in each q^2 interval is performed. Though different measurements use different bin-widths, the bin-edges are the same (a small difference is mentioned in the next paragraph)[2].

  The total branching fraction is then obtained from the sum of the partial branching fractions in the average q^2 spectrum, taking the correlations between q^2 bins into account. In addition to the systematic and statistical uncertainties and correlations corresponding to separate measurements, the shared sources of systematic uncertainty of all measurements are included as nuisance parameters in the likelihood [160].

- In the second stage, the average q^2 spectrum is then used to fit $|V_{ub}|$ and the relevant form-factor parameters (BCL [162] $3+1$: 3 form factor coefficients b_0, b_1, b_2 and $|V_{ub}|$). To constrain the high q^2 behavior of the spectrum, they use the FLAG lattice average [163] of two LQCD calculations [129, 130] and ref. [164] as LCSR inputs for constraining the low q^2 nature of the spectrum.

To obtain the average q^2-spectrum, we have repeated the binned maximum-likelihood fit. The average spectrum is consistent with that from HFLAV within 1σ. However, our fit quality is about 1 % while that for HFLAV is about 6 %, as given in table 4.1. This difference in the fit quality could be due to the non-availability of the information on the shared systematic uncertainties between measurements (like continuum subtraction, tracking efficiency, etc.) as used by HFLAV in their analysis.

Thus, in order to look for a possibility of improvement, one should carefully inspect all the datasets. A closer look at the data shows that BaBar(12) untagged analysis [75] of the

[2]The highest edge of the highest bin in the most recently published Belle Hadronic-tagged result [76] is quoted to be 26 GeV^2, whereas for the other measurements, it is 26.4 GeV^2. HFLAV [160, 161] seems to be using a different highest-bin-result for $\Delta\mathcal{B}$ than that published by Belle. However, we have consistently used the published results from ref. [76].

TH-3118_176121005

$\Delta q^2\ [GeV^2]$	$\left(\Delta\mathcal{B}\left(B^0 \to \pi^- \ell^+ \nu_\ell\right)/\Delta q^2\right)\ [10^{-7}]$		
	HFLAV Average	Our Average	Average (Dropping BaBar(11) [73])
0-2	72.0±7.0	67.0±6.4	64.9 ± 6.7
2-4	71.4±4.6	67.4±4.7	66.6 ± 4.8
4-6	67.0±3.9	65.9±3.9	63.7 ± 4.2
6-8	75.6±4.3	73.7±4.2	69.6 ± 4.6
8-10	64.4±4.3	60.2±4.4	64.3 ± 4.7
10-12	71.7±4.6	70.4±4.8	73.4 ± 5.2
12-14	66.7±4.7	63.0±4.8	64.8 ± 5.1
14-16	63.3±4.8	61.0±4.8	63.2 ± 5.1
16-18	62.0±4.4	60.5±4.5	60.5 ± 4.8
18-20	43.2±4.3	41.5±4.2	40.6 ± 4.4
20-22	42.5±4.1	39.7±4.1	43.2 ± 4.3
22-24	34.0±4.2	29.9±4.4	33.5 ± 4.7
24-26.4	11.7±2.6	10.4±2.7	11.8 ± 2.7
p-value	6%	$\approx 1\%$	24.8%

Table 4.1: Comparison between our and HFLAV's average q^2 spectrum.

$B^{0,+}$ modes have much better statistics/yield (almost double) than the one published in the previous year: BaBar(11) [73]. It also has the following advantages over the BaBar(11) analysis:

- The event selection has been optimized over the entire fit region instead of the signal-enhanced region, as was done previously.
- The tighter selections produce a dataset with a better signal to background ratio and higher purity in the $B \to \pi l \nu$ decays.
- This analysis uses the full BaBar dataset compared to only a subset used in the analysis of 2011.

The analysis method in BaBar(11) is considerably different from that of BaBar(12) and also from the analyses by Belle. Therefore, we drop the BaBar(11) datapoints in 6 q^2-bins as a first attempt to look for the possibility of improvement while extracting the average partial branching fraction in each q^2 interval from a binned maximum-likelihood fit to data, leading to an improvement in the fit quality from 1% to 24.8%. The result has been shown in the fourth column in table 4.1. The average q^2-spectrum generated in this scenario is consistent with HFLAV and our averages with all data. Figure 4.1 compares all the three average q^2-spectrums as given in table 4.1.

For the BCL fit of the average q^2 spectrum in the second stage, we are able to somewhat reproduce their result for $|V_{ub}|$ and the form-factor parameters (second and third column of table 4.2), using tables 81 and 82 of ref. [160]. If we use our own averaged q^2 spectrum

TH-3118_176121005

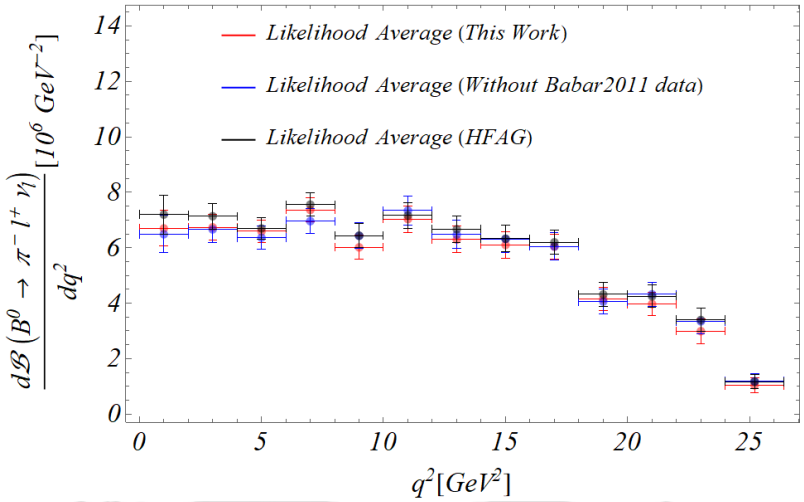

Figure 4.1: The comparison of our average q^2 spectrum of the partial branching fractions in $B \to \pi\ell\nu$ decays with the one obtained by HFLAV.

(all data) instead, the fit-probability increases a lot, but the value of $|V_{ub}|$ decreases (i.e. goes away from the inclusive result) even more (fourth column of table 4.2). However, from a fit to our q^2 average spectrum as obtained without BaBar(11), we get a similar value of $|V_{ub}|$ as HFLAV and the quality of fit is also good with a p-value of 64% (fifth column of table 4.2).

Params	HFLAV Result (p-value = 47%)	Our Result Using HFLAV's avg (p-value = 48%)	Our Result Using our avg (p-value = 80%)	From our avg Without BaBar(11) [73] (p-value = 64%)
$V_{ub} \times 10^3$	3.67(15)	3.66(14)	3.60(12)	3.66(13)
b_0^+	0.418(12)	0.417(12)	0.419(12)	0.420(12)
b_1^+	-0.399(33)	-0.406(31)	-0.395(31)	-0.410(31)
b_2^+	-0.578(130)	-0.605(148)	-0.638(150)	-0.740(154)

Table 4.2: Comparison between our and HFLAV's fit to the average q^2 spectrum along with the inputs from Lattice and LCSR ($q^2 = 0$).

4.2.2 $B \to \pi l\nu$ rates with $|V_{ub}|^{inc.}$

The differential decay width w.r.t. q^2 for a pseudoscalar to pseudoscalar semileptonic decay is given in 1.22. For the form-factor parametrization, we have followed two different approaches i.e. BCL [127] and BSZ [4] parametrizations, as discussed in section 2.1.2 and compared their results.

As is evident from eqs. 2.25 and 2.26, in the BCL parametrization the kinematic constraint $f_+(q^2 = 0) = f_0(q^2 = 0)$ leads to a complex relationship between the expansion

TH-3118_176121005

coefficients:

$$b_3^0 = 45.70(b_0^+ - b_0^0) - 12.78b_1^0 - 3.58b_2^0 + 12.85b_1^+ + 3.44b_2^+ + 1.21b_3^+. \tag{4.1}$$

Using this equation, we have replaced b_3^0 in terms of the other coefficients in the fit which helps to reduce one parameter from the fit.

Updated inputs from LCSR are available for the form-factors $f_+(q^2)$ and $f_T(q^2)$ at $q^2 = -15, -10, -5, 0, 5$ and for $f_0(q^2)$ at $q^2 = -15, -10, -5, 5$ GeV^2 [2]. The value of f_0 at $q^2 = 0$ is obtained via the QCD relation $f_+(0) = f_0(0)$. While RBC-UKQCD [130] provides synthetic data points for $f_{+,0}(q^2)$ with full covariance matrices (both systematic and statistical) at $q^2 = 19,\ 22.6,\ 25.1$ GeV^2, Fermilab-MILC [129] only provides the fit-results for their coefficients. Using the results of the 'only lattice' fit, we generate correlated synthetic data-points at exactly the same q^2 values as RBC-UKQCD, with an extra point for f_+ at $q^2 = 20.5$ GeV^2.

Armed with 22 data points (9 from LCSR, 13 from Lattice (3 for each of $f_{+,0}$ from RBC-UKQCD, 4 for f_+ and 3 for f_0 from Fermilab-MILC), the next obvious step would be to check how the decay distribution fits to the average q^2 spectrum i.e. we extract $|V_{ub}|$ using the average partial branching fractions as given in table 4.1 and the above-mentioned form-factor inputs. We perform two fits, the results of which are shown in the last two columns of table 4.3 and it shows that in both the fits the extracted values of $|V_{ub}|$ have increased from that obtained in table 4.2 (fourth and fifth columns, respectively). If, instead, we start from the avg. q^2 spectrum of the fourth column of table 4.1 (fit w/o BaBar(11); has a considerable fit-probability of 24.8%), and reintroduce the data from BaBar(11) during the second fit, along with the new 22 data-points from lattice and LCSR, we end up with the second column of table 4.3. The parameter space is same as the third column of table 4.3, but with meaningless significance ($\sim 0.8\%$). This reinforces the fact that the BaBar(11) dataset is quite at odds with all other data-sets.

To understand the effect of the inconsistency in data on the decay rate distributions, we have derived the $B \to \pi l \nu$ decay rate distributions using the form-factors extracted only from the LCSR and lattice inputs as discussed above in both the BSZ [4] and BCL [127] expansions. For a stable and conservative estimate of the uncertainties of the form-factors, we truncate the series at different orders, starting from 0 to 4 for both f_+ and f_0 and perform a model selection procedure incorporating both AIC and AIC$_c$. We conclude that the optimal description of the synthetic data is obtained when both f_0 and f_+ are truncated at $N = 3$, thus leading to seven parameters (4 for f_+ and 3 for f_0). The extracted values of the formfactor parameters in BSZ and BCL expansion are given in table 4.4.

We have used the latest $|V_{ub}|^{inc.}$ value from Belle given in eqn 1.41 to get the shape and height of the distribution which will help us understand the reason for the discrepancy between the inclusive and exclusive determinations. Using the above fit results and $|V_{ub}|$

TH-3118_176121005

Parameters	Our Avg. q^2 spec. w/o BaBar(11) + New Lattice & LCSR + BaBar(11) re-introduced (p value = 0.75%)	Our Avg. q^2 spec. + New Lattice & LCSR (p value = 20.9%)	Our Avg. q^2 spec. w/o BaBar(11) + New Lattice & LCSR (p value = 31%)
$V_{ub} \times 10^3$	3.78(13)	3.78(13)	3.89(14)
b_0^+	0.410(12)	0.410(12)	0.408(12)
b_1^+	−0.526(44)	−0.526(44)	−0.561(46)
b_2^+	−0.39(13)	−0.39(13)	−0.40(13)
b_3^+	0.59(24)	0.59(24)	0.59(25)
b_0^0	0.540(16)	0.540(16)	0.536(16)
b_1^0	−1.617(66)	−1.617(66)	−1.647(66)
b_2^0	1.294(146)	1.294(146)	1.257(146)

Table 4.3: The extracted values of $|V_{ub}|$ and the other form-factor parameters using our average q^2 spectrum of the partial branching fractions and the new lattice and LCSR inputs. Fourth column uses the avg. q^2 spectrum without BaBar(11) data (last column of table 4.1), while the third uses that from the third column of table 4.1 (with all data). In the second column of this table, we repeat the last fit after reintroducing BaBar(11) data again.

BSZ				BCL			
$\chi^2_{\rm min}$/DOF	p-value(%)	Parameters	Values	$\chi^2_{\rm min}$/DOF	p-value(%)	Parameters	Values
4.48/15	99.6	a_0^+	0.213(22)	12.88/15	61	b_0^+	0.396(13)
		a_1^+	-0.65(14)			b_1^+	-0.707(70)
		a_2^+	0.263(425)			b_2^+	-0.36(18)
		a_3^+	0.67(31)			b_3^+	0.77(32)
		a_1^0	0.41(17)			b_0^0	0.521(17)
		a_2^0	1.46(51)			b_1^0	-1.756(78)
		a_3^0	1.78(49)			b_2^0	1.15(16)

Table 4.4: Fit results of form factor parameters with only LCSR and lattice input used to create the plots in figure 4.2.

from different inclusive estimates, if we calculate the theoretical predictions of the binned branching fractions, then any large deviation of the predictions from the actual measurements could potentially diagnose the source of the apparent tension between $|V_{ub}|^{\rm inc}$ and $|V_{ub}|^{\rm exc}$. In figure 4.2, we have compared the theoretical predictions for the binned differential branching fractions against the existing experimental data.[3]. We observe that the q^2 distribution of the differential branching fraction in both the form-factor parametrizations can explain almost all the available data except a few which are lying entirely outside of the theoretical C.I. bands. In section 4.3, we will analyse the impact of these datapoints on the extracted value of $|V_{ub}|$.

[3]Note that in these plots, we do not incorporate the data from the combined mode analysis by BaBar 2012 [75] since they are consistent with the corresponding single-mode analysis.

TH-3118_176121005

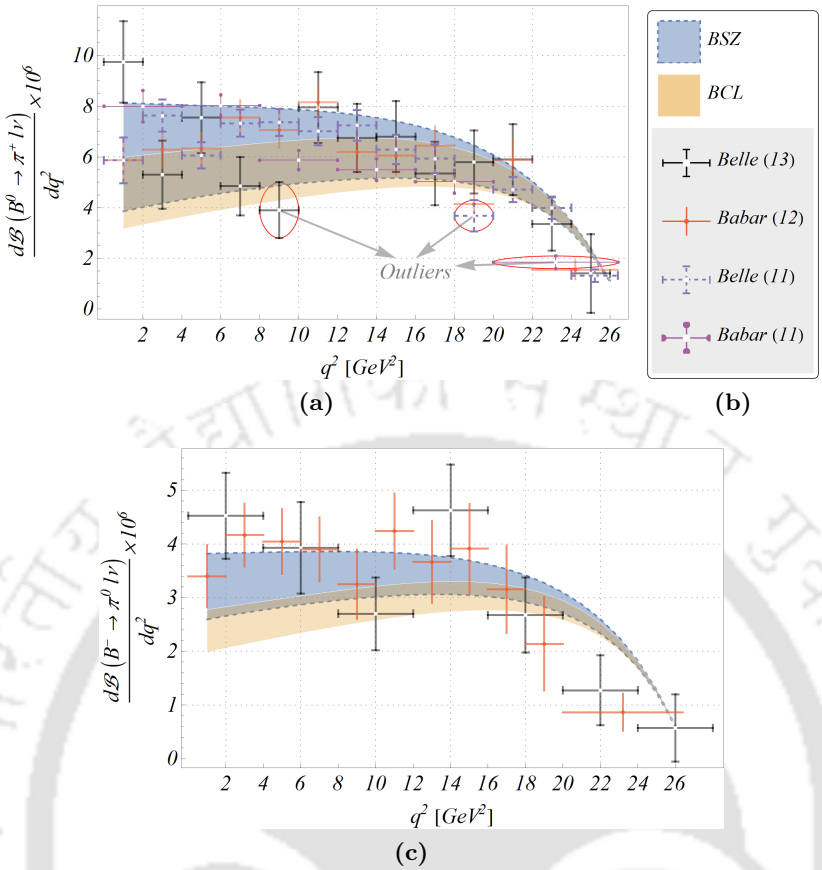

Figure 4.2: Differential branching fraction plots superposed on experimental data-points, with form factors fitted from lattice and LCSR, and $|V_{ub}|$ corresponds to that obtained from the latest Belle Inclusive Measurement [1].

4.3 Main results

We think that instead of extracting $|V_{ub}|$ through a two-stage procedure for which the first fit is of very poor quality, we should directly use the individual data-points for a simultaneous extraction of $|V_{ub}|$ and the parameters corresponding to the chosen form-factor parametrization. This provides us with a single value for the fit probability to draw our inference from instead of a two stage fit. We follow the same principle of using individual data-points for the lattice inputs from different collaborations.

To proceed further, we have defined different fit scenarios involving the available experimental inputs from Belle and BaBar. The following are the lists of those data-sets:

- ***Fit 1***: B^0 decays from Belle (2011) and Belle (2013); B^- decays from Belle(2013); the combined modes from BaBar (2011) and BaBar (2012). We have subdivided this set further depending on whether or not LCSR inputs are taken into account, like the following:

  (1) *Fit 1A*: Experimental data (Fit 1) + synthetic Lattice data points,

TH-3118_176121005

Form-Factors	Fit Index	$[B^0 \to \pi^-]$ $q^2: 4-8$ BaBar (11)	$[B^0 \to \pi^-]$ $q^2: 20-26.4$ BaBar (11)	$[B^0 \to \pi^-]$ $q^2: 10-12$ BaBar (12)	$[B^0 \to \pi^-]$ $q^2: 20-22$ BaBar (12)	$[B^0 \to \pi^-]$ $q^2: 18-20$ Belle (11)	$[B^0 \to \pi^+]$ $q^2: 0.0111637-2$ Belle (13)	$[B^0 \to \pi^+]$ $q^2: 8-10$ Belle (13)
BSZ	Fit 1A	2.46	−2.30	2.08	–	–	–	−2.42
	Fit 1B	2.52	−2.42	2.07	–	–	–	−2.41
	Fit 2A	–	–	–	–	−2.02	–	−2.43
	Fit 2B	–	–	–	–	−2.07	–	−2.42
	Fit 3A	2.40	−2.35	2.00	2.01	–	–	−2.44
	Fit 3B	2.45	−2.46	–	–	–	–	−2.43
BCL	Fit 1A	2.45	−2.30	2.07	–	–	–	−2.42
	Fit 1B	2.59	−2.56	2.07	–	–	–	−2.40
	Fit 2A	–	–	–	–	−2.03	–	−2.45
	Fit 2B	–	–	–	–	−2.18	2.00	−2.42
	Fit 3A	2.36	−2.36	–	2.00	–	–	−2.45
	Fit 3B	2.48	−2.61	–	–	–	–	−2.44

Table 4.5: List of Pulls ($> 2\ \sigma$) for different fits (with experimental data) in this analysis.

(2) *Fit 1B*: Experimental data (Fit 1) + synthetic Lattice data points + LCSR.

- ***Fit 2***: B^0 decays from Belle (2011), BaBar (2012), and Belle (2013); B^- decays from BaBar (2012) and Belle(2013). As above we have defined the following sets:
  - *Fit 2A*: Experimental data (Fit 2) + synthetic Lattice data points,
  - *Fit 2B*: Experimental data (Fit 2) + synthetic Lattice data points + LCSR.
- ***Fit 3***: The combined modes from BaBar (2011) along with the *Fit 2* dataset, with and without LCSR as follows:
  - *Fit 3A*: Experimental data (Fit 3) + synthetic Lattice data points,
  - *Fit 3B*: Experimental data (Fit 3) + synthetic Lattice data points + LCSR.

Fit 1 contains all data-sets other than the inputs from the single-mode analysis of BaBar(12) [75], though we have considered the combined mode analysis from the same publication. In *Fit 3* we have included the single-mode analysis data of BaBar(12) and have dropped the combined one. In *Fit 2*, we have dropped the inputs from BaBar(11) dataset to understand the impact of BaBar(11) four-mode analysis data on the fit-quality as well as the value of $|V_{ub}|$.

For all the fit scenarios we have obtained the respective 'pulls' between the data and the fitted distributions which for the i^{th} data-point is defined as

$$pull_i = \frac{\mathcal{O}_i^{exp} - \mathcal{O}_i^{fit}}{\sigma_i^{exp}}\,. \tag{4.2}$$

TH-3118_176121005

BSZ Parametrization								
Run Name	Full				Dropped Pull > 2			
	$\chi^2_{\rm min}$/DOF	p-value(%)	$V_{ub} \times 10^3$		$\chi^2_{\rm min}$/DOF	p-value(%)	$V_{ub} \times 10^3$	
			Frequentist	Bayesian			Freq.	Bayes
Fit 1A	73.4/56	5.92	3.69(14)	3.67(14)	46.6/52	68.68	3.79(15)	$3.77\binom{15}{16}$
Fit 1B	77./65	14.57	3.74(13)	$3.73\binom{13}{14}$	49.3/61	85.77	3.83(14)	$3.82\binom{14}{16}$
Fit 2A	59.5/61	53.17	3.81(14)	3.79(15)	46./59	89.26	3.86(15)	$3.85\binom{15}{16}$
Fit 2B	62./70	74.23	3.85(14)	$3.83\binom{13}{15}$	48.3/68	96.63	3.91(14)	$3.89\binom{14}{15}$
Fit 3A	82.2/67	9.98	3.70(14)	3.69(14)	53.3/62	77.56	3.76(14)	$3.76\binom{15}{14}$
Fit 3B	85.9/76	20.54	3.75(13)	$3.74\binom{13}{14}$	62./73	81.79	3.84(14)	3.83(14)
BCL Parametrization								
Run Name	Full				Dropped Pull > 2			
	$\chi^2_{\rm min}$/DOF	p-value(%)	$V_{ub} \times 10^3$		$\chi^2_{\rm min}$/DOF	p-value(%)	$V_{ub} \times 10^3$	
			Freq.	Bayes			Freq.	Bayes
Fit 1A	73.5/56	5.84	3.69(14)	$3.67\binom{13}{15}$	46.7/52	68.34	3.79(15)	3.78(15)
Fit 1B	92.1/65	1.51	3.79(13)	$3.78\binom{14}{13}$	63.2/61	39.84	3.89(14)	$3.87\binom{14}{15}$
Fit 2A	60.1/61	50.8	3.81(14)	3.81(15)	46.5/59	88.19	3.87(15)	$3.85\binom{14}{15}$
Fit 2B	75.9/70	29.42	3.91(14)	3.90(15)	58.3/67	76.64	3.96(14)	$3.96\binom{16}{14}$
Fit 3A	82.7/67	9.35	3.70(14)	$3.69\binom{13}{14}$	57.8./63	66.09	3.77(14)	3.76(15)
Fit 3B	101.4/76	2.73	3.80(13)	$3.79\binom{13}{15}$	76.3/73	37.27	3.90(14)	$3.89\binom{14}{15}$

Table 4.6: Freq. and Bayesian

where σ_i^{exp} is the experimental uncertainty.

In table 4.5, we present the observables for which the pulls are greater than 2. We find that in all the scenarios, $\mathcal{B}(B^0 \to \pi^-)^{[8,10]}$ from Belle(13), and in all the scenarios involving BaBar(11), $\mathcal{B}(B^0 \to \pi^-)^{[4,8]}$ and $\mathcal{B}(B^0 \to \pi^-)^{[20,26.4]}$ from BaBar(11) have pulls greater than 2. In table 4.6, we have shown the extracted values of $|V_{ub}|$ in different fit scenarios with full datasets and also after dropping the data-points having pulls greater than 2, shown in the right panel of the same table. We have performed the fit following both frequentist and Bayesian approaches and compared them.

A few observations are in order here:

- Since the posterior is very nearly of a multi-Gaussian nature, the results obtained in the frequentist maximum likelihood estimate (MLE) and the medians of the marginal posteriors from the Bayesian analysis are almost identical; though, in a few cases, we have obtained slightly asymmetric 1 σ credible intervals (area between the $\sim 0.16 \to 0.5$, and $\sim 0.5 \to 0.84$ Quantiles of the marginal posterior) in the Bayesian analysis.

- For the BSZ parametrization, the fit quality improves on including LCSR, whereas for the BCL case, the fit worsens with the inclusion of LCSR. For *Fit 2*, the fit-probability is reasonably good due to the absence of the BaBar 2011 data set. However, in all the scenarios, the fit quality increases by a considerable amount

TH-3118_176121005

on dropping a few data-points with pull > 2.

- Whenever both Lattice and LCSR data are included, the BCL form factor parametrization results in a slightly larger $|V_{ub}|$ than that obtained from BSZ, but with reduced fit-probability. The difference in the best fit values is about 1%, and the results are extremely consistent with each other. We will comment on this observation at a later stage.

- In all the fits, the extracted $|V_{ub}|$ increases by $\geq 1\%$ with the inclusion of the new LCSR inputs.

- We have truncated the BSZ and BCL expansions at $N = 3$ 2.24 and $N_z = 4$ 2.25 respectively, resulting in 4 parameters for f_+ and 3 for f_0 (due to the kinematic constraint). To check the stability of the results, we have analysed the inputs truncating the series at the next order in both the series expansions, i.e., $N = 4$ for BSZ and $N_z = 5$ for BCL. We find that the extracted values of $|V_{ub}|$ are consistent (within their errors) with the one presented in table 4.6, however, the newly added higher-order coefficients of the expansions remain mostly unconstrained at the present level of precision, and they have negligible impact on the precision extraction of $|V_{ub}|$.

- Irrespective of the fit scenario, the extracted $|V_{ub}|$ increases on dropping the data-points with pull > 2. This indicates that the data with large 'pull' have an impact on the extracted values of $|V_{ub}|$ too.

- As shall be seen shortly, the partial rates $\mathcal{B}(B^0 \to \pi^-)^{[20,26.4]}$ (BaBar(11)) and $\mathcal{B}(B^0 \to \pi^-)^{[18,20]}$ (Belle(11)) are highly sensitive to the extracted value of $|V_{ub}|$.

In figure 4.3, we have compared the extracted values in different fit scenarios as given in table 4.6 with the inclusive determinations. We find that our determination for $|V_{ub}|^{exc.}$ is still not consistent at 1 σ with the values extracted by HFLAV following *GGOU* and *BLNP*, though they are consistent with the new measurement of $|V_{ub}|^{inc.}$ from Belle [1].

Next, we check the deviations of the data with the predictions of differential decay rates obtained only from the lattice and LCSR inputs with three different values of $|V_{ub}|^{inc.}$:

$$\begin{aligned} |V_{ub}| &= (4.10 \pm 0.09 \pm 0.22 \pm 0.15) \times 10^{-3}, && \text{Belle (New) [1]}, \\ |V_{ub}| &= (4.32^{+0.17}_{-0.18}) \times 10^{-3} && \text{HFLAV } (GGOU) \text{ [160]}, \\ |V_{ub}| &= (4.44^{+0.25}_{-0.26}) \times 10^{-3} && \text{HFLAV } (BLNP) \text{[160]}. \end{aligned} \tag{4.3}$$

The deviation corresponding to the i^{th} observable is defined as

$$dev_i = \frac{\mathcal{O}_i^{exp} - \mathcal{O}_i^{SM}}{\sqrt{(\sigma_i^{exp})^2 + (\sigma_i^{SM})^2}}, \tag{4.4}$$

TH-3118_176121005

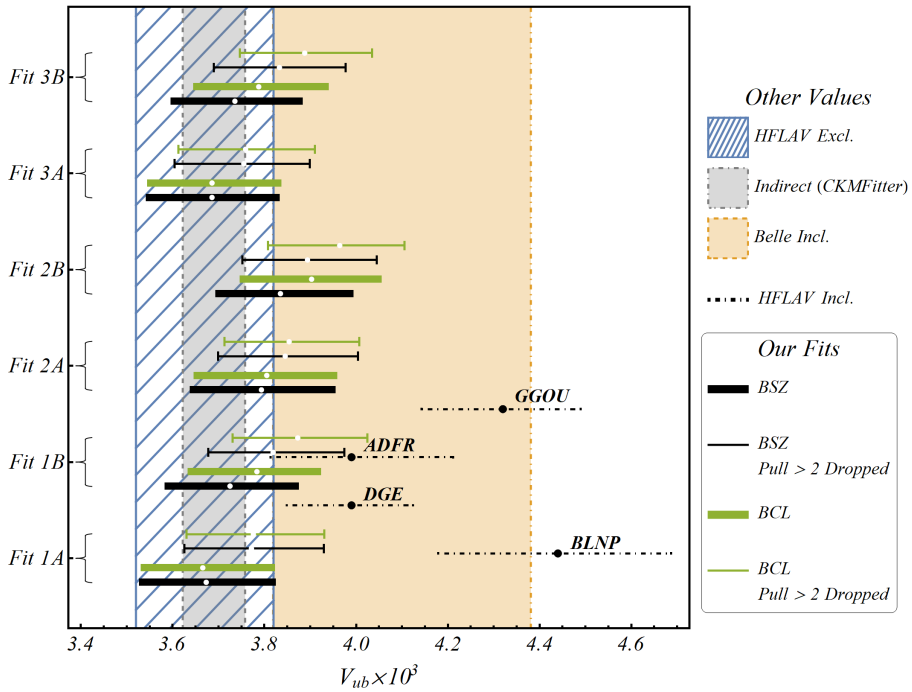

Figure 4.3: Comparison of various $|V_{ub}|$ results obtained in this work with other measurements.

where σ_i^{SM} contains the uncertainties in the decay rates due to form-factor parameters and $|V_{ub}|^{inc.}$. The results of this analysis are shown in table 4.7. As expected, on using the values of $|V_{ub}|^{inc.}$ from HFLAV, at least four to five data-points have a deviation > 2. On the other hand, with the new Belle-measurement, it is only the partial rates $\mathcal{B}(B^0 \to \pi^-)^{[20,26.4]}$ (BaBar(11)) and $\mathcal{B}(B^0 \to \pi^+)^{[0.01,2]}$ (Belle(13)) which have deviation > 2 (both in BSZ and BCL). However, $\mathcal{B}(B^0 \to \pi^+)^{[0.01,2]}$ (Belle(13)) has a rather minor effect on $|V_{ub}|$. The partial decay rates $\mathcal{B}(B^0 \to \pi^-)^{[20,26.4]}$ (BaBar(11)), $\mathcal{B}(B^0 \to \pi^-)^{[18,20]}$ (Belle(11)) and $\mathcal{B}(B^0 \to \pi^-)^{[8,10]}$ (Belle(13)) are the common data points which have pull > 2 in the analyses given in tables 4.5 and 4.7, respectively.

Form-Factors	Inclusive $\lvert V_{ub}\rvert$ used	$[B^0 \to \pi^-]$ q^2 : 18 − 20 Belle (11)	$[B^0 \to \pi^-]$ q^2 : 20 − 26.4 BaBar (11)	$[B^0 \to \pi^-]$ q^2 : 18 − 20 BaBar (12)	$[B^+ \to \pi^0]$ q^2 : 20 − 26.4 BaBar (12)	$[B^0 \to \pi^+]$ q^2 : 0.0111637 − 2 Belle (13)	$[B^0 \to \pi^+]$ q^2 : 8 − 10 Belle (13)
BSZ	HFLAV (GGOU)	−2.55	−3.54	−2.13	−2.35	–	−2.04
	HFLAV (BLNP)	−2.50	−3.27	−2.14	−2.41	–	−2.09
	Belle (New)	–	−2.32	–	–	2.22	–
BCL	HFLAV (GGOU)	−2.32	−3.49	–	−2.28	2.30	–
	HFLAV (BLNP)	−2.32	−3.23	–	−2.35	2.07	–
	Belle (New)	–	−2.29	–	–	2.54	–

Table 4.7: List of deviations of theoretical predictions from actual experimental data ($> 2\ \sigma$).

TH-3118_176121005

On the basis of these observations, we define a few additional scenarios:

- ***Fit 2B-I***: Input used in *Fit 2B* without the data on $\mathcal{B}(B^0 \to \pi^-)^{[18,20]}$ (Belle 2011).
- ***Fit 3B-I***: Input used in *Fit 3B* without the data on $\mathcal{B}(B^0 \to \pi^-)^{[20,26.4]}$ (BaBar 2011).
- ***Fit 3B-II***: Input used in *Fit 3B* without the data on $\mathcal{B}(B^0 \to \pi^-)^{[18,20]}$ (Belle 2011) and $\mathcal{B}(B^0 \to \pi^-)^{[20,26.4]}$ (BaBar 2011).

Fit Scenario	BSZ				BCL			
	χ^2/DOF	p-value(%)	$V_{ub} \times 10^3$		χ^2/DOF	p-value(%)	$V_{ub} \times 10^3$	
			Frequentist	Bayesian			Frequentist	Bayesian
F2B-I	55.4/69	88.14	3.90(14)	$3.89^{+0.14}_{-0.15}$	68.85/69	48.25	3.96(14)	$3.95^{+0.14}_{-0.15}$
F3B-I	78.86/75	35.8	3.83(14)	3.83(13)	93.6/75	7.19	3.89(14)	3.89(14)
F3B-II	72.96/74	51.25	3.88(14)	$3.87^{+0.14}_{-0.15}$	87.2/74	13.99	3.94(14)	$3.93^{+0.14}_{-0.15}$

Table 4.8: Final table of comparison for $|V_{ub}|^{exc.}$ obtained in this work.

The results in the above-mentioned fit scenarios are given in table 4.8. A comparison between identical cases, like *Fit 2B* and *Fit 3B*, in tables 4.6 and 4.8 shows that one can extract exactly similar values of $|V_{ub}|^{exc.}$ even by dropping only one or two data-points mentioned above. This means that even in the presence of other data-points which do not fit comfortably with other data, the most influential data-points in determining $|V_{ub}|^{exc.}$ are the partial branching fractions $\mathcal{B}(B^0 \to \pi^-)^{[18,20]}$ (Belle(11)) and $\mathcal{B}(B^0 \to \pi^-)^{[20,26.4]}$ (BaBar(11)).

Finally, to understand the slight shift ($\approx 1\%$) in the best fit values of $|V_{ub}|$ in BCL and BSZ expansion of the form factors, we need to compare the form factors obtained from the two separate expansions. As an example, in figure 4.4 we have compared the form factors obtained from the fit results in 'Fit-2B'. Following are a few observations:

- The slight difference in the extracted $|V_{ub}|$ is not due to the form factor $f_+(q^2)$, which provides the leading contributions to the decay rate. We can see from figure 4.4a that the extracted q^2 distributions of f_+ in both the parameterizations are completely consistent with each other. Also, both distributions satisfy all the lattice or LCSR pseudo data points.
- The difference in the extracted $|V_{ub}|$ between the two formalisms is due to the slight mismatch in the extracted values of $f_0(q^2)$ in a part of the q^2 region, which we can see from figure 4.4b. For $15 \leq q^2 \leq 23$ (in GeV^2) the extracted values of $f_0(q^2)$ have a slight mismatch for the two different expansions. However, the extracted values are in good agreement with lattice or LCSR data points in both the cases.

TH-3118_176121005

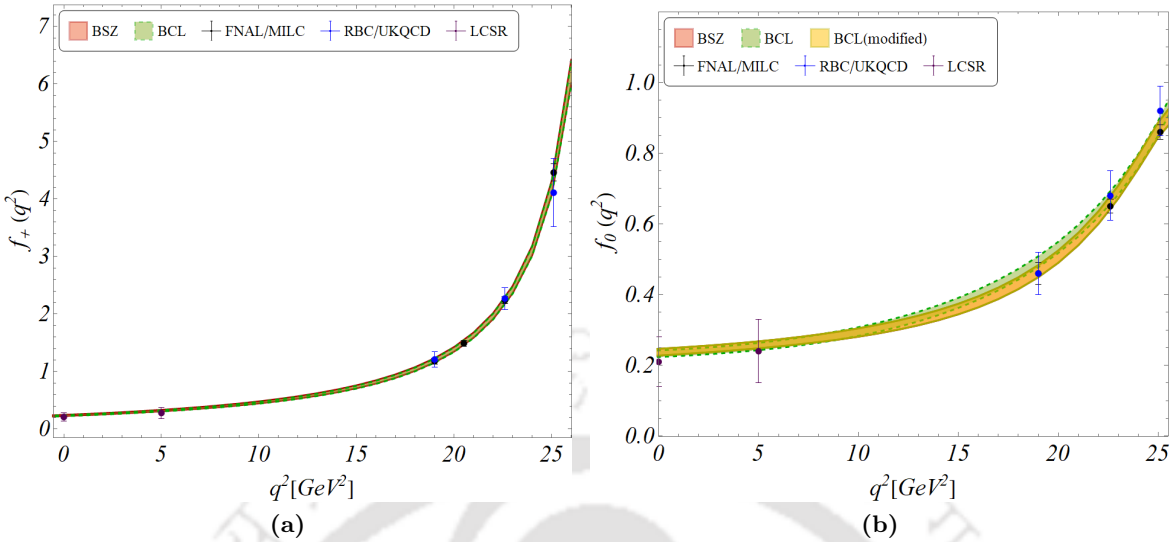

Figure 4.4: Comparison of q^2 distributions of the form factors in BSZ and BCL parametrizations. The lattice inputs and the LCSR pseudo data points at $q^2 = 0$ and 5 GeV^2 are also shown in the figure.

- The observed difference in $f_0(q^2)$ is because the BSZ expansion uses the pole due to B^* scalar meson while BCL expansion does not as discussed in section 2.1.2.2. Our conclusion is based on the following observations:
  - In the fits, after dropping the LCSR data points at $q^2 = 5, -5, -10$ and -15 GeV^2, the extracted values of $|V_{ub}|$ in both the expansions completely match. This indicates the role of the pole factor $1/(1 - q^2/M_{B^*}^2)$ in the fit.
  - As a trial, we modified the BCL expansion of $f_0(z)$ in 2.26 after multiplying it by a similar pole factor as used in BSZ expansion and fitted the coefficients using the inputs given in 'Fit-2B'. Utilizing this fit result, we have extracted $f_0(q^2)$ and compared it with the BSZ one. The results are shown in figure 4.4b as BCL (modified), and we find absolute agreement between the two results. Also, the extracted values of $|V_{ub}|$ in both the fits become identical.

4.4 Summary

We have extracted $|V_{ub}|$ analyzing all the available inputs on the exclusive $B \to \pi l \nu$ decays. This includes the data on the partial branching fractions, inputs from lattice and LCSR. We have commented on some of the issues of the earlier fits done by HFLAV, which relied upon obtaining an average q^2 spectrum of the partial width from all the available data on the decay rates on $B \to \pi l \nu$ at the first stage and using these results to extract $|V_{ub}|$ at the second stage. We have arrived at a fit with very low probability for the average q^2 spectrum at the first stage. We have identified BaBar(11) data (at least a part of it) as

TH-3118_176121005

a probable source of such a bad quality fit. The average q^2 spectrum of the decay rates without that data-set has an appreciable fit-probability. With this q^2 averaged spectrum, in the second stage, we have extracted $|V_{ub}|$ with and without the data from BaBar(11). The quality of fit is much better without the data from BaBar(11). We have repeated the same analysis with the new inputs from LCSR and noticed an increase in the best-estimate of $|V_{ub}|$ by roughly about 6%.

We simultaneously fit all the data (instead of a two-stage fit) after defining different fit scenarios. In this process, we have identified outliers, i.e. data-points inconsistent with the others. The goal is to check if some of these outliers are also influential in the extraction of $|V_{ub}|$. We found a few data-points that compromise the fit-quality, and at the same time, influence the extraction of $|V_{ub}|$. Our best results are the following:

- Without the input from BaBar(11) (full data-set) and $\mathcal{B}(B^0 \to \pi^-)^{[18,20]}$ (Belle(11)), we obtain $|V_{ub}| = (3.95^{+0.14}_{-0.15}) \times 10^{-3}$.
- From the full dataset after dropping $\mathcal{B}(B^0 \to \pi^-)^{[18,20]}$ (Belle(11)) and $\mathcal{B}(B^0 \to \pi^-)^{[20,26.4]}$ (BaBar(11)), the extracted $|V_{ub}| = (3.93^{+0.14}_{-0.15}) \times 10^{-3}$.

Both the values are consistent with the one extracted from inclusive $B \to X_u \ell \nu_\ell$ decays from Belle within 1 σ.

TH-3118_176121005

Chapter 5

Study of the $b \to d\ell\ell$ transitions in the Standard Model and test of New Physics sensitivities.

5.1 Introduction

In this chapter[1], we study the exclusive $b \to d\ell\ell$ transitions introduced in section 1.4. Unlike the $b \to s\ell\ell$ modes, there is less amount of information available on the relevant exclusive decay modes from experiment[2] as well as theory, like the non-availability of the lattice inputs on $B \to \rho$ form factors. The exclusive decays corresponding to $b \to d\ell\ell$ transition considered in this chapter are $B \to \pi\ell\ell$ and $B \to \rho\ell\ell$. Till date, we do not have data available on the $B \to \rho\ell\ell$ decays. However, there are some measurements on the branching fraction (BR) and CP-asymmetry in $B^{\pm} \to \pi^{\pm}\mu\mu$ decays reported by LHCb [109]. Theoretically, the main aspects challenging a precise estimate for these modes lie in handling the form factors and the long-distance effects arising from the presence of $c\bar{c}$ and $u\bar{u}$ resonant states within the allowed range of the dilepton invariant-mass.

An exclusive neutral current $B \to \pi\ell\ell$ transition is characterized by three form factors: $f_{+,0,T}(q^2)$ which are correlated in the analysis of Fermilab-MILC [129] and also LCSR analyses. Thus, a combined study of the $B \to \pi\ell\ell$ and $B \to \pi\ell\nu_\ell$ decay modes using all the available inputs is relevant and necessary. The situation is a bit grim for the form factors associated with the $B \to \rho$ transitions for which no lattice estimates exist till date. All these form factors are calculated in the LCSR approach, which are available for a few values of q^2, including the value at $q^2 = 0$ [2, 4], and they are fully correlated. Here also a simultaneous study of the available inputs in $B \to \rho\ell\nu_\ell$ and $B \to \rho\ell\ell$ decays is important. In light of the above-mentioned arguments, we look into the exclusive $B \to \pi(\rho)\ell\nu_\ell$ and

[1]The main results and other contents of this chapter have been arXived with the pre-print number " 2208.14463" [165] and communicated to JHEP for publication.

[2]This might be due to the low branching ratio of the $b \to d\ell\ell$ modes.

TH-3118_176121005

$B \to \pi(\rho)\ell\ell$ decay modes incorporating all available lattice, LCSR and experimental inputs. Both the decay rates $\Gamma(B \to \pi\ell\nu_\ell)$ and $\Gamma(B \to \rho\ell\nu_\ell)$ are proportional to $|V_{ub}|^2$ which is the only common link between the $B \to \pi$ and $B \to \rho$ decay channels we are considering here.

In section 5.2, we discuss the theoretical framework relevant to the decay modes considered in this chapter and in section 5.3, we mention about the form factor inputs used in this work. In section 5.4, we present the analysis method and armed with an estimate of $|V_{ub}|$ along with the corresponding form factor parameters from the fit, we provide the SM estimates of several observables subject to the $B \to \pi(\rho)\ell\ell$ decays within the range $0.1 \lesssim q^2 \lesssim 6$ (GeV^2) and also test the sensitivities of all these observables towards new physics in a few well-motivated benchmark NP scenarios. Finally, we summarize the results obtained in this chapter in section 5.5.

5.2 Theoretical Background

As mentioned earlier, the differential decay rate w.r.t. q^2 for $\bar{B} \to \pi\ell\nu_\ell$ decays is given in eq. 1.22 and for $\bar{B} \to \rho\ell\nu_\ell$ decays is given in eq. 1.23. Therefore, to extract $|V_{ub}|$, we need information on the form-factors at different values of q^2.

The effective Hamiltonian for semileptonic $b \to d\ell\ell$ transitions similar to $b \to s\ell\ell$ at the scale $\mu \sim m_b$ is given in 2.5 with the operator basis as 2.7. The theoretical approach is based on the QCDF framework, discussed in section 2.1.1.2.

The amplitude for $B \to \pi\ell\ell$ decays reads:

$$\mathcal{M}(B \to \pi\ell^+\ell^-) = \frac{G_F}{\sqrt{2}}\frac{\alpha_{\rm em}}{\pi}\Bigg[\left(\bar{\ell}\gamma_\mu\ell\right)\left(p^\mu + p'^\mu\right)\Bigg(\left(\lambda_t C_{9,\pi}^{(t)} + \lambda_u C_{9,\pi}^{(u)}\right) f_{B\pi}^+(q^2) + \frac{2m_b}{m_B + m_\pi}\lambda_t f_{B\pi}^T(q^2) C_7^{\rm eff}\Bigg) + \left(\bar{\ell}\gamma_\mu\gamma_5\ell\right)\left(p^\mu + p'^\mu\right)\lambda_t f_{B\pi}^+(q^2) C_{10}\Bigg], \quad (5.1)$$

where the coefficients $C_{9,P}^{(t)}$ and $C_{9,P}^{(u)}$ include the non-factorizable corrections and they are defined as

$$C_{9,\pi}^{(t)}(q^2) = C_9 + \frac{2m_b}{M_B}\frac{\mathcal{T}_\pi^{(t)}(q^2)}{\xi_\pi(q^2)}, \quad (5.2)$$

$$C_{9,\pi}^{(u)}(q^2) = \frac{2m_b}{M_B}\frac{\mathcal{T}_\pi^{(u)}(q^2)}{\xi_\pi(q^2)}. \quad (5.3)$$

$\mathcal{T}_\pi^{(t,u)}$ are defined in eq. 2.9. The factorization scheme in QCDF is such that the relation $\xi_\pi \equiv f_+$ holds exactly to all orders in perturbation theory. The most general form

TH-3118_176121005

of the amplitude $\mathcal{T}_\pi$ is given by [122]

$$\mathcal{T}_\pi^i = \xi_\pi \Big[C_\pi^{(0,i)} + \frac{\alpha_s C_F}{4\pi} \big(C_\pi^{(f,i)} + C_\pi^{(nf,i)} \big) \Big] + \frac{\pi^2 f_B f_\pi}{N_c M_B} \sum_\pm \int_0^\infty \frac{d\omega}{\omega} \Phi_{B,\pm}(\omega) \int_0^1 du\, \phi_\pi(u) T_{\pi,\pm}^{(i)}(u,\omega) \tag{5.4}$$

with $i = u$ or t quark. $C_F = 4/3$, $N_c = 3$ and f_B and f_π refer to the B and π meson decay constants respectively. The distribution amplitudes for the B meson and light mesons are discussed in section 2.1.1.2.

In eq. 5.4, the leading order contributions to the $\mathcal{T}_\pi^{(i)}$ are defined as

$$C_\pi^{(0,t)} = \frac{M_B}{2m_b} Y(q^2), \qquad C_\pi^{(0,u)} = \frac{M_B}{2m_b} Y^u(q^2), \tag{5.5}$$

where the contributions from the $\mathcal{O}_{1,\ldots,6}$ matrix elements are incorporated in $Y(q^2)$. The detailed mathematical expressions for $C_\pi^{(nf,i)}$, $T_{\pi,\pm}^{(0,i)}(u,\omega)$ (WA contribution), and $T_{\pi,\pm}^{(nf,i)}(u,\omega)$ are obtained from refs. [122, 123][3]. The decay distribution for $B \to \pi\ell\ell$ decays w.r.t the kinematic variables is given in eq. 1.25.

The decay distribution for $B \to \rho\ell\ell$ transitions is given in eq. 1.29. Here also, we need to add the corresponding non-factorizable corrections to the amplitudes given in eq. 2.12. Following the QCDF approach, the transversity amplitudes $\mathcal{T}_a$ can be written as

$$\mathcal{T}_a = \xi_a \Big(C_a^{(0)} + \frac{\alpha_s C_F}{4\pi} C_a^{(1)} \Big) + \frac{\pi^2 f_B f_{\rho,a}}{N_c M_B} \Xi_a \sum_\pm \int_0^\infty \frac{d\omega}{\omega} \Phi_{B,\pm}(\omega) \int_0^1 du\, \phi_{\rho,a}(u) T_{a,\pm}(u,\omega), \tag{5.6}$$

where "a" stands for the polarization of the vector meson in the final state ($a \to ||$ or $\perp$), $\Xi_\perp = 1$, $\Xi_{||} = m_\rho/E$, $E = (M_B^2 - q^2)/(2M_B)$ refers to the energy of the final state meson and ξ_a refer to the form factors in the heavy quark and high energy limit.

5.3 Inputs

Apart from the Lattice inputs as discussed in section 4.2.2 for the $B \to \pi$ transitions, we have also used the inputs from the JLQCD collaboration [166] for $f_{+,0}(q^2)$ at three q^2 points with full covariance matrices (both systematic and statistical). We have used the inputs on the form factors obtained by LCSR approaches [2, 3]. The analysis in [3] uses the two-particle twist-two pion LCDA, and the results are more precise than those obtained in [2] which is a leading-order (LO) calculation with the ill-known B-meson LCDA. The inputs in ref. [2] play a sub-dominant role in our fits, since the estimated errors in [2] are larger as compared to the one obtained in ref. [3].

For $B \to \rho$ transitions, the LCSR data points along with the respective covariance

[3]For the $B \to P$ transitions the expressions for the non-factorizable corrections are extracted from the results of [122, 123] using the following replacement: $C_\pi^{nf} = -C_{||}^{nf}$, $T_{\pi,\pm}^{(0)}(u,\omega) = -T_{||,\pm}^{(0)}(u,\omega)$, and $T_{\pi,\pm}^{(nf)}(u,\omega) = -T_{||,\pm}^{(nf)}(u,\omega)$

TH-3118_176121005

matrix are given in ref. [2] for $q^2 = -15, -10, -5, 0, 5$ GeV^2, which we directly use in our fits. In ref. [4], the fit-results for the coefficients of the z-expansion are given using which, we generate correlated synthetic data-points for the form factors A_1, A_2, V, T_1 and T_3 at q^2 = 0,5,10 GeV^2 and for A_0 and T_2 at q^2 = 5,10 GeV^2 [4] respectively. The LCSR results in ref [4] have been derived up to twist-3 $\mathcal{O}(\alpha_s)$ using the ρ meson LCDA, and the extracted values are relatively more precise than the ones obtained in [2]. The computation of the $B \to \rho$ form factors in ref. [2] relies on the narrow-width approximation of the ρ meson and uses the B-meson LCDA, whereas the computation in ref. [4] goes beyond the narrow-width approximation. The ρ meson DA is characterized by the longitudinal and transverse component of the decay constant $f_\rho^{\parallel}$ and $f_\rho^{\perp}$, respectively. The inputs on $f_\rho^{\parallel}$ are obtained from the measurements of the decay widths: $\Gamma(e^+e^- \to \rho^0(\to \pi\pi))$ and $\Gamma(\tau^+ \to \rho^+(\pi\pi)\nu)$ respectively [167]. In these experiments, the ρ-meson is detected as a Breit-Wigner peak in the invariant mass distribution of produced pions ($\rho \to \pi\pi$), while the transverse component $f_\rho^{\perp}$ is obtained from the lattice estimates of the ratio $f_\rho^{\parallel}/f_\rho^{\perp}$.

μ_b	4.8 GeV	f_B	190.0 ± 1.3 MeV [168]
$\alpha_s(\mu_b)$	0.214	$\lambda_{B,+}^{-1}$	(3 ± 1) GeV^{-1} [122]
$\alpha_{\rm em}$	1/137	G_F	1.166×10^{-5} GeV^{-2}
$m_{c,pole}$	1.4 GeV	$m_{b,pole}$	4.8 GeV
f_π	130.2 ± 0.8 MeV [168]	a_2^π	0.116^{+19}_{-20} [169]
$f_\rho^{\perp}$	160 ± 7 MeV [4]	$a_{2,\rho}^{\perp}$	0.14 ± 0.06 [4]
$f_\rho^{\parallel}$	213 ± 5 MeV [4]	$a_{2,\rho}^{\parallel}$	0.17 ± 0.07 [4]

Table 5.1: Inputs used in the analysis.

Other inputs relevant to our analysis are given in table 5.1. The values of the WCs are taken at $\mu_b = 4.8$ GeV [92]. We have truncated the BSZ expansion (eq. 2.24) at $N = 3$ for $B \to \pi$ transitions and at $N = 2$ for $B \to \rho$ transitions. We have checked that if we go to the next order $N = 3$ for $B \to \rho$ transition, the newly added higher-order coefficients remain mostly unconstrained, and they have a negligible impact on the precision extraction of $|V_{ub}|$ and other related observables which we will discuss in the next section.

5.4 Analysis and results

We have considered the measurements on the partial branching fractions in bins of dilepton invariant mass squared (q^2) for the exclusive $b \to u\ell\nu$ and $b \to d\ell\ell$ transitions as discussed in section 1.5. The expressions for the differential decay widths for $B \to \pi\ell\nu$ and $B \to \rho\ell\nu$ contain $|V_{ub}|$ as the overall normalizing constant as shown in eqs 1.22 and 1.23. As can be

[4] At $q^2 = 0$, A_0 is related to A_1 and A_2 and T_2 is related to T_1, thus they aren't independent. In order to keep the covariance matrix positive semi-definite, we don't include the datapoints for A_0 and T_2 at $q^2 = 0$.

TH-3118_176121005

seen from eq. 2.5, the loop-induced processes $B \to \pi\ell\ell$ and $B \to \rho\ell\ell$ are sensitive to the products of the CKM matrix elements $\lambda_u = V_{ub}V_{ud}^*$ and $\lambda_t = V_{tb}V_{td}^*$ respectively. Thus, to make the $|V_{ub}|$ dependence explicit, we define the product of the elements as

$$V_{ub}V_{ud}^* = |V_{ub}||V_{ud}|e^{-i\gamma}, \qquad V_{tb}V_{td}^* = |V_{tb}||V_{td}|e^{i\beta}, \tag{5.7}$$

where angles are defined in eq. 1.17.

We perform a statistical frequentist analysis utilizing the available experimental inputs on $B \to \pi\ell\nu$, $B \to \rho\ell\nu$ and $B \to \pi\ell\ell$ modes [73–76, 109], and the available lattice and LCSR inputs on the respective form factors in these decays and $B \to \rho\ell\ell$. We have extracted the coefficients of the BSZ expansion defined in eq. 2.24 along with the magnitude of $|V_{ub}|$. Here, we take the parameters $|V_{ud}|\cos(\gamma)$, $|V_{ud}|\sin(\gamma)$, $|V_{tb}||V_{td}|\cos(\beta)$, $|V_{tb}||V_{td}|\sin(\beta)$, the product $f_B f_\pi$ (f_B and f_π are decay constants of the B and π mesons) and the inverse moment of B meson ($\lambda_{B,+}^{-1}$) as nuisance parameters in the fits. The inputs on the CKM parameters are taken from [89]. The fit result is given in table 5.2, using which we provide predictions for the branching ratios, direct CP asymmetries and isospin asymmetry for $B \to \pi\ell\ell$ and various angular observables for $B \to \rho\ell\ell$ transitions. Apart from the precise predictions in the SM, we have also tested the NP sensitivities of the observables. We have considered NP effects in the operators $\mathcal{O}_9$, $\mathcal{O}_9'$, $\mathcal{O}_{10}$ and $\mathcal{O}_{10}'$ defined in eq. 3.2 with the corresponding WCs ΔC_9, C_9', ΔC_{10}, C_{10}'.

$B \to \pi$ form factors		$B \to \rho$ form factors	
Parameters	Fitted Values	Parameters	Fitted Values
$a_0^{f_+}$	0.260±0.008	$a_1^{A_0}$	-0.879±0.153
$a_1^{f_+}$	-0.639±0.065	$a_2^{A_0}$	1.074±0.951
$a_2^{f_+}$	-0.067±0.210	$a_0^{A_1}$	0.242±0.013
$a_3^{f_+}$	0.485±0.160	$a_1^{A_1}$	0.468±0.086
$a_1^{f_0}$	0.301±0.063	$a_2^{A_1}$	0.307±0.281
$a_2^{f_0}$	0.350±0.181	a_0^{V}	0.309±0.017
$a_3^{f_0}$	0.354±0.168	a_1^{V}	-0.742±0.115
$a_0^{f_T}$	0.252±0.011	a_2^{V}	1.216±0.827
$a_1^{f_T}$	-0.701±0.101	$a_0^{A_2}$	0.220±0.017
$a_2^{f_T}$	-0.455±0.396	$a_1^{A_2}$	-0.397±0.096
$a_3^{f_T}$	-0.015±0.365	$a_2^{A_2}$	0.405±1.002
$\|V_{ub}\| \times 10^3$	3.60±0.10	$a_0^{T_1}$	0.262±0.015
$V_{tb}V_{td}cos\beta$	0.0079±0.0001	$a_1^{T_1}$	-0.643±0.091
$V_{tb}V_{td}sin\beta$	0.00324±0.00008	$a_2^{T_1}$	0.909±0.645
$V_{ud}cos\gamma$	0.404±0.019	$a_1^{T_2}$	0.556±0.084
$V_{ud}sin\gamma$	0.887±0.009	$a_2^{T_2}$	0.714±0.336
$f_B f_\pi$	0.0247±0.00023	$a_0^{T_3}$	0.190±0.014
$\lambda_{B,+}^{-1}$	2.988±0.999	$a_1^{T_3}$	-0.374±0.081
		$a_2^{T_3}$	1.267±0.798

Table 5.2: Fit results using all the available inputs.

TH-3118_176121005

5.4.1 $B \to \pi\ell\ell$ transitions

In this section, we study the modes $B^\pm \to \pi^\pm\ell\ell$ and $\bar{B}^0(B^0) \to \pi^0\ell\ell$ for which the q^2-dependent direct CP asymmetries are defined as :

$$A_{CP}^{+}(q^2) = \frac{d\mathcal{B}(B^- \to \pi^-\ell\ell)/dq^2 - d\mathcal{B}(B^+ \to \pi^+\ell\ell)/dq^2}{d\mathcal{B}(B^- \to \pi^-\ell\ell)/dq^2 + d\mathcal{B}(B^+ \to \pi^+\ell\ell)/dq^2}\,, \tag{5.8}$$

$$A_{CP}^{0}(q^2) = \frac{d\mathcal{B}(\bar{B}^0 \to \pi^0\ell\ell)/dq^2 - d\mathcal{B}(B^0 \to \pi^0\ell\ell)/dq^2}{d\mathcal{B}(\bar{B}^0 \to \pi^0\ell\ell)/dq^2 + d\mathcal{B}(B^0 \to \pi^0\ell\ell)/dq^2} \tag{5.9}$$

The definition of the q^2-dependent CP-averaged isospin asymmetry corresponds to the LHCb definition [170] :

$$A_I = \frac{d\mathcal{B}(B^0 \to \pi^0\ell\ell)/dq^2 - (\tau_0/\tau_+)d\mathcal{B}(B^+ \to \pi^+\ell\ell)/dq^2}{d\mathcal{B}(B^0 \to \pi^0\ell\ell)/dq^2 + (\tau_0/\tau_+)d\mathcal{B}(B^+ \to \pi^+\ell\ell)/dq^2}, \tag{5.10}$$

where τ_0 and τ_+ are B^0 and B^+ meson lifetimes. Additionally, we have incorporated the interesting observables:

$$R_\pi^{\pm(0)} = \frac{\Gamma(B^{\pm(0)} \to \pi^{\pm(0)}\mu\mu)}{\Gamma(B^{\pm(0)} \to \pi^{\pm(0)}ee)}, \tag{5.11}$$

which are Lepton Flavour Universality (LFU) conserving in the SM and are potentially sensitive to new physics.

In table 5.3, we have provided predictions for the various observables in the four q^2 bins using the fit results given in table 5.2. The uncertainty corresponds to the uncertainty in determining the form factors, CKM elements and the decay constants. The q^2-distributions of the relevant branching fractions and the CP, isospin-asymmetries defined above are shown in figs. 5.1. In figs. 5.1a, 5.1b, 5.1c, and 5.1d, we have shown the variation of differential branching fraction with q^2 for both $B^\pm \to \pi^\pm\ell\ell$ and $\bar{B}(B) \to \pi^0\ell\ell$ modes, comparing which we notice that the decay spectra for $\bar{B}(B) \to \pi^0\ell\ell$ is nearly flat, whereas for $B^\pm \to \pi^\pm\ell\ell$ is highly q^2 dependent which is also reflected in the q^2 variations of the CP and isospin-asymmetries. This is due to the differences in the q^2 behaviour of the weak annihilation contributions in the neutral and charged B decays at the leading order in α_s as discussed in section 2.1.1.2. The dominant contribution in $\bar{B}(B) \to \pi^0\ell\ell$ decays comes from C_9^t defined in eq. 5.2 and the contribution from C_9^u is negligible. However, for $B^\pm \to \pi^\pm\ell\ell$ decays, the contribution from C_9^u becomes equally important at the low q^2 regions since the weak annihilation contribution is proportional to the WC $C_2 \sim 1$. Due to the reasoning as presented in section 2.1.1.2, $\mathcal{T}_\pi^{(u)}(q^2)$ is more sensitive to the variation of q^2 as compared to $\mathcal{T}_\pi^{(t)}(q^2)$. Also, $\lambda_{B,-}^{-1}$ acting as a source of strong phase is larger at the low q^2 regions. Thus, the large imaginary contribution of $C_{9,P}^{(u)}$ at low q^2 for $B^\pm$ decays results in the large CP asymmetry at low q^2. The CP asymmetry for B^0 decays is

TH-3118_176121005

small, as weak annihilation is mostly mediated by loop-suppressed QCD penguins. Isospin asymmetry is also generated by hard-spectator interactions and is more pronounced at low q^2, as shown in fig. 5.1g.

Observables	Predictions in a few q^2-bins (GeV^2)			
	[0.1-1]	[1-2]	[2-4]	[4-6]
$B(B^0 \to \pi^0\ell\ell) \times 10^8$	0.0499(28)	0.0503(28)	0.0985(54)	0.0976(51)
$B(\bar{B}^0 \to \pi^0\ell\ell) \times 10^8$	0.0283(21)	0.0330(23)	0.0674(44)	0.0696(43)
$B(B^- \to \pi^-\ell\ell) \times 10^8$	0.0444(28)	0.0538(43)	0.1308(92)	0.1465(92)
$B(B^+ \to \pi^+\ell\ell) \times 10^8$	0.1950(70)	0.1551(65)	0.251(12)	0.223(11)
$\langle A^0_{CP} \rangle$	-0.276(15)	-0.2074(69)	-0.1873(56)	-0.1681(55)
$\langle A^+_{CP} \rangle$	-0.629(12)	-0.486(16)	-0.316(11)	-0.2077(72)
$\langle A_I \rangle$	-0.479(11)	-0.3992(50)	-0.3625(23)	-0.3445(11)
$\langle \bar{R}^0_\pi \rangle$	0.99195(13)	1.00007(13)	1.00039(13)	1.00050(12)
$\langle R^-_\pi \rangle$	0.99043(34)	1.00022(19)	1.00044(14)	1.00051(13)

Table 5.3: Predictions of observables for $B \to \pi\ell\ell$ decays in the SM, obtained using the fit results given in table 5.2.

We have shown the q^2 variations of all the observables mentioned above in the four specific NP scenarios in fig. 5.1: we have set $Re(\Delta C_i) = Re(C'_i) = 1$ and imaginary component of the new WCs to 0 or 1, in order to be able to distinguish the sensitivities of the observables towards the new phase. Following are a few observations from fig. 5.1:

- None of the observables discussed above for $B \to \pi\ell\ell$ decays can distinguish the effects of $\mathcal{O}_9$ ($\mathcal{O}_{10}$) from that of $\mathcal{O}'_9$ ($\mathcal{O}'_{10}$) as the q^2-distributions are the same for $\mathcal{O}_9$ ($\mathcal{O}_{10}$) and $\mathcal{O}'_9$ ($\mathcal{O}'_{10}$).
- For the scenarios with $\mathcal{O}_{10}$ or $\mathcal{O}'_{10}$, the branching fractions are lower than the corresponding SM predictions, while for the scenario with $\mathcal{O}_9$ or $\mathcal{O}'_9$, there is increase in the values of branching fractions from that of the SM. As expected, it is hard to distinguish the impact of the imaginary WCs in the branching fractions.
- The CP-asymmetries are sensitive only to ΔC_{10} and C'_{10}. The values of the CP-asymmetric observables predicted in the specified NP scenarios will be lower than that of the SM for these two WC's.
- Contrary to the CP-asymmetries, the isospin asymmetry A_I is sensitive to ΔC_9 and C'_9 in the region $2 < q^2 < 6$ GeV^2 and the predicted value will be higher than that of the SM. In the low q^2 regions it will be difficult to see the impact of the NP over that of the SM.

Once measurements are available, any deviation from the respective SM predictions will hint towards a particular type of NP scenario since different observables are sensitive

TH-3118_176121005

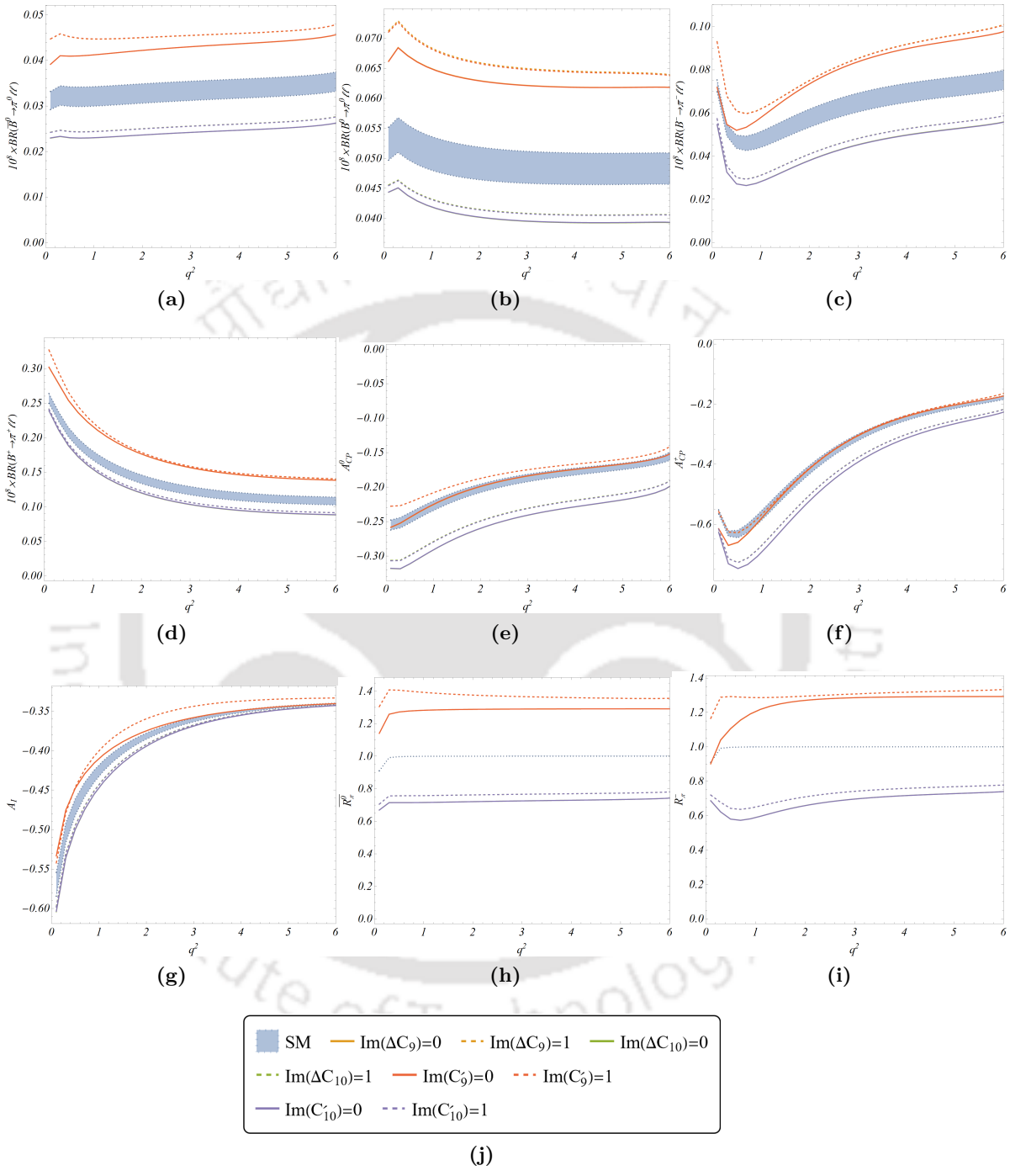

Figure 5.1: The q^2 dependence for the $B \to \pi ll$ observables in the SM and the four different NP scenarios with NP Wilson coefficients $\Delta C_{9,10}$ and $C'_{9,10}$. For the NP scenarios, the plots show the dependence of the observables on the imaginary parts of the respective NP's for the benchmark values of 1 and 0 while the real part is fixed at 1. For details, please see the legend.

TH-3118_176121005

to different NP scenarios. For example, the NP scenario with the operator $\mathcal{O}_9$ or $\mathcal{O}'_9$ will show deviations in A_I and the respective branching fractions but not in A_{CP}s. On the other hand, seeing deviations in A_{CP}s but not in A_I will be an indication of the scenario with the operator $\mathcal{O}_{10}$ or $\mathcal{O}'_{10}$. The predictions of these observables for a few benchmark points of the new WCs are given in tables C.1 and C.2 respectively, which could be tested in future experiments. Also, these results clearly indicate the pattern of NP effects in those observables.

5.4.2 $B \to \rho\ell\ell$ transitions

In section 1.4, we have pointed out the angular observables relevant for the $B \to \rho\ell\ell$ decays. In the following subsections, we study $B^\pm \to \rho^\pm(\to \pi^\pm\pi^0)\ell\ell$ and $\bar{B}(B) \to \rho^0(\to \pi^+\pi^-)\ell\ell$ decay modes. We provide predictions of observables associated with the angular anaylsis for these channels considering the $\pi\pi$ system in the final state in a P-wave configuration.

5.4.2.1 $B^\pm \to \rho^\pm\ell\ell$ transitions

For $B^\pm \to \rho^\pm\ell\ell$ decays, ρ^+ or ρ^- will be reconstructed via the decays $\rho^+ \to \pi^+\pi^0$ and $\rho^- \to \pi^-\pi^0$, respectively. The CP-averaged, asymmetric and optimized observables corresponding to the untagged decay distribution are given in eqs 1.31 and 1.33 respectively. Tagging of B^+ or B^- is possible at both the LHCb and Belle. Hence, it is also possible to directly probe the angular coefficients corresponding to the B^+ or B^- decays separately, the definitions of observables are provided in eqs 1.34 and 1.35.

Bin[GeV^2]	[0.1-1]	[1-2]	[2-4]	[4-6]
$\langle P_1^- \rangle$	0.0042(33)	0.0030(47)	-0.048(21)	-0.086(34)
$\langle P_2^- \rangle$	-0.1262(50)	-0.422(13)	-0.177(28)	0.241(22)
$\langle P_3^- \rangle$	0.00040(25)	0.0024(15)	0.0048(28)	0.0052(28)
$\langle P_4^{'-} \rangle$	-0.117(29)	-0.159(19)	-0.366(15)	-0.474(12)
$\langle P_5^{'-} \rangle$	0.9343(64)	0.568(32)	-0.302(41)	-0.744(25)
$\langle P_6^{'-} \rangle$	-0.179(22)	-0.078(40)	0.012(46)	-0.048(48)
$\langle P_8^{'-} \rangle$	0.095(16)	-0.1176(72)	-0.078(14)	-0.047(18)
$\langle BR^- \rangle \times 10^9$	2.32(21)	1.004(89)	2.08(19)	2.48(21)
$\langle A_{FB}^- \rangle$	-0.1076(41)	-0.206(18)	-0.057(11)	0.105(13)
$\langle F_L^- \rangle$	0.203(19)	0.631(32)	0.765(21)	0.700(24)
$\langle R_\rho^- \rangle$	0.98067(29)	0.99566(39)	0.99610(38)	0.99683(27)

Table 5.4: SM Predictions of observables for $B^- \to \rho^-\ell\ell$.

For the charged B decays, we can define the same set of observables for both the LHCb and Belle. Using the fit results given in table 5.2, we have predicted the angular observables, the longitudinal polarization fraction F_L of the ρ meson, the forward-backward

TH-3118_176121005

asymmetry A_{FB} associated with the B^- and B^+ decays in a few q^2-bins which are presented in tables 5.4 and 5.5, respectively. In addition, we have predicted the corresponding branching fractions and the LFU ratios $R_\rho^\pm = \Gamma(B^\pm \to \rho^\pm \mu\mu)/\Gamma(B^\pm \to \rho^\pm ee)$ in the SM. Also, we have tested the NP sensitivities of all these observables.

Bin[GeV^2]	[0.1-1]	[1-2]	[2-4]	[4-6]
$\langle {P_1}^+ \rangle$	0.0038(32)	0.0034(52)	-0.048(20)	-0.087(34)
$\langle {P_2}^+ \rangle$	-0.1219(36)	-0.411(12)	-0.176(37)	0.291(20)
$\langle {P_3}^+ \rangle$	0.00057(41)	0.0031(21)	0.0059(36)	0.0055(30)
$\langle {P'_4}^+ \rangle$	0.347(12)	0.182(15)	-0.224(19)	-0.448(11)
$\langle {P'_5}^+ \rangle$	0.350(15)	0.062(25)	-0.495(32)	-0.809(21)
$\langle {P'_6}^+ \rangle$	-0.065(28)	-0.168(38)	-0.271(38)	-0.244(37)
$\langle {P'_8}^+ \rangle$	-0.153(27)	-0.059(31)	-0.067(26)	-0.082(19)
$\langle BR^+ \rangle \times 10^9$	4.11(25)	2.06(14)	2.94(23)	2.78(23)
$\langle A_{FB}^+ \rangle$	-0.0634(40)	-0.107(11)	-0.0412(95)	0.119(14)
$\langle F_L^+ \rangle$	0.448(25)	0.782(18)	0.823(15)	0.716(23)
$\langle {R_\rho}^+ \rangle$	0.98448(36)	0.99768(20)	0.99721(27)	0.99718(24)

Table 5.5: SM Predictions of observables for $B^+ \to \rho^+ \ell\ell$.

Observables	NP sensitivities	Observables	NP sensitivities
A_3	$Im(C'_9)$	P_1	$Re(C'_9)$, $Re(C'_{10})$
A_4	$Im(\Delta C_9)$, $Im(C'_9)$	P_2	$Re(\Delta C_9)$
A_5	$Im(\Delta C_{10})$, $Re(C'_{10})$, $Im(C'_{10})$	P_3	$Re(C'_9)$
A_6	$Im(\Delta C_{10})$	P'_4	$Re(\Delta C_{10})$, $Re(C'_{10})$
A_7	$Im(\Delta C_{10})$, $Im(C'_{10})$	P'_5	$Re(\Delta C_9)$, $Re(C'_{10})$
A_8	$Im(\Delta C_9)$, $Im(C'_{10})$, $Im(C'_9)$	P'_6	Hard to distinguish from SM
A_9	$Im(C'_9)$, $Im(C'_{10})$	P'_8	Hard to distinguish from SM
A_{CP}	$Re(C'_9)$, $Re(C'_{10})$, $Re(\Delta C_9)$, $Re(\Delta C_{10})$ (limited q^2 regions)	P_2^+ P_2^-	$Re(\Delta C_9)$ $Re(\Delta C_9)$, $Im(\Delta C_{10})$
A_{FB}	$Re(\Delta C_9)$	P_3^+, P_3^-	$Im(C'_9)$, $Re(C'_9)$, $Im(C'_{10})$
F_L	$Re(\Delta C_9)$ (limited q^2 regions), hard to probe, need more precision	${P'_6}^+$, ${P'_6}^-$	$Im(C'_{10})$, $Im(\Delta C_{10})$
$R(\rho)$	All the four scenarios, real and imaginary components	${P'_8}^+$, ${P'_8}^-$	$Im(C'_9)$, $Im(C'_{10})$, $Im(\Delta C_9)$

Table 5.6: The observables along with the respective new physics scenarios which affect them the most. In the NP scenarios, the q^2 sensitivity of these observables can be visualized from the corresponding plots provided in the text.

In the SM, the observables $P_1^{-(+)}$ and $P_3^{-(+)}$ are negligibly small owing to the smallness of $J_3(\bar{J}_3)$ and $J_9(\bar{J}_9)$ which is due to a partial cancellation between the modulus of the two transversity amplitudes in J_3, whereas $J_9 \propto Im(A_\perp^L A_{||}^{L^*})$ which is negligibly small as seen from eq. A.4. In table 5.7, we have shown the predicted values of the CP-optimized (P_i, P'_i) and CP-asymmetric (A_i) observables. The angular coefficients J_3 and J_9 are small in the SM, which results in the smallness of A_3 and A_9. As is evident, apart

TH-3118_176121005

Bin[GeV^2]	[0.1-1]	[1-2]	[2-4]	[4-6]
$\langle A_{CP} \rangle$	-0.280(25)	-0.345(18)	-0.1728(92)	-0.0584(42)
$\langle A_3 \rangle$	-0.0000018(262)	-0.000039(84)	0.000022(127)	0.00044(29)
$\langle A_4 \rangle$	-0.1017(62)	-0.0684(60)	-0.0144(25)	0.0043(21)
$\langle A_5 \rangle$	0.0259(43)	0.0687(84)	0.0534(80)	0.0315(67)
$\langle A_{6s} \rangle$	0.0024(20)	0.0056(55)	0.00057(795)	-0.018(11)
$\langle A_7 \rangle$	-0.0056(40)	0.0297(35)	0.0589(47)	0.0470(40)
$\langle A_8 \rangle$	0.0502(73)	-0.0031(69)	0.0011(33)	0.0093(11)
$\langle A_9 \rangle$	0.000043(38)	0.000096(79)	0.000109(76)	0.000085(52)
$\langle P_1 \rangle$	0.0027(21)	0.0027(41)	-0.043(19)	-0.084(33)
$\langle P_2 \rangle$	-0.0826(26)	-0.3472(100)	-0.159(23)	0.257(13)
$\langle P_3 \rangle$	0.00032(22)	0.0023(15)	0.0048(28)	0.0051(28)
$\langle P_4^{'} \rangle$	0.1529(97)	0.048(11)	-0.271(15)	-0.452(11)
$\langle P_5^{'} \rangle$	0.422(11)	0.225(19)	-0.386(29)	-0.764(21)
$\langle P_6^{'} \rangle$	-0.080(21)	-0.120(34)	-0.137(38)	-0.148(42)
$\langle P_8^{'} \rangle$	-0.056(12)	-0.072(19)	-0.068(19)	-0.064(18)
$\langle BR \rangle \times 10^9$	3.21(22)	1.53(11)	2.51(21)	2.63(22)
$\langle F_L \rangle$	0.360(25)	0.733(22)	0.799(17)	0.708(23)
$\langle A_{FB} \rangle$	-0.0793(40)	-0.139(13)	-0.0479(86)	0.113(11)
$\langle R_\rho \rangle$	0.98311(36)	0.99702(25)	0.99675(32)	0.99701(25)

Table 5.7: The SM predictions of the CP-averaged and CP-asymmetric observables in $B^\pm \to \rho^\pm \ell\ell$ decays as measurable both at the LHCb and Belle.

from A_3 and A_9, the other CP-asymmetric observables aren't suppressed in the SM for $b \to d\ell\ell$ transitions, as happens in the case of $b \to s\ell\ell$, where the term containing the CP-violating phase is doubly Cabibbo-suppressed. The asymmetric observables are sensitive to the difference between J and $\bar{J}$ whereas the optimized observables are proportional to J (for B^-) or $\bar{J}$ (for B^+). Therefore, the pattern of the numerical results for the asymmetric observables depicted in table 5.7 can be gauged from the corresponding values for the optimized observables provided in tables 5.4 and 5.5. For eg., among all the CP-asymmetric observables, A_{CP} and A_4 have the maximum values in terms of magnitude, and is one or two orders enhanced w.r.t the rest of the asymmetric observables for $q^2 \leq 2$. These semileptonic decays are sensitive to the weak phases β and γ, respectively, which change sign between the amplitudes for B^+ and B^- decays. However, the strong phases also play an essential role. The large values of A_4 and A_{CP} is due to the large difference between the values of $J_4(J_{1c,2c})$ and $\bar{J}_4(\bar{J}_{1c,2c})$ which are sensitive to the strong phases in $A_0^{L,R}$ (eq. A.1) originating from the leading order weak annihilation corrections in $\mathcal{T}_{||}^{(u),WA+nf)}$ as given in eq. 2.12. The q^2 dependence of the strong phase in $\lambda_{B,+}^{-1}$ will partially contribute to the q^2 variations of $A_0^{L,R}$. In fig. 5.2, we show the variations of the observables listed in table 5.7 with q^2 for which the SM predictions are represented by blue thick regions. Almost similar kinds of q^2 variations are obtained for the related

TH-3118_176121005

observables in $B^{\pm}$ decays defined in eq. 1.35 which we have not shown separately. We have presented a few of them in fig. 5.3 for which the q^2 variations are slightly different than the corresponding observables obtained from the CP-averaged distributions.

We have also tested the NP sensitivities in the four 1-operator scenarios of all the observables described above, which are shown in figs. 5.2 and 5.3, respectively. Apart from a few observables, which are shown in fig. 5.3, the NP sensitivities of the observables associated with the B^+ or B^- decays are similar to the one obtained from the CP-averaged rates; hence we have not shown them separately. The observables like $P^{\pm}_{2,3}, P'^{\pm}_6, P'^{\pm}_8$ have different dependences on a couple of new WCs which are shown in fig. 5.3 which can be compared with the figs. 5.2j, 5.2k, 5.2n, and 5.2o, respectively. The information contained in those figures has been summarized in table 5.6. Apart from A_{CP}, rest of the CP-asymmetric observables are sensitive to the imaginary parts of one or more NP scenarios. However, A_{CP} is sensitive to all four scenarios, only to the real components, and in a limited region: $0.5 \leq q^2 \leq 2$ GeV^2. Similarly, the LFU ratio R_ρ is sensitive to all the NP scenarios, both to the real and imaginary components. We find that there are observables sensitive to only a particular type of NP scenario. Hence, any deviations from the SM predictions in one or more of these observables will indicate the presence of the respective new interaction. The q^2 variations of different observables are different in different NP scenarios and are very much indicative.

It is difficult to distinguish the contributions of NP from respective SM predictions in the observables P'_6 and P'_8 obtained from the CP-averaged decay rate as seen from figs. 5.2n, and 5.2o. Instead, the observables $P'^{\pm}_{6,8}$ are sensitive to different new interactions as shown in figs. 5.3e, 5.3f, 5.3g, and 5.3h, respectively. For both these observables, the NP dependencies in the B^+ and B^- channels are opposite; hence, in the observables obtained from the CP-averaged rates, those dependencies are lost due to a relative cancellation. P_3 is sensitive only to $Re(C'_9)$ while $P^{\pm}_3$ are sensitive to $Im(C'_{9,10})$ in addition to $Re(C'_9)$. Due to a relative cancellation between the observables P^+_3 and P^-_3, the sensitivities towards the respective imaginary components are lost in their corresponding CP-average. Like P_2, P^+_2 is sensitive to $Re(\Delta C_9)$ and has a little sensitivity to the imaginary part of ΔC_{10}. However, the predicted value is slightly lower than the corresponding SM predictions, which is hard to probe. On the other hand, P^-_2 is sensitive to both $Re(\Delta C_9)$ and $Im(\Delta C_{10})$ and in both these scenarios, the magnitude of the predicted values is higher than the respective SM predictions. Here, again due to a relative cancellation the sensitivity towards $Im(\Delta C_{10})$ is lost in P_2.

Following the presentation of the NP dependence of the observables for the $B \to \pi$ sector; we also tabulate the NP dependence of the observables for the $B \to \rho$ sector corresponding to the same four q^2 bins and for benchmark combinations of the real and imaginary NP WCs. For the charged modes, the observables corresponding to the untagged case that can be measured at both Belle and LHCb are provided in tables C.3, C.4, C.5, C.6, C.7,

TH-3118_176121005

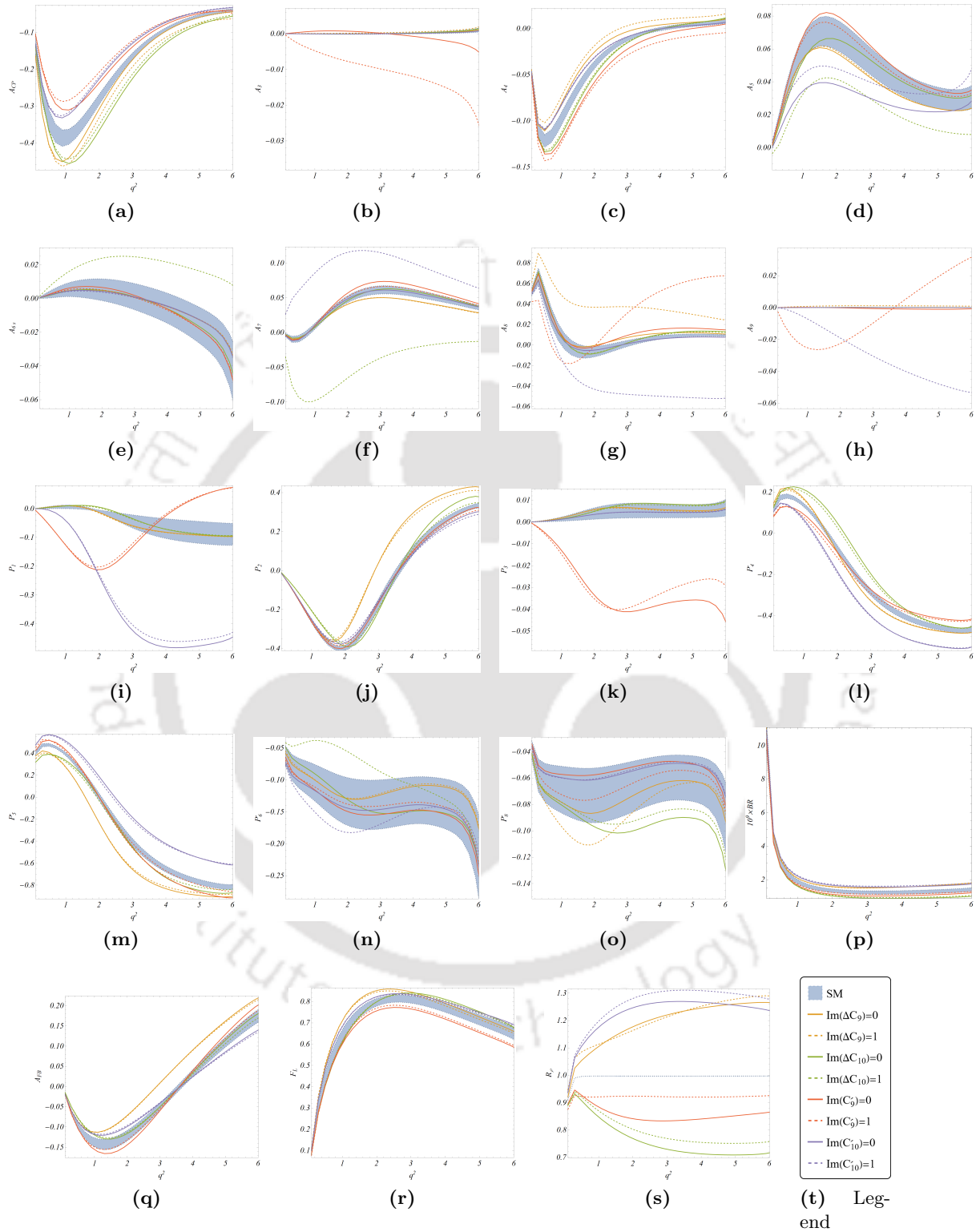

(t) Legend

Figure 5.2: The q^2 dependence of the observables in $B^{\pm} \to \rho^{\pm} ll$ decays, which are measurable at both the LHCb and Belle. The variations are shown in the SM and in the four different NP scenarios with NP Wilson coefficients $\Delta C_{9,10}$ and $C'_{9,10}$. For the benchmarks, please see the legend.

TH-3118_176121005

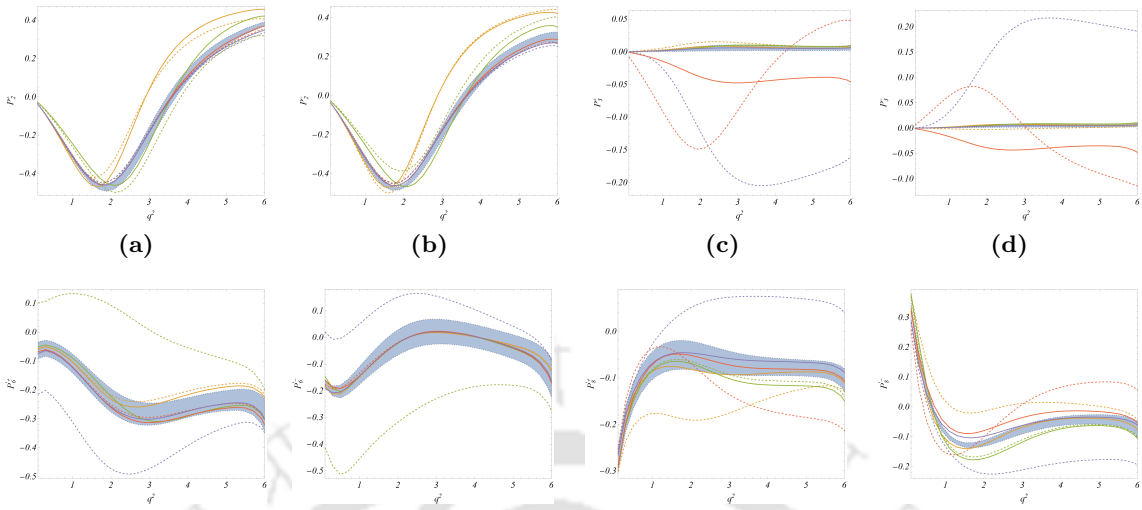

Figure 5.3: The study of the q^2 dependencies of a few tagged observables in $B^+ \to \rho^+ ll$ and $B^- \to \rho^- ll$ decays, which are measurable at both the LHCb and Belle. The caption will be similar to the one given in fig. 5.2; also, we follow the legends of that figure.

C.8,C.9 and C.10. We highlight only those observables for the tagged case which have different NP dependence than the corresponding observables obtained from the CP-averaged distribution; such observables are displayed in tables C.11, C.12,C.13 and C.14. From a comparison with the respective SM predictions, one can look for possible deviations which can be statistically significant. The trend or the pattern of NP effects, which are also dependent on q^2 regions, is apparent in the respective predictions.

5.4.2.2 $B^0 \to \rho^0 \ell\ell$ transitions

For $B^0 \to \rho^0(\to \pi\pi)\ell\ell$ decay, the ρ meson is reconstructed via the decay, $\rho^0 \to \pi^+\pi^-$, to a flavor non-specific final state. Therefore, the final state can arise from the decay of both B^0 and $\bar{B}^0$ mesons. The interference between $B^0 - \bar{B}^0$ oscillations and decay leads to the time dependencies in the decay amplitudes which also impact the corresponding angular coefficients J_i and $\tilde{J}_i$ which are presented as:

$$J_i(t) = J_i(A_H \to A_H(t)), \qquad \tilde{J}_i(t) = J_i(A_H \to \tilde{A}_H(t)). \tag{5.12}$$

The time dependencies of the CP-averaged angular coefficients are given by

$$\begin{aligned} J_i(t) + \tilde{J}_i(t) &= e^{-\Gamma t}\left[(J_i + \tilde{J}_i)\cosh(y\Gamma t) - h_i \sinh(y\Gamma t)\right], \\ J_i(t) - \tilde{J}_i(t) &= e^{-\Gamma t}\left[(J_i - \tilde{J}_i)\cosh(x\Gamma t) - s_i \sinh(x\Gamma t)\right], \end{aligned} \tag{5.13}$$

where $x = \Delta m/\Gamma$ and $y = \Delta\Gamma/2\Gamma$. $\Delta\Gamma = \Gamma_L - \Gamma_H$ and $\Delta m = M_H - M_L$ are the lifetime and mass differences between the mass eigenstates. For B_d^0 decays, the lifetime

TH-3118_176121005

Bin[GeV^2]	[0.1-1]	[1-2]	[2-4]	[4-6]
$\langle A_5 \rangle$	-0.0023(50)	0.0016(75)	0.0071(71)	0.0158(67)
$\langle A_{6s} \rangle$	0.0028(23)	0.0065(64)	0.00062(854)	-0.019(12)
$\langle A_8 \rangle$	0.0143(43)	0.0062(39)	0.0033(17)	0.00186(42)
$\langle A_9 \rangle$	0.000051(45)	0.000112(91)	0.000117(82)	0.000087(53)
$\langle P_1 \rangle$	0.0028(23)	0.0027(42)	-0.044(19)	-0.084(33)
$\langle P_4^{'} \rangle$	0.2044(41)	0.047(11)	-0.287(15)	-0.457(11)
$\langle P_6^{'} \rangle$	-0.114(26)	-0.163(36)	-0.165(39)	-0.157(42)
$\langle BR \rangle \times 10^9$	1.26(10)	0.613(51)	1.083(96)	1.19(10)
$\langle F_L \rangle$	0.278(26)	0.697(26)	0.786(19)	0.701(24)
$\langle R_\rho \rangle$	0.98245(39)	0.99660(29)	0.99652(34)	0.99694(25)

Table 5.8: Predictions of observables, in the SM, for $\bar{B}(B) \to \rho^0 \ell\ell$ decays measurable at LHCb and Belle.

difference is negligible. The detailed mathematical expression for the s_i and h_i are given in ref. [171]. The time-integrated CP-averaged rates and CP-asymmetries, as measured at hadronic machines and B-factories are defined in terms of the modified angular functions [171]

$$\left\langle J_i + \tilde{J}_i \right\rangle_{\text{LHCb}} = \frac{1}{\Gamma}\left[\frac{J_i + \tilde{J}_i}{1-y^2} - \frac{y}{1-y^2} \times h_i\right], \quad \left\langle J_i + \tilde{J}_i \right\rangle_{\text{Belle}} = \frac{2}{\Gamma}\left[\frac{J_i + \tilde{J}_i}{1-y^2}\right] \tag{5.14}$$

$$\left\langle J_i - \tilde{J}_i \right\rangle_{\text{LHCb}} = \frac{1}{\Gamma}\left[\frac{J_i - \tilde{J}_i}{1+x^2} - \frac{x}{1+x^2} \times s_i\right], \quad \left\langle J_i - \tilde{J}_i \right\rangle_{\text{Belle}} = \frac{2}{\Gamma}\left[\frac{J_i - \tilde{J}_i}{1+x^2}\right] \tag{5.15}$$

At Belle, the flavour of the decaying B^0 meson can be tagged and thus, the corresponding angular coefficients J_i or $\tilde{J}_i$ can be extracted. Whereas at LHCb, tagging is not possible for this decay chain. Hence from an untagged measurement of the differential decay rate, one extracts the CP averaged angular coefficients $(J_i + \tilde{J}_i)$ defined in eq. 1.36. Hence, at the LHCb, apart from the branching fraction and LFUV observable R_ρ, the following observables can be measured: $A_{5,6s,8,9}$, P_1, $P'_{4,6}$ and F_L. This set of observables can also be measured at Belle. In the limit $y \to 0$, which is true for the B^0 system, the measured values will be the same in both experiments except the branching fraction, for which the value measured by Belle will be twice that of the one measured by LHCb[5]. However, at Belle, apart from these observables a few additional observables, resulting from the time average $\left\langle J_i - \tilde{J}_i \right\rangle$, can be measured which are the following: A_{CP}, $A_{3,4,7}$, $P_{2,3}$, $P'_{5,8}$, and A_{FB}. The respective predictions in the SM for the observables measuarable at the LHCb and Belle are given in tables 5.8 and 5.9, respectively.

At Belle, tagging is possible. Hence it is possible to measure the observables defined in

[5]Note that for the time average, at the LHCb, the integration over time will be over the range $0 \leq t \leq \infty$ while that for Belle will be $-\infty \leq t \leq \infty$.

TH-3118_176121005

eqs. 1.34 and 1.35 for $B^0 \to \rho^0 \ell\ell$ and $\bar{B}^0 \to \rho^0 \ell\ell$ decays, for which we have presented the respective predictions in the SM in tables 5.10 and 5.11, respectively. Unlike the $B^\pm \to \rho^\pm \ell\ell$ decays, the SM predictions for the observables defined for B^0 and $\bar{B}^0$ decays are much consistent with each other. This is due to the fact that the hard-spectator contribution from the leading order WA diagrams ($\mathcal{T}_{||}^{(u),WA}$) are negligible for $B^0(\bar{B}^0) \to \rho^0 \ell\ell$ decays which plays a major role for the differences in the predictions for a few observables in B^+ and B^- decays. This could be the reason for A_4 in neutral B decays being two orders of magnitude suppressed relative to that in the $B^\pm$ decays.

Bin[GeV^2]	[0.1-1]	[1-2]	[2-4]	[4-6]
$\langle A_{CP} \rangle$	-0.034(12)	-0.0325(53)	-0.01670(88)	-0.0115(20)
$\langle A_3 \rangle$	0.0000012(195)	-0.000028(62)	0.000015(86)	0.00028(18)
$\langle A_4 \rangle$	-0.0075(18)	-0.0060(23)	-0.00048(206)	0.0040(21)
$\langle A_7 \rangle$	-0.0025(30)	-0.0024(26)	-0.00020(107)	-0.00015(55)
$\langle P_2 \rangle$	-0.0545(17)	-0.2238(64)	-0.101(15)	0.1617(83)
$\langle P_3 \rangle$	0.00021(13)	0.00148(95)	0.0031(18)	0.0032(18)
$\langle P_5' \rangle$	0.3365(43)	0.166(13)	-0.241(19)	-0.479(13)
$\langle P_8' \rangle$	-0.0205(69)	-0.036(10)	-0.040(10)	-0.039(10)
$\langle A_{FB} \rangle$	-0.0591(27)	-0.1017(95)	-0.0324(57)	0.0725(73)

Table 5.9: Predictions of observables, in the SM, for $\bar{B}(B) \to \rho^0 \ell\ell$ decays measurable only at Belle.

In the SM and in a few new physics scenarios, the respective q^2 variations of the observables listed in tables 5.8 and 5.9 are shown in fig. 5.4. We note that for the neutral B decays, the variations of CP-asymmetric observables with q^2 are less significant than the charged B decays, particularly in the observables A_{CP} and $A_{4,5,7,8}$. For the rest of the observables, the q^2 variations are almost similar to that observed for the charged B decays shown in fig. 5.2. Apart from A_{CP} and A_5, the NP sensitivities for the rest of the observables in the neutral B decays are almost identical to the respective observables in $B^\pm$ decays shown in table 5.6. For the neutral B decays, A_{CP} is sensitive to $Im(\Delta C_9)$ and $Re(\Delta C_{10})$ whereas A_5 is sensitive only to $Im(\Delta C_{10})$, the NP sensitivities of the rest of the observables can be seen from table 5.6. Like the B^+ and B^- decays, here also we see that the observables $P^0_{2,3}(\bar{P}^0_{2,3})$ and $P'^0_{6,8}(\bar{P}'^0_{6,8})$ have different NP sensitivities. We can see from fig. 5.5 that in the specific NP scenarios, significant deviations in the predictions of $P'^0_{6,8}$ and $\bar{P}'^0_{6,8}$ are possible, which are lost due to relative cancellations in the CP-averaged observables $P'_{6,8}$ shown in figs. 5.4n and 5.4o, respectively. Thus, along with the observables obtained from the CP-averaged distribution, whenever tagging is possible, the measurement of the tagged observables is equally important in the context of NP searches.

In tables C.19, C.20, C.21, C.22, C.23, C.24, C.25, C.26, C.27 and C.28, we provide

TH-3118_176121005

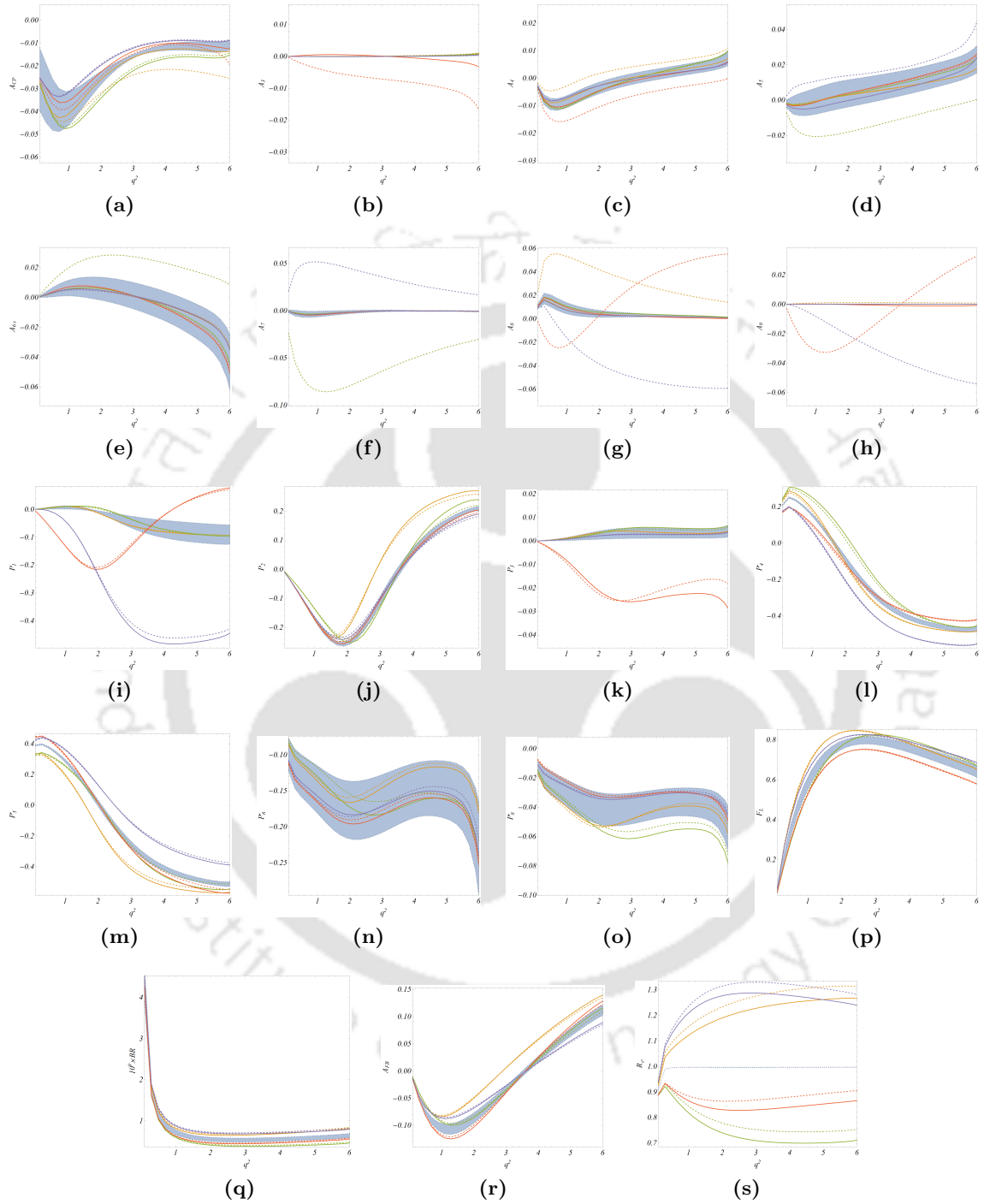

Figure 5.4: The q^2 dependence for the CP-averaged and CP-asymmetric observables in $B^0(\bar{B}^0) \to \rho^0 ll$ decays in the SM and in the NP scenarios. Among the listed obsevables $A_{5,6s,8,9}$, P_1, $P'_{4,6}$, F_L and Branching ratio are measurable at both the LHCb and Belle and the rest are measurable only at the Belle. The legends are similar to the one used in fig. 5.2.

TH-3118_176121005

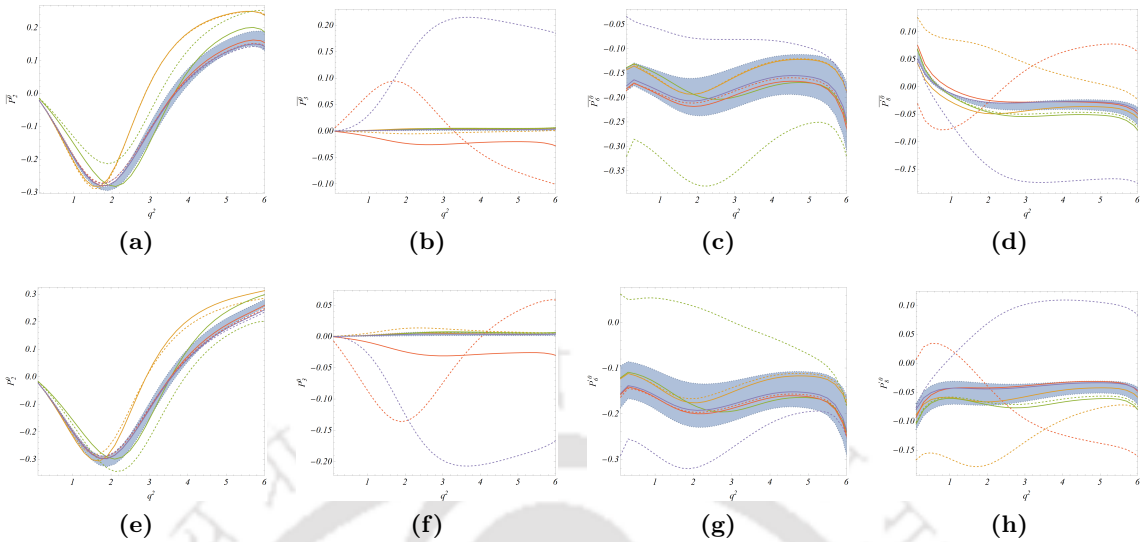

Figure 5.5: The q^2 dependence for the $P_2^0(\bar{P}_2^0)$, $P_3^0(\bar{P}_3^0)$, $P_6'^0(\bar{P}_6'^0)$, $P_8'^0(\bar{P}_8'^0)$ associated with $\bar{B}(B) \to \rho^0 ll$ decays measurable only at the Belle.

the predictions in the NP scenarios for the observables associated with the neutral modes. Also, as discussed in the case of the charged B decays, for the B^0 and $\bar{B}^0$ decays we have given the predictions in the NP scenarios for the tagged observables $P_{2,3}^0(\bar{P}_{2,3}^0)$, $P_{6,8}'^0(\bar{P}_{6,8}'^0)$ in tables C.15, C.16, C.17 & C.18. All these predictions can be tested in future measurements.

5.5 Summary

In this chapter, we have analysed the decay modes $B \to \pi(\rho)\ell\nu_\ell$ and $B \to \pi(\rho)\ell^+\ell^-$ using all the available experimental inputs on the branching fractions, and the lattice and LCSR inputs on the form factors. We extract the form factor coefficients and the CKM element $|V_{ub}|$ using all these inputs and the available correlations between them. Using this fit result for $B \to \pi\ell\ell$ decays, we have predicted CP and isospin-asymmetries along with the respective branching fractions. Also, we have predicted LFU ratios like $R_\pi^{-/0}$. We have checked the q^2 distributions of all these observables and predicted the values, along with the respective errors, in a few q^2-bins. From the angular distribution of $B^{\pm(0)} \to \rho^{\pm(0)}\ell\ell$ decays we have obtained the CP-averaged and CP-asymmetric observables along with the respective branching fractions and $R_\rho^{\pm,0}$. Here also we have predicted all these observables in the SM in a few q^2-bins using the fit results for the form factors.

For the charged B decays, the observables are predicted for both the B^+ and B^- decays following the tagging method, which can be measured both at the LHCb and Belle. Also, we have predicted the associated untagged observables. On the contrary, for the neutral B decays, tagging is possible only at Belle but not at LHCb. Hence, there are observables measurable both at Belle and LHCb and a few observables measurable only at Belle. We

TH-3118_176121005

Bin[GeV^2]	[0.1-1]	[1-2]	[2-4]	[4-6]
$\langle P_1^0 \rangle$	0.0039(32)	0.0034(51)	-0.048(21)	-0.087(34)
$\langle P_2^0 \rangle$	-0.0787(33)	-0.267(14)	-0.112(30)	0.197(19)
$\langle P_3^0 \rangle$	0.00040(29)	0.0021(15)	0.0040(23)	0.0036(20)
$\langle P_4'^0 \rangle$	0.2544(67)	0.063(13)	-0.296(16)	-0.468(10)
$\langle P_5'^0 \rangle$	0.393(11)	0.171(20)	-0.267(25)	-0.516(17)
$\langle P_6'^0 \rangle$	-0.125(38)	-0.166(45)	-0.170(42)	-0.157(41)
$\langle P_8'^0 \rangle$	-0.061(20)	-0.052(20)	-0.050(15)	-0.043(11)
$\langle BR^0 \rangle \times 10^9$	2.60(21)	1.27(10)	2.20(19)	2.41(20)
$\langle A_{FB}^0 \rangle$	-0.0592(32)	-0.103(11)	-0.0323(92)	0.086(12)
$\langle F_L^0 \rangle$	0.283(25)	0.698(25)	0.788(18)	0.699(24)
$\langle R_\rho^0 \rangle$	0.98257(39)	0.99670(29)	0.99657(33)	0.99697(25)

Table 5.10: Predictions of observables, in the SM, for $B^0 \to \rho^0 \ell\ell$ decays, which are measurable at Belle.

Bin[GeV^2]	[0.1-1]	[1-2]	[2-4]	[4-6]
$\langle \bar{P}_1^0 \rangle$	0.0041(33)	0.0031(49)	-0.048(21)	-0.086(34)
$\langle \bar{P}_2^0 \rangle$	-0.0770(22)	-0.2559(41)	-0.110(22)	0.137(21)
$\langle \bar{P}_3^0 \rangle$	0.00021(12)	0.00132(81)	0.0028(16)	0.0031(17)
$\langle \bar{P}_4'^0 \rangle$	0.2334(35)	0.037(12)	-0.306(17)	-0.463(13)
$\langle \bar{P}_5'^0 \rangle$	0.412(10)	0.189(22)	-0.238(29)	-0.459(21)
$\langle \bar{P}_6'^0 \rangle$	-0.148(23)	-0.187(33)	-0.176(40)	-0.163(45)
$\langle \bar{P}_8'^0 \rangle$	0.0143(41)	-0.0252(25)	-0.0345(69)	-0.036(10)
$\langle \bar{BR}^0 \rangle \times 10^9$	2.43(21)	1.19(10)	2.13(19)	2.35(20)
$\langle \bar{A}_{FB}^0 \rangle$	-0.0589(25)	-0.1001(98)	-0.0324(79)	0.059(10)
$\langle \bar{F}_L^0 \rangle$	0.273(26)	0.696(27)	0.784(19)	0.703(24)
$\langle \bar{R}_\rho^0 \rangle$	0.98232(39)	0.99650(32)	0.99646(35)	0.99690(25)

Table 5.11: Predictions of observables, in the SM, for $\bar{B}^0 \to \rho^0 \ell\ell$ decays measurable at Belle.

separate and predict them in the SM in a few q^2-bins.

For all these observables, we have checked the sensitivities towards some NP contributions from a few additional operators beyond the SM. To look for deviations, we have studied the individual q^2 variations of all these observables in the different NP scenarios and compared them with the respective distributions in the SM. Many observables are sensitive to the NP contributions we have considered, and one can distinguish the effects from the respective SM predictions. From a comparative study of the respective NP sensitivities, one can identify the effect of a particular type of scenario from the rest. Therefore, if we observe deviations in the measured values from the respective SM predictions, it will be possible to identify the type of NP scenario from the pattern of the results. Moreover, we have noted that a few observables defined from a tagged analysis

TH-3118_176121005

are sensitive to some NP scenarios and the respective sensitivities are lost due to a relative cancellation while defining the related CP-averaged observables, which could be obtained from the untagged decay distribution. In the context of NP searches, the measurement of the tagged observables is equally important as the related CP-averaged observables.

TH-3118_176121005

Chapter 6

Constraining the ratio $|V_{ub}|/|V_{cb}|$ from exclusive decays.

6.1 Introduction

In this chapter[1], with the objective of determining the least precisely measured ratio $|V_{ub}|/|V_{cb}|$, as discussed in section 1.5, we simultaneously analysis the mesonic $b \to cl\nu$ and $b \to ul\nu$ modes for a combined extraction of $|V_{cb}|^{exc}$ and $|V_{ub}|^{exc}$ respectively. In chapter 4, we have analysed the $B \to \pi l\nu$ decay mode for the exclusive determination of $|V_{ub}|$ and found that our best results are consistent with the one extracted from the inclusive $B \to X_u \ell \nu_\ell$ decays from Belle [1] within 1 σ confidence interval. Apart from $B \to \pi l\nu$ decay modes, the decay rates for $B \to \rho(\omega) l\nu$ modes also depend on the CKM matrix element $|V_{ub}|$ and should be considered for a combined extraction of exclusive $|V_{ub}|$. In PDG [72], averages are given based on $B \to D^{(*)} l\nu$ decays for $|V_{cb}|^{exc.}$ and $B \to \pi l\nu$ decays for $|V_{ub}|^{exc.}$ (the values are given in eqs 1.39 and 1.40). The $B_s \to D_s^{(*)} l\nu$ modes also probe $|V_{cb}|$ and are utilised for the determination of exclusive $|V_{cb}|$ in this chapter.

In section 6.2, we discuss the theory relevant to the various decay modes considered in this chapter. In section 6.3, we mention about the available data in the respective channels along with the Lattice and LCSR inputs. As an initial step, we determine the ratio independently from the $b \to cl\nu$ and $b \to ul\nu$ modes. Next, we incorporate the measurements on the ratio $\text{BR}(B_s \to K\mu\nu)/\text{BR}(B_s \to D_s\mu\nu)$ in the two q^2-bins, given in eq 1.43 to understand the role of these inputs on the ratio $|V_{ub}|/|V_{cb}|$, the results are presented in section 6.4. Finally, we summarize the results obtained in this chapter in section 6.5.

[1]The main results of this chapter have been taken from a work in progress with A. Biswas and S. Nandi which will be arXived soon.

TH-3118_176121005

6.2 Theory

6.2.1 B decays to pseudoscalar mesons

In this analysis, we consider $B(B_s) \to \pi(K)l\nu$ ($B(B_s) \to D(D_s)l\nu$) decays corresponding to $b \to u(c)$ transitions. The differential decay rate for B-decays to pseudoscalar mesons are function of the form factors $f_{+,0}(q^2)$, as given in eq. 1.22. We parameterize the form factors corresponding to $B(B_s) \to \pi(K)l\nu$ and $B(B_s) \to D(D_s)l\nu$ transitions according to BSZ (eq. 2.24) and BGL (eq. 2.29) parametrizations respectively.

We provide the values of the constants in table 2.4 and pole masses used in $B \to D^{(*)}$ and $B_s \to D_s^{(*)}$ channels in tables 2.2 and 2.3 respectively. The outer functions are expressed as in eq. 2.33.

6.2.2 B decays to vector mesons

6.2.2.1 $B \to \rho(\omega)l\nu$ transitions

For these decays, the experimental measurements are given on the partial branching fractions in bins of dilepton invariant mass squared q^2, the differential decay distribution is function of the form factors $V(q^2)$, $A_0(q^2)$, $A_1(q^2)$ and $A_2(q^2)$ as seen from eqs. 1.23,1.24. We follow the BSZ parametrization given in eq. 2.24 to parameterize the respective form factors.

6.2.2.2 $B(B_s) \to D^*(D_s^*)l\nu$ transitions

For $B \to D^*l\nu$ decays, the experimental measurements are provided for the differential distributions in the variables w, $\cos\theta_l$, $\cos\theta_v$ and χ in 10 bins [70]. The expression for the four-fold distribution is obtained from [172, 173]. We follow the BGL basis of form factors (f, g, F_1, F_2) for these decay modes which are expanded as given in eq. 2.29, with the values of the pole masses given in tables 2.2 and 2.3 and outer functions given in eq. 2.34.

6.3 Inputs

For $B \to \pi l\nu$ decay modes, the experimental data, Lattice and LCSR inputs considered in this analysis are same as those used in chapter 5. For $B \to \rho l\nu$ modes, all the inputs are same as chapter 5 except for an additional LCSR input [5]. For $B \to \omega l\nu$ transitions, the experimental inputs correspond to the measurements on the partial branching fractions in bins of q^2 from BaBar and Belle collaborations [75–77, 174]. No lattice estimates exist till date on the $B \to \rho(\omega)$ form factors. In ref [5], the LCSR datapoints for the form factors are provided at $q^2 = 0$, whereas in ref. [4], the fit-results for the coefficients of the

TH-3118_176121005

z-expansion are given using which we generate correlated synthetic data-points for the form factors A_1, A_2 and V at q^2 = 0,4,8 GeV^2 and for A_0 at q^2 = 4,8 GeV^2 [2].

The form factor inputs corresponding to $B_s \to K^-$ transitions are available from Lattice QCD collaborations, namely Fermilab-MILC [175] and RBC/UKQCD [130]. Also the authors of ref. [176] have provided the value of the form factor f_+ only at $q^2 = 0$ following the LCSR approach. For $B_s \to D_s$ transitions, there are existing results from Lattice groups, namely Fermilab-MILC [177] and HPQCD [178] where the fit results of the respective form factor parameters are provided following BGL and BCL parametrizations respectively. We have generated correlated synthetic datapoints for the form factors f_+ and f_0 from the MILC analysis at w = 1, 1.08 and 1.16 and from the HPQCD analysis at w = 1, 1.06 and 1.12. In ref. [179], the correlated form factor inputs are given for $B_s \to D_s^{(*)}$ modes using the Light-Cone sum rules with B_s meson distribution amplitude at q^2 = -15, -10, -5 and 0 GeV^2, which calls for a combined analysis of $B_s \to D_s^{(*)}\mu\nu$ transitions. For $B_s \to D_s^*$ modes, there is a lattice QCD calculation of the axial vector form factor at zero recoil [180]. In ref. [181], the values of the form factors A_0, A_1, A_2 and V are given for the first time at non-zero recoil, namely at w = 1, 1.04, 1.08 and 1.12. LHCb has recently provided a measurement of $|V_{cb}|$ using the $B_s \to D_s^{(*)}\mu\nu$ decay modes [182]. Using their fit results for the form factor parameters and other relevant inputs, we have created correlated synthetic datapoints for the partial branching fractions for $B_s \to D_s l\nu$ channel in 6 w-bins and for $B_s \to D_s^* l\nu$ channel in 5 w-bins.

In 2015, the Belle collaboration had analyzed the $B \to Dl\nu$ decay and provided measurements for the differential decay width in 10 w-bins for both the charged and neutral B decays with electrons and muons in the final state [71]. In 2018, it presented the results for the differential distributions in w, cosθ_l, cosθ_v and χ in 10 bins for the $B \to D^* l\nu$ decay mode [70]. In addition to these experimental results, we also consider the inputs for the hadronic form factors available from various sources. For the $B \to D$ form factors, we take lattice inputs from the Fermilab-MILC collaboration [183] and the HPQCD collaboration [184]. In [183], the form factors f_+ and f_0 are given at three values of the recoil variable w = 1, 1.08 and 1.16, whereas in [184], the fit results for the form factor parameters following BCL expansion are provided, using which we created synthetic data-points for f_+ and f_0 at w = 1, 1.06 and 1.12. The lattice inputs for the form factors of $B \to D^*$ mode are taken from the Fermilab-MILC collaboration [185] where the values of the form factors g, f, F_1 and F_2 are provided for the first time at non-zero values of the recoil, namely w = 1.03, 1.10 and 1.17 respectively. The authors of ref [2] have provided correlated form factors for $B \to D^{(*)}$ channel at q^2 = -15, -10, -5 and 0 GeV^2 following the LCSR approach.

[2] At $q^2 = 0$, A_0 is related to A_1 and A_2, thus it isn't independent. So, in order to keep the covariance matrix positive semi-definite, we don't include the datapoint for A_0 at $q^2 = 0$.

TH-3118_176121005

6.4 Results

For the various decay modes sensitive to $|V_{ub}|$ and $|V_{cb}|$, we study the impact of the form factor inputs from the available sources on the extraction of $|V_{ub}|^{exc.}$ and $|V_{cb}|^{exc.}$. For $B \to \pi l\nu$ modes, we consider the datapoints from each Lattice collaboration separately along with the experimental measurements with or without the inputs from LCSR analysis [3] which are relatively more precise as compared to the one obtained in ref [2] and thus play dominant role in the fits. The fit results are shown in table 6.1 where we also show the impact of the LCSR inputs on $|V_{ub}|$ extracted from $B \to \rho l\nu$ and $B \to \omega l\nu$ decay modes. Finally, we combine all the channels for an exclusive determination of $|V_{ub}|$. In table 6.2, we show $|V_{cb}|^{exc.}$ obtained from the various $b \to cl\nu$ transitions separately and also from a combined analysis. With the result $|V_{cb}| = (40.4 \pm 0.6) \times 10^{-3}$ from the combined analysis, we have calculated $|V_{ub}|/|V_{cb}|$ for all the inputs in table 6.1, as shown in the fifth column. From the combined $b \to u(c)l\nu$ modes, we obtain $|V_{ub}|/|V_{cb}| = 0.088 \pm 0.003$.

Mode	Inputs	p value (%)	$\|V_{ub}\| \times 10^3$	$\|V_{ub}\|/\|V_{cb}\|$
$B \to \pi l\nu$	Experiment+JLQCD [166]	11.7	3.93 ± 0.41	0.097 ± 0.010
	Experiment+JLQCD+LCSR [3]	20.6	3.65 ± 0.24	0.090 ± 0.006
	Experiment+MILC [186]	9.9	3.67 ± 0.14	0.091 ± 0.004
	Experiment+MILC+LCSR [3]	8.4	3.71 ± 0.13	0.092 ± 0.003
	Experiment+RBC/UKQCD [130]	10.3	3.60 ± 0.31	0.089 ± 0.008
	Experiment+RBC/UKQCD+LCSR [3]	18.3	3.43 ± 0.22	0.085 ± 0.006
	Experiment+ All Lattice [130, 166, 186]	0.18	3.62 ± 0.12	0.090 ± 0.003
	Experiment+ All Lattice+LCSR [2, 3]	2.8	3.62 ± 0.11	0.090 ± 0.003
$B \to \rho l\nu$	Experiment+LCSR [2]	36	3.66 ± 1.07	0.091 ± 0.027
	Experiment+LCSR [4]	6.4	3.08 ± 0.28	0.076 ± 0.007
	All combined [2, 4, 5]	86.7	3.22 ± 0.26	0.080 ± 0.007
$B \to \omega l\nu$	Experiment+LCSR [4, 5]	89.7	3.09 ± 0.33	0.076 ± 0.008
All modes	All inputs combined	22	3.55 ± 0.10	0.088 ± 0.003

Table 6.1: A comparative study of the impact of the form factor inputs for different channels on the extraction of $|V_{ub}|$.

Mode	Inputs	p value (%)	$\|V_{cb}\| \times 10^3$
$B \to Dl\nu$	Experiment+Lattice [183, 184]+LCSR [2]	90.2	41.0 ± 1.1
$B \to D^* l\nu$	Experiment+MILC [185] +LCSR [2]	13.7	38.9 ± 0.9
$B_s \to D_s^{(*)} l\nu$	Experiment+Lattice [178, 181] +LCSR [179]	99.9	41.9 ± 1.1
All modes	All inputs combined	76	40.4 ± 0.6

Table 6.2: A comparative study of the extraction of $|V_{cb}|$ in different channels.

TH-3118_176121005

Mode	Inputs	p value (%)	$\|V_{ub}\| \times 10^3$	$\|V_{cb}\| \times 10^3$	$\|V_{ub}\|/\|V_{cb}\|$
$B \to \pi l\nu$ and $b \to cl\nu$	Experiment+Lattice	1	3.56 ± 0.11	40.7 ± 0.6	0.088 ± 0.003
	Experiment+Lattice+ LCSR	1.6	3.50 ± 0.10	40.7 ± 0.6	0.086 ± 0.003
	Experiment+Lattice+ LCSR (without $f_+^{B_s\to K}$)	9.8	3.62 ± 0.10	40.3 ± 0.6	0.090 ± 0.003
$b \to c(u)l\nu$	Experiment+Lattice+ LCSR	10	3.45 ± 0.08	40.7 ± 0.6	0.085 ± 0.002
	Experiment+Lattice+ LCSR (without $f_+^{B_s\to K}$)	28.9	3.55 ± 0.09	40.4 ± 0.6	0.088 ± 0.002

Table 6.3: Extraction of the ratio $|V_{ub}|/|V_{cb}|$ from combined $b \to c(u)l\nu$ modes including the ratio $R_{BF} = \frac{\mathrm{BR}(B_s\to K\mu\nu)}{\mathrm{BR}(B_s\to D_s\mu\nu)}$ in the two bins [8].

Next, we incorporate the measurements on the ratio $\mathrm{BR}(B_s \to K\mu\nu)/\mathrm{BR}(B_s \to D_s\mu\nu)$ in the two bins in the combined fit to analyse the impact on $|V_{ub}|/|V_{cb}|$ ratio, the results are shown in table 6.3. We also separately study the effect of the inputs on the $B \to \pi l\nu$ modes along with the $b \to cl\nu$ modes (with or without the LCSR inputs on the form factors) on the ratio since it is the most promising channel in the extraction of $|V_{ub}|^{exc.}$, the results are shown in table 6.3. We find that the LCSR input on the form factor f_+ at $q^2 = 0$ in the $B_s \to K$ channel has influence on the extracted value of $|V_{ub}|$, dropping which we get an enhanced value of $|V_{ub}|$, as shown in the last row of table 6.3. We also study the effect of the branching fraction ratio in each bin separately on the extracted value of $|V_{ub}|/|V_{cb}|$, the results are shown in table 6.4. We have shown the plots for the form factors in the $B \to \pi(\rho,\omega)l\nu$ channels in figs. 6.1, 6.2 and 6.3 respectively. From fig 6.1, we find that the form factors obtained from the fit to only experimental data and Lattice inputs from JLQCD in the $B \to \pi\ell\nu$ channel have larger uncertainties which get subsequently reduced on including other Lattice and LCSR inputs. In figs 6.2 and 6.3, the form factor plots are shown for the $B \to \rho\ell\nu$ and $B \to \omega\ell\nu$ channels corresponding to analyses with the inputs in only $B \to \rho\ell\nu$ or $B \to \omega\ell\nu$ modes and from combined exclusive $b \to u\ell\nu$ modes.

6.5 Summary

In this chapter, [3] we have considered mesonic $b \to c(u)\ell\nu$ decay modes for eg. $B \to \pi(\rho,\omega)\ell\nu$ and $B(B_s) \to D^{(*)}(D_s^{(*)})\ell\nu$ with the available experimental data and inputs on the form factors for a combined extraction of $|V_{ub}|$ and $|V_{cb}|$. From these results, we have determined the ratio $|V_{ub}|/|V_{cb}|$ which is proportional to a side of the CKM unitarity

[3] The main results of this chapter have been taken from a work in progress with A. Biswas and S. Nandi and will be arXived very soon.

TH-3118_176121005

Mode	Inputs	p value (%)	$\|V_{ub}\| \times 10^3$	$\|V_{cb}\| \times 10^3$	$\|V_{ub}\|/\|V_{cb}\|$
$b \to c(u)l\nu$ + $R_{\rm BF}^{\rm Low}$	Experiment+Lattice+ LCSR	9.9	3.44 ± 0.09	40.6 ± 0.6	0.085 ± 0.002
	Experiment+Lattice+ LCSR (without $f_+^{B_s\to K}$)	28.8	3.56 ± 0.10	40.3 ± 0.6	0.088 ± 0.003
$b \to c(u)l\nu$ + $R_{\rm BF}^{\rm High}$	Experiment+Lattice+ LCSR	13	3.48 ± 0.09	40.5 ± 0.6	0.086 ± 0.002
	Experiment+Lattice+ LCSR (without $f_+^{B_s\to K}$)	33.6	3.56 ± 0.09	40.3 ± 0.6	0.088 ± 0.003

Table 6.4: Extraction of the ratio $|V_{ub}|/|V_{cb}|$ from combined $b \to c(u)l\nu$ modes along with the ratio $R_{BF} = \frac{\mathrm{BR}(B_s\to K\mu\nu)}{\mathrm{BR}(B_s\to D_s\mu\nu)}$ in either low or high bin [8].

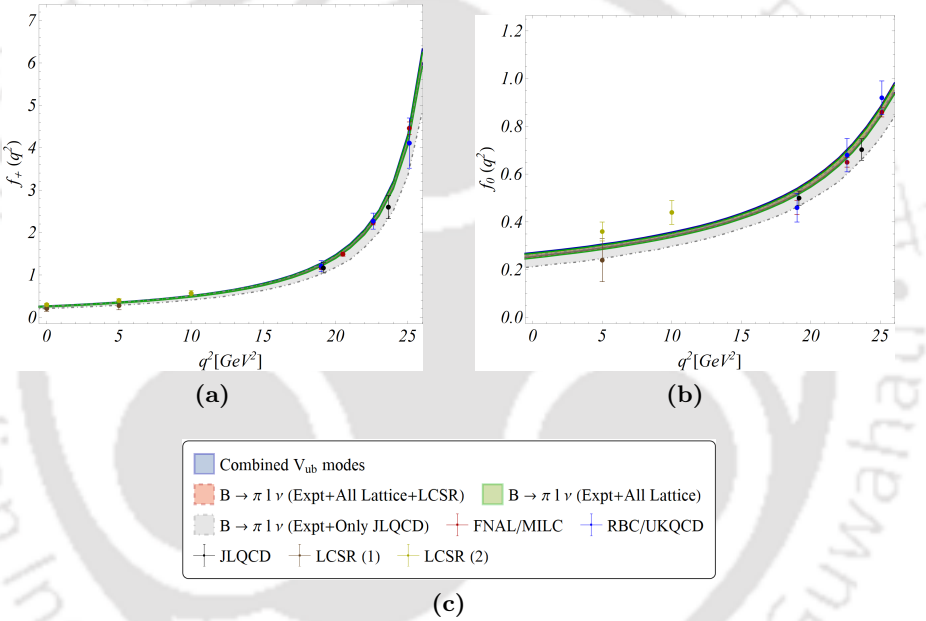

Figure 6.1: The q^2 distributions of the form factors f_+ and f_0 for $B \to \pi l\nu$ modes. The lattice and LCSR datapoints are also shown in the plots. The labels "LCSR(1)" and "LCSR(2)" refer to the inputs from LCSR [2] and [3] respectively.

triangle. There has been a recent measurement of the ratio $\frac{\mathrm{BR}(B_s\to K\mu\nu)}{\mathrm{BR}(B_s\to D_s\mu\nu)} \propto \frac{|V_{ub}|^2}{|V_{cb}|^2}$ from LHCb in two bins of $B_s \to K$ momentum transfer. As an initial step, we determine the ratio independently from $b \to c(u)\ell\nu$ modes, also separately studying the effect of the various form factor inputs for different channels on the extracted values of $|V_{ub}|$ and $|V_{cb}|$. Then we incorporate the measurements on the branching fraction ratios in the two bins separately and also simultaneously to see the impact on the $|V_{ub}|/|V_{cb}|$ ratio. We find that the LCSR input on f_+ at $q^2 = 0$ in the $B_s \to K$ channel influences the measurement of $|V_{ub}|/|V_{cb}|$. Our value for $|V_{ub}|/|V_{cb}|$ is consistent with the determination from the ratio of partial rates of baryonic decays $\mathrm{BR}(\Lambda_b \to p\mu\nu)/\mathrm{BR}(\Lambda_b \to \Lambda_c\mu\nu)$ measured by LHCb.

TH-3118_176121005

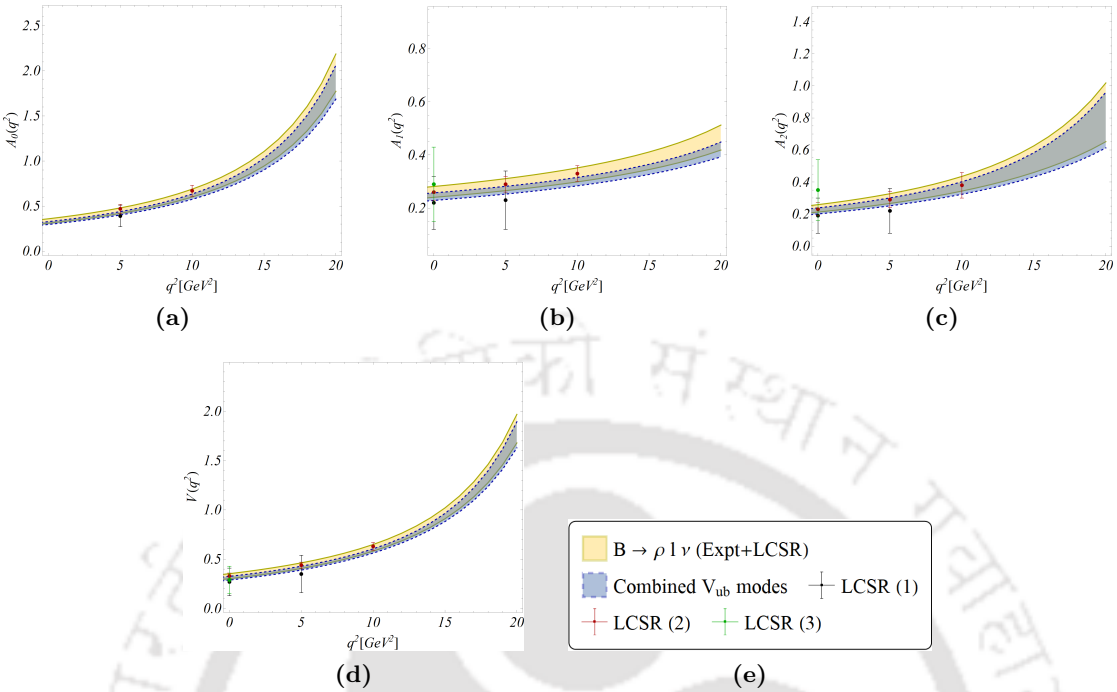

Figure 6.2: The q^2 distributions of the form factors A_0, A_1, A_2 and V for $B \to \rho l\nu$ modes. The LCSR datapoints are also shown in the plots. The labels "LCSR(1)", "LCSR(2)" and "LCSR(3)" refer to the inputs from LCSR [2], [4] and [5] respectively.

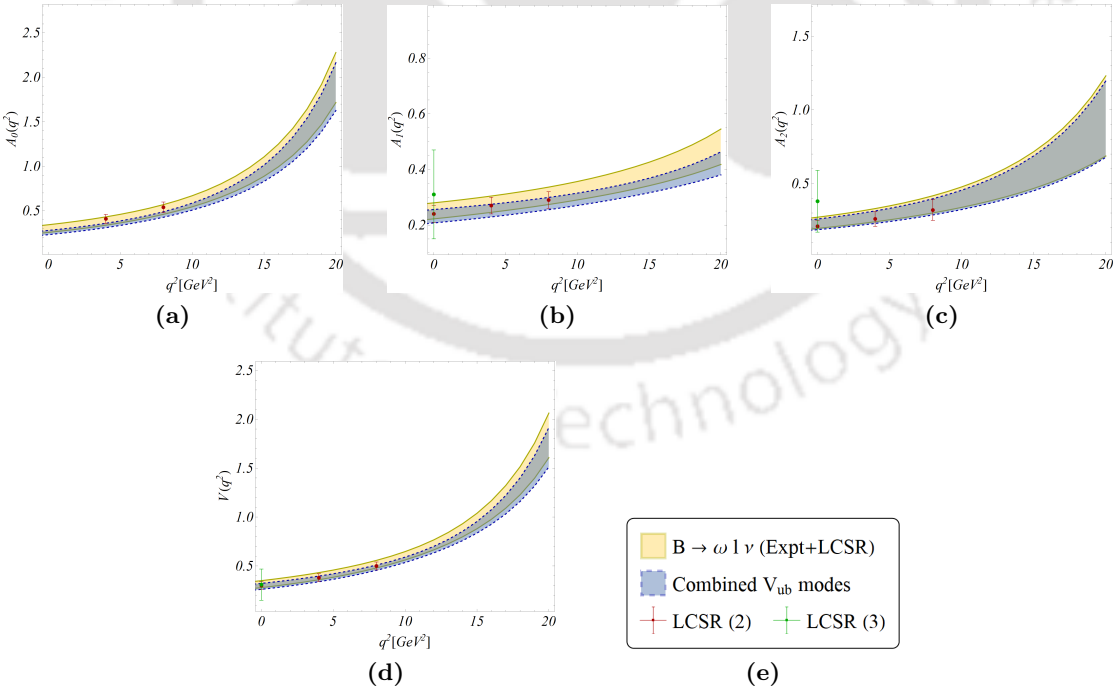

Figure 6.3: The q^2 distributions of the form factors A_0, A_1, A_2 and V for $B \to \omega l\nu$ modes. The LCSR datapoints are also shown in the plots. The labels "LCSR(2)" and "LCSR(3)" refer to the inputs from LCSR [4] and [5] respectively.

TH-3118_176121005

Chapter 7

Summary and outlook

In this thesis, we have studied the semileptonic decays of B mesons including the flavor changing charged and neutral current transitions and the related phenomenology. With the absence of any direct detection of new particles at the colliders so far, the precision measurements of several observables in the flavor sector play very crucial role to analyze the possible signatures of new physics through the comparison with their respective predictions in the SM. Over the last few years, some anomalous results have been observed in the B meson decays in the low energy experiments. The observables $R_{K^{(*)}}$ defined to test Lepton Flavor Universality and a few angular observables (for eg. P_5') have shown deviations from their respective SM predictions. The source of this discrepancy could be the poorly understood hadronic effects in the SM or the presence of new interactions beyond the SM. We have considered the possibility of new physics effects in the neutral current sector in this thesis. Incorporating the available measurements from various experimental collaborations in the $b \to s\ell\ell$ channel and following a model-independent effective field theory framework with dimension six operators with complex WCs, we have checked whether each of the one-operator scenarios can provide plausible explanations to the observed anomalies. It has been found that the operator $\mathcal{O}_9$ in both the cases with real and complex WCs turns out to be the only one-operator scenario compatible with the present data. More precise data in the future might prefer more complex multi-operator scenarios or models. Also, in general, in a new physics model, besides the one-operator scenarios, some multi-operator scenarios may also influence the transitions under study. Thus, with the aim to look for various possible combinations of the operators that can accommodate the available data in this channel, we have adopted the model selection procedures like Akaike Information Criterion and Cross-Validation. It has been observed that apart from the one-operator scenario $\mathcal{O}_9$ with complex WC, some two, three and four operator scenarios are also selected in this analysis, with the operator $\mathcal{O}_9$ common among them. For the selected scenarios, we have provided predictions for $R_K^{(*)}$ and P_5' in the specific bins and compared them with the corresponding measurements. Our best model can accommodate all the observed data on $R_K^{(*)}$ and P_5' at 1-σ CL, except the $R_{K^*}^{low}(LHCb)$ which is difficult to be explained by any

TH-3118_176121005

of the selected models at 1-σ CL. This is because at low-q^2, the $B \to K^*\ell\ell$ decay rates are dominated by $1/q^2$ enhanced photon contributions and a NP contact interaction that explains R_K and $R_{K^*}^{Cen}$ affects $R_{K^*}^{Low}$ typically by at most 10%. Also, some analyses in the literature have addressed the possibility of explaining $R_{K^*}^{Low}$ with tensor operators which we have not considered in this thesis.

We have also explored the exclusive $b \to d\ell\ell$ ($B \to \pi\ell\ell$ and $B \to \rho\ell\ell$) transitions, which similar to the $b \to s\ell\ell$ modes are loop-suppressed in the SM, but unlike $b \to s\ell\ell$ sector have a non-vanishing direct CP- asymmetry. The parts of the exclusive $b \to d\ell\ell$ decay amplitudes proportional to $\lambda_u = V_{ub}V_{ud}^*$ and $\lambda_t = V_{tb}V_{td}^*$ have the same order of Cabibbo suppression and have different strong phases, in addition to a relative CKM phase. The form factors arising in $B \to \pi ll$ ($B \to \rho ll$) and $B \to \pi l\nu_l$ ($B \to \rho l\nu_l$) decays are correlated in the analyses of Fermilab-MILC and LCSR. An interesting fact is that both the decay rates $\Gamma(B \to \pi\ell\nu_\ell)$ and $\Gamma(B \to \rho\ell\nu_\ell)$ are proportional to $|V_{ub}|^2$ which is the only common link between the $B \to \pi$ and $B \to \rho$ decay channels we have considered in this thesis. From a combined analysis of all the available experimental data in $B \to \pi\ell\nu$, $B \to \rho\ell\nu$ and $B \to \pi\ell\ell$ channels and the most up-to-date Lattice and LCSR inputs on the form-factors, we have simultaneously extracted $|V_{ub}|$ along with the form-factor parameters. Using these extracted values, we have provided predictions for various observables in $B \to \pi(\rho)\ell\ell$ channels corresponding to both charged and neutral B-meson decays which can be verified at LHCb and Belle. We have separately studied observables obtained from the tagged and CP-averaged decay distributions. For B meson decays to CP eigenstates such as $B^0 \to \rho^0\ell\ell$, the same final state can arise from both B and $\bar{B}$ decays. The interference between $B^0 - \bar{B}^0$ oscillations and mixing results in time-dependent amplitudes. Tagging isn't possible at LHCb for such modes, thus observables obtained only from CP-averaged distribution can be measured, whereas at Belle, also observables obtained from tagged analyses as well as from CP-asymmetric distribution can be measured. We have found that the CP- asymmetric observables for $b \to d\ell\ell$ modes gain sizeable contributions in the SM. We have also studied the new physics effects in these decay modes as these channels are more sensitive to the BSM contributions due to their low branching ratios in the SM. It has been observed that different observables are sensitive to different NP scenarios differently, thus if deviations are observed in the future measurements from their respective SM predictions, the pattern of the results will signify the presence of the particular type of NP scenario. It has also been noted that a few observables obtained from a tagged analysis are sensitive to some NP scenarios and the respective sensitivities are lost due to a relative cancellation while defining the related observables, which could be obtained from the untagged decay distribution. Thus, in the context of NP searches, the measurement of the tagged observables is equally important as these related CP-averaged observables.

The precise estimate of the ratio $|V_{ub}|/|V_{cb}|$ is of utmost importance since it plays

TH-3118_176121005

an essential role in the determination of the sides of the Unitarity Triangle. It can be measured directly or indirectly from the extraction of $|V_{ub}|$ and $|V_{cb}|$ from the respective exclusive and inclusive $b \to u\ell\nu_\ell$ and $b \to c\ell\nu_\ell$ decays. For a long time, there exists a tension between the exclusive and inclusive determinations from semileptonic B-meson decays for both $|V_{ub}|$ and $|V_{cb}|$. It is hard to accommodate this discrepancy in a new physics scenario. We have relooked into the exclusive $B \to \pi\ell\nu$ modes for the extraction of $|V_{ub}|$. So far, the method utilised by HFLAV for the extraction of $|V_{ub}|^{exc.}$ from $B \to \pi\ell\nu$ transitions invloves a two-stage procedure. In the first stage, incorporating the experimental measurements, they determine the average partial branching fraction in each q^2 interval from a binned maximum-likelihood fit with p-value ~ 6 % which is considered to be of marginal significance. In the second stage, they use these average q^2 spectrum along with the Lattice and LCSR (at $q^2 = 0$) inputs to extract $|V_{ub}|$ (p-value ~ 47 %). We have reanalysed the $B \to \pi\ell\nu$ modes simultaneously with the available experimental data and newly available form factor inputs from Lattice and LCSR, while commenting on the effect of outliers on the fits. We have mentioned a few scenarios in the extraction of $|V_{ub}|^{exc}$ and found that the BaBar 2011 dataset impacts the extracted value of $|V_{ub}|$. Without including these datapoints in our analysis results in a value for $|V_{ub}|^{exc}$ which is consistent with the recent inclusive measurement from Belle within 1σ. We have also considered other exclusive $b \to u\ell\nu$ channels for eg. $B \to \rho(\omega)\ell\nu$ and the exclusive $b \to c\ell\nu$ channels for eg. $B(B_s) \to D^{(*)}(D_s^{(*)})\ell\nu$ for the extractions of $|V_{ub}|$ and $|V_{cb}|$, respectively. There has been a recent measurement of the ratio $\frac{\mathrm{BR}(B_s \to K\mu\nu)}{\mathrm{BR}(B_s \to D_s\mu\nu)} \propto \frac{|V_{ub}|^2}{|V_{cb}|^2}$ from LHCb in two bins of $B_s \to K$ momentum transfer. Initially, we have determined the ratio independently from $b \to c(u)\ell\nu$ mesonic modes, also separately analyzing the impact of the form factor inputs from Lattice QCD and LCSR computations for different channels on the extracted values of $|V_{ub}|$ and $|V_{cb}|$. Then we have introduced the measurements on the branching fraction ratios in the two bins separately and also simultaneously to study the effect on the $|V_{ub}|/|V_{cb}|$ ratio. Our result for $|V_{ub}|/|V_{cb}|$ is consistent with that obtained from the measurement of the ratio of partial rates of baryonic decays from LHCb.

In this thesis, we have addressed some important issues related to flavor physics and basic aspects of the Standard Model. Due to the lack of significant observation of new particles at the colliders so far, it is interesting to look for complementary hints of new physics signals from low energy experiments. The precision of measurements of rare B-decays have also improved significantly over the past few years with several hints towards the presence of physics beyond the SM. In the coming years, the improvement in precision of the theoretical calculations and experimental measurements in various channels will provide solid proofs for the presence of physics beyond the SM and may also help pinpoint a particular type of NP scenario. The results from the upcoming Belle II upgrade and future colliders will pave the way for an exciting future in the area of flavor physics that will help the high energy physics community in better understanding of the SM and also

TH-3118_176121005

in the search for new physics.

TH-3118_176121005

Appendix A

The transversity amplitudes and angular coefficients corresponding to $B(B_s) \to V(V = K^*, \rho(\phi))\ell\ell$ decays:

Here, we provide the explicit form of the eight transversity amplitudes (up to corrections of $O(\alpha_s)$ for B meson decays to vector mesons in the final state [126].

$$
\begin{aligned}
A_{\perp L,R} &= N\sqrt{2}\lambda^{1/2}\Bigg[\Big[(C_9^{eff}+C_9^{eff\prime})\mp(C_{10}^{eff}+C_{10}^{eff\prime})\Big]\frac{V(q^2)}{m_B+m_V}+\frac{2m_b}{q^2}(C_7^{eff}+C_7^{eff\prime})T_1(q^2)\Bigg],\\
A_{\|L,R} &= -N\sqrt{2}(m_B^2-m_V^2)\Bigg[\Big[(C_9^{eff}-C_9^{eff\prime})\mp(C_{10}^{eff}-C_{10}^{eff\prime})\Big]\frac{A_1(q^2)}{m_B-m_V}\\
&\quad+\frac{2m_b}{q^2}(C_7^{eff}-C_7^{eff\prime})T_2(q^2)\Bigg],\\
A_{0L,R} &= -\frac{N}{2m_V\sqrt{q^2}}\Bigg\{\Big[(C_9^{eff}-C_9^{eff\prime})\mp(C_{10}^{eff}-C_{10}^{eff\prime})\Big],\\
&\quad\times\Bigg[(m_B^2-m_V^2-q^2)(m_B+m_V)A_1(q^2)-\lambda\frac{A_2(q^2)}{m_B+m_V}\Bigg]\\
&\quad+2m_b(C_7^{eff}-C_7^{eff\prime})\Bigg[(m_B^2+3m_V^2-q^2)T_2(q^2)-\frac{\lambda}{m_B^2-m_V^2}T_3(q^2)\Bigg]\Bigg\},\\
A_t &= \frac{N}{\sqrt{q^2}}\lambda^{1/2}\left[2(C_{10}^{eff}-C_{10}^{eff\prime})+\frac{q^2}{m_\mu}(C_P-C_P^\prime)\right]A_0(q^2),\\
A_S &= -2N\lambda^{1/2}(C_S-C_S^\prime)A_0(q^2)
\end{aligned}
\tag{A.1}
$$

where

$$
N = V_{tb}V_{tp}^*\left[\frac{G_F^2\alpha^2}{3\cdot 2^{10}\pi^5 m_B^3}q^2\lambda^{1/2}\beta_\mu\right]^{1/2}, \tag{A.2}
$$

$p = s, d$ quarks.

TH-3118_176121005

$$\lambda = M_B^4 + M_V^4 + q^4 - 2(M_B^2 M_V^2 + M_B^2 q^2 + M_V^2 q^2), \qquad \beta_\mu = \sqrt{1 - 4\frac{m_\mu^2}{q^2}}, \tag{A.3}$$

With the eight transversity amplitudes defined above, the angular coefficients J_i in eq. 1.30 can be written as

$$\begin{aligned}
J_1^s &= \frac{(2+\beta_\mu^2)}{4}\left[|A_\perp^L|^2 + |A_\parallel^L|^2 + (L \to R)\right] + \frac{4m_\mu^2}{q^2} Re\left(A_\perp^L A_\perp^{R*} + A_\parallel^L A_\parallel^{R*}\right), \\
J_1^c &= |A_0^L|^2 + |A_0^R|^2 + \frac{4m_\mu^2}{q^2}\left[|A_t|^2 + 2Re(A_0^L A_0^{R*})\right] + \beta_\mu^2 |A_S|^2, \\
J_2^s &= \frac{\beta_\mu^2}{4}\left[|A_\perp^L|^2 + |A_\parallel^L|^2 + (L \to R)\right], \\
J_2^c &= -\beta_\mu^2\left[|A_0^L|^2 + (L \to R)\right], \\
J_3 &= \frac{1}{2}\beta_\mu^2\left[|A_\perp^L|^2 - |A_\parallel^L|^2 + (L \to R)\right], \\
J_4 &= \frac{1}{\sqrt{2}}\beta_\mu^2\left[Re(A_0^L A_\parallel^{L*}) + (L \to R)\right], \\
J_5 &= \sqrt{2}\beta_\mu\left[Re(A_0^L A_\perp^{L*}) - (L \to R) - \frac{m_\mu}{\sqrt{q^2}} Re(A_\parallel^L A_S^* + A_\parallel^R A_S^*)\right], \\
J_6^s &= 2\beta_\mu\left[Re(A_\parallel^L A_\perp^{L*}) - (L \to R)\right], \\
J_6^c &= 4\beta_\mu \frac{m_\mu}{\sqrt{q^2}} Re\left[A_0^L A_S^* + (L \to R)\right], \\
J_7 &= \sqrt{2}\beta_\mu\left[Im(A_0^L A_\parallel^{L*}) - (L \to R) + \frac{m_\mu}{\sqrt{q^2}} Im(A_\perp^L A_S^* + A_\perp^R A_S^*)\right], \\
J_8 &= \frac{1}{\sqrt{2}}\beta_\mu^2\left[Im(A_0^L A_\perp^{L*}) + (L \to R)\right], \\
J_9 &= \beta_\mu^2\left[Im(A_\parallel^{L*} A_\perp^L) + (L \to R)\right].
\end{aligned} \tag{A.4}$$

TH-3118_176121005

Appendix B

The matrix element and coefficients relevant to $B \to P(P = K, \pi)\ell\ell$ decays:

The matrix element for B-meson decays to pseudoscalar mesons can be written as [91]

$$\mathcal{M} = i\frac{G_F \alpha_e}{\sqrt{2}\pi} V_{tb} V_{tp}^* \, \xi_P(q^2) \Big(F_V \, p_B^\mu \, [\bar{l}\gamma_\mu l] + F_A \, p_B^\mu \, [\bar{l}\gamma_\mu\gamma_5 l] + (F_S + \cos\theta F_T)\,[\bar{l}l] + (F_P + \cos\theta F_{T5})\,[\bar{l}\gamma_5 l] \Big) \tag{B.1}$$

The functions $F_i \equiv F_i(q^2)$, $i = S, P, A, V, T, T5$ are given as

$$F_A = C_{10}, \qquad F_T = \frac{2\sqrt{\lambda}\,\beta_l}{M_B + M_P} \frac{f_T(q^2)}{f_+(q^2)} C_T^l \,, \qquad F_{T5} = \frac{2\sqrt{\lambda}\,\beta_l}{M_B + M_P} \frac{f_T(q^2)}{f_+(q^2)} C_{T5}^l,$$

$$F_P = \frac{1}{2}\frac{M_B^2 - M_P^2}{m_b - m_s}\frac{f_0(q^2)}{f_+(q^2)}(m_b C_P^l + m_b C_P^{ll}) + m_l C_{10}\left[\frac{M_B^2 - M_P^2}{q^2}\left(\frac{f_0(q^2)}{f_+(q^2)} - 1\right) - 1\right],$$

$$F_S = \frac{1}{2}\frac{M_B^2 - M_P^2}{m_b - m_s}\frac{f_0(q^2)}{f_+(q^2)}(m_b C_S^l + m_b C_S^{ll}), \quad F_V = C_9 + \frac{2m_b}{M_B}\frac{\mathcal{T}_P(q^2)}{\xi_P(q^2)} + \frac{8m_l}{M_B + M_P}\frac{f_T(q^2)}{f_+(q^2)} C_T^l, \tag{B.2}$$

where

$$\lambda = M_B^4 + M_P^4 + q^4 - 2(M_B^2 M_P^2 + M_B^2 q^2 + M_P^2 q^2), \qquad \beta_l = \sqrt{1 - 4\frac{m_l^2}{q^2}}, \tag{B.3}$$

TH-3118_176121005

The coefficients a_l, b_l and c_l appearing in eq. 1.25 are expressed as

$$\begin{aligned}
\frac{a_l(q^2)}{\Gamma_0\,\sqrt{\lambda}\,\beta_l\,\xi_P^2} &= q^2\left(\beta_l^2|F_S|^2 + |F_P|^2\right) + \frac{\lambda}{4}(|F_A|^2 + |F_V|^2) \\
&\quad + 2m_l(M_B^2 - M_P^2 + q^2)Re(F_P F_A^*) + 4m_l^2 M_B^2|F_A|^2, \\
\frac{b_l(q^2)}{\Gamma_0\,\sqrt{\lambda}\,\beta_l\,\xi_P^2} &= 2\Big\{q^2\left[\beta_l^2 Re(F_S F_T^*) + Re(F_P F_{T5}^*)\right] \\
&\quad + m_l\left[\sqrt{\lambda}\beta_l Re(F_S F_V^*) + (M_B^2 - M_P^2 + q^2)Re(F_{T5}F_A^*)\right]\Big\}, \\
\frac{c_l(q^2)}{\Gamma_0\,\sqrt{\lambda}\,\beta_l\,\xi_P^2} &= q^2\left(\beta_l^2|F_T|^2 + |F_{T5}|^2\right) - \frac{\lambda}{4}\beta_l^2(|F_A|^2 + |F_V|^2) + 2m_l\sqrt{\lambda}\beta_l Re(F_T F_V^*)
\end{aligned} \tag{B.4}$$

where

$$\Gamma_0 = \frac{G_F^2\alpha_e^2|V_{tb}V_{tp}^*|^2}{512\pi^5 M_B^3}. \tag{B.5}$$

TH-3118_176121005

Appendix C

NP predictions for observables defined in chapter 5.

In this appendix, we present the numerical estimates for the various observables defined in chapter 5 corresponding to a few benchmark values of the real and imaginary parts of the NP Wilson coefficients $\Delta C_{9,10}$ and $C'_{9,10}$ taken one at a time.

TH-3118_176121005

Bin	C_i^{NP}	$Re(C_i^{NP})$	$Im(C_i^{NP})$	Observables		
				$A_{\rm CP}^0$	$A_{\rm CP}^+$	A_I
0.1-1	$\Delta C_9/C_9'$	1	1	-0.258(17)	-0.631(16)	-0.4533(88)
		1	−1	-0.274(12)	-0.660(16)	-0.4507(95)
		−1	1	-0.239(20)	-0.532(11)	-0.500(11)
		−1	−1	-0.263(11)	-0.5590(84)	-0.504(12)
		1	0	-0.275(15)	-0.662(16)	-0.4575(99)
		−1	0	-0.262(16)	-0.5609(80)	-0.511(12)
	$\Delta C_{10}/C_{10}'$	1	1	-0.336(19)	-0.720(10)	-0.503(12)
		1	−1	-0.336(19)	-0.720(10)	-0.503(12)
		−1	1	-0.212(12)	-0.518(12)	-0.4514(91)
		−1	−1	-0.212(12)	-0.518(12)	-0.4514(91)
		1	0	-0.353(20)	-0.742(10)	-0.512(13)
		−1	0	-0.219(13)	-0.532(13)	-0.4568(99)
1-2	$\Delta C_9/C_9'$	1	1	-0.1895(65)	-0.480(18)	-0.3755(36)
		1	−1	-0.2115(71)	-0.472(17)	-0.3999(46)
		−1	1	-0.1694(63)	-0.441(15)	-0.3887(49)
		−1	−1	-0.2035(68)	-0.429(14)	-0.4274(65)
		1	0	-0.2070(63)	-0.492(17)	-0.3904(46)
		−1	0	-0.1948(57)	-0.454(13)	-0.4126(63)
	$\Delta C_{10}/C_{10}'$	1	1	-0.2558(83)	-0.580(18)	-0.4127(59)
		1	−1	-0.2558(83)	-0.580(18)	-0.4127(59)
		−1	1	-0.1571(54)	-0.381(14)	-0.3844(40)
		−1	−1	-0.1571(54)	-0.381(14)	-0.3844(40)
		1	0	-0.2687(80)	-0.605(17)	-0.4179(65)
		−1	0	-0.1623(49)	-0.393(14)	-0.3870(44)
2-4	$\Delta C_9/C_9'$	1	1	-0.1749(53)	-0.308(11)	-0.3451(17)
		1	−1	-0.1845(57)	-0.298(11)	-0.3718(25)
		−1	1	-0.1622(47)	-0.295(11)	-0.3431(18)
		−1	−1	-0.1772(57)	-0.280(10)	-0.3858(33)
		1	0	-0.1855(57)	-0.314(11)	-0.3598(23)
		−1	0	-0.1778(51)	-0.3018(99)	-0.3666(28)
	$\Delta C_{10}/C_{10}'$	1	1	-0.2313(69)	-0.384(13)	-0.3690(28)
		1	−1	-0.2313(69)	-0.384(13)	-0.3690(28)
		−1	1	-0.1417(43)	-0.2425(89)	-0.3556(18)
		−1	−1	-0.1417(43)	-0.2425(89)	-0.3556(18)
		1	0	-0.2429(73)	-0.403(13)	-0.3715(33)
		−1	0	-0.1463(43)	-0.2508(89)	-0.3568(21)
4-6	$\Delta C_9/C_9'$	1	1	-0.1565(54)	-0.1974(72)	-0.3346(11)
		1	−1	-0.1647(53)	-0.1982(68)	-0.3525(13)
		−1	1	-0.1470(54)	-0.1905(72)	-0.3299(11)
		−1	−1	-0.1600(51)	-0.1920(65)	-0.3588(15)
		1	0	-0.1656(45)	-0.2043(63)	-0.3441(11)
		−1	0	-0.1607(43)	-0.2005(60)	-0.3451(13)
	$\Delta C_{10}/C_{10}'$	1	1	-0.2071(67)	-0.2544(87)	-0.3471(14)
		1	−1	-0.2071(67)	-0.2544(87)	-0.3471(14)
		−1	1	-0.1275(42)	-0.1585(56)	-0.34182(89)
		−1	−1	-0.1275(42)	-0.1585(56)	-0.34182(89)
		1	0	-0.2171(59)	-0.2666(80)	-0.3481(16)
		−1	0	-0.1315(36)	-0.1637(50)	-0.34230(100)

Table C.1: The dependence of the CP and Isospin asymmetry observables corresponding to $B \to \pi ll$ on the real and imaginary parts of the NP WC's $\Delta C_{9,10}$ and $C'_{9,10}$ for the q^2 bins $0.1-1$, $1-2$, $2-4$ and $4-6$ GeV^2 for a few benchmark values of the real and imaginary parts of the corresponding WC's. The $+, 0$ superscript over A_{CP} denotes the charge of the initial state B and the final state π meson.

TH-3118_176121005

Bin	C_i^{NP}	$Re(C_i^{NP})$	$Im(C_i^{NP})$	Observables					
				$\overline{\text{BR}}^0$ $\times 10^8$	BR $\times 10^8$	BR^- $\times 10^8$	BR^+ $\times 10^8$	$\bar{R}_\pi^0$	R_π^-
0.1-1	$\Delta C_9/C_9'$	1	1	0.0396(28)	0.0672(40)	0.0565(44)	0.2492(95)	1.3878(41)	1.260(22)
		1	−1	0.0353(27)	0.0618(36)	0.0470(40)	0.2291(85)	1.2341(72)	1.047(28)
		−1	1	0.0263(18)	0.0429(26)	0.0523(25)	0.1715(63)	0.9217(67)	1.170(26)
		−1	−1	0.0219(16)	0.0375(22)	0.0428(21)	0.1513(51)	0.7680(67)	0.957(23)
		1	0	0.0354(26)	0.0622(34)	0.0479(38)	0.2346(83)	1.25(14)	1.07(11)
		−1	0	0.0224(16)	0.0383(21)	0.0444(19)	0.1578(52)	0.789(84)	0.995(77)
	$\Delta C_{10}/C_{10}'$	1	1	0.0213(16)	0.0429(25)	0.0293(19)	0.1799(62)	0.7466(51)	0.6537(47)
		1	−1	0.0213(16)	0.0429(25)	0.0293(19)	0.1799(62)	0.7466(51)	0.6537(47)
		−1	1	0.0402(28)	0.0618(37)	0.0700(45)	0.2207(85)	1.4093(86)	1.5633(85)
		−1	−1	0.0402(28)	0.0618(37)	0.0700(45)	0.2207(85)	1.4093(86)	1.5633(85)
		1	0	0.0196(15)	0.0410(22)	0.0261(16)	0.1762(57)	0.691(78)	0.585(54)
		−1	0	0.0382(27)	0.0596(33)	0.0661(41)	0.2162(78)	1.35(14)	1.48(14)
1-2	$\Delta C_9/C_9'$	1	1	0.0457(31)	0.0671(38)	0.0698(60)	0.1979(87)	1.3851(26)	1.2965(95)
		1	−1	0.0419(30)	0.0644(37)	0.0706(57)	0.1966(86)	1.2700(42)	1.3132(77)
		−1	1	0.0296(20)	0.0416(23)	0.0488(36)	0.1256(52)	0.8966(52)	0.908(11)
		−1	−1	0.0258(18)	0.0390(23)	0.0497(34)	0.1242(51)	0.7814(23)	0.924(13)
		1	0	0.0416(28)	0.0632(36)	0.0656(54)	0.1920(83)	1.27(13)	1.23(15)
		−1	0	0.0258(17)	0.0383(22)	0.0453(31)	0.1206(49)	0.785(78)	0.848(93)
	$\Delta C_{10}/C_{10}'$	1	1	0.0252(18)	0.0424(23)	0.0368(33)	0.1382(55)	0.7617(23)	0.6846(61)
		1	−1	0.0252(18)	0.0424(23)	0.0368(33)	0.1382(55)	0.7617(23)	0.6846(61)
		−1	1	0.0464(31)	0.0636(37)	0.0826(61)	0.1839(83)	1.4050(40)	1.536(10)
		−1	−1	0.0464(31)	0.0636(37)	0.0826(61)	0.1839(83)	1.4050(40)	1.536(10)
		1	0	0.0233(17)	0.0403(23)	0.0330(28)	0.1338(53)	0.708(73)	0.617(77)
		−1	0	0.0441(28)	0.0612(35)	0.0779(56)	0.1788(80)	1.34(13)	1.46(16)
2-4	$\Delta C_9/C_9'$	1	1	0.0921(60)	0.1311(72)	0.171(12)	0.323(16)	1.3670(18)	1.3085(43)
		1	−1	0.0873(57)	0.1267(70)	0.177(12)	0.327(16)	1.2950(23)	1.3520(31)
		−1	1	0.0585(37)	0.0812(44)	0.1085(76)	0.1993(95)	0.8686(33)	0.8298(38)
		−1	−1	0.0537(35)	0.0768(43)	0.1142(74)	0.2030(95)	0.7966(18)	0.8733(59)
		1	0	0.0853(56)	0.1240(69)	0.165(12)	0.314(15)	1.27(12)	1.27(13)
		−1	0	0.0523(34)	0.0749(42)	0.1034(69)	0.1925(92)	0.780(75)	0.795(80)
	$\Delta C_{10}/C_{10}'$	1	1	0.0517(35)	0.0827(45)	0.0969(72)	0.2172(100)	0.7664(23)	0.7405(35)
		1	−1	0.0517(35)	0.0827(45)	0.0969(72)	0.2172(100)	0.7664(23)	0.7405(35)
		−1	1	0.0942(60)	0.1252(70)	0.188(13)	0.309(15)	1.3973(39)	1.4414(61)
		−1	−1	0.0942(60)	0.1252(70)	0.188(13)	0.309(15)	1.3973(39)	1.4414(61)
		1	0	0.0479(33)	0.0786(43)	0.0890(67)	0.2085(97)	0.714(71)	0.684(74)
		−1	0	0.0897(57)	0.1204(68)	0.179(12)	0.299(15)	1.34(13)	1.38(14)
4-6	$\Delta C_9/C_9'$	1	1	0.0944(57)	0.1293(67)	0.194(12)	0.289(15)	1.3571(20)	1.3259(26)
		1	−1	0.0907(56)	0.1264(66)	0.196(12)	0.293(15)	1.3044(23)	1.3387(26)
		−1	1	0.0593(36)	0.0798(41)	0.1205(76)	0.1771(89)	0.8535(28)	0.8228(27)
		−1	−1	0.0557(34)	0.0769(40)	0.1223(73)	0.1804(88)	0.8008(19)	0.8357(31)
		1	0	0.0881(55)	0.1231(67)	0.186(12)	0.281(15)	1.27(12)	1.27(12)
		−1	0	0.0538(33)	0.0743(40)	0.1134(71)	0.1702(87)	0.777(70)	0.778(72)
	$\Delta C_{10}/C_{10}'$	1	1	0.0538(34)	0.0819(42)	0.1126(73)	0.1893(92)	0.7742(16)	0.7689(20)
		1	−1	0.0538(34)	0.0819(42)	0.1126(73)	0.1893(92)	0.7742(16)	0.7689(20)
		−1	1	0.0962(57)	0.1243(66)	0.204(12)	0.281(14)	1.3838(28)	1.3928(35)
		−1	−1	0.0962(57)	0.1243(66)	0.204(12)	0.281(14)	1.3838(28)	1.3928(35)
		1	0	0.0501(32)	0.0779(42)	0.1047(69)	0.1806(91)	0.724(67)	0.718(68)
		−1	0	0.0918(56)	0.1195(65)	0.194(12)	0.270(14)	1.33(12)	1.33(12)

Table C.2: The dependence of the Branching ratio and R_π on the NP WC's $\Delta C_{9,10}$ and $C'_{9,10}$ for the q^2 bins $0.1-1$, $1-2$, $2-4$ and $4-6$ GeV^2 for a few benchmark values of the real and imaginary parts of the corresponding WC's. The $-, 0$ superscript over R_π denotes the charge of the initial state B and the final state π meson.

TH-3118_176121005

Bin	C_i^{NP}	$Re(C_i^{NP})$	$Im(C_i^{NP})$	Observables				
				A_4	A_5	A_{6s}	A_7	A_8
0.1-1	ΔC_9	1	1	-0.0862(71)	0.0240(40)	0.0022(19)	-0.0052(37)	0.0752(68)
		1	−1	-0.0995(56)	0.0249(42)	0.0023(20)	-0.0054(38)	0.0173(79)
		−1	1	-0.0995(68)	0.0259(42)	0.0024(20)	-0.0056(40)	0.0821(63)
		−1	−1	-0.1144(52)	0.0269(44)	0.0025(21)	-0.0058(41)	0.0199(76)
		1	0	-0.0937(63)	0.0247(41)	0.0023(19)	-0.0053(38)	0.0472(74)
		−1	0	-0.1081(60)	0.0267(44)	0.0025(21)	-0.0058(41)	0.0522(70)
	ΔC_{10}	1	1	-0.1087(64)	0.0082(16)	0.00726(51)	-0.0769(41)	0.0536(77)
		1	−1	-0.1087(64)	0.0328(59)	-0.0035(28)	0.0680(38)	0.0536(77)
		−1	1	-0.0918(59)	0.0191(31)	0.0073(13)	-0.0675(50)	0.0453(66)
		−1	−1	-0.0918(59)	0.0399(70)	-0.0018(34)	0.0548(46)	0.0453(66)
		1	0	-0.1100(64)	0.0208(34)	0.0019(16)	-0.0045(32)	0.0542(78)
		−1	0	-0.0928(59)	0.0298(49)	0.0027(23)	-0.0064(46)	0.0457(67)
	C_9'	1	1	-0.1181(54)	0.0277(46)	0.0026(22)	-0.0060(43)	0.0272(75)
		1	−1	-0.1026(70)	0.0267(43)	0.0025(21)	-0.0058(41)	0.0760(66)
		−1	1	-0.0967(54)	0.0242(40)	0.0022(19)	-0.0052(37)	0.0246(76)
		−1	−1	-0.0838(68)	0.0234(39)	0.0022(18)	-0.0050(36)	0.0675(69)
		1	0	-0.1115(62)	0.0275(45)	0.0025(22)	-0.0059(43)	0.0527(71)
		−1	0	-0.0911(61)	0.0240(40)	0.0022(19)	-0.0052(37)	0.0469(73)
	C_{10}'	1	1	-0.0922(59)	0.0241(70)	0.0021(19)	0.0550(46)	0.0378(68)
		1	−1	-0.0922(59)	0.0060(27)	0.0023(18)	-0.0678(50)	0.0531(66)
		−1	1	-0.1081(63)	0.0481(59)	0.0024(22)	0.0677(38)	0.0443(78)
		−1	−1	-0.1081(63)	0.0268(25)	0.0027(21)	-0.0765(41)	0.0623(76)
		1	0	-0.0931(59)	0.0152(47)	0.0022(19)	-0.0065(46)	0.0459(67)
		−1	0	-0.1094(64)	0.0379(37)	0.0026(22)	-0.0045(32)	0.0540(78)
1-2	ΔC_9	1	1	-0.0443(64)	0.0603(77)	0.0049(49)	0.0260(32)	0.0402(62)
		1	−1	-0.0561(49)	0.0569(73)	0.0046(46)	0.0246(31)	-0.0371(63)
		−1	1	-0.0761(72)	0.0758(87)	0.0062(61)	0.0327(37)	0.0427(68)
		−1	−1	-0.0886(57)	0.0705(83)	0.0057(56)	0.0305(36)	-0.0533(68)
		1	0	-0.0516(55)	0.0600(76)	0.0049(47)	0.0259(32)	0.00043(634)
		−1	0	-0.0852(62)	0.0753(87)	0.0061(60)	0.0325(38)	-0.0072(71)
	ΔC_{10}	1	1	-0.0817(69)	0.0399(47)	0.0207(21)	-0.0840(47)	-0.0036(82)
		1	−1	-0.0817(69)	0.082(11)	-0.0108(87)	0.1365(47)	-0.0036(82)
		−1	1	-0.0536(50)	0.0541(64)	0.0158(33)	-0.0430(43)	-0.0024(54)
		−1	−1	-0.0536(50)	0.081(11)	-0.0048(79)	0.1015(45)	-0.0024(54)
		1	0	-0.0846(70)	0.0630(75)	0.0051(51)	0.0272(32)	-0.0038(85)
		−1	0	-0.0548(50)	0.0693(86)	0.0056(56)	0.0299(36)	-0.0024(55)
	C_9'	1	1	-0.0933(63)	0.0742(87)	0.0060(59)	0.0321(38)	-0.0134(66)
		1	−1	-0.0805(78)	0.0801(94)	0.0065(64)	0.0346(40)	0.0151(73)
		−1	1	-0.0539(46)	0.0547(69)	0.0044(44)	0.0236(28)	-0.0152(61)
		−1	−1	-0.0424(60)	0.0578(73)	0.0047(47)	0.0250(30)	0.0053(66)
		1	0	-0.0900(68)	0.0796(92)	0.0065(64)	0.0344(40)	0.00033(705)
		−1	0	-0.0495(51)	0.0576(72)	0.0047(46)	0.0248(30)	-0.0054(64)
	C_{10}'	1	1	-0.0549(52)	0.049(10)	0.0042(45)	0.1040(47)	-0.0319(57)
		1	−1	-0.0549(52)	0.0270(46)	0.0048(44)	-0.0440(44)	0.0270(56)
		−1	1	-0.0788(65)	0.120(12)	0.0059(64)	0.1317(42)	-0.0459(81)
		−1	−1	-0.0788(65)	0.0877(80)	0.0068(62)	-0.0810(45)	0.0389(80)
		1	0	-0.0562(53)	0.0390(73)	0.0046(46)	0.0307(37)	-0.0025(56)
		−1	0	-0.0815(66)	0.1072(97)	0.0066(65)	0.0262(31)	-0.0036(82)

Table C.3: The dependence of the asymmetric observables corresponding to $B^{\pm} \to \rho^{\pm} ll$ on the real and imaginary parts of the NP WC's $\Delta C_{9,10}$ and $C'_{9,10}$ for the q^2 bins $0.1 - 1$ and $1 - 2$ GeV^2 for a few benchmark values of the real and imaginary parts of the corresponding WC's.

TH-3118_176121005

Bin	C_i^{NP}	$Re(C_i^{NP})$	$Im(C_i^{NP})$	Observables				
				A_4	A_5	A_{6s}	A_7	A_8
2-4	ΔC_9	1	1	0.00090(380)	0.0439(67)	0.00048(655)	0.0484(42)	0.0368(28)
		1	−1	-0.0117(15)	0.0409(63)	0.00043(610)	0.0451(38)	-0.0218(32)
		−1	1	-0.0159(41)	0.0627(92)	0.00069(929)	0.0691(53)	0.0360(32)
		−1	−1	-0.0318(30)	0.0567(83)	0.00059(841)	0.0624(46)	-0.0451(41)
		1	0	-0.0058(23)	0.0437(67)	0.00047(652)	0.0482(41)	0.0067(28)
		−1	0	-0.0253(28)	0.0622(91)	0.00066(924)	0.0686(51)	-0.0069(38)
	ΔC_{10}	1	1	-0.0186(32)	0.0300(42)	0.0243(28)	-0.0392(47)	0.0014(43)
		1	−1	-0.0186(32)	0.072(13)	-0.023(14)	0.1519(79)	0.0014(43)
		−1	1	-0.0104(18)	0.0367(49)	0.0138(40)	0.000014(3959)	0.00081(239)
		−1	−1	-0.0104(18)	0.0605(100)	-0.013(11)	0.1071(56)	0.00081(239)
		1	0	-0.0196(34)	0.0539(82)	0.00057(803)	0.0594(50)	0.0015(45)
		−1	0	-0.0107(19)	0.0500(75)	0.00053(744)	0.0551(44)	0.00083(246)
	C_9'	1	1	-0.0324(31)	0.0577(84)	0.00061(857)	0.0636(47)	0.0292(38)
		1	−1	-0.0163(42)	0.0641(94)	0.00070(952)	0.0707(55)	-0.0152(35)
		−1	1	-0.0115(15)	0.0403(61)	0.00042(600)	0.0444(37)	0.0112(33)
		−1	−1	0.00089(375)	0.0433(67)	0.00046(646)	0.0478(41)	-0.0201(35)
		1	0	-0.0259(28)	0.0636(92)	0.00068(945)	0.0701(53)	0.0086(33)
		−1	0	-0.0057(23)	0.0431(66)	0.00046(642)	0.0475(40)	-0.0040(32)
	C_{10}'	1	1	-0.0110(19)	0.0409(97)	0.000049(6207)	0.1133(65)	-0.0477(34)
		1	−1	-0.0110(19)	0.0191(41)	0.00089(605)	0.000022(4185)	0.0494(34)
		−1	1	-0.0170(28)	0.096(13)	-0.000029(9404)	0.1385(62)	-0.0734(47)
		−1	−1	-0.0170(28)	0.0628(66)	0.0013(92)	-0.0358(43)	0.0761(50)
		1	0	-0.0114(20)	0.0309(70)	0.00048(632)	0.0584(49)	0.00088(261)
		−1	0	-0.0178(30)	0.0834(92)	0.00064(973)	0.0539(42)	0.0014(41)
4-6	ΔC_9	1	1	0.0126(39)	0.0246(53)	-0.0144(90)	0.0367(32)	0.0296(13)
		1	−1	0.00078(78)	0.0237(51)	-0.0139(87)	0.0353(30)	-0.0062(15)
		−1	1	0.0090(39)	0.0375(79)	-0.022(14)	0.0559(46)	0.03188(77)
		−1	−1	-0.0086(13)	0.0354(75)	-0.021(13)	0.0528(42)	-0.0217(21)
		1	0	0.0068(23)	0.0250(53)	-0.0146(91)	0.0372(32)	0.0117(11)
		−1	0	-0.000056(1628)	0.0384(81)	-0.022(14)	0.0572(46)	0.0045(13)
	ΔC_{10}	1	1	0.0057(28)	0.0110(19)	0.0158(26)	-0.0155(39)	0.0123(15)
		1	−1	0.0057(28)	0.051(12)	-0.052(21)	0.1080(64)	0.0123(15)
		−1	1	0.0030(15)	0.0174(32)	0.0017(52)	0.0088(32)	0.00656(81)
		−1	−1	0.0030(15)	0.0387(89)	-0.035(15)	0.0747(42)	0.00656(81)
		1	0	0.0060(28)	0.0329(70)	-0.019(12)	0.0490(44)	0.0130(16)
		−1	0	0.0031(15)	0.0289(62)	-0.017(11)	0.0430(35)	0.00676(84)
	C_9'	1	1	-0.0082(11)	0.0341(72)	-0.020(12)	0.0508(39)	0.0628(25)
		1	−1	0.0086(38)	0.0362(76)	-0.021(13)	0.0539(44)	-0.0353(14)
		−1	1	0.00080(80)	0.0243(52)	-0.0142(89)	0.0362(31)	0.0380(19)
		−1	−1	0.0130(40)	0.0253(55)	-0.0149(92)	0.0377(33)	-0.0318(15)
		1	0	-0.000055(1565)	0.0368(77)	-0.022(13)	0.0549(44)	0.0160(15)
		−1	0	0.0070(23)	0.0257(55)	-0.0150(94)	0.0382(33)	0.0040(10)
	C_{10}'	1	1	0.0033(16)	0.036(10)	-0.0149(91)	0.0814(50)	-0.0515(20)
		1	−1	0.0033(16)	0.0093(30)	-0.0137(88)	0.0096(36)	0.0657(27)
		−1	1	0.0049(23)	0.059(11)	-0.022(13)	0.0936(47)	-0.0768(23)
		−1	−1	0.0049(23)	0.0194(22)	-0.020(13)	-0.0135(34)	0.0981(28)
		−1	−1	0.0049(23)	0.0194(22)	-0.020(13)	-0.0135(34)	0.0981(28)
		1	0	0.0034(17)	0.0232(69)	-0.0148(92)	0.0470(41)	0.00738(94)
		−1	0	0.0052(25)	0.0409(59)	-0.022(14)	0.0421(34)	0.0112(13)

Table C.4: The dependence of the asymmetric observables corresponding to $B^{\pm} \to \rho^{\pm} ll$ on the real and imaginary parts of the NP WC's $\Delta C_{9,10}$ and $C'_{9,10}$ for the q^2 bins $2-4$ and $4-6$ GeV^2 for a few benchmark values of the real and imaginary parts of the corresponding WC's.

TH-3118_176121005

Bin	C_i^{NP}	$Re(C_i^{NP})$	$Im(C_i^{NP})$	Observables		
				A_3	A_9	$A_{\rm CP}$
0.1-1	ΔC_9	1	1	0.000051(47)	0.00040(24)	-0.342(25)
		1	−1	-0.000066(48)	-0.00034(21)	-0.329(27)
		−1	1	0.000072(45)	0.00044(25)	-0.216(22)
		−1	−1	-0.000053(40)	-0.00036(22)	-0.197(25)
		1	0	-0.0000065(326)	0.000037(40)	-0.339(26)
		−1	0	0.000011(20)	0.000048(37)	-0.210(24)
	ΔC_{10}	1	1	0.0000019(280)	0.000046(41)	-0.299(28)
		1	−1	0.0000019(280)	0.000046(41)	-0.299(28)
		−1	1	0.0000017(236)	0.000039(34)	-0.252(22)
		−1	−1	0.0000017(236)	0.000039(34)	-0.252(22)
		1	0	0.0000019(283)	0.000046(42)	-0.303(28)
		−1	0	0.0000017(239)	0.000039(35)	-0.255(22)
	C_9'	1	1	-0.00222(83)	-0.01372(63)	-0.209(24)
		1	−1	0.00275(34)	0.01336(75)	-0.217(24)
		−1	1	-0.00249(29)	-0.01204(77)	-0.325(26)
		−1	−1	0.00188(73)	0.01166(63)	-0.328(26)
		1	0	0.00031(25)	0.000083(236)	-0.216(24)
		−1	0	-0.00027(25)	0.0000068(2486)	-0.330(26)
	C_{10}'	1	1	0.0000017(237)	-0.00210(16)	-0.253(22)
		1	−1	0.0000017(237)	0.00218(13)	-0.253(22)
		−1	1	0.0000019(279)	-0.00246(17)	-0.297(28)
		−1	−1	0.0000019(279)	0.00255(14)	-0.297(28)
		1	0	0.0000017(240)	0.000039(35)	-0.256(22)
		−1	0	0.0000019(282)	0.000046(42)	-0.301(28)
1-2	ΔC_9	1	1	0.00011(12)	0.00099(55)	-0.409(20)
		1	−1	-0.00020(12)	-0.00080(46)	-0.348(19)
		−1	1	0.00018(12)	0.00128(72)	-0.298(16)
		−1	−1	-0.00021(12)	-0.00097(55)	-0.230(19)
		1	0	-0.000052(95)	0.000073(74)	-0.387(19)
		−1	0	-0.000020(68)	0.000120(84)	-0.271(17)
	ΔC_{10}	1	1	-0.000046(101)	0.000115(94)	-0.413(21)
		1	−1	-0.000046(101)	0.000115(94)	-0.413(21)
		−1	1	-0.000030(66)	0.000075(62)	-0.270(15)
		−1	−1	-0.000030(66)	0.000075(62)	-0.270(15)
		1	0	-0.000048(104)	0.000119(98)	-0.427(21)
		−1	0	-0.000031(68)	0.000077(63)	-0.277(15)
	C_9'	1	1	-0.0063(23)	-0.0256(22)	-0.255(15)
		1	−1	0.0083(13)	0.0276(25)	-0.298(18)
		−1	1	-0.00575(85)	-0.0187(20)	-0.346(18)
		−1	−1	0.0048(20)	0.0201(19)	-0.383(20)
		1	0	0.00078(75)	-0.0000084(5228)	-0.285(17)
		−1	0	-0.00063(64)	0.00017(46)	-0.373(19)
	C_{10}'	1	1	-0.000031(68)	-0.0129(13)	-0.277(15)
		1	−1	-0.000031(68)	0.0131(11)	-0.277(15)
		−1	1	-0.000045(97)	-0.0185(16)	-0.398(20)
		−1	−1	-0.000045(97)	0.0188(16)	-0.398(20)
		1	0	-0.000032(69)	0.000079(64)	-0.284(15)
		−1	0	-0.000046(101)	0.000115(95)	-0.412(21)

Table C.5: The dependence of the asymmetric observables corresponding to $B^{\pm} \to \rho^{\pm} ll$ on the real and imaginary parts of the NP WC's $\Delta C_{9,10}$ and $C'_{9,10}$ for the q^2 bins $0.1-1$ and $1-2$ GeV^2 for a few benchmark values of the real and imaginary parts of the corresponding WC's.

TH-3118_176121005

Bin	C_i^{NP}	$Re(C_i^{NP})$	$Im(C_i^{NP})$	Observables		
				A_3	A_9	$A_{\rm CP}$
2-4	ΔC_9	1	1	0.00029(23)	0.00117(61)	-0.202(12)
		1	−1	-0.00022(11)	-0.00095(51)	-0.1535(94)
		−1	1	0.00038(24)	0.00172(90)	-0.1704(84)
		−1	−1	-0.00032(12)	-0.00129(68)	-0.106(12)
		1	0	0.000027(138)	0.000074(65)	-0.183(10)
		−1	0	0.000012(101)	0.000149(91)	-0.1428(87)
	ΔC_{10}	1	1	0.000028(164)	0.000140(99)	-0.223(12)
		1	−1	0.000028(164)	0.000140(99)	-0.223(12)
		−1	1	0.000016(92)	0.000079(55)	-0.1250(69)
		−1	−1	0.000016(92)	0.000079(55)	-0.1250(69)
		1	0	0.000030(172)	0.00015(10)	-0.235(12)
		−1	0	0.000016(94)	0.000081(57)	-0.1287(71)
	C_9'	1	1	-0.0098(36)	-0.0094(16)	-0.1272(70)
		1	−1	0.0111(20)	0.0092(18)	-0.1525(86)
		−1	1	-0.0069(11)	-0.0056(11)	-0.1650(90)
		−1	−1	0.0074(28)	0.0072(11)	-0.185(11)
		1	0	0.00011(108)	-0.00062(45)	-0.1458(78)
		−1	0	-0.000039(916)	0.00060(38)	-0.1802(100)
	C_{10}'	1	1	0.000017(97)	-0.0305(30)	-0.1322(74)
		1	−1	0.000017(97)	0.0307(30)	-0.1322(74)
		−1	1	0.000026(149)	-0.0469(43)	-0.203(11)
		−1	−1	0.000026(149)	0.0471(42)	-0.203(11)
		1	0	0.000017(100)	0.000086(60)	-0.1363(76)
		−1	0	0.000027(157)	0.000135(95)	-0.213(11)
4-6	ΔC_9	1	1	0.00092(47)	0.00105(51)	-0.079(10)
		1	−1	0.0000044(1353)	-0.00092(46)	-0.0406(30)
		−1	1	0.00104(51)	0.00166(82)	-0.0747(85)
		−1	−1	-0.00034(12)	-0.00133(66)	-0.0178(73)
		1	0	0.00047(29)	0.000049(39)	-0.0614(54)
		−1	0	0.00034(24)	0.000132(72)	-0.0477(26)
	ΔC_{10}	1	1	0.00058(38)	0.000113(69)	-0.0773(55)
		1	−1	0.00058(38)	0.000113(69)	-0.0773(55)
		−1	1	0.00031(20)	0.000060(37)	-0.0413(31)
		−1	−1	0.00031(20)	0.000060(37)	-0.0413(31)
		1	0	0.00061(40)	0.000119(73)	-0.0820(57)
		−1	0	0.00032(21)	0.000062(38)	-0.0425(31)
	C_9'	1	1	-0.0159(53)	0.0198(19)	-0.0486(49)
		1	−1	0.0124(27)	-0.0230(21)	-0.0487(40)
		−1	1	-0.0077(16)	0.0156(16)	-0.0572(39)
		−1	−1	0.0125(43)	-0.0146(16)	-0.0576(35)
		1	0	-0.0023(15)	-0.00101(20)	-0.0511(46)
		−1	0	0.0023(14)	0.00084(18)	-0.0594(38)
	C_{10}'	1	1	0.00034(22)	-0.0481(42)	-0.0449(33)
		1	−1	0.00034(22)	0.0483(42)	-0.0449(33)
		−1	1	0.00050(33)	-0.0718(56)	-0.0671(47)
		−1	−1	0.00050(33)	0.0720(56)	-0.0671(47)
		1	0	0.00035(23)	0.000068(41)	-0.0465(34)
		−1	0	0.00053(35)	0.000103(63)	-0.0705(50)

Table C.6: The dependence of the asymmetric observables corresponding to $B^{\pm} \to \rho^{\pm} ll$ on the real and imaginary parts of the NP WC's $\Delta C_{9,10}$ and $C'_{9,10}$ for the q^2 bins $2-4$ and $4-6$ GeV^2 for a few benchmark values of the real and imaginary parts of the corresponding WC's.

TH-3118_176121005

Bin	C_i^{NP}	Re	Im	Observables						
				P_1	P_2	P_3	P_4'	P_5'	P_6'	P_8'
0.1-1	ΔC_9	1	1	0.0035(26)	-0.0800(26)	0.00044(27)	0.178(10)	0.3473(88)	-0.072(18)	-0.068(12)
		1	−1	0.0036(27)	-0.0813(25)	0.00042(29)	0.1865(82)	0.3609(89)	-0.075(19)	-0.053(14)
		−1	1	0.0016(15)	-0.0825(26)	0.00023(14)	0.099(11)	0.467(14)	-0.081(21)	-0.0565(90)
		−1	−1	0.0016(16)	-0.0838(25)	0.00021(14)	0.1061(87)	0.491(14)	-0.085(22)	-0.040(12)
		1	0	0.0036(27)	-0.0810(26)	0.00043(29)	0.1864(92)	0.3583(91)	-0.074(19)	-0.061(13)
		−1	0	0.0016(16)	-0.0835(26)	0.00022(14)	0.1065(99)	0.486(14)	-0.085(22)	-0.049(10)
	ΔC_{10}	1	1	0.0030(23)	-0.0623(18)	0.00033(22)	0.182(11)	0.343(11)	-0.042(20)	-0.061(13)
		1	−1	0.0030(23)	-0.0625(22)	0.00033(22)	0.182(11)	0.338(11)	-0.087(14)	-0.061(13)
		−1	1	0.0021(18)	-0.1004(28)	0.00031(21)	0.1142(82)	0.471(11)	-0.071(25)	-0.050(11)
		−1	−1	0.0021(18)	-0.1006(33)	0.00031(21)	0.1142(82)	0.467(11)	-0.107(21)	-0.050(11)
		1	0	0.0031(23)	-0.0626(20)	0.00033(22)	0.187(11)	0.346(11)	-0.066(17)	-0.062(13)
		−1	0	0.0021(18)	-0.1009(31)	0.00031(21)	0.1177(83)	0.475(11)	-0.090(23)	-0.050(11)
	C_9'	1	1	-0.0385(28)	-0.0839(26)	-0.00391(44)	0.1086(90)	0.462(14)	-0.087(23)	-0.056(12)
		1	−1	-0.0377(23)	-0.0826(26)	-0.0029(11)	0.101(11)	0.439(13)	-0.083(21)	-0.0397(92)
		−1	1	0.0421(22)	-0.0813(25)	0.0035(13)	0.1821(80)	0.3865(88)	-0.073(19)	-0.068(14)
		−1	−1	0.0417(27)	-0.0801(25)	0.00436(55)	0.1734(97)	0.3720(88)	-0.070(18)	-0.053(12)
		1	0	-0.0382(25)	-0.0836(26)	-0.00343(80)	0.109(10)	0.457(14)	-0.087(22)	-0.049(11)
		−1	0	0.0421(23)	-0.0810(25)	0.00395(91)	0.1820(90)	0.3837(90)	-0.073(19)	-0.061(13)
	C_{10}'	1	1	-0.0047(20)	-0.0810(26)	0.00031(21)	0.1146(82)	0.502(11)	-0.107(21)	-0.050(11)
		1	−1	-0.0047(20)	-0.0810(25)	0.00031(21)	0.1146(82)	0.497(11)	-0.071(25)	-0.050(11)
		−1	1	0.0101(22)	-0.0830(26)	0.00033(22)	0.181(11)	0.3080(97)	-0.086(14)	-0.061(13)
		−1	−1	0.0101(22)	-0.0830(26)	0.00033(22)	0.181(11)	0.302(10)	-0.042(19)	-0.061(13)
		1	0	-0.0047(21)	-0.0813(26)	0.00031(21)	0.1181(83)	0.505(11)	-0.090(23)	-0.050(11)
		−1	0	0.0102(23)	-0.0833(26)	0.00033(22)	0.187(11)	0.310(10)	-0.065(17)	-0.062(13)
1-2	ΔC_9	1	1	0.0032(42)	-0.325(12)	0.0035(21)	0.056(14)	0.054(23)	-0.115(32)	-0.106(20)
		1	−1	0.0035(43)	-0.3213(100)	0.0032(21)	0.039(13)	0.052(22)	-0.111(31)	-0.059(23)
		−1	1	-0.0012(26)	-0.3426(97)	0.00143(92)	0.0094(107)	0.403(15)	-0.123(34)	-0.082(13)
		−1	−1	-0.00094(268)	-0.3398(81)	0.00129(90)	-0.0065(86)	0.381(15)	-0.116(33)	-0.032(16)
		1	0	0.0045(47)	-0.331(11)	0.0034(22)	0.059(13)	0.054(23)	-0.116(32)	-0.084(22)
		−1	0	-0.00031(293)	-0.3472(92)	0.00138(92)	0.0129(95)	0.403(15)	-0.123(34)	-0.058(15)
	ΔC_{10}	1	1	0.0089(75)	-0.2911(83)	0.0026(17)	0.134(11)	0.178(18)	-0.045(34)	-0.084(22)
		1	−1	0.0089(75)	-0.290(11)	0.0026(17)	0.134(11)	0.214(16)	-0.164(24)	-0.084(22)
		−1	1	-0.0051(21)	-0.3663(83)	0.0019(11)	-0.050(11)	0.215(21)	-0.080(37)	-0.058(15)
		−1	−1	-0.0051(21)	-0.366(10)	0.0019(11)	-0.050(11)	0.239(20)	-0.161(31)	-0.058(15)
		1	0	0.0101(83)	-0.297(10)	0.0027(17)	0.152(11)	0.202(17)	-0.108(30)	-0.087(23)
		−1	0	-0.0045(20)	-0.3722(95)	0.0020(13)	-0.042(11)	0.232(20)	-0.123(35)	-0.059(15)
	C_9'	1	1	-0.1716(90)	-0.3403(90)	-0.0241(28)	-0.0070(92)	0.236(20)	-0.126(35)	-0.076(17)
		1	−1	-0.1750(53)	-0.3441(92)	-0.0190(77)	0.010(12)	0.250(21)	-0.133(37)	-0.036(14)
		−1	1	0.1661(33)	-0.3235(92)	0.0222(82)	0.035(11)	0.189(16)	-0.101(28)	-0.093(21)
		−1	−1	0.1664(74)	-0.3269(95)	0.0274(35)	0.051(13)	0.197(17)	-0.105(29)	-0.062(19)
		1	0	-0.1760(70)	-0.3493(95)	-0.0220(53)	0.014(10)	0.250(21)	-0.133(37)	-0.058(16)
		−1	0	0.1704(50)	-0.3316(97)	0.0253(59)	0.054(12)	0.197(17)	-0.105(29)	-0.080(20)
	C_{10}'	1	1	-0.1117(76)	-0.3253(92)	0.0021(14)	-0.053(11)	0.351(17)	-0.170(32)	-0.061(16)
		1	−1	-0.1117(76)	-0.3253(92)	0.0021(14)	-0.053(11)	0.379(16)	-0.085(39)	-0.061(16)
		−1	1	0.1223(82)	-0.3432(94)	0.0023(15)	0.126(11)	0.00065(2141)	-0.154(23)	-0.079(21)
		−1	−1	0.1223(82)	-0.3431(94)	0.0023(15)	0.126(11)	0.037(21)	-0.042(33)	-0.079(21)
		1	0	-0.1130(80)	-0.3314(95)	0.0022(14)	-0.044(11)	0.373(17)	-0.130(36)	-0.062(16)
		−1	0	0.1258(88)	-0.3502(98)	0.0023(15)	0.142(11)	0.019(22)	-0.101(28)	-0.082(21)

Table C.7: The dependence of the optimized observables corresponding to $B^{\pm} \to \rho^{\pm} ll$ on the real and imaginary parts of the NP WC's $\Delta C_{9,10}$ and $C'_{9,10}$ for the q^2 bins $0.1 - 1$ and $1 - 2$ GeV^2 for a few benchmark values of the real and imaginary parts of the corresponding WC's.

TH-3118_176121005

Bin	C_i^{NP}	$Re(C_i^{NP})$	$Im(C_i^{NP})$	Observables						
				P_1	P_2	P_3	P_4'	P_5'	P_6'	P_8'
2-4	ΔC_9	1	1	-0.056(25)	0.039(23)	0.0059(34)	-0.311(15)	-0.614(28)	-0.119(33)	-0.089(19)
		1	−1	-0.055(25)	0.039(23)	0.0058(34)	-0.325(15)	-0.588(26)	-0.115(32)	-0.057(22)
		−1	1	-0.036(15)	-0.306(17)	0.0030(18)	-0.253(13)	-0.070(26)	-0.144(40)	-0.071(13)
		−1	−1	-0.035(14)	-0.307(15)	0.0029(18)	-0.268(12)	-0.065(24)	-0.135(38)	-0.032(16)
		1	0	-0.055(25)	0.042(25)	0.0062(36)	-0.312(15)	-0.626(28)	-0.122(34)	-0.076(21)
		−1	0	-0.034(14)	-0.322(17)	0.0031(19)	-0.249(13)	-0.071(26)	-0.146(41)	-0.053(15)
	ΔC_{10}	1	1	-0.035(14)	-0.177(23)	0.0070(41)	-0.197(18)	-0.430(32)	-0.087(44)	-0.092(25)
		1	−1	-0.035(14)	-0.167(26)	0.0070(41)	-0.197(18)	-0.347(30)	-0.189(31)	-0.092(25)
		−1	1	-0.050(22)	-0.132(19)	0.0031(19)	-0.337(12)	-0.360(25)	-0.094(37)	-0.047(13)
		−1	−1	-0.050(22)	-0.128(20)	0.0031(19)	-0.337(12)	-0.317(24)	-0.147(31)	-0.047(13)
		1	0	-0.032(13)	-0.187(26)	0.0076(45)	-0.179(19)	-0.414(33)	-0.147(40)	-0.098(27)
		−1	0	-0.049(22)	-0.135(20)	0.0033(19)	-0.332(12)	-0.349(25)	-0.124(35)	-0.049(14)
	C_9'	1	1	-0.114(23)	-0.146(21)	-0.0377(54)	-0.278(12)	-0.394(29)	-0.140(39)	-0.066(16)
		1	−1	-0.127(21)	-0.148(21)	-0.037(14)	-0.264(13)	-0.424(31)	-0.151(42)	-0.033(13)
		−1	1	0.032(23)	-0.138(20)	0.043(15)	-0.311(15)	-0.308(23)	-0.110(31)	-0.084(21)
		−1	−1	0.021(24)	-0.139(21)	0.0444(67)	-0.299(15)	-0.323(24)	-0.115(32)	-0.059(18)
		1	0	-0.124(22)	-0.155(22)	-0.040(10)	-0.260(13)	-0.429(32)	-0.153(42)	-0.053(15)
		−1	0	0.031(23)	-0.146(21)	0.046(11)	-0.298(16)	-0.328(25)	-0.117(32)	-0.075(20)
	C_{10}'	1	1	-0.386(18)	-0.142(20)	0.0041(23)	-0.388(13)	-0.190(26)	-0.168(35)	-0.054(15)
		1	−1	-0.386(18)	-0.142(20)	0.0041(23)	-0.388(13)	-0.133(25)	-0.108(42)	-0.054(15)
		−1	1	0.330(18)	-0.144(22)	0.0046(28)	-0.159(15)	-0.660(27)	-0.152(26)	-0.074(21)
		−1	−1	0.330(18)	-0.144(22)	0.0046(28)	-0.159(15)	-0.583(27)	-0.070(36)	-0.074(21)
		1	0	-0.402(18)	-0.149(21)	0.0043(25)	-0.384(13)	-0.168(26)	-0.144(40)	-0.056(16)
		−1	0	0.352(18)	-0.152(23)	0.0048(28)	-0.142(15)	-0.653(28)	-0.117(32)	-0.078(22)
4-6	ΔC_9	1	1	-0.089(35)	0.3739(84)	0.0051(27)	-0.469(11)	-0.863(21)	-0.116(33)	-0.067(16)
		1	−1	-0.089(35)	0.3772(84)	0.0053(28)	-0.474(11)	-0.842(19)	-0.114(32)	-0.061(19)
		−1	1	-0.075(29)	0.043(17)	0.0037(21)	-0.433(10)	-0.488(20)	-0.170(47)	-0.055(12)
		−1	−1	-0.075(28)	0.043(17)	0.0040(23)	-0.439(10)	-0.468(19)	-0.163(46)	-0.047(16)
		1	0	-0.089(35)	0.3935(88)	0.0054(30)	-0.470(11)	-0.885(21)	-0.119(34)	-0.066(19)
		−1	0	-0.075(28)	0.045(18)	0.0041(23)	-0.432(11)	-0.504(21)	-0.175(49)	-0.053(15)
	ΔC_{10}	1	1	-0.087(34)	0.279(14)	0.0076(41)	-0.436(13)	-0.805(24)	-0.143(48)	-0.088(24)
		1	−1	-0.087(34)	0.289(14)	0.0076(41)	-0.436(13)	-0.752(21)	-0.159(35)	-0.088(24)
		−1	1	-0.081(31)	0.206(11)	0.0033(18)	-0.4681(94)	-0.674(18)	-0.124(40)	-0.044(12)
		−1	−1	-0.081(31)	0.210(12)	0.0033(18)	-0.4681(94)	-0.648(18)	-0.132(33)	-0.044(12)
		1	0	-0.088(35)	0.310(15)	0.0083(45)	-0.432(14)	-0.833(24)	-0.161(44)	-0.094(25)
		−1	0	-0.081(31)	0.216(12)	0.0034(19)	-0.4669(95)	-0.683(19)	-0.133(38)	-0.045(13)
	C_9'	1	1	0.043(32)	0.236(13)	-0.0280(55)	-0.413(11)	-0.790(19)	-0.154(43)	-0.058(16)
		1	−1	0.031(32)	0.237(13)	-0.043(14)	-0.410(11)	-0.828(20)	-0.161(45)	-0.042(13)
		−1	1	-0.191(31)	0.225(12)	0.050(15)	-0.496(10)	-0.612(18)	-0.119(34)	-0.072(19)
		−1	−1	-0.203(31)	0.225(12)	0.0356(71)	-0.493(10)	-0.629(19)	-0.122(34)	-0.059(17)
		1	0	0.044(32)	0.250(13)	-0.037(10)	-0.407(11)	-0.850(20)	-0.165(46)	-0.053(15)
		−1	0	-0.203(32)	0.237(12)	0.045(12)	-0.495(10)	-0.646(20)	-0.125(35)	-0.068(19)
	C_{10}'	1	1	-0.452(28)	0.218(12)	0.0044(23)	-0.5424(87)	-0.547(21)	-0.153(38)	-0.051(14)
		1	−1	-0.452(28)	0.218(12)	0.0044(23)	-0.5424(87)	-0.508(20)	-0.144(46)	-0.051(14)
		−1	1	0.316(31)	0.244(14)	0.0048(27)	-0.346(12)	-0.969(18)	-0.126(29)	-0.070(19)
		−1	−1	0.316(31)	0.245(14)	0.0048(27)	-0.346(12)	-0.916(17)	-0.114(39)	-0.070(19)
		−1	−1	0.316(31)	0.245(14)	0.0048(27)	-0.346(12)	-0.916(17)	-0.114(39)	-0.070(19)
		1	0	-0.471(28)	0.229(13)	0.0046(25)	-0.5446(89)	-0.549(21)	-0.155(43)	-0.053(15)
		−1	0	0.338(31)	0.258(14)	0.0051(28)	-0.337(12)	-0.992(18)	-0.126(35)	-0.073(20)

Table C.8: The dependence of the optimized observables corresponding to $B^{\pm} \to \rho^{\pm} ll$ on the real and imaginary parts of the NP WC's $\Delta C_{9,10}$ and $C'_{9,10}$ for the q^2 bins $2-4$ and $4-6$ GeV^2 for a few benchmark values of the real and imaginary parts of the corresponding WC's.

TH-3118_176121005

Bin	C_i^{NP}	$Re(C_i^{NP})$	$Im(C_i^{NP})$	Observables			
				BR$\times 10^9$	F_L	$A_{\rm FB}$	R_ρ
0.1-1	ΔC_9	1	1	3.47(23)	0.416(26)	-0.0701(41)	1.061(10)
		1	−1	3.35(22)	0.405(26)	-0.0726(41)	1.0248(89)
		−1	1	3.22(22)	0.331(24)	-0.0828(40)	0.9856(49)
		−1	−1	3.10(22)	0.317(24)	-0.0859(39)	0.9497(64)
		1	0	3.37(23)	0.407(26)	-0.0721(41)	1.0317(86)
		−1	0	3.13(22)	0.319(24)	-0.0853(39)	0.9566(63)
	ΔC_{10}	1	1	3.01(21)	0.330(24)	-0.0626(28)	0.9205(47)
		1	−1	3.01(21)	0.330(24)	-0.0628(31)	0.9205(47)
		−1	1	3.56(24)	0.402(25)	-0.0901(49)	1.0896(88)
		−1	−1	3.56(24)	0.402(25)	-0.0902(51)	1.0896(88)
		1	0	2.97(21)	0.324(24)	-0.0635(30)	0.9095(56)
		−1	0	3.52(24)	0.398(25)	-0.0911(50)	1.0786(79)
	C_9'	1	1	3.01(21)	0.327(24)	-0.0847(39)	0.9200(51)
		1	−1	3.12(22)	0.342(24)	-0.0815(40)	0.9560(40)
		−1	1	3.45(23)	0.394(26)	-0.0740(40)	1.0544(79)
		−1	−1	3.56(24)	0.405(25)	-0.0715(40)	1.0904(91)
		1	0	3.03(21)	0.329(24)	-0.0841(40)	0.9269(52)
		−1	0	3.47(23)	0.395(26)	-0.0735(40)	1.0614(75)
	C_{10}'	1	1	3.55(24)	0.404(25)	-0.0724(40)	1.0852(89)
		1	−1	3.55(24)	0.404(25)	-0.0724(40)	1.0852(89)
		−1	1	3.02(21)	0.329(24)	-0.0836(41)	0.9249(47)
		−1	−1	3.02(21)	0.329(24)	-0.0836(40)	0.9249(47)
		1	0	3.51(24)	0.400(25)	-0.0732(40)	1.0742(80)
		−1	0	2.99(21)	0.323(24)	-0.0846(41)	0.9139(57)
1-2	ΔC_9	1	1	1.75(14)	0.794(18)	-0.101(11)	1.137(13)
		1	−1	1.85(14)	0.803(17)	-0.0950(100)	1.205(13)
		−1	1	1.389(95)	0.648(26)	-0.181(14)	0.904(11)
		−1	−1	1.493(98)	0.670(25)	-0.168(14)	0.972(11)
		1	0	1.76(14)	0.798(17)	-0.100(11)	1.142(12)
		−1	0	1.397(93)	0.655(26)	-0.180(14)	0.909(11)
	ΔC_{10}	1	1	1.282(88)	0.717(24)	-0.124(11)	0.8343(39)
		1	−1	1.282(88)	0.717(24)	-0.123(11)	0.8343(39)
		−1	1	1.96(15)	0.750(20)	-0.138(13)	1.2734(67)
		−1	−1	1.96(15)	0.750(20)	-0.137(13)	1.2734(67)
		1	0	1.239(85)	0.714(24)	-0.128(11)	0.8059(46)
		−1	0	1.91(14)	0.749(20)	-0.141(13)	1.2450(60)
	C_9'	1	1	1.418(94)	0.705(23)	-0.150(13)	0.9228(68)
		1	−1	1.313(91)	0.685(24)	-0.163(14)	0.8545(63)
		−1	1	1.93(14)	0.772(19)	-0.111(11)	1.2539(84)
		−1	−1	1.82(14)	0.761(20)	-0.117(12)	1.1856(94)
		1	0	1.322(89)	0.692(24)	-0.161(14)	0.8601(66)
		−1	0	1.83(14)	0.766(20)	-0.117(11)	1.1912(80)
	C_{10}'	1	1	1.91(14)	0.768(19)	-0.113(11)	1.2429(83)
		1	−1	1.91(14)	0.768(19)	-0.113(11)	1.2429(83)
		−1	1	1.329(90)	0.692(25)	-0.159(14)	0.8648(56)
		−1	−1	1.329(90)	0.692(25)	-0.159(14)	0.8648(56)
		1	0	1.87(14)	0.767(19)	-0.116(11)	1.2145(77)
		−1	0	1.285(86)	0.688(25)	-0.164(15)	0.8364(62)

Table C.9: The dependence of the Branching Ratio and the observables F_L, A_{FB} and R_ρ corresponding to $B^\pm \to \rho^\pm ll$ on the real and imaginary parts of the NP WC's $\Delta C_{9,10}$ and $C'_{9,10}$ for the q^2 bins $0.1-1$ and $1-2$ GeV^2 for a few benchmark values of the real and imaginary parts of the corresponding WC's.

TH-3118_176121005

Bin	C_i^{NP}	$Re(C_i^{NP})$	$Im(C_i^{NP})$	Observables			
				BR$\times 10^9$	F_L	$A_{\rm FB}$	R_ρ
2-4	ΔC_9	1	1	3.05(27)	0.826(15)	0.0103(62)	1.2117(90)
		1	−1	3.28(28)	0.838(14)	0.0096(57)	1.3017(68)
		−1	1	2.14(17)	0.724(22)	-0.127(14)	0.8490(81)
		−1	−1	2.36(18)	0.751(20)	-0.115(12)	0.9390(97)
		1	0	3.07(27)	0.836(14)	0.0102(61)	1.2174(74)
		−1	0	2.15(17)	0.739(21)	-0.126(13)	0.8547(77)
	ΔC_{10}	1	1	1.94(16)	0.823(16)	-0.0471(82)	0.7722(35)
		1	−1	1.94(16)	0.823(16)	-0.0446(84)	0.7722(35)
		−1	1	3.47(28)	0.777(18)	-0.0443(77)	1.3777(52)
		−1	−1	3.47(28)	0.777(18)	-0.0429(78)	1.3777(52)
		1	0	1.85(15)	0.828(16)	-0.0483(87)	0.7331(41)
		−1	0	3.37(28)	0.779(18)	-0.0449(80)	1.3386(47)
	C_9'	1	1	2.32(18)	0.765(19)	-0.0518(90)	0.9219(78)
		1	−1	2.09(17)	0.741(21)	-0.058(10)	0.8296(61)
		−1	1	3.33(28)	0.826(15)	-0.0362(65)	1.3212(47)
		−1	−1	3.09(27)	0.815(16)	-0.0389(71)	1.2289(71)
		1	0	2.10(16)	0.755(20)	-0.0571(100)	0.8364(57)
		−1	0	3.11(27)	0.824(15)	-0.0387(70)	1.2357(54)
	C_{10}'	1	1	3.28(28)	0.821(15)	-0.0382(66)	1.3031(47)
		1	−1	3.28(28)	0.821(15)	-0.0382(66)	1.3031(47)
		−1	1	2.13(17)	0.750(21)	-0.054(10)	0.8468(52)
		−1	−1	2.13(17)	0.750(21)	-0.054(10)	0.8468(52)
		1	0	3.18(27)	0.825(15)	-0.0394(68)	1.2640(49)
		−1	0	2.03(16)	0.752(21)	-0.057(11)	0.8077(50)
4-6	ΔC_9	1	1	3.37(28)	0.712(23)	0.162(14)	1.2772(38)
		1	−1	3.50(28)	0.725(22)	0.155(14)	1.3270(34)
		−1	1	2.21(18)	0.661(26)	0.0217(86)	0.8374(49)
		−1	−1	2.34(18)	0.683(24)	0.0205(82)	0.8872(57)
		1	0	3.32(28)	0.723(23)	0.164(15)	1.2595(33)
		−1	0	2.16(17)	0.676(25)	0.0221(88)	0.8197(41)
	ΔC_{10}	1	1	1.98(17)	0.740(23)	0.109(11)	0.7526(43)
		1	−1	1.98(17)	0.740(23)	0.113(12)	0.7526(43)
		−1	1	3.72(30)	0.680(24)	0.0990(97)	1.4110(67)
		−1	−1	3.72(30)	0.680(24)	0.1010(98)	1.4110(67)
		1	0	1.87(16)	0.748(22)	0.117(12)	0.7102(50)
		−1	0	3.61(28)	0.682(24)	0.103(10)	1.3686(60)
	C_9'	1	1	2.43(19)	0.657(25)	0.122(11)	0.9225(83)
		1	−1	2.29(18)	0.637(27)	0.129(12)	0.8692(75)
		−1	1	3.42(28)	0.743(21)	0.0867(90)	1.2952(57)
		−1	−1	3.28(28)	0.732(22)	0.0904(94)	1.2419(64)
		1	0	2.25(18)	0.649(26)	0.131(12)	0.8533(70)
		−1	0	3.23(28)	0.742(21)	0.0916(95)	1.2259(63)
	C_{10}'	1	1	3.42(28)	0.740(21)	0.0851(89)	1.2955(54)
		1	−1	3.42(28)	0.740(21)	0.0852(89)	1.2955(54)
		−1	1	2.29(18)	0.642(27)	0.131(12)	0.8681(69)
		−1	−1	2.29(18)	0.642(27)	0.131(12)	0.8681(69)
		−1	−1	2.29(18)	0.642(27)	0.131(12)	0.8681(69)
		1	0	3.31(28)	0.744(21)	0.0880(92)	1.2531(57)
		−1	0	2.18(17)	0.643(27)	0.138(13)	0.8257(64)

Table C.10: The dependence of the Branching Ratio and the observables F_L, A_{FB} and R_ρ corresponding to $B^\pm \to \rho^\pm ll$ on the real and imaginary parts of the NP WC's $\Delta C_{9,10}$ and $C'_{9,10}$ for the q^2 bins $2-4$ and $4-6$ GeV^2 for a few benchmark values of the real and imaginary parts of the corresponding WC's.

TH-3118_176121005

Bin	C_i^{NP}	$Re(C_i^{NP})$	$Im(C_i^{NP})$	Observables			
				P_2^-	P_2^+	P_3^-	P_3^+
0.1	ΔC_9	1	1	-0.1293(52)	-0.1220(39)	-0.00042(29)	0.0017(11)
1		1	−1	-0.1261(52)	-0.1247(37)	0.00157(96)	-0.00022(35)
		−1	1	-0.1256(49)	-0.1188(36)	-0.00067(42)	0.00125(78)
		−1	−1	-0.1228(49)	-0.1212(34)	0.00110(67)	-0.00044(33)
		1	0	-0.1279(52)	-0.1235(38)	0.00059(37)	0.00074(54)
		−1	0	-0.1244(49)	-0.1201(35)	0.00022(14)	0.00041(29)
	ΔC_{10}	1	1	-0.0880(42)	-0.0966(28)	0.00040(25)	0.00057(42)
		1	−1	-0.1005(36)	-0.0853(38)	0.00040(25)	0.00057(42)
		−1	1	-0.1505(64)	-0.1570(43)	0.00039(25)	0.00056(41)
		−1	−1	-0.1628(57)	-0.1459(53)	0.00039(25)	0.00056(41)
		1	0	-0.0944(39)	-0.0911(28)	0.00040(25)	0.00057(42)
		−1	0	-0.1569(61)	-0.1517(44)	0.00039(25)	0.00056(41)
	$C_9^{'}$	1	1	-0.1256(50)	-0.1214(36)	0.0252(16)	-0.0344(17)
		1	−1	-0.1257(50)	-0.1213(36)	-0.0362(11)	0.0249(22)
		−1	1	-0.1260(50)	-0.1217(36)	0.0370(11)	-0.0239(25)
		−1	−1	-0.1260(50)	-0.1217(36)	-0.0245(16)	0.0356(20)
		1	0	-0.1258(50)	-0.1215(36)	-0.00546(59)	-0.0047(17)
		−1	0	-0.1262(50)	-0.1219(36)	0.00627(70)	0.0059(21)
	$C_{10}^{'}$	1	1	-0.1269(51)	-0.1223(37)	0.00615(51)	-0.00474(47)
		1	−1	-0.1266(51)	-0.1226(37)	-0.00536(53)	0.00587(55)
		−1	1	-0.1251(49)	-0.1205(36)	0.00615(51)	-0.00475(47)
		−1	−1	-0.1247(50)	-0.1208(36)	-0.00536(53)	0.00588(55)
		1	0	-0.1269(51)	-0.1226(37)	0.00039(25)	0.00057(41)
		−1	0	-0.1251(50)	-0.1208(36)	0.00040(25)	0.00057(41)
1-2	ΔC_9	1	1	-0.4508(72)	-0.386(21)	-0.0021(16)	0.0096(57)
		1	−1	-0.390(12)	-0.4420(82)	0.0093(54)	-0.0011(20)
		−1	1	-0.418(11)	-0.370(13)	-0.0028(17)	0.0054(32)
		−1	−1	-0.380(13)	-0.4055(83)	0.0049(28)	-0.0019(14)
		1	0	-0.429(11)	-0.421(16)	0.0041(25)	0.0047(32)
		−1	0	-0.404(13)	-0.393(10)	0.00122(79)	0.0019(13)
	ΔC_{10}	1	1	-0.319(17)	-0.3722(99)	0.0027(17)	0.0035(23)
		1	−1	-0.387(12)	-0.308(20)	0.0027(17)	0.0035(23)
		−1	1	-0.421(11)	-0.4647(53)	0.0020(13)	0.0026(18)
		−1	−1	-0.4712(50)	-0.416(19)	0.0020(13)	0.0026(18)
		1	0	-0.361(15)	-0.347(12)	0.0028(17)	0.0035(23)
		−1	0	-0.4533(85)	-0.447(12)	0.0021(13)	0.0027(18)
	$C_9^{'}$	1	1	-0.405(11)	-0.396(11)	0.0769(61)	-0.1255(62)
		1	−1	-0.406(11)	-0.395(11)	-0.1296(26)	0.076(10)
		−1	1	-0.407(11)	-0.398(11)	0.1345(32)	-0.071(12)
		−1	−1	-0.408(11)	-0.397(11)	-0.0729(67)	0.1317(78)
		1	0	-0.413(12)	-0.403(12)	-0.0267(38)	-0.0249(83)
		−1	0	-0.415(12)	-0.405(12)	0.0316(45)	0.031(10)
	$C_{10}^{'}$	1	1	-0.408(11)	-0.398(11)	0.0749(57)	-0.0638(42)
		1	−1	-0.407(11)	-0.399(11)	-0.0703(61)	0.0697(46)
		−1	1	-0.406(11)	-0.395(11)	0.0762(62)	-0.0648(41)
		−1	−1	-0.404(11)	-0.396(11)	-0.0715(62)	0.0708(50)
		1	0	-0.415(12)	-0.405(12)	0.0023(14)	0.0030(20)
		−1	0	-0.413(12)	-0.402(12)	0.0024(15)	0.0031(21)

Table C.11: The dependence of some of the optimized observables corresponding to $B^+ \to \rho^+ ll$ and $B^- \to \rho^- ll$ on the real and imaginary parts of the NP WC's $\Delta C_{9,10}$ and $C'_{9,10}$ for the q^2 bins $0.1 - 1$ and $1 - 2$ GeV^2 for a few benchmark values of the real and imaginary parts of the corresponding WC's.

TH-3118_176121005

Bin	C_i^{NP}	$Re(C_i^{NP})$	$Im(C_i^{NP})$	Observables			
				P_2^-	P_2^+	P_3^-	P_3^+
2-4	ΔC_9	1	1	0.051(35)	0.038(31)	-0.0011(18)	0.0131(70)
		1	−1	0.044(30)	0.048(40)	0.0124(67)	-0.00018(276)
		−1	1	-0.363(19)	-0.303(30)	-0.0039(23)	0.0092(50)
		−1	−1	-0.310(13)	-0.361(22)	0.0082(45)	-0.0027(21)
		1	0	0.050(34)	0.045(37)	0.0067(38)	0.0075(44)
		−1	0	-0.351(15)	-0.345(28)	0.0028(17)	0.0040(25)
	ΔC_{10}	1	1	-0.125(25)	-0.273(28)	0.0072(42)	0.0087(53)
		1	−1	-0.268(37)	-0.114(58)	0.0072(42)	0.0087(53)
		−1	1	-0.112(20)	-0.177(24)	0.0031(18)	0.0038(23)
		−1	−1	-0.173(28)	-0.108(37)	0.0031(18)	0.0038(23)
		1	0	-0.215(30)	-0.211(45)	0.0079(46)	0.0095(57)
		−1	0	-0.148(25)	-0.148(31)	0.0032(19)	0.0040(23)
	$C_9^{'}$	1	1	-0.159(25)	-0.160(33)	0.0024(75)	-0.0840(89)
		1	−1	-0.160(25)	-0.159(33)	-0.080(14)	-0.0021(189)
		−1	1	-0.157(25)	-0.157(33)	0.087(15)	0.013(21)
		−1	−1	-0.158(25)	-0.156(33)	0.0062(90)	0.0925(98)
		1	0	-0.169(26)	-0.168(35)	-0.0407(92)	-0.045(13)
		−1	0	-0.166(26)	-0.165(35)	0.049(11)	0.055(15)
	$C_{10}^{'}$	1	1	-0.163(24)	-0.159(32)	0.1998(49)	-0.1862(73)
		1	−1	-0.160(24)	-0.162(32)	-0.1915(77)	0.1965(38)
		−1	1	-0.157(26)	-0.154(34)	0.2108(75)	-0.1961(61)
		−1	−1	-0.154(26)	-0.157(34)	-0.2019(73)	0.2070(68)
		1	0	-0.170(25)	-0.169(34)	0.0044(25)	0.0054(32)
		−1	0	-0.165(27)	-0.164(36)	0.0047(28)	0.0058(35)
4-6	ΔC_9	1	1	0.4069(92)	0.3748(77)	0.0017(18)	0.0082(41)
		1	−1	0.354(20)	0.436(14)	0.0087(44)	0.0021(21)
		−1	1	0.011(23)	0.069(27)	-0.0013(14)	0.0081(41)
		−1	−1	0.010(20)	0.086(36)	0.0078(39)	-0.00023(171)
		1	0	0.398(16)	0.4214(79)	0.0057(32)	0.0056(30)
		−1	0	0.011(22)	0.081(32)	0.0039(22)	0.0046(26)
	ΔC_{10}	1	1	0.337(13)	0.249(16)	0.0079(43)	0.0080(43)
		1	−1	0.205(42)	0.388(28)	0.0079(43)	0.0080(43)
		−1	1	0.219(12)	0.206(14)	0.0033(18)	0.0035(20)
		−1	−1	0.164(24)	0.267(26)	0.0033(18)	0.0035(20)
		1	0	0.298(28)	0.347(17)	0.0086(47)	0.0088(47)
		−1	0	0.199(18)	0.246(20)	0.0034(19)	0.0037(20)
	$C_9^{'}$	1	1	0.218(20)	0.268(20)	-0.0905(69)	0.0303(75)
		1	−1	0.220(20)	0.265(19)	0.022(15)	-0.106(13)
		−1	1	0.211(19)	0.258(19)	-0.012(16)	0.113(15)
		−1	−1	0.212(19)	0.256(18)	0.0972(91)	-0.0193(85)
		1	0	0.232(21)	0.281(20)	-0.037(11)	-0.0403(100)
		−1	0	0.223(20)	0.270(19)	0.045(13)	0.049(12)
	$C_{10}^{'}$	1	1	0.203(19)	0.251(20)	0.2030(18)	-0.1843(92)
		1	−1	0.206(18)	0.249(20)	-0.1940(61)	0.1938(57)
		−1	1	0.225(21)	0.275(20)	0.2166(47)	-0.1959(94)
		−1	−1	0.228(21)	0.273(19)	-0.2069(42)	0.2062(82)
		1	0	0.215(20)	0.263(20)	0.0047(26)	0.0050(27)
		−1	0	0.240(23)	0.289(20)	0.0051(28)	0.0054(30)

Table C.12: The dependence of some of the optimized observables corresponding to $B^+ \to \rho^+ ll$ and $B^- \to \rho^- ll$ on the real and imaginary parts of the NP WC's $\Delta C_{9,10}$ and $C'_{9,10}$ for the q^2 bins $2-4$ and $4-6$ GeV^2 for a few benchmark values of the real and imaginary parts of the corresponding WC's.

TH-3118_176121005

Bin	C_i^{NP}	$Re(C_i^{NP})$	$Im(C_i^{NP})$	Observables			
				$P_6^{'-}$	$P_6^{'+}$	$P_8^{'-}$	$P_8^{'+}$
0.1-1	ΔC_9	1	1	-0.175(21)	-0.059(25)	0.180(14)	-0.211(26)
		1	−1	-0.181(23)	-0.062(27)	-0.037(16)	-0.085(29)
		−1	1	-0.159(19)	-0.068(30)	0.202(12)	-0.227(24)
		−1	−1	-0.164(20)	-0.072(31)	0.0052(176)	-0.082(27)
		1	0	-0.183(22)	-0.061(26)	0.075(16)	-0.150(28)
		−1	0	-0.166(20)	-0.071(31)	0.108(15)	-0.158(26)
	ΔC_{10}	1	1	-0.460(19)	0.111(23)	0.118(19)	-0.161(29)
		1	−1	0.130(23)	-0.213(22)	0.118(19)	-0.161(29)
		−1	1	-0.365(21)	0.066(34)	0.075(13)	-0.142(25)
		−1	−1	0.0093(229)	-0.219(32)	0.075(13)	-0.142(25)
		1	0	-0.173(21)	-0.051(22)	0.124(20)	-0.163(29)
		−1	0	-0.182(22)	-0.077(33)	0.077(13)	-0.143(25)
	C_9'	1	1	-0.170(21)	-0.074(32)	0.0027(162)	-0.113(28)
		1	−1	-0.163(19)	-0.071(31)	0.207(12)	-0.198(25)
		−1	1	-0.176(22)	-0.059(26)	-0.036(15)	-0.112(29)
		−1	−1	-0.168(20)	-0.058(25)	0.176(15)	-0.183(27)
		1	0	-0.171(20)	-0.073(32)	0.110(15)	-0.158(26)
		−1	0	-0.177(22)	-0.059(26)	0.075(16)	-0.149(28)
	C_{10}'	1	1	0.0093(230)	-0.220(32)	0.048(13)	-0.127(25)
		1	−1	-0.367(21)	0.067(34)	0.103(12)	-0.159(25)
		−1	1	0.130(23)	-0.212(22)	0.075(20)	-0.143(28)
		−1	−1	-0.458(19)	0.111(23)	0.161(18)	-0.178(29)
		1	0	-0.183(22)	-0.077(33)	0.077(13)	-0.144(25)
		−1	0	-0.172(20)	-0.051(22)	0.124(20)	-0.162(29)
1-2	ΔC_9	1	1	-0.083(43)	-0.159(34)	-0.012(11)	-0.182(30)
		1	−1	-0.071(36)	-0.168(39)	-0.2239(72)	0.033(37)
		−1	1	-0.077(40)	-0.166(37)	0.0108(85)	-0.149(24)
		−1	−1	-0.066(34)	-0.170(40)	-0.1902(57)	0.076(27)
		1	0	-0.079(40)	-0.166(37)	-0.1302(97)	-0.079(35)
		−1	0	-0.074(38)	-0.172(39)	-0.1011(70)	-0.038(27)
	ΔC_{10}	1	1	-0.378(37)	0.122(35)	-0.1516(91)	-0.066(35)
		1	−1	0.229(39)	-0.403(30)	-0.1516(91)	-0.066(35)
		−1	1	-0.246(38)	0.017(42)	-0.0867(55)	-0.049(26)
		−1	−1	0.101(37)	-0.371(37)	-0.0867(55)	-0.049(26)
		1	0	-0.079(40)	-0.144(33)	-0.1601(97)	-0.068(36)
		−1	0	-0.075(38)	-0.180(40)	-0.0890(56)	-0.050(27)
	C_9'	1	1	-0.074(38)	-0.182(41)	-0.1423(62)	-0.043(29)
		1	−1	-0.083(42)	-0.186(42)	-0.0054(63)	-0.062(27)
		−1	1	-0.066(34)	-0.145(33)	-0.193(11)	-0.053(33)
		−1	−1	-0.071(36)	-0.147(33)	-0.0780(83)	-0.068(31)
		1	0	-0.081(42)	-0.188(43)	-0.0806(55)	-0.054(29)
		−1	0	-0.070(36)	-0.148(33)	-0.1423(97)	-0.061(32)
	C_{10}'	1	1	0.108(40)	-0.394(40)	-0.1899(56)	0.014(27)
		1	−1	-0.263(40)	0.018(45)	0.0051(81)	-0.118(28)
		−1	1	0.213(36)	-0.376(27)	-0.2891(89)	0.017(32)
		−1	−1	-0.351(36)	0.113(32)	0.0077(122)	-0.140(34)
		1	0	-0.080(41)	-0.191(43)	-0.0950(57)	-0.053(28)
		−1	0	-0.073(38)	-0.134(30)	-0.1483(92)	-0.063(34)

Table C.13: The dependence of some of the optimized observables corresponding to $B^+ \to \rho^+ ll$ and $B^- \to \rho^- ll$ on the real and imaginary parts of the NP WC's $\Delta C_{9,10}$ and $C'_{9,10}$ for the q^2 bins $0.1 - 1$ and $1 - 2$ GeV^2 for a few benchmark values of the real and imaginary parts of the corresponding WC's.

TH-3118_176121005

Bin	C_i^{NP}	$Re(C_i^{NP})$	$Im(C_i^{NP})$	Observables			
				$P_6^{'-}$	$P_6^{'+}$	$P_8^{'-}$	$P_8^{'+}$
2-4	ΔC_9	1	1	0.010(42)	-0.226(28)	0.0096(166)	-0.171(20)
		1	−1	0.0094(366)	-0.244(36)	-0.132(16)	0.0026(302)
		−1	1	0.012(49)	-0.271(37)	0.0114(87)	-0.138(17)
		−1	−1	0.011(41)	-0.282(45)	-0.1499(73)	0.072(24)
		1	0	0.010(41)	-0.243(33)	-0.070(17)	-0.090(27)
		−1	0	0.012(47)	-0.288(42)	-0.0800(85)	-0.036(22)
	ΔC_{10}	1	1	-0.237(50)	0.015(47)	-0.110(18)	-0.090(34)
		1	−1	0.262(47)	-0.552(27)	-0.110(18)	-0.090(34)
		−1	1	-0.108(40)	-0.091(39)	-0.0518(92)	-0.048(18)
		−1	−1	0.127(37)	-0.392(31)	-0.0518(92)	-0.048(18)
		1	0	0.014(52)	-0.285(38)	-0.119(20)	-0.095(36)
		−1	0	0.0100(397)	-0.249(36)	-0.0536(95)	-0.049(19)
	C_9'	1	1	0.011(45)	-0.281(40)	0.0034(136)	-0.130(23)
		1	−1	0.013(49)	-0.295(41)	-0.0796(67)	0.0012(197)
		−1	1	0.0092(364)	-0.220(31)	-0.065(18)	-0.110(27)
		−1	−1	0.0098(388)	-0.227(32)	-0.134(13)	-0.0073(254)
		1	0	0.013(49)	-0.301(42)	-0.038(10)	-0.069(22)
		−1	0	0.0099(392)	-0.232(33)	-0.103(16)	-0.062(27)
	C_{10}'	1	1	0.149(43)	-0.457(35)	-0.2082(98)	0.069(22)
		1	−1	-0.126(47)	-0.106(45)	0.087(13)	-0.181(21)
		−1	1	0.205(36)	-0.435(23)	-0.297(14)	0.088(27)
		−1	−1	-0.186(41)	0.012(37)	0.124(17)	-0.230(27)
		1	0	0.012(47)	-0.292(41)	-0.063(11)	-0.058(22)
		−1	0	0.010(40)	-0.221(31)	-0.091(16)	-0.074(28)
4-6	ΔC_9	1	1	-0.040(40)	-0.185(26)	-0.0019(184)	-0.124(14)
		1	−1	-0.036(35)	-0.194(31)	-0.078(18)	-0.048(22)
		−1	1	-0.057(57)	-0.270(40)	0.014(12)	-0.115(10)
		−1	−1	-0.049(49)	-0.285(48)	-0.094(12)	-0.00030(2094)
		1	0	-0.039(39)	-0.196(29)	-0.044(19)	-0.090(18)
		−1	0	-0.056(55)	-0.291(45)	-0.046(13)	-0.062(17)
	ΔC_{10}	1	1	-0.196(53)	-0.102(48)	-0.065(24)	-0.111(24)
		1	−1	0.095(47)	-0.389(24)	-0.065(24)	-0.111(24)
		−1	1	-0.111(42)	-0.141(39)	-0.032(12)	-0.057(13)
		−1	−1	0.029(39)	-0.287(29)	-0.032(12)	-0.057(13)
		1	0	-0.054(53)	-0.262(37)	-0.070(26)	-0.118(25)
		−1	0	-0.043(42)	-0.221(35)	-0.033(12)	-0.059(14)
	C_9'	1	1	-0.050(49)	-0.254(39)	0.079(16)	-0.186(15)
		1	−1	-0.052(51)	-0.265(40)	-0.122(12)	0.031(14)
		−1	1	-0.039(38)	-0.197(30)	0.016(19)	-0.155(20)
		−1	−1	-0.040(40)	-0.202(31)	-0.141(17)	0.013(19)
		1	0	-0.053(53)	-0.272(41)	-0.021(15)	-0.084(15)
		−1	0	-0.041(41)	-0.207(32)	-0.064(19)	-0.075(20)
	C_{10}'	1	1	0.034(46)	-0.334(32)	-0.179(14)	0.066(17)
		1	−1	-0.130(49)	-0.163(45)	0.105(15)	-0.198(14)
		−1	1	0.074(37)	-0.308(22)	-0.248(19)	0.087(23)
		−1	−1	-0.153(41)	-0.082(39)	0.145(20)	-0.263(18)
		1	0	-0.050(50)	-0.258(40)	-0.039(14)	-0.069(16)
		−1	0	-0.041(41)	-0.205(31)	-0.054(20)	-0.092(21)

Table C.14: The dependence of some of the optimized observables corresponding to $B^+ \to \rho^+ ll$ and $B^- \to \rho^- ll$ on the real and imaginary parts of the NP WC's $\Delta C_{9,10}$ and $C'_{9,10}$ for the q^2 bins $2-4$ and $4-6$ GeV^2 for a few benchmark values of the real and imaginary parts of the corresponding WC's.

TH-3118_176121005

Bin	C_i^{NP}	$Re(C_i^{NP})$	$Im(C_i^{NP})$	Observables			
				$\overline{P_2^0}$	P_2^0	$\overline{P_3^0}$	P_3^0
0.1-1	ΔC_9	1	1	-0.0784(22)	-0.0791(36)	-0.00067(42)	0.00146(91)
		1	−1	-0.0772(21)	-0.0803(33)	0.00131(80)	-0.00046(37)
		−1	1	-0.0764(21)	-0.0769(32)	-0.00079(48)	0.00115(71)
		−1	−1	-0.0753(21)	-0.0778(30)	0.00097(59)	-0.00056(37)
		1	0	-0.0779(22)	-0.0798(34)	0.00033(20)	0.00051(37)
		−1	0	-0.0759(21)	-0.0775(31)	0.000099(64)	0.00030(22)
	ΔC_{10}	1	1	-0.0513(19)	-0.0645(18)	0.00021(12)	0.00040(29)
		1	−1	-0.0636(19)	-0.0530(39)	0.00021(12)	0.00040(29)
		−1	1	-0.0896(27)	-0.1034(31)	0.00020(12)	0.00039(29)
		−1	−1	-0.1016(27)	-0.0921(53)	0.00020(12)	0.00039(29)
		1	0	-0.0576(17)	-0.0588(25)	0.00021(12)	0.00040(29)
		−1	0	-0.0957(26)	-0.0979(40)	0.00020(12)	0.00039(29)
	C_9'	1	1	-0.0766(21)	-0.0784(32)	0.0270(11)	-0.0328(11)
		1	−1	-0.0767(21)	-0.0783(32)	-0.0339(11)	0.0269(18)
		−1	1	-0.0768(21)	-0.0786(33)	0.0344(11)	-0.0262(20)
		−1	−1	-0.0769(21)	-0.0785(33)	-0.0267(11)	0.0337(15)
		1	0	-0.0768(21)	-0.0785(32)	-0.00346(27)	-0.0029(13)
		−1	0	-0.0770(22)	-0.0787(33)	0.00388(29)	0.0038(15)
	C_{10}'	1	1	-0.0775(22)	-0.0789(33)	0.00587(43)	-0.00499(41)
		1	−1	-0.0772(22)	-0.0792(33)	-0.00545(42)	0.00578(46)
		−1	1	-0.0764(21)	-0.0777(32)	0.00587(44)	-0.00499(41)
		−1	−1	-0.0760(21)	-0.0780(32)	-0.00546(43)	0.00579(46)
		1	0	-0.0774(22)	-0.0791(33)	0.00021(12)	0.00040(29)
		−1	0	-0.0763(21)	-0.0780(32)	0.00021(12)	0.00040(29)
1-2	ΔC_9	1	1	-0.2640(47)	-0.257(20)	-0.0037(23)	0.0084(50)
		1	−1	-0.2417(27)	-0.281(14)	0.0079(46)	-0.0027(21)
		−1	1	-0.2497(47)	-0.243(13)	-0.0034(20)	0.0050(28)
		−1	−1	-0.2355(41)	-0.2577(91)	0.0043(25)	-0.0025(16)
		1	0	-0.2584(35)	-0.274(18)	0.0024(14)	0.0032(22)
		−1	0	-0.2462(46)	-0.254(11)	0.00060(39)	0.00138(96)
	ΔC_{10}	1	1	-0.1798(67)	-0.2536(70)	0.00149(91)	0.0024(16)
		1	−1	-0.2470(79)	-0.189(21)	0.00149(91)	0.0024(16)
		−1	1	-0.2459(20)	-0.3097(74)	0.00111(68)	0.0018(11)
		−1	−1	-0.2962(78)	-0.260(21)	0.00111(68)	0.0018(11)
		1	0	-0.2182(53)	-0.226(13)	0.00152(93)	0.0024(17)
		−1	0	-0.2755(36)	-0.290(14)	0.00113(69)	0.0018(13)
	C_9'	1	1	-0.2456(36)	-0.257(13)	0.0865(43)	-0.1169(40)
		1	−1	-0.2460(37)	-0.256(13)	-0.1191(22)	0.0856(81)
		−1	1	-0.2467(35)	-0.258(13)	0.1220(22)	-0.0821(92)
		−1	−1	-0.2472(35)	-0.258(13)	-0.0845(45)	0.1214(50)
		1	0	-0.2504(39)	-0.261(14)	-0.0165(20)	-0.0158(57)
		−1	0	-0.2517(37)	-0.263(14)	0.0192(23)	0.0201(70)
	C_{10}'	1	1	-0.2481(38)	-0.258(13)	0.0726(52)	-0.0657(42)
		1	−1	-0.2464(35)	-0.259(13)	-0.0701(52)	0.0698(43)
		−1	1	-0.2463(36)	-0.256(13)	0.0739(55)	-0.0667(42)
		−1	−1	-0.2446(36)	-0.257(13)	-0.0713(54)	0.0709(46)
		1	0	-0.2519(39)	-0.263(14)	0.00129(78)	0.0021(14)
		−1	0	-0.2502(38)	-0.261(14)	0.00131(80)	0.0021(15)

Table C.15: The dependence of some of the optimized observables corresponding to tagged $\bar{B}^0 \to \rho^0 ll$ and $B^0 \to \rho^0 ll$ on the real and imaginary parts of the NP WC's $\Delta C_{9,10}$ and $C'_{9,10}$ for the q^2 bins $0.1-1$ and $1-2$ GeV^2 for a few benchmark values of the real and imaginary parts of the corresponding WC's.

TH-3118_176121005

Bin	C_i^{NP}	$Re(C_i^{NP})$	$Im(C_i^{NP})$	Observables			
				$\overline{P_2^0}$	P_2^0	$\overline{P_3^0}$	P_3^0
2-4	ΔC_9	1	1	0.032(27)	0.024(26)	-0.0037(23)	0.0112(60)
		1	−1	0.029(25)	0.028(30)	0.0105(56)	-0.0028(25)
		−1	1	-0.219(16)	-0.197(25)	-0.0050(28)	0.0084(46)
		−1	−1	-0.199(12)	-0.221(21)	0.0073(40)	-0.0039(23)
		1	0	0.032(27)	0.028(29)	0.0040(22)	0.0049(30)
		−1	0	-0.219(14)	-0.218(25)	0.00150(91)	0.0027(17)
	ΔC_{10}	1	1	-0.049(16)	-0.201(19)	0.0042(23)	0.0059(35)
		1	−1	-0.195(36)	-0.045(51)	0.0042(23)	0.0059(35)
		−1	1	-0.057(14)	-0.124(18)	0.0018(10)	0.0025(16)
		−1	−1	-0.120(25)	-0.057(32)	0.0018(10)	0.0025(16)
		1	0	-0.133(24)	-0.135(37)	0.0045(26)	0.0064(39)
		−1	0	-0.092(20)	-0.094(25)	0.0019(11)	0.0026(16)
	C_9'	1	1	-0.099(20)	-0.101(27)	0.0178(63)	-0.0691(72)
		1	−1	-0.100(20)	-0.101(27)	-0.0642(88)	0.013(14)
		−1	1	-0.098(20)	-0.100(27)	0.0679(92)	-0.0056(154)
		−1	−1	-0.098(20)	-0.099(27)	-0.0126(70)	0.0746(77)
		1	0	-0.105(21)	-0.107(28)	-0.0244(52)	-0.0295(86)
		−1	0	-0.103(21)	-0.105(28)	0.0292(60)	0.036(10)
	C_{10}'	1	1	-0.102(20)	-0.101(26)	0.1973(51)	-0.1887(66)
		1	−1	-0.099(20)	-0.103(26)	-0.1924(67)	0.1956(41)
		−1	1	-0.098(21)	-0.097(28)	0.2080(69)	-0.1987(60)
		−1	−1	-0.095(21)	-0.100(27)	-0.2029(67)	0.2061(63)
		1	0	-0.106(21)	-0.107(28)	0.0025(15)	0.0036(22)
		−1	0	-0.102(22)	-0.104(29)	0.0027(16)	0.0039(23)
4-6	ΔC_9	1	1	0.234(14)	0.2532(81)	-0.00053(103)	0.0067(33)
		1	−1	0.216(18)	0.280(14)	0.0068(34)	-0.000057(1290)
		−1	1	-0.0064(201)	0.057(24)	-0.0028(16)	0.0071(35)
		−1	−1	-0.0053(179)	0.065(29)	0.0066(33)	-0.0019(15)
		1	0	0.236(17)	0.278(11)	0.0035(19)	0.0037(20)
		−1	0	-0.0062(201)	0.064(27)	0.0023(13)	0.0031(17)
	ΔC_{10}	1	1	0.2207(87)	0.147(10)	0.0047(26)	0.0053(28)
		1	−1	0.087(41)	0.285(32)	0.0047(26)	0.0053(28)
		−1	1	0.1379(91)	0.129(12)	0.0020(11)	0.0023(13)
		−1	−1	0.081(23)	0.190(25)	0.0020(11)	0.0023(13)
		1	0	0.169(27)	0.236(18)	0.0051(28)	0.0058(31)
		−1	0	0.114(17)	0.165(18)	0.0021(11)	0.0024(13)
	C_9'	1	1	0.125(19)	0.181(19)	-0.0789(47)	0.0410(57)
		1	−1	0.125(19)	0.179(18)	0.0381(95)	-0.0912(88)
		−1	1	0.120(18)	0.174(18)	-0.031(10)	0.095(10)
		−1	−1	0.121(18)	0.173(18)	0.0819(57)	-0.0330(61)
		1	0	0.132(20)	0.190(19)	-0.0216(66)	-0.0267(65)
		−1	0	0.127(19)	0.183(19)	0.0266(77)	0.0323(77)
	C_{10}'	1	1	0.115(18)	0.170(19)	0.1994(31)	-0.1876(80)
		1	−1	0.118(17)	0.168(18)	-0.1940(57)	0.1938(55)
		−1	1	0.128(20)	0.186(19)	0.2125(47)	-0.1996(81)
		−1	−1	0.131(19)	0.184(18)	-0.2068(47)	0.2063(74)
		1	0	0.123(19)	0.178(19)	0.0028(15)	0.0033(18)
		−1	0	0.137(21)	0.195(19)	0.0031(17)	0.0035(20)

Table C.16: The dependence of some of the optimized observables corresponding to tagged $\bar{B}^0 \to \rho^0 ll$ and $B^0 \to \rho^0 ll$ on the real and imaginary parts of the NP WC's $\Delta C_{9,10}$ and $C'_{9,10}$ for the q^2 bins $2-4$ and $4-6$ GeV^2 for a few benchmark values of the real and imaginary parts of the corresponding WC's.

TH-3118_176121005

Bin	C_i^{NP}	$Re(C_i^{NP})$	$Im(C_i^{NP})$	Observables			
				$\overline{P_6'^0}$	$P_6'^0$	$\overline{P_8'^0}$	$P_8'^0$
0.1-1	ΔC_9	1	1	-0.131(20)	-0.110(33)	0.0924(28)	-0.148(20)
		1	−1	-0.134(21)	-0.113(35)	-0.0900(33)	0.026(22)
		−1	1	-0.155(24)	-0.132(40)	0.1345(45)	-0.159(16)
		−1	−1	-0.161(25)	-0.136(42)	-0.0821(54)	0.050(18)
		1	0	-0.135(21)	-0.113(35)	0.0021(32)	-0.063(21)
		−1	0	-0.162(25)	-0.137(42)	0.0288(53)	-0.057(18)
	ΔC_{10}	1	1	-0.278(22)	0.050(35)	0.0164(47)	-0.068(22)
		1	−1	0.027(18)	-0.258(29)	0.0164(47)	-0.068(22)
		−1	1	-0.270(26)	-0.018(44)	0.0121(35)	-0.052(17)
		−1	−1	-0.045(23)	-0.251(38)	0.0121(35)	-0.052(17)
		1	0	-0.129(20)	-0.107(33)	0.0168(49)	-0.070(23)
		−1	0	-0.160(25)	-0.136(42)	0.0122(35)	-0.053(17)
	C_9'	1	1	-0.166(26)	-0.140(43)	-0.0625(47)	0.027(18)
		1	−1	-0.159(24)	-0.137(41)	0.1105(51)	-0.137(16)
		−1	1	-0.130(20)	-0.109(33)	-0.0652(28)	0.0031(211)
		−1	−1	-0.127(20)	-0.108(33)	0.0722(35)	-0.125(20)
		1	0	-0.167(26)	-0.141(43)	0.0264(52)	-0.057(18)
		−1	0	-0.130(20)	-0.110(34)	0.0045(33)	-0.062(21)
	C_{10}'	1	1	-0.045(23)	-0.253(39)	-0.0116(39)	-0.030(17)
		1	−1	-0.271(26)	-0.018(44)	0.0358(32)	-0.074(17)
		−1	1	0.027(17)	-0.257(29)	-0.0156(52)	-0.039(22)
		−1	−1	-0.277(22)	0.049(35)	0.0481(45)	-0.097(22)
		1	0	-0.161(25)	-0.137(42)	0.0123(35)	-0.053(17)
		−1	0	-0.128(20)	-0.106(33)	0.0167(49)	-0.070(23)
1-2	ΔC_9	1	1	-0.181(32)	-0.154(40)	0.0798(52)	-0.174(19)
		1	−1	-0.175(31)	-0.162(45)	-0.1536(28)	0.056(25)
		−1	1	-0.185(33)	-0.161(43)	0.1122(14)	-0.157(13)
		−1	−1	-0.182(33)	-0.167(47)	-0.1294(16)	0.083(16)
		1	0	-0.183(32)	-0.162(43)	-0.0399(42)	-0.063(23)
		−1	0	-0.190(34)	-0.169(46)	-0.0097(13)	-0.040(16)
	ΔC_{10}	1	1	-0.349(31)	0.047(45)	-0.0304(30)	-0.062(23)
		1	−1	0.014(28)	-0.340(34)	-0.0304(30)	-0.062(23)
		−1	1	-0.300(34)	-0.036(48)	-0.0196(20)	-0.041(16)
		−1	−1	-0.066(32)	-0.292(41)	-0.0196(20)	-0.041(16)
		1	0	-0.174(31)	-0.151(41)	-0.0316(31)	-0.064(24)
		−1	0	-0.187(34)	-0.168(46)	-0.0200(20)	-0.042(16)
	C_9'	1	1	-0.203(36)	-0.180(49)	-0.0563(35)	-0.0037(170)
		1	−1	-0.200(35)	-0.179(48)	0.0255(38)	-0.079(15)
		−1	1	-0.160(29)	-0.141(38)	-0.0634(49)	-0.026(22)
		−1	−1	-0.158(28)	-0.141(38)	0.0013(35)	-0.086(20)
		1	0	-0.208(37)	-0.185(50)	-0.0156(15)	-0.043(16)
		−1	0	-0.163(29)	-0.144(39)	-0.0317(34)	-0.058(22)
	C_{10}'	1	1	-0.070(34)	-0.310(43)	-0.1070(34)	0.038(17)
		1	−1	-0.320(36)	-0.039(51)	0.0653(43)	-0.126(17)
		−1	1	0.013(26)	-0.317(32)	-0.1448(44)	0.051(22)
		−1	−1	-0.324(30)	0.044(42)	0.0883(56)	-0.167(22)
		1	0	-0.200(35)	-0.179(48)	-0.0214(21)	-0.045(17)
		−1	0	-0.161(29)	-0.141(38)	-0.0293(30)	-0.060(23)

Table C.17: The dependence of some of the optimized observables corresponding to tagged $\bar{B}^0 \to \rho^0 ll$ and $B^0 \to \rho^0 ll$ on the real and imaginary parts of the NP WC's $\Delta C_{9,10}$ and $C'_{9,10}$ for the q^2 bins $0.1-1$ and $1-2$ GeV^2 for a few benchmark values of the real and imaginary parts of the corresponding WC's.

TH-3118_176121005

Bin	C_i^{NP}	$Re(C_i^{NP})$	$Im(C_i^{NP})$	Observables			
				$\overline{P_6'^0}$	$P_6'^0$	$\overline{P_8'^0}$	$P_8'^0$
2-4	ΔC_9	1	1	-0.155(36)	-0.140(33)	0.0426(88)	-0.134(12)
		1	−1	-0.147(33)	-0.151(39)	-0.1219(82)	0.031(19)
		−1	1	-0.180(41)	-0.166(41)	0.0787(45)	-0.1321(79)
		−1	−1	-0.173(38)	-0.178(47)	-0.1158(35)	0.064(14)
		1	0	-0.157(36)	-0.152(37)	-0.0435(89)	-0.057(16)
		−1	0	-0.185(41)	-0.180(46)	-0.0214(42)	-0.039(12)
	ΔC_{10}	1	1	-0.347(42)	0.0032(523)	-0.0479(92)	-0.069(20)
		1	−1	-0.015(38)	-0.351(33)	-0.0479(92)	-0.069(20)
		−1	1	-0.232(36)	-0.059(41)	-0.0235(47)	-0.035(10)
		−1	−1	-0.069(33)	-0.235(33)	-0.0235(47)	-0.035(10)
		1	0	-0.194(42)	-0.186(45)	-0.0515(99)	-0.074(22)
		−1	0	-0.156(36)	-0.152(38)	-0.0243(50)	-0.036(11)
	C_9'	1	1	-0.185(42)	-0.180(45)	0.0273(83)	-0.092(12)
		1	−1	-0.183(41)	-0.178(44)	-0.0788(47)	0.018(11)
		−1	1	-0.144(33)	-0.140(35)	0.0053(99)	-0.097(17)
		−1	−1	-0.143(32)	-0.139(35)	-0.0774(64)	-0.011(16)
		1	0	-0.194(44)	-0.188(47)	-0.0273(52)	-0.039(11)
		−1	0	-0.150(34)	-0.145(36)	-0.0377(78)	-0.056(17)
	C_{10}'	1	1	-0.081(38)	-0.274(38)	-0.1684(57)	0.098(13)
		1	−1	-0.271(42)	-0.069(48)	0.1135(73)	-0.178(12)
		−1	1	-0.012(30)	-0.276(28)	-0.2311(67)	0.133(18)
		−1	−1	-0.273(35)	0.0023(414)	0.1558(94)	-0.242(16)
		1	0	-0.183(41)	-0.178(44)	-0.0286(57)	-0.042(12)
		−1	0	-0.150(34)	-0.144(36)	-0.0397(80)	-0.058(17)
4-6	ΔC_9	1	1	-0.129(36)	-0.118(30)	0.0027(110)	-0.0787(79)
		1	−1	-0.124(34)	-0.125(33)	-0.078(11)	-0.0055(138)
		−1	1	-0.185(51)	-0.171(44)	0.0333(76)	-0.0868(50)
		−1	−1	-0.177(47)	-0.183(50)	-0.0825(68)	0.021(12)
		1	0	-0.131(36)	-0.126(33)	-0.040(11)	-0.045(11)
		−1	0	-0.190(52)	-0.187(49)	-0.0272(77)	-0.0368(92)
	ΔC_{10}	1	1	-0.265(49)	-0.079(51)	-0.050(14)	-0.060(14)
		1	−1	-0.071(42)	-0.242(31)	-0.050(14)	-0.060(14)
		−1	1	-0.186(41)	-0.095(41)	-0.0246(70)	-0.0298(76)
		−1	−1	-0.092(37)	-0.177(32)	-0.0246(70)	-0.0298(76)
		1	0	-0.180(49)	-0.172(43)	-0.054(15)	-0.064(15)
		−1	0	-0.144(40)	-0.141(37)	-0.0255(73)	-0.0308(79)
	C_9'	1	1	-0.172(47)	-0.167(44)	0.0735(99)	-0.1392(87)
		1	−1	-0.170(47)	-0.166(43)	-0.1325(70)	0.0743(82)
		−1	1	-0.133(37)	-0.128(34)	0.044(12)	-0.128(12)
		−1	−1	-0.132(36)	-0.128(34)	-0.1151(97)	0.036(12)
		1	0	-0.180(49)	-0.175(46)	-0.0316(85)	-0.0338(85)
		−1	0	-0.138(38)	-0.133(35)	-0.037(11)	-0.048(12)
	C_{10}'	1	1	-0.107(43)	-0.205(36)	-0.1689(85)	0.102(11)
		1	−1	-0.218(47)	-0.111(47)	0.1113(92)	-0.1717(81)
		−1	1	-0.056(33)	-0.192(26)	-0.232(11)	0.140(14)
		−1	−1	-0.207(39)	-0.063(41)	0.153(12)	-0.234(10)
		1	0	-0.169(47)	-0.164(43)	-0.0299(85)	-0.0360(91)
		−1	0	-0.139(38)	-0.134(35)	-0.042(12)	-0.050(12)

Table C.18: The dependence of some of the optimized observables corresponding to tagged $\bar{B}^0 \to \rho^0 ll$ and $B^0 \to \rho^0 ll$ on the real and imaginary parts of the NP WC's $\Delta C_{9,10}$ and $C'_{9,10}$ for the q^2 bins $2-4$ and $4-6$ GeV^2 for a few benchmark values of the real and imaginary parts of the corresponding WC's.

TH-3118_176121005

Bin	C_i^{NP}	$Re(C_i^{NP})$	$Im(C_i^{NP})$	Observables		
				P_1	P_4'	P_6'
0.1-1	ΔC_9	1	1	0.0037(28)	0.2265(54)	-0.099(22)
		1	−1	0.0037(28)	0.2326(34)	-0.101(23)
		−1	1	0.0017(16)	0.1430(59)	-0.121(27)
		−1	−1	0.0017(16)	0.1494(31)	-0.125(29)
		1	0	0.0038(28)	0.2361(42)	-0.102(23)
		−1	0	0.0017(17)	0.1533(44)	-0.126(29)
	ΔC_{10}	1	1	0.0032(25)	0.2535(42)	-0.090(25)
		1	−1	0.0032(25)	0.2535(42)	-0.103(19)
		−1	1	0.0022(19)	0.1466(39)	-0.116(30)
		−1	−1	0.0022(19)	0.1466(39)	-0.125(25)
		1	0	0.0032(25)	0.2640(43)	-0.099(23)
		−1	0	0.0022(19)	0.1515(39)	-0.122(28)
	C_9'	1	1	-0.0403(28)	0.1531(32)	-0.128(29)
		1	−1	-0.0399(23)	0.1466(60)	-0.124(28)
		−1	1	0.0439(23)	0.2269(34)	-0.099(23)
		−1	−1	0.0440(28)	0.2210(52)	-0.096(22)
		1	0	-0.0402(26)	0.1571(45)	-0.129(29)
		−1	0	0.0442(25)	0.2303(41)	-0.099(23)
	C_{10}'	1	1	-0.0049(21)	0.1471(39)	-0.126(25)
		1	−1	-0.0049(21)	0.1471(39)	-0.116(30)
		−1	1	0.0106(23)	0.2526(42)	-0.102(19)
		−1	−1	0.0106(23)	0.2526(42)	-0.090(25)
		1	0	-0.0049(22)	0.1521(39)	-0.123(28)
		−1	0	0.0107(23)	0.2630(42)	-0.099(22)
1-2	ΔC_9	1	1	0.0033(43)	0.045(14)	-0.149(33)
		1	−1	0.0036(45)	0.048(13)	-0.151(34)
		−1	1	-0.0012(26)	-0.0095(94)	-0.162(36)
		−1	−1	-0.00096(275)	-0.0061(88)	-0.165(38)
		1	0	0.0046(50)	0.060(13)	-0.154(34)
		−1	0	-0.00031(299)	0.0052(89)	-0.169(38)
	ΔC_{10}	1	1	0.0091(78)	0.144(10)	-0.133(38)
		1	−1	0.0091(78)	0.144(10)	-0.157(28)
		−1	1	-0.0052(21)	-0.060(11)	-0.152(39)
		−1	−1	-0.0052(21)	-0.060(11)	-0.167(33)
		1	0	0.0104(85)	0.166(10)	-0.151(34)
		−1	0	-0.0045(20)	-0.051(11)	-0.163(37)
	C_9'	1	1	-0.1769(92)	-0.0067(95)	-0.179(40)
		1	−1	-0.1780(52)	-0.010(10)	-0.177(39)
		−1	1	0.1713(34)	0.044(12)	-0.137(31)
		−1	−1	0.1695(77)	0.040(12)	-0.136(30)
		1	0	-0.1803(70)	0.0056(97)	-0.184(41)
		−1	0	0.1748(52)	0.054(12)	-0.140(31)
	C_{10}'	1	1	-0.1143(78)	-0.063(12)	-0.176(34)
		1	−1	-0.1143(78)	-0.063(12)	-0.160(41)
		−1	1	0.1255(86)	0.1357(99)	-0.148(26)
		−1	−1	0.1255(86)	0.1357(99)	-0.125(35)
		1	0	-0.1157(82)	-0.054(12)	-0.172(38)
		−1	0	0.1290(92)	0.1556(98)	-0.142(32)

Table C.19: The dependence of the optimized observables corresponding to $\bar{B}(B) \to \rho^0 ll$ on the real and imaginary parts of the NP WC's $\Delta C_{9,10}$ and $C'_{9,10}$ for the q^2 bins $0.1-1$ and $1-2$ GeV^2 for a few benchmark values of the real and imaginary parts of the corresponding WC's.

TH-3118_176121005

Bin	C_i^{NP}	$Re(C_i^{NP})$	$Im(C_i^{NP})$	Observables		
				P_1	P_4'	P_6'
2-4	ΔC_9	1	1	-0.056(25)	-0.331(15)	-0.138(33)
		1	−1	-0.056(25)	-0.330(15)	-0.140(34)
		−1	1	-0.036(15)	-0.280(13)	-0.167(39)
		−1	−1	-0.035(14)	-0.278(13)	-0.169(41)
		1	0	-0.056(25)	-0.325(16)	-0.145(34)
		−1	0	-0.034(14)	-0.268(13)	-0.176(42)
	ΔC_{10}	1	1	-0.035(15)	-0.212(19)	-0.160(45)
		1	−1	-0.035(15)	-0.212(19)	-0.176(33)
		−1	1	-0.050(22)	-0.351(12)	-0.139(37)
		−1	−1	-0.050(22)	-0.351(12)	-0.146(31)
		1	0	-0.033(14)	-0.194(20)	-0.179(42)
		−1	0	-0.049(22)	-0.346(12)	-0.147(35)
	C_9'	1	1	-0.116(23)	-0.288(13)	-0.175(42)
		1	−1	-0.127(21)	-0.293(13)	-0.174(41)
		−1	1	0.033(23)	-0.315(16)	-0.134(32)
		−1	−1	0.021(24)	-0.319(15)	-0.133(32)
		1	0	-0.125(22)	-0.280(13)	-0.184(44)
		−1	0	0.032(23)	-0.310(16)	-0.139(33)
	C_{10}'	1	1	-0.389(19)	-0.403(13)	-0.168(36)
		1	−1	-0.389(19)	-0.403(13)	-0.159(42)
		−1	1	0.333(19)	-0.170(15)	-0.141(27)
		−1	−1	0.333(19)	-0.170(15)	-0.128(37)
		1	0	-0.405(19)	-0.400(13)	-0.170(41)
		−1	0	0.355(18)	-0.153(15)	-0.142(34)
4-6	ΔC_9	1	1	-0.089(35)	-0.475(11)	-0.121(32)
		1	−1	-0.089(35)	-0.475(11)	-0.122(33)
		−1	1	-0.075(29)	-0.443(11)	-0.175(47)
		−1	−1	-0.075(28)	-0.442(11)	-0.177(48)
		1	0	-0.090(35)	-0.474(11)	-0.126(34)
		−1	0	-0.075(28)	-0.439(11)	-0.186(50)
	ΔC_{10}	1	1	-0.087(34)	-0.442(14)	-0.166(48)
		1	−1	-0.087(34)	-0.442(14)	-0.155(36)
		−1	1	-0.081(31)	-0.4724(95)	-0.138(40)
		−1	−1	-0.081(31)	-0.4724(95)	-0.133(34)
		1	0	-0.088(35)	-0.438(14)	-0.172(45)
		−1	0	-0.081(31)	-0.4713(97)	-0.140(38)
	C_9'	1	1	0.043(32)	-0.417(11)	-0.167(45)
		1	−1	0.031(32)	-0.420(11)	-0.166(44)
		−1	1	-0.192(32)	-0.497(10)	-0.128(34)
		−1	−1	-0.203(31)	-0.500(10)	-0.127(34)
		1	0	0.044(32)	-0.414(11)	-0.175(47)
		−1	0	-0.204(32)	-0.499(11)	-0.133(36)
	C_{10}'	1	1	-0.452(28)	-0.5475(91)	-0.154(39)
		1	−1	-0.452(28)	-0.5475(91)	-0.160(46)
		−1	1	0.316(31)	-0.350(12)	-0.123(29)
		−1	−1	0.316(31)	-0.350(12)	-0.132(39)
		−1	−1	0.316(31)	-0.350(12)	-0.132(39)
		1	0	-0.471(28)	-0.5498(92)	-0.163(44)
		−1	0	0.338(31)	-0.342(12)	-0.135(36)

Table C.20: The dependence of the optimized observables corresponding to $\bar{B}(B) \to \rho^0 ll$ on the real and imaginary parts of the NP WC's $\Delta C_{9,10}$ and $C'_{9,10}$ for the q^2 bins $2-4$ and $4-6$ GeV^2 for a few benchmark values of the real and imaginary parts of the corresponding WC's.

TH-3118_176121005

Bin	C_i^{NP}	$Re(C_i^{NP})$	$Im(C_i^{NP})$	Observables			
				A_5	A_{6s}	A_8	A_9
0.1-1	ΔC_9	1	1	-0.0022(46)	0.0026(22)	0.0474(42)	0.00047(27)
		1	−1	-0.0022(47)	0.0027(23)	-0.0221(47)	-0.00039(24)
		−1	1	-0.0024(51)	0.0029(23)	0.0529(36)	0.00052(31)
		−1	−1	-0.0024(52)	0.0029(25)	-0.0233(43)	-0.00042(25)
		1	0	-0.0022(47)	0.0027(23)	0.0130(46)	0.000044(47)
		−1	0	-0.0024(52)	0.0029(25)	0.0153(39)	0.000057(44)
	ΔC_{10}	1	1	-0.01521(92)	0.00872(59)	0.0155(47)	0.000055(49)
		1	−1	0.0115(73)	-0.0042(34)	0.0155(47)	0.000055(49)
		−1	1	-0.0135(30)	0.0085(16)	0.0127(38)	0.000045(40)
		−1	−1	0.0083(83)	-0.0021(39)	0.0127(38)	0.000045(40)
		1	0	-0.0019(41)	0.0023(20)	0.0157(47)	0.000056(50)
		−1	0	-0.0026(57)	0.0032(27)	0.0128(39)	0.000046(41)
	C_9'	1	1	-0.0025(54)	0.0030(26)	-0.0157(41)	-0.01627(61)
		1	−1	-0.0025(53)	0.0030(25)	0.0449(37)	0.01617(82)
		−1	1	-0.0021(46)	0.0026(22)	-0.0128(46)	-0.01390(86)
		−1	−1	-0.0021(45)	0.0025(22)	0.0387(43)	0.01370(66)
		1	0	-0.0025(54)	0.0030(26)	0.0151(39)	0.00010(27)
		−1	0	-0.0021(46)	0.0026(22)	0.0133(46)	0.0000073(2899)
	C_{10}'	1	1	0.0075(83)	0.0024(22)	0.0038(40)	-0.00245(18)
		1	−1	-0.0160(30)	0.0027(21)	0.0217(38)	0.00254(14)
		−1	1	0.0143(72)	0.0029(26)	0.0046(47)	-0.00295(20)
		−1	−1	-0.01405(99)	0.0032(25)	0.0262(46)	0.00306(17)
		1	0	-0.0043(57)	0.0026(22)	0.0129(39)	0.000046(41)
		−1	0	0.00013(406)	0.0031(26)	0.0156(47)	0.000056(50)
1-2	ΔC_9	1	1	0.0013(63)	0.0054(54)	0.0480(38)	0.00109(61)
		1	−1	0.0014(63)	0.0054(54)	-0.0389(42)	-0.00094(55)
		−1	1	0.0017(79)	0.0069(68)	0.0620(32)	0.00143(80)
		−1	−1	0.0018(81)	0.0069(69)	-0.0486(39)	-0.00117(67)
		1	0	0.0014(65)	0.0056(56)	0.0049(38)	0.000083(84)
		−1	0	0.0018(83)	0.0072(71)	0.0074(37)	0.000141(98)
	ΔC_{10}	1	1	-0.0197(14)	0.0248(26)	0.0077(47)	0.00014(11)
		1	−1	0.023(13)	-0.013(10)	0.0077(47)	0.00014(11)
		−1	1	-0.0114(37)	0.0177(37)	0.0047(28)	0.000084(69)
		−1	−1	0.015(11)	-0.0054(89)	0.0047(28)	0.000084(69)
		1	0	0.0016(72)	0.0062(61)	0.0080(50)	0.00014(12)
		−1	0	0.0016(73)	0.0063(63)	0.0048(30)	0.000087(71)
	C_9'	1	1	0.0019(86)	0.0074(73)	-0.0114(36)	-0.0314(27)
		1	−1	0.0018(85)	0.0073(73)	0.0236(39)	0.0310(28)
		−1	1	0.0013(60)	0.0052(52)	-0.0068(38)	-0.0219(23)
		−1	−1	0.0013(60)	0.0052(51)	0.0178(41)	0.0220(21)
		1	0	0.0019(88)	0.0077(76)	0.0065(36)	0.0000067(6169)
		−1	0	0.0013(62)	0.0053(53)	0.0057(39)	0.00019(51)
	C_{10}'	1	1	0.013(11)	0.0048(51)	-0.0284(35)	-0.0145(15)
		1	−1	-0.0171(40)	0.0054(50)	0.0380(33)	0.0147(14)
		−1	1	0.030(12)	0.0071(76)	-0.0431(51)	-0.0221(20)
		−1	−1	-0.0156(16)	0.0081(74)	0.0578(47)	0.0224(19)
		1	0	-0.0022(75)	0.0052(52)	0.0050(31)	0.000089(72)
		−1	0	0.0074(70)	0.0079(78)	0.0076(47)	0.00014(11)

Table C.21: The dependence of the asymmetric observables corresponding to $\bar{B}(B) \to \rho^0 ll$ on the real and imaginary parts of the NP WC's $\Delta C_{9,10}$ and $C'_{9,10}$ for the q^2 bins $0.1-1$ and $1-2$ GeV^2 for a few benchmark values of the real and imaginary parts of the corresponding WC's.

TH-3118_176121005

Bin	C_i^{NP}	$Re(C_i^{NP})$	$Im(C_i^{NP})$	Observables			
				A_5	A_{6s}	A_8	A_9
2-4	ΔC_9	1	1	0.0056(56)	0.00050(670)	0.0324(18)	0.00120(63)
		1	−1	0.0056(57)	0.00048(676)	-0.0276(23)	-0.00106(57)
		−1	1	0.0079(79)	0.00071(942)	0.0460(17)	0.00174(92)
		−1	−1	0.0080(80)	0.00068(954)	-0.0390(25)	-0.00146(78)
		1	0	0.0058(57)	0.00051(696)	0.0026(16)	0.000079(69)
		−1	0	0.0083(83)	0.00073(995)	0.0039(18)	0.000160(98)
	ΔC_{10}	1	1	-0.0136(14)	0.0267(33)	0.0044(23)	0.00015(11)
		1	−1	0.028(13)	-0.025(15)	0.0044(23)	0.00015(11)
		−1	1	-0.0047(32)	0.0146(43)	0.0023(11)	0.000083(58)
		−1	−1	0.0174(95)	-0.013(11)	0.0023(11)	0.000083(58)
		1	0	0.0074(74)	0.00065(886)	0.0046(23)	0.00016(11)
		−1	0	0.0066(66)	0.00057(784)	0.0024(13)	0.000085(60)
	C_9'	1	1	0.0082(82)	0.00071(975)	0.0255(22)	-0.0107(18)
		1	−1	0.0081(80)	0.00073(965)	-0.0203(23)	0.0093(19)
		−1	1	0.0056(56)	0.00047(664)	0.0190(22)	-0.0062(14)
		−1	−1	0.0055(55)	0.00048(660)	-0.0121(23)	0.0074(11)
		1	0	0.0085(85)	0.00076(1018)	0.0026(14)	-0.00067(49)
		−1	0	0.0057(57)	0.00050(685)	0.0035(18)	0.00063(40)
	C_{10}'	1	1	0.0167(98)	0.000061(6554)	-0.0488(28)	-0.0322(32)
		1	−1	-0.0094(36)	0.00094(639)	0.0538(27)	0.0324(32)
		−1	1	0.032(11)	-0.000013(10236)	-0.0775(39)	-0.0511(47)
		−1	−1	-0.0094(16)	0.0014(100)	0.0854(37)	0.0514(46)
		1	0	0.0038(69)	0.00052(668)	0.0026(13)	0.000090(63)
		−1	0	0.0118(68)	0.00073(1063)	0.0041(22)	0.00015(10)
4-6	ΔC_9	1	1	0.0120(51)	-0.0144(90)	0.01868(74)	0.00105(51)
		1	−1	0.0121(52)	-0.0146(91)	-0.01607(98)	-0.00096(48)
		−1	1	0.0181(77)	-0.022(13)	0.02829(94)	0.00164(81)
		−1	−1	0.0184(78)	-0.022(14)	-0.0242(14)	-0.00141(70)
		1	0	0.0125(53)	-0.0150(92)	0.00142(37)	0.000050(39)
		−1	0	0.0192(82)	-0.023(14)	0.00233(48)	0.000135(74)
	ΔC_{10}	1	1	-0.0041(11)	0.0164(27)	0.00248(55)	0.000116(71)
		1	−1	0.035(12)	-0.054(22)	0.00248(55)	0.000116(71)
		−1	1	0.0036(30)	0.0017(53)	0.00130(29)	0.000061(38)
		−1	−1	0.0243(89)	-0.035(16)	0.00130(29)	0.000061(38)
		1	0	0.0166(71)	-0.020(12)	0.00263(59)	0.000124(75)
		−1	0	0.0144(61)	-0.017(11)	0.00134(31)	0.000063(39)
	C_9'	1	1	0.0176(75)	-0.021(13)	0.0505(15)	0.0210(20)
		1	−1	0.0175(74)	-0.021(13)	-0.0487(16)	-0.0228(21)
		−1	1	0.0125(53)	-0.0149(92)	0.0376(15)	0.0164(17)
		−1	−1	0.0124(53)	-0.0148(92)	-0.0325(15)	-0.0146(16)
		1	0	0.0184(78)	-0.022(14)	0.00074(27)	-0.00104(20)
		−1	0	0.0129(55)	-0.0154(95)	0.00251(51)	0.00086(18)
	C_{10}'	1	1	0.027(11)	-0.0152(92)	-0.0583(23)	-0.0491(43)
		1	−1	-0.00039(297)	-0.0139(90)	0.0612(22)	0.0492(43)
		−1	1	0.037(11)	-0.023(14)	-0.0879(26)	-0.0739(57)
		−1	−1	-0.00479(85)	-0.021(13)	0.0922(23)	0.0741(57)
		−1	−1	-0.00479(85)	-0.021(13)	0.0922(23)	0.0741(57)
		1	0	0.0140(70)	-0.0151(94)	0.00147(33)	0.000069(42)
		−1	0	0.0170(57)	-0.023(14)	0.00225(51)	0.000106(65)

Table C.22: The dependence of the asymmetric observables corresponding to $\bar{B}(B) \to \rho^0 ll$ on the real and imaginary parts of the NP WC's $\Delta C_{9,10}$ and $C'_{9,10}$ for the q^2 bins $2-4$ and $4-6$ GeV^2 for a few benchmark values of the real and imaginary parts of the corresponding WC's.

TH-3118_176121005

Bin	C_i^{NP}	$Re(C_i^{NP})$	$Im(C_i^{NP})$	Observables		
				BR$\times 10^9$	F_L	R_ρ
0.1-1	ΔC_9	1	1	1.36(11)	0.348(28)	1.063(12)
		1	−1	1.34(11)	0.340(28)	1.047(11)
		−1	1	1.24(11)	0.238(23)	0.9705(65)
		−1	−1	1.22(10)	0.228(23)	0.9538(72)
		1	0	1.33(11)	0.338(28)	1.042(10)
		−1	0	1.22(10)	0.226(22)	0.9490(76)
	ΔC_{10}	1	1	1.164(99)	0.236(24)	0.9083(56)
		1	−1	1.164(99)	0.236(24)	0.9083(56)
		−1	1	1.42(11)	0.337(27)	1.109(11)
		−1	−1	1.42(11)	0.337(27)	1.109(11)
		1	0	1.147(99)	0.228(23)	0.8953(67)
		−1	0	1.40(11)	0.331(27)	1.0956(95)
	C_9'	1	1	1.18(10)	0.237(23)	0.9185(57)
		1	−1	1.20(10)	0.247(23)	0.9354(52)
		−1	1	1.39(11)	0.329(28)	1.0818(99)
		−1	−1	1.41(11)	0.336(28)	1.099(11)
		1	0	1.17(10)	0.234(23)	0.9139(63)
		−1	0	1.38(11)	0.327(28)	1.0772(91)
	C_{10}'	1	1	1.41(11)	0.338(27)	1.103(11)
		1	−1	1.41(11)	0.338(27)	1.103(11)
		−1	1	1.17(10)	0.234(24)	0.9135(57)
		−1	−1	1.17(10)	0.234(24)	0.9135(57)
		1	0	1.40(11)	0.333(27)	1.0904(95)
		−1	0	1.154(99)	0.226(23)	0.9005(68)
1-2	ΔC_9	1	1	0.737(65)	0.777(20)	1.198(14)
		1	−1	0.729(64)	0.776(20)	1.185(14)
		−1	1	0.579(46)	0.613(29)	0.941(12)
		−1	−1	0.570(45)	0.609(29)	0.928(12)
		1	0	0.712(63)	0.776(20)	1.158(13)
		−1	0	0.554(44)	0.604(30)	0.902(12)
	ΔC_{10}	1	1	0.497(41)	0.670(28)	0.8077(33)
		1	−1	0.497(41)	0.670(28)	0.8077(33)
		−1	1	0.810(68)	0.725(23)	1.3175(57)
		−1	−1	0.810(68)	0.725(23)	1.3175(57)
		1	0	0.476(40)	0.664(29)	0.7747(39)
		−1	0	0.790(66)	0.723(23)	1.2845(52)
	C_9'	1	1	0.536(43)	0.649(28)	0.8717(62)
		1	−1	0.544(44)	0.653(28)	0.8844(68)
		−1	1	0.764(66)	0.740(23)	1.2416(89)
		−1	−1	0.771(66)	0.742(22)	1.2543(84)
		1	0	0.519(42)	0.645(28)	0.8448(67)
		−1	0	0.747(64)	0.740(23)	1.2148(80)
	C_{10}'	1	1	0.788(68)	0.745(22)	1.2820(79)
		1	−1	0.788(68)	0.745(22)	1.2820(79)
		−1	1	0.518(42)	0.642(29)	0.8431(55)
		−1	−1	0.518(42)	0.642(29)	0.8431(55)
		1	0	0.768(66)	0.743(22)	1.2490(74)
		−1	0	0.498(41)	0.635(30)	0.8102(60)

Table C.23: The dependence of the Branching Ratio and the observables F_L and R_ρ corresponding to $\bar{B}(B) \to \rho^0 ll$ on the real and imaginary parts of the NP WC's $\Delta C_{9,10}$ and $C'_{9,10}$ for the q^2 bins $0.1 - 1$ and $1 - 2$ GeV^2 for a few benchmark values of the real and imaginary parts of the corresponding WC's.

TH-3118_176121005

Bin	C_i^{NP}	$Re(C_i^{NP})$	$Im(C_i^{NP})$	Observables		
				BR$\times 10^9$	F_L	R_ρ
2-4	ΔC_9	1	1	1.38(13)	0.823(15)	1.2730(72)
		1	−1	1.37(12)	0.823(15)	1.2619(75)
		−1	1	0.978(82)	0.720(23)	0.9001(88)
		−1	−1	0.966(80)	0.720(23)	0.8890(85)
		1	0	1.33(12)	0.827(15)	1.2252(74)
		−1	0	0.926(77)	0.721(23)	0.8523(79)
	ΔC_{10}	1	1	0.821(75)	0.808(18)	0.7551(37)
		1	−1	0.821(75)	0.808(18)	0.7551(37)
		−1	1	1.53(13)	0.766(19)	1.4060(54)
		−1	−1	1.53(13)	0.766(19)	1.4060(54)
		1	0	0.775(71)	0.813(18)	0.7131(43)
		−1	0	1.48(13)	0.768(19)	1.3639(49)
	C_9'	1	1	0.946(79)	0.735(22)	0.8706(63)
		1	−1	0.955(81)	0.737(22)	0.8792(66)
		−1	1	1.39(13)	0.810(16)	1.2828(52)
		−1	−1	1.40(13)	0.811(16)	1.2914(47)
		1	0	0.905(76)	0.737(22)	0.8326(57)
		−1	0	1.35(12)	0.814(16)	1.2449(52)
	C_{10}'	1	1	1.44(13)	0.813(16)	1.3257(41)
		1	−1	1.44(13)	0.813(16)	1.3257(41)
		−1	1	0.908(77)	0.730(23)	0.8354(52)
		−1	−1	0.908(77)	0.730(23)	0.8354(52)
		1	0	1.40(13)	0.816(16)	1.2837(45)
		−1	0	0.862(73)	0.731(23)	0.7934(47)
4-6	ΔC_9	1	1	1.56(13)	0.712(23)	1.3104(26)
		1	−1	1.55(13)	0.713(23)	1.2995(33)
		−1	1	1.037(84)	0.665(25)	0.8691(49)
		−1	−1	1.024(83)	0.665(25)	0.8582(47)
		1	0	1.50(13)	0.716(23)	1.2613(33)
		−1	0	0.978(80)	0.668(25)	0.8200(41)
	ΔC_{10}	1	1	0.891(78)	0.731(23)	0.7463(44)
		1	−1	0.891(78)	0.731(23)	0.7463(44)
		−1	1	1.70(14)	0.674(25)	1.4216(70)
		−1	−1	1.70(14)	0.674(25)	1.4216(70)
		1	0	0.839(74)	0.739(23)	0.7028(52)
		−1	0	1.64(13)	0.676(24)	1.3781(62)
	C_9'	1	1	1.067(85)	0.638(27)	0.8944(78)
		1	−1	1.075(86)	0.641(26)	0.9017(77)
		−1	1	1.51(13)	0.731(22)	1.2669(60)
		−1	−1	1.52(13)	0.732(22)	1.2742(57)
		1	0	1.019(81)	0.641(26)	0.8543(71)
		−1	0	1.46(13)	0.736(22)	1.2269(64)
	C_{10}'	1	1	1.55(13)	0.735(22)	1.3031(55)
		1	−1	1.55(13)	0.735(22)	1.3031(55)
		−1	1	1.031(82)	0.632(27)	0.8647(70)
		−1	−1	1.031(82)	0.632(27)	0.8647(70)
		−1	−1	1.031(82)	0.632(27)	0.8647(70)
		1	0	1.50(13)	0.740(21)	1.2596(59)
		−1	0	0.979(79)	0.633(28)	0.8212(65)

Table C.24: The dependence of the Branching Ratio and the observables F_L and R_ρ corresponding to $\bar{B}(B) \to \rho^0 ll$ on the real and imaginary parts of the NP WC's $\Delta C_{9,10}$ and $C'_{9,10}$ for the q^2 bins $2-4$ and $4-6$ GeV^2 for a few benchmark values of the real and imaginary parts of the corresponding WC's.

TH-3118_176121005

Bin	C_i^{NP}	$Re(C_i^{NP})$	$Im(C_i^{NP})$	Observables			
				$A_{\rm CP}$	A_3	A_4	A_7
0.1-1	ΔC_9	1	1	-0.0373(98)	0.000038(35)	-0.0037(28)	-0.0023(27)
		1	−1	-0.035(12)	-0.000048(35)	-0.0105(11)	-0.0023(28)
		−1	1	-0.031(11)	0.000054(33)	-0.0037(23)	-0.0025(30)
		−1	−1	-0.028(14)	-0.000040(30)	-0.01123(72)	-0.0026(30)
		1	0	-0.036(11)	-0.0000049(240)	-0.0072(21)	-0.0024(28)
		−1	0	-0.030(13)	0.0000079(149)	-0.0076(15)	-0.0026(31)
	ΔC_{10}	1	1	-0.037(13)	0.0000013(211)	-0.0081(20)	-0.0567(31)
		1	−1	-0.037(13)	0.0000013(211)	-0.0081(20)	0.0527(26)
		−1	1	-0.030(11)	0.0000011(172)	-0.0066(16)	-0.0476(36)
		−1	−1	-0.030(11)	0.0000011(172)	-0.0066(16)	0.0420(31)
		1	0	-0.037(13)	0.0000013(213)	-0.0082(20)	-0.0020(23)
		−1	0	-0.030(11)	0.0000011(174)	-0.0067(16)	-0.0028(33)
	C_9'	1	1	-0.033(13)	-0.00166(62)	-0.01167(76)	-0.0027(32)
		1	−1	-0.027(12)	0.00209(25)	-0.0039(23)	-0.0026(31)
		−1	1	-0.038(11)	-0.00181(21)	-0.0102(11)	-0.0023(27)
		−1	−1	-0.033(11)	0.00139(54)	-0.0036(27)	-0.0022(26)
		1	0	-0.030(13)	0.00024(19)	-0.0079(16)	-0.0027(32)
		−1	0	-0.036(11)	-0.00020(18)	-0.0070(20)	-0.0023(27)
	C_{10}'	1	1	-0.030(11)	0.0000011(173)	-0.0066(16)	0.0422(31)
		1	−1	-0.030(11)	0.0000011(173)	-0.0066(16)	-0.0478(36)
		−1	1	-0.036(13)	0.0000012(210)	-0.0080(19)	0.0524(26)
		−1	−1	-0.036(13)	0.0000012(210)	-0.0080(19)	-0.0564(31)
		1	0	-0.030(11)	0.0000011(174)	-0.0067(16)	-0.0028(34)
		−1	0	-0.037(13)	0.0000013(213)	-0.0081(20)	-0.0020(23)
1-2	ΔC_9	1	1	-0.0381(26)	0.000075(90)	-0.00047(358)	-0.0020(22)
		1	−1	-0.0274(57)	-0.000150(89)	-0.0094(13)	-0.0020(22)
		−1	1	-0.0343(42)	0.000128(88)	-0.00097(327)	-0.0025(27)
		−1	−1	-0.0207(95)	-0.000159(91)	-0.01233(64)	-0.0025(28)
		1	0	-0.0337(38)	-0.000038(69)	-0.0050(25)	-0.0020(22)
		−1	0	-0.0286(70)	-0.000015(50)	-0.0068(19)	-0.0026(28)
	ΔC_{10}	1	1	-0.0401(65)	-0.000035(76)	-0.0074(28)	-0.0840(40)
		1	−1	-0.0401(65)	-0.000035(76)	-0.0074(28)	0.0797(27)
		−1	1	-0.0246(40)	-0.000021(47)	-0.0046(17)	-0.0524(35)
		−1	−1	-0.0246(40)	-0.000021(47)	-0.0046(17)	0.0480(25)
		1	0	-0.0418(68)	-0.000037(79)	-0.0077(28)	-0.0022(25)
		−1	0	-0.0252(41)	-0.000022(48)	-0.0047(18)	-0.0023(25)
	C_9'	1	1	-0.0318(65)	-0.0048(19)	-0.01314(74)	-0.0027(28)
		1	−1	-0.0245(56)	0.00588(89)	-0.0010(35)	-0.0027(28)
		−1	1	-0.0347(46)	-0.00424(63)	-0.0089(11)	-0.0019(21)
		−1	−1	-0.0296(40)	0.0033(14)	-0.00044(341)	-0.0019(21)
		1	0	-0.0293(63)	0.00058(55)	-0.0073(20)	-0.0028(30)
		−1	0	-0.0330(44)	-0.00045(46)	-0.0048(23)	-0.0019(21)
	C_{10}'	1	1	-0.0253(42)	-0.000022(48)	-0.0047(18)	0.0493(27)
		1	−1	-0.0253(42)	-0.000022(48)	-0.0047(18)	-0.0539(37)
		−1	1	-0.0384(62)	-0.000034(73)	-0.0071(27)	0.0764(23)
		−1	−1	-0.0384(62)	-0.000034(73)	-0.0071(27)	-0.0805(36)
		1	0	-0.0260(43)	-0.000023(49)	-0.0048(18)	-0.0024(26)
		−1	0	-0.0400(65)	-0.000035(76)	-0.0074(28)	-0.0021(23)

Table C.25: The dependence of the asymmetric observables corresponding to $\bar{B}^0(B^0) \to \rho^0 ll$ which can be measured only at Belle on the real and imaginary parts of the NP WC's $\Delta C_{9,10}$ and $C'_{9,10}$ for the q^2 bins $0.1-1$ and $1-2$ GeV^2 for a few benchmark values of the real and imaginary parts of the corresponding WC's.

TH-3118_176121005

Bin	C_i^{NP}	$Re(C_i^{NP})$	$Im(C_i^{NP})$	Observables			
				$A_{\rm CP}$	A_3	A_4	A_7
2-4	ΔC_9	1	1	-0.0250(39)	0.00018(14)	0.0039(32)	-0.00016(84)
		1	−1	-0.0083(23)	-0.000150(78)	-0.0037(10)	-0.00016(85)
		−1	1	-0.0253(23)	0.00024(14)	0.0041(32)	-0.00022(119)
		−1	−1	-0.0017(62)	-0.000230(94)	-0.00669(40)	-0.00022(119)
		1	0	-0.0173(13)	0.000018(92)	0.00013(215)	-0.00016(87)
		−1	0	-0.0143(23)	0.0000082(685)	-0.0013(17)	-0.00023(125)
	ΔC_{10}	1	1	-0.0220(11)	0.000019(113)	-0.00063(273)	-0.0641(37)
		1	−1	-0.0220(11)	0.000019(113)	-0.00063(273)	0.0637(28)
		−1	1	-0.01184(63)	0.000010(61)	-0.00034(146)	-0.0345(21)
		−1	−1	-0.01184(63)	0.000010(61)	-0.00034(146)	0.0341(14)
		1	0	-0.0233(11)	0.000020(120)	-0.00067(289)	-0.00021(111)
		−1	0	-0.01220(65)	0.000011(62)	-0.00035(151)	-0.00018(98)
	C_9'	1	1	-0.0155(13)	-0.0070(26)	-0.00684(43)	-0.00023(122)
		1	−1	-0.01198(68)	0.0071(13)	0.0042(33)	-0.00023(120)
		−1	1	-0.01774(97)	-0.00482(82)	-0.0037(10)	-0.00015(83)
		−1	−1	-0.01530(81)	0.0047(19)	0.0039(31)	-0.00016(83)
		1	0	-0.01445(95)	0.000077(731)	-0.0013(18)	-0.00024(128)
		−1	0	-0.01707(85)	-0.000027(614)	0.00013(212)	-0.00016(86)
	C_{10}'	1	1	-0.01255(67)	0.000011(64)	-0.00036(155)	0.0362(16)
		1	−1	-0.01255(67)	0.000011(64)	-0.00036(155)	-0.0366(23)
		−1	1	-0.0199(10)	0.000018(102)	-0.00057(246)	0.0575(22)
		−1	−1	-0.0199(10)	0.000018(102)	-0.00057(246)	-0.0579(30)
		1	0	-0.01297(69)	0.000011(66)	-0.00037(161)	-0.00020(105)
		−1	0	-0.0210(11)	0.000019(108)	-0.00060(259)	-0.00018(100)
4-6	ΔC_9	1	1	-0.0233(59)	0.00058(29)	0.0076(30)	-0.00011(43)
		1	−1	-0.0020(11)	0.0000029(890)	0.00053(99)	-0.00011(43)
		−1	1	-0.0235(50)	0.00064(32)	0.0084(33)	-0.00017(65)
		−1	−1	0.0087(47)	-0.000227(80)	-0.00234(31)	-0.00017(65)
		1	0	-0.0131(28)	0.00030(19)	0.0042(21)	-0.00012(45)
		−1	0	-0.00792(65)	0.00022(14)	0.0032(18)	-0.00018(68)
	ΔC_{10}	1	1	-0.0154(26)	0.00038(24)	0.0053(28)	-0.0387(22)
		1	−1	-0.0154(26)	0.00038(24)	0.0053(28)	0.0384(23)
		−1	1	-0.0081(14)	0.00020(12)	0.0028(15)	-0.0203(11)
		−1	−1	-0.0081(14)	0.00020(12)	0.0028(15)	0.0201(11)
		1	0	-0.0164(28)	0.00040(25)	0.0057(28)	-0.00015(59)
		−1	0	-0.0084(15)	0.00020(12)	0.0029(15)	-0.00013(51)
	C_9'	1	1	-0.0127(28)	-0.0106(35)	-0.00224(29)	-0.00016(63)
		1	−1	-0.0082(20)	0.0077(17)	0.0081(31)	-0.00016(62)
		−1	1	-0.0123(18)	-0.0051(11)	0.00055(102)	-0.00012(44)
		−1	−1	-0.0092(11)	0.0079(27)	0.0078(31)	-0.00011(44)
		1	0	-0.0110(25)	-0.00145(96)	0.0031(18)	-0.00017(66)
		−1	0	-0.0111(16)	0.00147(89)	0.0044(21)	-0.00012(46)
	C_{10}'	1	1	-0.0088(15)	0.00022(13)	0.0031(16)	0.0219(13)
		1	−1	-0.0088(15)	0.00022(13)	0.0031(16)	-0.0222(13)
		−1	1	-0.0133(23)	0.00033(21)	0.0046(23)	0.0331(18)
		−1	−1	-0.0133(23)	0.00033(21)	0.0046(23)	-0.0334(17)
		−1	−1	-0.0133(23)	0.00033(21)	0.0046(23)	-0.0334(17)
		1	0	-0.0091(16)	0.00022(14)	0.0032(16)	-0.00015(55)
		−1	0	-0.0140(23)	0.00034(22)	0.0049(25)	-0.00013(51)

Table C.26: The dependence of the asymmetric observables corresponding to $\bar{B}^0(B^0) \to \rho^0 ll$ which can be measured only at Belle on the real and imaginary parts of the NP WC's $\Delta C_{9,10}$ and $C'_{9,10}$ for the q^2 bins $2-4$ and $4-6$ GeV^2 for a few benchmark values of the real and imaginary parts of the corresponding WC's.

TH-3118_176121005

Bin	C_i^{NP}	$Re(C_i^{NP})$	$Im(C_i^{NP})$	Observables				
				$A_{\rm FB}$	P_2	P_3	P_5'	P_8'
0.1-1	ΔC_9	1	1	-0.0520(28)	-0.0532(17)	0.00029(19)	0.2665(44)	-0.0267(69)
		1	−1	-0.0529(28)	-0.0534(16)	0.00028(19)	0.2722(46)	-0.0245(87)
		−1	1	-0.0625(26)	-0.0547(17)	0.00015(10)	0.3898(41)	-0.0144(43)
		−1	−1	-0.0636(25)	-0.0550(17)	0.00014(10)	0.4027(41)	-0.0113(64)
		1	0	-0.0531(28)	-0.0535(17)	0.00028(19)	0.2738(45)	-0.0260(79)
		−1	0	-0.0640(25)	-0.0551(17)	0.00014(10)	0.4064(40)	-0.0132(55)
	ΔC_{10}	1	1	-0.0472(18)	-0.0412(11)	0.00022(14)	0.2855(42)	-0.0234(79)
		1	−1	-0.0473(21)	-0.0413(15)	0.00022(14)	0.2835(45)	-0.0234(79)
		−1	1	-0.0659(33)	-0.0662(19)	0.00020(13)	0.3567(47)	-0.0172(57)
		−1	−1	-0.0660(35)	-0.0663(22)	0.00020(13)	0.3552(53)	-0.0172(57)
		1	0	-0.0480(19)	-0.0414(13)	0.00022(14)	0.2922(38)	-0.0241(81)
		−1	0	-0.0667(34)	-0.0665(20)	0.00021(13)	0.3616(47)	-0.0175(59)
	C_9'	1	1	-0.0632(25)	-0.0552(17)	-0.00257(29)	0.3793(45)	-0.0136(65)
		1	−1	-0.0620(26)	-0.0549(17)	-0.00195(77)	0.3670(44)	-0.0140(44)
		−1	1	-0.0536(27)	-0.0533(16)	0.00231(84)	0.2912(41)	-0.0244(85)
		−1	−1	-0.0528(28)	-0.0531(16)	0.00289(36)	0.2852(40)	-0.0246(68)
		1	0	-0.0635(25)	-0.0553(17)	-0.00227(53)	0.3827(45)	-0.0141(56)
		−1	0	-0.0539(27)	-0.0534(16)	0.00261(59)	0.2929(41)	-0.0249(78)
	C_{10}'	1	1	-0.0530(27)	-0.0534(17)	0.00021(13)	0.3801(50)	-0.0173(57)
		1	−1	-0.0530(27)	-0.0534(16)	0.00021(13)	0.3777(42)	-0.0173(57)
		−1	1	-0.0630(26)	-0.0549(17)	0.00022(14)	0.2557(47)	-0.0234(79)
		−1	−1	-0.0630(26)	-0.0549(17)	0.00022(14)	0.2525(49)	-0.0234(79)
		1	0	-0.0536(27)	-0.0536(17)	0.00021(13)	0.3850(44)	-0.0176(59)
		−1	0	-0.0639(26)	-0.0551(17)	0.00022(14)	0.2610(46)	-0.0240(81)
1-2	ΔC_9	1	1	-0.0698(75)	-0.2087(77)	0.0022(14)	0.044(15)	-0.048(11)
		1	−1	-0.0705(76)	-0.2095(62)	0.0021(14)	0.044(15)	-0.043(13)
		−1	1	-0.127(10)	-0.2184(62)	0.00091(59)	0.285(10)	-0.0261(59)
		−1	−1	-0.128(10)	-0.2191(52)	0.00083(58)	0.288(10)	-0.0204(87)
		1	0	-0.0721(78)	-0.2143(72)	0.0022(14)	0.045(16)	-0.046(12)
		−1	0	-0.132(11)	-0.2227(59)	0.00089(59)	0.296(10)	-0.0240(75)
	ΔC_{10}	1	1	-0.0931(84)	-0.1882(54)	0.0017(11)	0.151(12)	-0.043(12)
		1	−1	-0.0929(86)	-0.1876(73)	0.0017(11)	0.146(12)	-0.043(12)
		−1	1	-0.0970(92)	-0.2351(51)	0.00123(79)	0.164(14)	-0.0281(79)
		−1	−1	-0.0968(95)	-0.2347(66)	0.00123(79)	0.161(13)	-0.0281(79)
		1	0	-0.0970(88)	-0.1924(66)	0.0017(11)	0.154(12)	-0.045(13)
		−1	0	-0.0994(95)	-0.2390(60)	0.00125(81)	0.167(14)	-0.0287(81)
	C_9'	1	1	-0.116(10)	-0.2204(57)	-0.0156(19)	0.183(14)	-0.0273(92)
		1	−1	-0.115(10)	-0.2200(59)	-0.0122(49)	0.181(14)	-0.0263(62)
		−1	1	-0.0817(82)	-0.2097(59)	0.0144(53)	0.140(11)	-0.040(12)
		−1	−1	-0.0809(81)	-0.2092(60)	0.0176(23)	0.139(11)	-0.0395(99)
		1	0	-0.120(10)	-0.2249(62)	-0.0142(34)	0.188(15)	-0.0277(79)
		−1	0	-0.0835(83)	-0.2137(62)	0.0163(38)	0.143(11)	-0.041(11)
	C_{10}'	1	1	-0.0800(78)	-0.2093(59)	0.00136(87)	0.256(11)	-0.0296(83)
		1	−1	-0.0800(78)	-0.2092(59)	0.00136(87)	0.254(11)	-0.0296(83)
		−1	1	-0.119(11)	-0.2212(60)	0.00148(96)	0.026(15)	-0.041(11)
		−1	−1	-0.119(11)	-0.2211(60)	0.00148(96)	0.023(15)	-0.041(11)
		1	0	-0.0821(80)	-0.2133(61)	0.00139(89)	0.261(11)	-0.0303(85)
		−1	0	-0.124(11)	-0.2258(63)	0.00151(98)	0.025(15)	-0.042(12)

Table C.27: The dependence of the optimized observables corresponding to $\bar{B}^0(B^0) \to \rho^0 ll$ which can be measured only at Belle on the real and imaginary parts of the NP WC's $\Delta C_{9,10}$ and $C'_{9,10}$ for the q^2 bins $0.1-1$ and $1-2$ GeV^2 for a few benchmark values of the real and imaginary parts of the corresponding WC's.

TH-3118_176121005

Bin	C_i^{NP}	$Re(C_i^{NP})$	$Im(C_i^{NP})$	Observables				
				$A_{\rm FB}$	P_2	P_3	P_5'	P_8'
2-4	ΔC_9	1	1	0.0066(40)	0.025(15)	0.0037(21)	-0.380(18)	-0.047(10)
		1	−1	0.0066(40)	0.025(15)	0.0037(22)	-0.384(17)	-0.044(13)
		−1	1	-0.0809(88)	-0.193(10)	0.0019(11)	-0.030(16)	-0.0294(60)
		−1	−1	-0.0820(88)	-0.1950(98)	0.0018(11)	-0.030(16)	-0.0262(89)
		1	0	0.0068(41)	0.026(16)	0.0039(23)	-0.398(18)	-0.047(12)
		−1	0	-0.0855(92)	-0.204(10)	0.0020(11)	-0.032(17)	-0.0292(78)
	ΔC_{10}	1	1	-0.0325(57)	-0.112(15)	0.0045(26)	-0.241(20)	-0.056(14)
		1	−1	-0.0308(59)	-0.107(16)	0.0045(26)	-0.250(20)	-0.056(14)
		−1	1	-0.0293(51)	-0.084(12)	0.0020(11)	-0.206(16)	-0.0278(72)
		−1	−1	-0.0284(52)	-0.081(12)	0.0020(11)	-0.210(16)	-0.0278(72)
		1	0	-0.0336(61)	-0.119(17)	0.0049(28)	-0.262(22)	-0.059(15)
		−1	0	-0.0298(53)	-0.085(13)	0.0021(11)	-0.215(16)	-0.0288(75)
	C_9'	1	1	-0.0370(65)	-0.093(13)	-0.0240(34)	-0.256(20)	-0.0320(90)
		1	−1	-0.0367(64)	-0.093(13)	-0.0235(89)	-0.254(20)	-0.0288(60)
		−1	1	-0.0252(46)	-0.088(13)	0.0276(95)	-0.195(15)	-0.044(12)
		−1	−1	-0.0250(45)	-0.088(13)	0.0280(42)	-0.195(15)	-0.041(10)
		1	0	-0.0387(68)	-0.098(14)	-0.0250(64)	-0.268(21)	-0.0320(79)
		−1	0	-0.0259(47)	-0.093(14)	0.0292(72)	-0.203(16)	-0.044(12)
	C_{10}'	1	1	-0.0254(44)	-0.090(12)	0.0026(15)	-0.097(16)	-0.0320(83)
		1	−1	-0.0254(44)	-0.090(12)	0.0026(15)	-0.097(16)	-0.0320(83)
		−1	1	-0.0370(69)	-0.091(14)	0.0029(17)	-0.395(18)	-0.045(12)
		−1	−1	-0.0369(69)	-0.091(14)	0.0029(17)	-0.396(18)	-0.045(12)
		1	0	-0.0262(45)	-0.095(13)	0.0027(16)	-0.101(17)	-0.0333(86)
		−1	0	-0.0389(73)	-0.096(15)	0.0031(18)	-0.417(19)	-0.047(12)
4-6	ΔC_9	1	1	0.1014(90)	0.2350(53)	0.0032(17)	-0.535(13)	-0.0387(95)
		1	−1	0.1023(91)	0.2375(52)	0.0033(18)	-0.539(13)	-0.041(12)
		−1	1	0.0134(54)	0.027(10)	0.0024(13)	-0.293(12)	-0.0283(63)
		−1	−1	0.0136(54)	0.027(11)	0.0025(14)	-0.297(13)	-0.0315(95)
		1	0	0.1054(94)	0.2476(55)	0.0034(19)	-0.558(13)	-0.041(11)
		−1	0	0.0143(57)	0.029(11)	0.0026(14)	-0.311(13)	-0.0315(83)
	ΔC_{10}	1	1	0.0707(74)	0.1755(89)	0.0048(26)	-0.486(15)	-0.054(14)
		1	−1	0.0732(75)	0.1816(88)	0.0048(26)	-0.496(14)	-0.054(14)
		−1	1	0.0633(62)	0.1294(71)	0.0021(11)	-0.410(11)	-0.0268(72)
		−1	−1	0.0646(63)	0.1321(72)	0.0021(11)	-0.415(11)	-0.0268(72)
		1	0	0.0764(80)	0.1951(95)	0.0052(28)	-0.526(16)	-0.058(15)
		−1	0	0.0660(64)	0.1357(74)	0.0022(11)	-0.426(12)	-0.0277(75)
	C_9'	1	1	0.0808(76)	0.1489(80)	-0.0176(35)	-0.509(12)	-0.0337(92)
		1	−1	0.0801(75)	0.1486(80)	-0.0269(88)	-0.505(13)	-0.0276(67)
		−1	1	0.0571(59)	0.1416(74)	0.0313(97)	-0.389(12)	-0.042(12)
		−1	−1	0.0568(59)	0.1413(73)	0.0224(44)	-0.388(12)	-0.0376(98)
		1	0	0.0846(79)	0.1571(84)	-0.0235(64)	-0.533(13)	-0.0323(84)
		−1	0	0.0590(61)	0.1489(77)	0.0283(74)	-0.405(12)	-0.042(11)
	C_{10}'	1	1	0.0545(57)	0.1372(77)	0.0028(15)	-0.330(13)	-0.0311(83)
		1	−1	0.0546(57)	0.1373(77)	0.0028(15)	-0.331(13)	-0.0311(83)
		−1	1	0.0850(79)	0.1538(85)	0.0030(17)	-0.593(11)	-0.043(11)
		−1	−1	0.0850(79)	0.1539(86)	0.0030(17)	-0.593(11)	-0.043(11)
		1	0	0.0564(59)	0.1444(81)	0.0029(16)	-0.344(13)	-0.0323(86)
		−1	0	0.0895(84)	0.1624(90)	0.0032(18)	-0.625(12)	-0.045(12)

Table C.28: The dependence of the optimized observables corresponding to $\bar{B}^0(B^0) \to \rho^0 ll$ which can be measured only at Belle on the real and imaginary parts of the NP WC's $\Delta C_{9,10}$ and $C'_{9,10}$ for the q^2 bins $2-4$ and $4-6$ GeV^2 for a few benchmark values of the real and imaginary parts of the corresponding WC's.

TH-3118_176121005

TH-3118_176121005

Bibliography

[1] Belle collaboration, *Measurements of Partial Branching Fractions of Inclusive $B \to X_u \ell^+ \nu_\ell$ Decays with Hadronic Tagging*, *Phys. Rev. D* **104** (2021) 012008 [2102.00020].

[2] N. Gubernari, A. Kokulu and D. van Dyk, *$B \to P$ and $B \to V$ Form Factors from B-Meson Light-Cone Sum Rules beyond Leading Twist*, *JHEP* **01** (2019) 150 [1811.00983].

[3] D. Leljak, D. van Dyk and B. Melić, *The $\bar{B} \to \pi$ form factors from QCD and their impact on $|V_{ub}|$*, 2102.07233.

[4] A. Bharucha, D. M. Straub and R. Zwicky, *$B \to V \ell^+ \ell^-$ in the Standard Model from light-cone sum rules*, *JHEP* **08** (2016) 098 [1503.05534].

[5] J. Gao, C.-D. Lü, Y.-L. Shen, Y.-M. Wang and Y.-B. Wei, *Precision calculations of $b \to v$ form factors from soft-collinear effective theory sum rules on the light-cone*, *Phys. Rev. D* **101** (2020) 074035.

[6] D. Bigi, P. Gambino and S. Schacht, *$R(D^*)$, $|V_{cb}|$, and the Heavy Quark Symmetry relations between form factors*, *JHEP* **11** (2017) 061 [1707.09509].

[7] W. Altmannshofer and D. M. Straub, *New physics in $b \to s$ transitions after LHC run 1*, *Eur. Phys. J.* **C75** (2015) 382 [1411.3161].

[8] LHCb collaboration, *First observation of the decay $B_s^0 \to K^- \mu^+ \nu_\mu$ and Measurement of $|V_{ub}|/|V_{cb}|$*, *Phys. Rev. Lett.* **126** (2021) 081804 [2012.05143].

[9] S. L. Glashow, *Partial-symmetries of weak interactions*, *Nuclear Physics* **22** (1961) 579.

[10] S. Weinberg, *A model of leptons*, *Phys. Rev. Lett.* **19** (1967) 1264.

[11] A. Salam, *Weak and Electromagnetic Interactions*, *Conf. Proc. C* **680519** (1968) 367.

[12] UA1 collaboration, *Experimental Observation of Lepton Pairs of Invariant Mass Around 95-GeV/c**2 at the CERN SPS Collider*, *Phys. Lett. B* **126** (1983) 398.

[13] UA2 collaboration, *Evidence for $Z^0 \to e^+ e^-$ at the CERN $\bar{p}p$ Collider*, *Phys. Lett. B* **129** (1983) 130.

[14] UA2 collaboration, *Observation of Single Isolated Electrons of High Transverse Momentum in Events with Missing Transverse Energy at the CERN anti-p p Collider*, *Phys. Lett. B* **122** (1983) 476.

[15] UA1 collaboration, *Experimental Observation of Isolated Large Transverse Energy Electrons with Associated Missing Energy at $\sqrt{s} = 540$ GeV*, *Phys. Lett. B* **122** (1983) 103.

[16] J. E. Augustin, A. M. Boyarski, M. Breidenbach, F. Bulos, J. T. Dakin, G. J. Feldman et al., *Discovery of a narrow resonance in $e^+ e^-$ annihilation*, *Phys. Rev. Lett.* **33** (1974) 1406.

[17] J. J. Aubert, U. Becker, P. J. Biggs, J. Burger, M. Chen, G. Everhart et al., *Experimental observation of a heavy particle j*, *Phys. Rev. Lett.* **33** (1974) 1404.

[18] D0 collaboration, *Observation of the top quark*, *Phys. Rev. Lett.* **74** (1995) 2632 [hep-ex/9503003].

TH-3118_176121005

[19] CDF collaboration, *Observation of top quark production in $\bar{p}p$ collisions*, *Phys. Rev. Lett.* **74** (1995) 2626 [hep-ex/9503002].
[20] CMS collaboration, *Observation of a New Boson at a Mass of 125 GeV with the CMS Experiment at the LHC*, *Phys. Lett. B* **716** (2012) 30 [1207.7235].
[21] ATLAS collaboration, *Observation of a new particle in the search for the Standard Model Higgs boson with the ATLAS detector at the LHC*, *Phys. Lett. B* **716** (2012) 1 [1207.7214].
[22] Planck collaboration, *Planck 2018 results. I. Overview and the cosmological legacy of Planck*, *Astron. Astrophys.* **641** (2020) A1 [1807.06205].
[23] Super-Kamiokande collaboration, *Determination of solar neutrino oscillation parameters using 1496 days of Super-Kamiokande I data*, *Phys. Lett. B* **539** (2002) 179 [hep-ex/0205075].
[24] Super-Kamiokande collaboration, *Evidence for oscillation of atmospheric neutrinos*, *Phys. Rev. Lett.* **81** (1998) 1562 [hep-ex/9807003].
[25] KamLAND collaboration, *Measurement of neutrino oscillation with KamLAND: Evidence of spectral distortion*, *Phys. Rev. Lett.* **94** (2005) 081801 [hep-ex/0406035].
[26] MINOS collaboration, *Measurement of the Neutrino Mass Splitting and Flavor Mixing by MINOS*, *Phys. Rev. Lett.* **106** (2011) 181801 [1103.0340].
[27] M. B. Gavela, P. Hernandez, J. Orloff, O. Pene and C. Quimbay, *Standard model CP violation and baryon asymmetry. Part 2: Finite temperature*, *Nucl. Phys. B* **430** (1994) 382 [hep-ph/9406289].
[28] M. Fukugita and T. Yanagida, *Baryogenesis Without Grand Unification*, *Phys. Lett. B* **174** (1986) 45.
[29] S. Weinberg, *Gravitation and Cosmology: Principles and Applications of the General Theory of Relativity*. John Wiley and Sons, New York, 1972.
[30] M. Drees, *An Introduction to supersymmetry*, in *Inauguration Conference of the Asia Pacific Center for Theoretical Physics (APCTP)*, 11, 1996, hep-ph/9611409.
[31] M. Dine, *TASI lectures on the strong CP problem*, in *Theoretical Advanced Study Institute in Elementary Particle Physics (TASI 2000): Flavor Physics for the Millennium*, pp. 349–369, 6, 2000, hep-ph/0011376.
[32] R. Holman, S. D. H. Hsu, T. W. Kephart, E. W. Kolb, R. Watkins and L. M. Widrow, *Solutions to the strong CP problem in a world with gravity*, *Phys. Lett. B* **282** (1992) 132 [hep-ph/9203206].
[33] C. Abel et al., *Measurement of the Permanent Electric Dipole Moment of the Neutron*, *Phys. Rev. Lett.* **124** (2020) 081803 [2001.11966].
[34] J. H. Christenson, J. W. Cronin, V. L. Fitch and R. Turlay, *Evidence for the 2π decay of the k_2^0 meson*, *Phys. Rev. Lett.* **13** (1964) 138.
[35] NA48 collaboration, *Measurement of direct CP violation by NA48*, in *31st International Symposium on Multiparticle Dynamics*, pp. 7–14, 11, 2001, DOI [hep-ph/0111393].
[36] LHCb collaboration, *Observation of CP Violation in Charm Decays*, *Phys. Rev. Lett.* **122** (2019) 211803 [1903.08726].
[37] LHCb collaboration, *Observation of the Mass Difference Between Neutral Charm-Meson Eigenstates*, *Phys. Rev. Lett.* **127** (2021) 111801 [2106.03744].
[38] S. Stone, *The discovery of the b mesons*, in *AIP Conference Proceedings*, vol. 424, pp. 75–84, American Institute of Physics, 1998.
[39] Belle collaboration, *An Improved measurement of mixing induced CP violation in the neutral B meson system*, *Phys. Rev. D* **66** (2002) 071102 [hep-ex/0208025].
[40] BaBar collaboration, *Measurement of the CP-violating asymmetry amplitude $\sin 2\beta$*, *Phys.*

TH-3118_176121005

Rev. Lett. **89** (2002) 201802 [hep-ex/0207042].
[41] BABAR collaboration, *Observation of direct CP violation in $B^0 \to K^+\pi^-$ decays*, *Phys. Rev. Lett.* **93** (2004) 131801 [hep-ex/0407057].
[42] LHCB collaboration, *First observation of CP violation in the decays of B_s^0 mesons*, *Phys. Rev. Lett.* **110** (2013) 221601 [1304.6173].
[43] CDF collaboration, *Observation of $B_s^0 - \bar{B}_s^0$ Oscillations*, *Phys. Rev. Lett.* **97** (2006) 242003 [hep-ex/0609040].
[44] Y. Nir, *Flavour Physics and CP Violation*, in *7th CERN–Latin-American School of High-Energy Physics*, pp. 123–156, 2015, DOI [1605.00433].
[45] Z. Ligeti, *TASI Lectures on Flavor Physics*, in *Theoretical Advanced Study Institute in Elementary Particle Physics: Journeys Through the Precision Frontier: Amplitudes for Colliders*, pp. 297–340, 2015, DOI [1502.01372].
[46] Y. Grossman and P. Tanedo, *Just a Taste: Lectures on Flavor Physics*, in *Theoretical Advanced Study Institute in Elementary Particle Physics: Anticipating the Next Discoveries in Particle Physics*, pp. 109–295, 2018, DOI [1711.03624].
[47] L.-L. Chau and W.-Y. Keung, *Comments on the parametrization of the kobayashi-maskawa matrix*, *Phys. Rev. Lett.* **53** (1984) 1802.
[48] "Utfitter." http://www.utfit.org/UTfit/ResultsSummer2018.
[49] L. Wolfenstein, *Parametrization of the Kobayashi-Maskawa Matrix*, *Phys. Rev. Lett.* **51** (1983) 1945.
[50] "Ckm quark-mixing matrix." https://pdg.lbl.gov/2022/reviews/contents_sports.html.
[51] HFLAV collaboration, *Averages of b-hadron, c-hadron, and τ-lepton properties as of 2021*, 2206.07501.
[52] J. C. Hardy and I. S. Towner, *Superallowed 0 + → 0 + nuclear β decays: A critical survey with tests of the conserved vector current hypothesis and the standard model*, *Physical Review C* **71** (2005) 055501.
[53] D. Pocanic et al., *Precise measurement of the pi+ —> pi0 e+ nu branching ratio*, *Phys. Rev. Lett.* **93** (2004) 181803 [hep-ex/0312030].
[54] FLAVIANET WORKING GROUP ON KAON DECAYS collaboration, *An Evaluation of $|V_{us}|$ and precise tests of the Standard Model from world data on leptonic and semileptonic kaon decays*, *Eur. Phys. J. C* **69** (2010) 399 [1005.2323].
[55] N. Cabibbo, E. C. Swallow and R. Winston, *Semileptonic hyperon decays and CKM unitarity*, *Phys. Rev. Lett.* **92** (2004) 251803 [hep-ph/0307214].
[56] N. Cabibbo, E. C. Swallow and R. Winston, *Semileptonic hyperon decays*, *Ann. Rev. Nucl. Part. Sci.* **53** (2003) 39 [hep-ph/0307298].
[57] E. Gamiz, M. Jamin, A. Pich, J. Prades and F. Schwab, *Determination of m(s) and —V(us)— from hadronic tau decays*, *JHEP* **01** (2003) 060 [hep-ph/0212230].
[58] E. Gamiz, M. Jamin, A. Pich, J. Prades and F. Schwab, *V(us) and m(s) from hadronic tau decays*, *Phys. Rev. Lett.* **94** (2005) 011803 [hep-ph/0408044].
[59] CLEO collaboration, *Precision Measurement of B(D+ —> mu+ nu) and the Pseudoscalar Decay Constant f(D+)*, *Phys. Rev. D* **78** (2008) 052003 [0806.2112].
[60] BESIII collaboration, *Precision measurements of $B(D^+ \to \mu^+\nu_\mu)$, the pseudoscalar decay constant f_{D^+}, and the quark mixing matrix element $|V_{cd}|$*, *Phys. Rev. D* **89** (2014) 051104 [1312.0374].
[61] BESIII collaboration, *Measurement of the branching fraction for the semi-leptonic decay $D^{0(+)} \to \pi^{-(0)}\mu^+\nu_\mu$ and test of lepton universality*, *Phys. Rev. Lett.* **121** (2018) 171803

TH-3118_176121005

[1802.05492].
[62] CCFR collaboration, *Determination of the strange quark content of the nucleon from a next-to-leading order QCD analysis of neutrino charm production*, *Z. Phys. C* **65** (1995) 189 [hep-ex/9406007].
[63] T. Bolton, *Determining the CKM parameter V(cd) from neutrino N charm production*, hep-ex/9708014.
[64] BESIII collaboration, *Study of the $D^0 \to K^- \mu^+ \nu_\mu$ dynamics and test of lepton flavor universality with $D^0 \to K^- \ell^+ \nu_\ell$ decays*, *Phys. Rev. Lett.* **122** (2019) 011804 [1810.03127].
[65] BESIII collaboration, *Improved measurement of the absolute branching fraction of $D^+ \to \bar{K}^0 \mu^+ \nu_\mu$*, *Eur. Phys. J. C* **76** (2016) 369 [1605.00068].
[66] BESIII collaboration, *Measurement of the $D_s^+ \to \ell^+ \nu_\ell$ branching fractions and the decay constant $f_{D_s^+}$*, *Phys. Rev. D* **94** (2016) 072004 [1608.06732].
[67] BaBar collaboration, *Measurement of the Absolute Branching Fractions for $D_s^- \to \ell^- \bar{\nu}_\ell$ and Extraction of the Decay Constant f_{D_s}*, *Phys. Rev. D* **82** (2010) 091103 [1008.4080].
[68] Belle collaboration, *Measurements of branching fractions of leptonic and hadronic D_s^+ meson decays and extraction of the D_s^+ meson decay constant*, *JHEP* **09** (2013) 139 [1307.6240].
[69] The DELPHI Collaboration, *Measurement of —vcs— using w decays at lep2*, *Phys. Lett.* (1998) 209.
[70] Belle collaboration, *Measurement of the CKM matrix element $|V_{cb}|$ from $B^0 \to D^{*-} \ell^+ \nu_\ell$ at Belle*, *Phys. Rev. D* **100** (2019) 052007 [1809.03290].
[71] Belle collaboration, *Measurement of the decay $B \to D \ell \nu_\ell$ in fully reconstructed events and determination of the Cabibbo-Kobayashi-Maskawa matrix element $|V_{cb}|$*, *Phys. Rev. D* **93** (2016) 032006 [1510.03657].
[72] "Semileptonic b-hadron decays, determination of vcb, vub." https://pdg.lbl.gov/2020/reviews/rpp2020-rev-vcb-vub.pdf.
[73] BaBar collaboration, *Study of $B \to \pi \ell \nu$ and $B \to \rho \ell \nu$ Decays and Determination of $|V_{ub}|$*, *Phys. Rev. D* **83** (2011) 032007 [1005.3288].
[74] Belle collaboration, *Measurement of the decay $B^0 \to \pi^- \ell^+ \nu$ and determination of $|V_{ub}|$*, *Phys. Rev. D* **83** (2011) 071101 [1012.0090].
[75] BaBar collaboration, *Branching fraction and form-factor shape measurements of exclusive charmless semileptonic B decays, and determination of $|V_{ub}|$*, *Phys. Rev. D* **86** (2012) 092004 [1208.1253].
[76] Belle collaboration, *Study of Exclusive $B \to X_u \ell \nu$ Decays and Extraction of $\|V_{ub}\|$ using Full Reconstruction Tagging at the Belle Experiment*, *Phys. Rev. D* **88** (2013) 032005 [1306.2781].
[77] BaBar collaboration, *Measurement of the $B^+ \to \omega \ell^+ \nu$ branching fraction with semileptonically tagged B mesons*, *Phys. Rev. D* **88** (2013) 072006 [1308.2589].
[78] CDF, D0 collaboration, *Tevatron Combination of Single-Top-Quark Cross Sections and Determination of the Magnitude of the Cabibbo-Kobayashi-Maskawa Matrix Element $\mathbf{V_{tb}}$*, *Phys. Rev. Lett.* **115** (2015) 152003 [1503.05027].
[79] "Lhc top working group summary plots, single top quark production, nov. 2017." https://twiki.cern.ch/twiki/bin/view/LHCPhysics/LHCTopWGSummaryPlots.
[80] D0 collaboration, *Precision measurement of the ratio $\mathrm{B}(t \to Wb)/\mathrm{B}(t \to Wq)$ and Extraction of V_{tb}*, *Phys. Rev. Lett.* **107** (2011) 121802 [1106.5436].
[81] CMS collaboration, *Measurement of the ratio $\mathcal{B}(t \to Wb)/\mathcal{B}(t \to Wq)$ in pp collisions at $\sqrt{s} = 8$ TeV*, *Phys. Lett. B* **736** (2014) 33 [1404.2292].

TH-3118_176121005

[82] LHCb collaboration, *Precision measurement of the B_s^0-$\bar{B}_s^0$ oscillation frequency with the decay $B_s^0 \to D_s^- \pi^+$*, *New J. Phys.* **15** (2013) 053021 [1304.4741].
[83] LHCb collaboration, *Measurement of CP violation in $B^0 \to J/\psi K_S^0$ decays*, *Phys. Rev. Lett.* **115** (2015) 031601 [1503.07089].
[84] BaBar collaboration, *Measurement of Time-Dependent CP Asymmetry in B0 —> c anti-c K(*)0 Decays*, *Phys. Rev. D* **79** (2009) 072009 [0902.1708].
[85] Belle collaboration, *Precise measurement of the CP violation parameter $\sin 2\phi_1$ in $B^0 \to (c\bar{c})K^0$ decays*, *Phys. Rev. Lett.* **108** (2012) 171802 [1201.4643].
[86] Belle collaboration, *Evidence for direct CP violation in the decay B->D(*)K, D->KsPi+Pi- and measurement of the CKM phase phi3*, *Phys. Rev. D* **81** (2010) 112002 [1003.3360].
[87] BaBar collaboration, *Evidence for direct CP violation in the measurement of the Cabibbo-Kobayashi-Maskawa angle gamma with B-+ —> D(*) K(*)-+ decays*, *Phys. Rev. Lett.* **105** (2010) 121801 [1005.1096].
[88] LHCb collaboration, *Measurement of the CKM angle γ using $B^\pm \to DK^\pm$ with $D \to K_S^0\pi^+\pi^-, K_S^0 K^+ K^-$ decays*, *JHEP* **10** (2014) 097 [1408.2748].
[89] "Ckmfitter global fit results as of summer 19." http://ckmfitter.in2p3.fr/www/results/plots_spring21/num/ckmEval_results_spring21.html.
[90] Y. Sakaki, M. Tanaka, A. Tayduganov and R. Watanabe, *Testing leptoquark models in $\bar{B} \to D^{(*)}\tau\bar{\nu}$*, *Phys. Rev. D* **88** (2013) 094012 [1309.0301].
[91] C. Bobeth, G. Hiller and G. Piranishvili, *Angular distributions of $\bar{B} \to \bar{K}\ell^+\ell^-$ decays*, *JHEP* **12** (2007) 040 [0709.4174].
[92] W. Altmannshofer, P. Ball, A. Bharucha, A. J. Buras, D. M. Straub and M. Wick, *Symmetries and Asymmetries of $B \to K^*\mu^+\mu^-$ Decays in the Standard Model and Beyond*, *JHEP* **01** (2009) 019 [0811.1214].
[93] C. Bobeth, G. Hiller and G. Piranishvili, *CP Asymmetries in bar $B \to \bar{K}^*(\to \bar{K}\pi)\bar{\ell}\ell$ and Untagged $\bar{B}_s$, $B_s \to \phi(\to K^+K^-)\bar{\ell}\ell$ Decays at NLO*, *JHEP* **07** (2008) 106 [0805.2525].
[94] S. Descotes-Genon, J. Matias, M. Ramon and J. Virto, *Implications from clean observables for the binned analysis of $B- > K*\mu^+\mu^-$ at large recoil*, *JHEP* **01** (2013) 048 [1207.2753].
[95] LHCb collaboration, *Angular analysis of the $B^0 \to K^{*0}\mu^+\mu^-$ decay using 3 fb^{-1} of integrated luminosity*, *JHEP* **02** (2016) 104 [1512.04442].
[96] LHCb collaboration, *Search for lepton-universality violation in $B^+ \to K^+\ell^+\ell^-$ decays*, 1903.09252.
[97] LHCb collaboration, *Test of lepton universality with $B^0 \to K^{*0}\ell^+\ell^-$ decays*, *JHEP* **08** (2017) 055 [1705.05802].
[98] LHCb collaboration, *Measurement of CP-averaged observables in the $B^0 \to K^{*0}\mu^+\mu^-$ decay*, 2003.04831.
[99] D. Becirevic, N. Kosnik, F. Mescia and E. Schneider, *Complementarity of the constraints on New Physics from $B_s \to \mu^+\mu^-$ and from $B \to Kl^+l^-$ decays*, *Phys. Rev. D* **86** (2012) 034034 [1205.5811].
[100] M. Beneke, C. Bobeth and R. Szafron, *Power-enhanced leading-logarithmic QED corrections to $B_q \to \mu^+\mu^-$*, *JHEP* **10** (2019) 232 [1908.07011].
[101] A. Paul and D. M. Straub, *Constraints on new physics from radiative B decays*, *JHEP* **04** (2017) 027 [1608.02556].
[102] M. Misiak, A. Rehman and M. Steinhauser, *Towards $\overline{B} \to X_s\gamma$ at the NNLO in QCD without interpolation in m_c*, *JHEP* **06** (2020) 175 [2002.01548].
[103] LHCb collaboration, *Measurements of the S-wave fraction in $B^0 \to K^+\pi^-\mu^+\mu^-$ decays*

TH-3118_176121005

and the $B^0 \to K^*(892)^0\mu^+\mu^-$ *differential branching fraction*, JHEP **11** (2016) 047 [1606.04731].

[104] CMS collaboration, *Angular analysis of the decay* $B^+ \to K^+\mu^+\mu^-$ *in proton-proton collisions at* $\sqrt{s} = 8$ *TeV*, Phys. Rev. **D98** (2018) 112011 [1806.00636].

[105] LHCb collaboration, *Angular analysis and differential branching fraction of the decay* $B_s^0 \to \phi\mu^+\mu^-$, JHEP **09** (2015) 179 [1506.08777].

[106] Belle collaboration, *Test of lepton flavor universality in* $B \to K^*\ell^+\ell^-$ *decays at Belle*, 1904.02440.

[107] ATLAS collaboration, *Angular analysis of* $B_d^0 \to K^*\mu^+\mu^-$ *decays in pp collisions at* $\sqrt{s} = 8$ *TeV with the ATLAS detector*, JHEP **10** (2018) 047 [1805.04000].

[108] LHCb collaboration, *First observation of the decay* $B^+ \to \pi^+\mu^+\mu^-$, JHEP **12** (2012) 125 [1210.2645].

[109] LHCb collaboration, *First measurement of the differential branching fraction and CP asymmetry of the* $B^\pm \to \pi^\pm\mu^+\mu^-$ *decay*, JHEP **10** (2015) 034 [1509.00414].

[110] B. O. Lange, M. Neubert and G. Paz, *Theory of charmless inclusive B decays and the extraction of V(ub)*, Phys. Rev. D **72** (2005) 073006 [hep-ph/0504071].

[111] S. W. Bosch, M. Neubert and G. Paz, *Subleading shape functions in inclusive B decays*, JHEP **11** (2004) 073 [hep-ph/0409115].

[112] S. W. Bosch, B. O. Lange, M. Neubert and G. Paz, *Factorization and shape function effects in inclusive B meson decays*, Nucl. Phys. B **699** (2004) 335 [hep-ph/0402094].

[113] J. R. Andersen and E. Gardi, *Inclusive spectra in charmless semileptonic B decays by dressed gluon exponentiation*, JHEP **01** (2006) 097 [hep-ph/0509360].

[114] P. Gambino, P. Giordano, G. Ossola and N. Uraltsev, *Inclusive semileptonic B decays and the determination of —V(ub)—*, JHEP **10** (2007) 058 [0707.2493].

[115] U. Aglietti, F. Di Lodovico, G. Ferrera and G. Ricciardi, *Inclusive measure of —V(ub)— with the analytic coupling model*, Eur. Phys. J. C **59** (2009) 831 [0711.0860].

[116] LHCb collaboration, *Determination of the quark coupling strength* $|V_{ub}|$ *using baryonic decays*, Nature Phys. **11** (2015) 743 [1504.01568].

[117] G. Buchalla, A. J. Buras and M. E. Lautenbacher, *Weak decays beyond leading logarithms*, Rev. Mod. Phys. **68** (1996) 1125 [hep-ph/9512380].

[118] C. Bobeth, M. Misiak and J. Urban, *Photonic penguins at two loops and* m_t *dependence of* $BR[B \to X_s l^+ l^-]$, Nucl. Phys. B **574** (2000) 291 [hep-ph/9910220].

[119] H. Asatrian, H. Asatrian, C. Greub and M. Walker, *Two loop virtual corrections to* $B \to X_s l^+ l^-$ *in the standard model*, Phys. Lett. B **507** (2001) 162 [hep-ph/0103087].

[120] M. Beneke and T. Feldmann, *Symmetry breaking corrections to heavy to light B meson form-factors at large recoil*, Nucl. Phys. B **592** (2001) 3 [hep-ph/0008255].

[121] A. G. Grozin and M. Neubert, *Asymptotics of heavy meson form-factors*, Phys. Rev. D **55** (1997) 272 [hep-ph/9607366].

[122] M. Beneke, T. Feldmann and D. Seidel, *Systematic approach to exclusive* $B \to V l^+ l^-$, $V\gamma$ *decays*, Nucl. Phys. B **612** (2001) 25 [hep-ph/0106067].

[123] M. Beneke, T. Feldmann and D. Seidel, *Exclusive radiative and electroweak* $b \to d$ *and* $b \to s$ *penguin decays at NLO*, Eur. Phys. J. C **41** (2005) 173 [hep-ph/0412400].

[124] P. Ball and G. W. Jones, *Twist-3 distribution amplitudes of K* and phi mesons*, JHEP **03** (2007) 069 [hep-ph/0702100].

[125] P. Ball, V. M. Braun, Y. Koike and K. Tanaka, *Higher twist distribution amplitudes of vector mesons in QCD: Formalism and twist - three distributions*, Nucl. Phys. B **529** (1998) 323 [hep-ph/9802299].

[126] W. Altmannshofer and D. M. Straub, *Cornering New Physics in* $b \to s$ *Transitions*, JHEP

TH-3118_176121005

08 (2012) 121 [1206.0273].
[127] C. Bourrely, I. Caprini and L. Lellouch, *Model-independent description of B —> pi l nu decays and a determination of —V(ub)—*, *Phys. Rev. D* **79** (2009) 013008 [0807.2722].
[128] C. G. Boyd, B. Grinstein and R. F. Lebed, *Constraints on form factors for exclusive semileptonic heavy to light meson decays*, *Phys. Rev. Lett.* **74** (1995) 4603.
[129] Fermilab Lattice, MILC collaboration, *$|V_{ub}|$ from $B \to \pi\ell\nu$ decays and (2+1)-flavor lattice QCD*, *Phys. Rev. D* **92** (2015) 014024 [1503.07839].
[130] J. M. Flynn, T. Izubuchi, T. Kawanai, C. Lehner, A. Soni, R. S. Van de Water et al., *$B \to \pi\ell\nu$ and $B_s \to K\ell\nu$ form factors and $|V_{ub}|$ from 2+1-flavor lattice QCD with domain-wall light quarks and relativistic heavy quarks*, *Phys. Rev. D* **91** (2015) 074510 [1501.05373].
[131] Fermilab Lattice, MILC collaboration, *B-meson semileptonic form factors on (2+1+1)-flavor HISQ ensembles*, *PoS* **LATTICE2019** (2019) 236 [1912.13358].
[132] C. G. Boyd, B. Grinstein and R. F. Lebed, *Precision corrections to dispersive bounds on form factors*, *Phys. Rev. D* **56** (1997) 6895.
[133] R. Andrae, T. Schulze-Hartung and P. Melchior, *Dos and don'ts of reduced chi-squared*, *arXiv e-prints* (2010) arXiv:1012.3754 [1012.3754].
[134] S. S. Shapiro and M. B. Wilk, *An analysis of variance test for normality (complete samples)*, *Biometrika* **52** (1965) 591.
[135] G. M. Jenkins, *Time Series Analysis; Forecasting and Control [by] George EP Box and Gwilym M. Jenkins*. San Francisco: Holden-Day, 1970.
[136] S. S. Wilks, *The Large-Sample Distribution of the Likelihood Ratio for Testing Composite Hypotheses*, *Annals Math. Statist.* **9** (1938) 60.
[137] H. Akaike, *Selected Papers of Hirotugu Akaike*. Springer, New York, NY, 1998, 10.1007/978-1-4612-1694-0.
[138] N. Sugiura, *Further analysts of the data by akaike' s information criterion and the finite corrections*, *Communications in Statistics - Theory and Methods* **7** (1978) 13 [https://doi.org/10.1080/03610927808827599].
[139] J. E. Cavanaugh, *Unifying the derivations for the akaike and corrected akaike information criteria*, *Statistics & Probability Letters* **33** (1997) 201 .
[140] A. Biswas, S. Nandi, S. K. Patra and I. Ray, *New physics in $b \to s\ell\ell$ decays with complex Wilson coefficients*, *Nucl. Phys. B* **969** (2021) 115479 [2004.14687].
[141] S. Descotes-Genon, L. Hofer, J. Matias and J. Virto, *Global analysis of $b \to s\ell\ell$ anomalies*, *JHEP* **06** (2016) 092 [1510.04239].
[142] LHCb collaboration, *Differential branching fractions and isospin asymmetries of $B \to K^{(*)}\mu^+\mu^-$ decays*, *JHEP* **06** (2014) 133 [1403.8044].
[143] A. Abdesselam et al., *Test of lepton flavor universality in $B \to K\ell^+\ell^-$ decays*, 1908.01848.
[144] ATLAS collaboration, *Angular analysis of $B_d^0 \to K^*\mu^+\mu^-$ decays in pp collisions at $\sqrt{s} = 8$ TeV with the ATLAS detector*, *JHEP* **10** (2018) 047 [1805.04000].
[145] Belle collaboration, *Lepton-Flavor-Dependent Angular Analysis of $B \to K^*\ell^+\ell^-$*, *Phys. Rev. Lett.* **118** (2017) 111801 [1612.05014].
[146] M. Misiak and M. Steinhauser, *Weak radiative decays of the B meson and bounds on $M_{H^\pm}$ in the Two-Higgs-Doublet Model*, *Eur. Phys. J.* **C77** (2017) 201 [1702.04571].
[147] Heavy Flavor Averaging Group (HFAG) collaboration, *Averages of b-hadron, c-hadron, and τ-lepton properties as of summer 2014*, 1412.7515.
[148] LHCb collaboration, *Measurement of the ratio of branching fractions $BR(B_0 \to K^{*0}\gamma)/BR(B_{s0} \to \phi\gamma)$ and the direct CP asymmetry in $B_0 \to K^{*0}\gamma$*, *Nucl. Phys.* **B867** (2013) 1 [1209.0313].

TH-3118_176121005

[149] "Hflav $b_s \to \mu\mu$ average." https://hflav-eos.web.cern.ch/hflav-eos/rare/April2019/BS/OUTPUT/HTML/bs_table1.html.
[150] "Ckmfitter." http://ckmfitter.in2p3.fr/www/results/plots_summer19/ckm_res_summer19.html.
[151] Flavour Lattice Averaging Group collaboration, *FLAG Review 2019*, 1902.08191.
[152] B. Capdevila, U. Laa and G. Valencia, *Anatomy of a six-parameter fit to the $b \to s\ell^+\ell^-$ anomalies*, *Eur. Phys. J. C* **79** (2019) 462 [1811.10793].
[153] L.-S. Geng, B. Grinstein, S. Jäger, J. Martin Camalich, X.-L. Ren and R.-X. Shi, *Towards the discovery of new physics with lepton-universality ratios of $b \to s\ell\ell$ decays*, *Phys. Rev.* **D96** (2017) 093006 [1704.05446].
[154] J. Matias, F. Mescia, M. Ramon and J. Virto, *Complete Anatomy of $\bar{B}_d - > \bar{K}^{*0}(- > K\pi)l^+l^-$ and its angular distribution*, *JHEP* **04** (2012) 104 [1202.4266].
[155] W. Altmannshofer, P. Stangl and D. M. Straub, *Interpreting Hints for Lepton Flavor Universality Violation*, *Phys. Rev. D* **96** (2017) 055008 [1704.05435].
[156] B. Capdevila, A. Crivellin, S. Descotes-Genon, J. Matias and J. Virto, *Patterns of New Physics in $b \to s\ell^+\ell^-$ transitions in the light of recent data*, *JHEP* **01** (2018) 093 [1704.05340].
[157] D. Bardhan, P. Byakti and D. Ghosh, *Role of Tensor operators in R_K and R_{K^*}*, *Phys. Lett. B* **773** (2017) 505 [1705.09305].
[158] W. Altmannshofer, M. J. Baker, S. Gori, R. Harnik, M. Pospelov, E. Stamou et al., *Light resonances and the low-q^2 bin of R_{K^*}*, *JHEP* **03** (2018) 188 [1711.07494].
[159] A. Biswas, S. Nandi, S. K. Patra and I. Ray, *A closer look at the extraction of $—V_{ub}—$ from $B \to \pi\ell\nu$*, *JHEP* **07** (2021) 082 [2103.01809].
[160] HFLAV collaboration, *Averages of b-hadron, c-hadron, and τ-lepton properties as of 2018*, 1909.12524.
[161] HFLAV collaboration, *Averages of b-hadron, c-hadron, and τ-lepton properties as of summer 2016*, *Eur. Phys. J. C* **77** (2017) 895 [1612.07233].
[162] C. Bourrely, I. Caprini and L. Lellouch, *Model-independent description of $B —> pi\ l\ nu$ decays and a determination of $—V(ub)—$*, *Phys. Rev. D* **79** (2009) 013008 [0807.2722].
[163] S. Aoki et al., *Review of lattice results concerning low-energy particle physics*, *Eur. Phys. J. C* **77** (2017) 112 [1607.00299].
[164] A. Bharucha, *Two-loop Corrections to the $B to \pi$ Form Factor from QCD Sum Rules on the Light-Cone and $|V_{ub}|$*, *JHEP* **05** (2012) 092 [1203.1359].
[165] A. Biswas, S. Nandi, S. K. Patra and I. Ray, *Study of the $b \to d\ell\ell$ transitions in the Standard Model and test of New Physics sensitivities*, 2208.14463.
[166] JLQCD collaboration, *Form factors of $B \to \pi\ell\nu$ and a determination of $|V_{ub}|$ with Möbius domain-wall-fermions*, 2203.04938.
[167] "Ckmfitter global fit results as of summer 19." http://ckmfitter.in2p3.fr/www/results/plots_summer19/num/ckmEval_results_summer19.html.
[168] Y. Aoki et al., *FLAG Review 2021*, 2111.09849.
[169] RQCD collaboration, *Light-cone distribution amplitudes of pseudoscalar mesons from lattice QCD*, *JHEP* **08** (2019) 065 [1903.08038].
[170] LHCb collaboration, *Differential branching fractions and isospin asymmetries of $B \to K^{(*)}\mu^+\mu^-$ decays*, *JHEP* **06** (2014) 133 [1403.8044].
[171] S. Descotes-Genon and J. Virto, *Time dependence in $B \to V\ell\ell$ decays*, *JHEP* **04** (2015) 045 [1502.05509].
[172] D. Bečirević, M. Fedele, I. Nišandžić and A. Tayduganov, *Lepton Flavor Universality tests through angular observables of $\overline{B} \to D^{(*)}\ell\overline{\nu}$ decay modes*, 1907.02257.

TH-3118_176121005

[173] M. Algueró, S. Descotes-Genon, J. Matias and M. Novoa-Brunet, *Symmetries in $B \to D^* \ell \nu$ angular observables*, *JHEP* **06** (2020) 156 [2003.02533].
[174] BaBar collaboration, *Branching fraction measurement of $B^+ \to \omega \ell^+ \nu$ decays*, *Phys. Rev. D* **87** (2013) 032004 [1205.6245].
[175] Fermilab Lattice and MILC Collaborations collaboration, *$B_s \to k \ell \nu$ decay from lattice qcd*, *Phys. Rev. D* **100** (2019) 034501.
[176] A. Khodjamirian and A. V. Rusov, *$B_s \to K \ell \nu_\ell$ and $B_{(s)} \to \pi(K) \ell^+ \ell^-$ decays at large recoil and CKM matrix elements*, *JHEP* **08** (2017) 112 [1703.04765].
[177] J. A. Bailey et al., *$B_s \to D_s / B \to D$ Semileptonic Form-Factor Ratios and Their Application to $BR(B_s^0 \to \mu^+ \mu^-)$*, *Phys. Rev. D* **85** (2012) 114502 [1202.6346].
[178] E. McLean, C. T. H. Davies, J. Koponen and A. T. Lytle, *$B_s \to D_s \ell \nu$ Form Factors for the full q^2 range from Lattice QCD with non-perturbatively normalized currents*, *Phys. Rev. D* **101** (2020) 074513 [1906.00701].
[179] M. Bordone, N. Gubernari, D. van Dyk and M. Jung, *Heavy-Quark expansion for $\bar{B}_s \to D_s^{(*)}$ form factors and unitarity bounds beyond the $SU(3)_F$ limit*, *Eur. Phys. J. C* **80** (2020) 347 [1912.09335].
[180] E. McLean, C. T. H. Davies, A. T. Lytle and J. Koponen, *Lattice QCD form factor for $B_s \to D_s^* l \nu$ at zero recoil with non-perturbative current renormalisation*, *Phys. Rev. D* **99** (2019) 114512 [1904.02046].
[181] HPQCD collaboration, *$B_s \to D_s^*$form factors for the full q^2 range from lattice QCD*, *Phys. Rev. D* **105** (2022) 094506 [2105.11433].
[182] LHCb collaboration, *Measurement of $|V_{cb}|$ with $B_s^0 \to D_s^{(*)-} \mu^+ \nu_\mu$ decays*, *Phys. Rev. D* **101** (2020) 072004 [2001.03225].
[183] MILC collaboration, *$B \to D \ell \nu$ form factors at nonzero recoil and —V_{cb}— from 2+1-flavor lattice QCD*, *Phys. Rev. D* **92** (2015) 034506 [1503.07237].
[184] HPQCD collaboration, *$B \to D l \nu$ form factors at nonzero recoil and extraction of $|V_{cb}|$*, *Phys. Rev. D* **92** (2015) 054510 [1505.03925].
[185] Fermilab Lattice, MILC collaboration, *Semileptonic form factors for $B \to D^* \ell \nu$ at nonzero recoil from 2 + 1-flavor lattice QCD*, 2105.14019.
[186] Fermilab Lattice, MILC collaboration, *$B \to \pi \ell \ell$ form factors for new-physics searches from lattice QCD*, *Phys. Rev. Lett.* **115** (2015) 152002 [1507.01618].

TH-3118_176121005